Hyperspectral, thermal and LiDAR remote sensing for red band needle blight detection in pine plantation forests

Magdalena Śmigaj

School of Engineering

Newcastle University

Thesis submitted for the degree of

Doctor of Philosophy

May, 2018

Abstract

Climate change indirectly affects the distribution and abundance of forest insect pests and pathogens, as well as the severity of tree diseases. Red band needle blight is a disease which has a particularly significant economic impact on pine plantation forests worldwide, affecting diameter and height growth. Monitoring its spread and intensity is complicated by the fact that the diseased trees are often only visible from aircraft in the advanced stages of the epidemic. There is therefore a need for a more robust method to map the extent and severity of the disease. This thesis examined the use of a range of remote sensing techniques and instrumentation, including thermography, hyperspectral imaging and laser scanning, for the identification of tree stress symptoms caused by the onset of red band needle blight. Three study plots, located in a plantation forest within the Loch Lomond and the Trossachs National Park that exhibited a range of red band needle blight infection levels, were established and surveyed. Airborne hyperspectral and LiDAR data were acquired for two Lodgepole pine stands, whilst for one Scots pine stand, airborne LiDAR and Unmanned Aerial Vehicle-borne (UAV-borne) thermal imagery were acquired alongside leaf spectroscopic measurements. Analysis of the acquired data demonstrated the potential for the use of thermographic, hyperspectral and LiDAR sensors for detection of red band needle blight-induced changes in pine trees. The three datasets were sensitive to different disease symptoms, i.e. thermography to alterations in transpiration, LiDAR to defoliation, and hyperspectral imagery to changes in leaf biochemical properties. The combination of the sensors could therefore enhance the ability to diagnose the infection.

Executive summary

Climate change will affect forests directly, for example through extended periods of drought, and indirectly, for example by affecting the distribution and abundance of forest pathogens and pests. One of the diseases which currently poses a significant risk to British forests is red band needle blight, which affects over 60 species of pine worldwide. In the late 1990s, it started spreading significantly across the UK, and since then it has caused serious damage to Scots, Corsican and Lodgepole pine crops. The rate of spread is particularly worrying as the disease's preferred host species cover an area of approximately 408,000 ha, constituting 15% of the total Great Britain's forest cover. Red band needle blight infection usually starts in the lower tree on older foliage and spreads upward, systematically defoliating the affected tree. Visual aerial surveillance is unproductive as the infection is often only visible from the aircraft in the advanced stages of the epidemic. There is therefore a need for a more robust method to map the extent and severity of the disease. This study examines the use of a range of remote sensing techniques and instrumentation, including thermography, hyperspectral imaging and laser scanning, for the identification of tree stress symptoms caused by the onset of red band needle blight.

Three study plots, located in a plantation forest within the Loch Lomond and the Trossachs National Park that exhibited a range of red band needle blight infection levels, were established and surveyed. Airborne hyperspectral and LiDAR data were acquired for two Lodgepole pine stands, whilst for the third Scots pine stand, airborne LiDAR and Unmanned Aerial Vehicle-borne (UAV-borne) thermal imagery were acquired. Furthermore, Scots pine foliage was collected to perform leaf spectroscopic measurements.

The UAV-borne thermal imagery was acquired with a miniature microbolometer thermal sensor. The performance of the imager was first investigated during laboratory-based and field-based experiments. Tests suggested that a rapid change in the camera's temperature is reflected in subsequent images. However, the expected rate of temperature change experienced during UAV launch and altitude gain would not have significant effect on the quality of acquired thermal imagery. Furthermore, it was shown that obtaining absolute temperatures of non-blackbody objects can be accurately performed with such a camera, providing the emissivity of surfaces is accurately known. Average difference between temperatures recorded for a high emissivity target and surface temperature

measurements were 1.39°C at 25 m range, and 1.04°C at 7 m range, which is within the accuracy threshold (±2.2°C) of the type K thermocouple used here. To assess the potential for using such a low-cost sensor to investigate tree stress in coniferous species, two experiments on drought-stressed larch trees in a greenhouse environment were conducted. Following calibration and a basic normalisation for background radiation, both the spatial and temporal variation of canopy temperature was well characterised. Very mild stress did not exhibit itself, as the temperature readings for both stressed and healthy plants were similar. However, higher stress levels, showed a clear distinction (temperature difference of 1.5°C) between the plants. The UAV-borne thermal imagery of the Scots pine plot was acquired at different times of the day to examine the influence of timing on the signal. Canopy temperatures of sixty sample trees were extracted, following registration to a LiDAR-derived canopy height model. Correlation was found with field-assessed disease level, with the highest score found at the time of highest solar radiation (correlation coefficient of 0.64 at p<0.001).

Leaf spectroscopy of green and partially chlorotic needles affected by red band needle blight was performed to identify the best spectral regions for detecting the infection. Three approaches for spectra analysis were investigated: spectral indices, derivative-based indices and continuum removal analysis, all of which highlighted the green, red and NIR parts of the electromagnetic spectrum as the most promising. Among the derivative metrics tested for separating the spectral response of the two sample groups, the best were based on first order derivative values retrieved in the green to red-edge region (leave-one-out cross validation accuracy of 87.5–90%). Broad-band indices showed varied performance sensitive to band placement (for example Enhanced Vegetation Index achieved 77.5–87.5%, whilst Renormalised Difference Vegetation Index yielded 55.0–82.5%); all of the 11 investigated narrow-band vegetation indices showed a more consistent performance, exceeding 75% success rate. The results informed airborne hyperspectral analysis performed on Lodgepole pine plantation sites. A k-means clustering algorithm was used to segment individual trees from the LiDAR point cloud, and create canopy cover masks to extract spectral signatures from the plots. Furthermore, a number of metrics describing canopy structure were extracted from the segmented point clusters. A good separation was found between the more diseased and consequently more defoliated plot, and the healthier pine stand using a number of spectral indices: the Enhanced Vegetation Index (72.3–93.2%), Normalised Difference Water Index (56.6–78.3%), Normalised Green-Red Difference Index (49.9–97.1%) and Photochemical Reflectance Index (81.1%). Similarly a distinction was found when intra-canopy

distribution of LiDAR returns were analysed. The clearest difference (of 13%) was found in the percentage of ground returns within the canopy extents. Nevertheless, no correlations between the LiDAR metrics or spectral indices and the visually estimated disease levels were found at an individual tree level, which could be due to limited spatial resolution of the imagery and the disease metric being insufficiently sensitive by not taking into account the level of defoliation.

The study demonstrated potential for the use of thermographic, hyperspectral and LiDAR sensors for detection of red band needle blight-induced changes in pine trees. The three datasets are sensitive to different disease symptoms, i.e. thermography to alterations in transpiration, LiDAR to defoliation, and hyperspectral imagery to changes in leaf biochemical properties. The combination of the sensors could therefore enhance the ability to diagnose the infection. During the hyperspectral analysis, common broad-band indices were generally shown to be more reliable, and consequently superior to narrow-band indices, demonstrating scope for use of multispectral imagery, providing bands are carefully chosen. There is therefore vast potential for the use of UAVs with low-cost sensors, currently capable of providing multispectral imagery. The very fine spatial resolution provided by such platforms would facilitate tree-level analysis of the diseased trees.

Acknowledgements

Related publications

The following publications contain work related to or derived from this thesis:

Smigaj, M., Gaulton, R., Suarez, J.C. and Barr, S.L. (2017) 'Use of Miniature Thermal Cameras for Detection of Physiological Stress in Conifers', *Remote Sensing*, 9(9), 957.

Smigaj, M., Gaulton, R., Barr, S.L. and Suarez, J.C. (2016) 'Investigating the performance of a low-cost thermal imager for forestry applications', *Proc. SPIE 10004, Image and Signal Processing for Remote Sensing XXII*, 100041E.

Smigaj, M., Gaulton, R., Barr, S.L. and Suárez, J.C. (2015) 'UAV-borne Thermal Imaging for Forest Health Monitoring: Detection of Disease-Induced Canopy Temperature Increase', *International Archives of the Photogrammetry, Remote Sensing and Spatial Information Sciences*, XL-3/W3, 349-354.

x

Table of contents

List of figures

List of tables

List of abbreviations

3FLD	3 bands Fraunhofer Line Depth
AIC	Akaike Information Criterion
ANN	Artificial neural network
AR	Autoregressive
ARF	Airborne Research Facility
ARIMA	Autoregressive Integrated Moving Average
B	Blue
BD	Band depth
CCF	Cross-correlation function
cFLD	Corrected Fraunhofer Line Depth
CHM	Canopy height model
CR	Continuum removal
CTD	Canopy temperature depression
CWSI	Crop Water Stress Index
DART	Discrete Anisotropic Radiative Transfer
DBH	Diameter at breast height
DEM	Digital elevation model
DWR	Downwelling radiance
DWSI	Disease Water Stress Index
eFLD	Extended Fraunhofer Line Depth
EVI	Enhanced Vegetation Index
EWDI	Enhanced Wetness Disturbance Index
EWT	Equivalent Water Thickness
FLD	Fraunhofer Line Depth
FLiES	Forest Light Environmental Simulator
FLIGHT	Three-dimensional Forest Light Interaction
FN	False negative
FP	False positive
FPA	Focal Plane Array
FTIR	Fourier Transform Infrared
FWHD	Full-width half-depth
GCP	Ground Control Point

GNDVI	Green Normalised Difference Vegetative Index
G	Green
GWC	Gravimetric water content
iFLD	Improved Fraunhofer Line Depth
INFORM	Invertible Forest Reflectance Model
LAI	Leaf Area Index
LiDAR	Light Detection And Ranging
LOOCV	Leave-one-out cross-validation
MA	Moving Average
MLC	Multi-level classification
MIR	Mid Infrared
mSR	modified Simple Ratio
MTVI	Modified Triangular Vegetation Index
MWU	Mann-Whitneu U
NBD	Normalised band depth
NBI	Narrow-band indices
NDSWIR	Normalised Difference SWIR Index
NDVI	Normalised Difference Vegetation Index
NDWI	Normalised Difference Water Index
NERC	Natural Environment Research Council
NGRDI	Normalised Green Red Difference Index
NIR	Near Infrared
PLSR	Partial Least Squares Regression
PPK	Post-processed Kinematic
PRI	Photochemical Reflectance Index
RDVI	Renormalised Difference Vegetation Index
R	Red
REP	Red Edge Position
RMSE	Root Mean Squared Error
RMSEP	Root Mean Squared Error of Prediction
RSR	Reduced simple ratio
RVSI	Red-edge Vegetation Stress Index
SAR	Synthetic Aperture Radar
SDA	Stepwise discriminant analysis
SfM	Structure from Motion

SFM	Spectral Fitting Method
SOD	Sudden oak death
SPRINT	Spreading of Photons for Radiation Interaction
SR	Simple ratio
SVM	Support vector machine
SWIR	Shortwave Infrared
TIR	Thermal Infrared
TM	Thematic Mapper
TP	True Positive
TVI	Triangular Vegetation Index
UAV	Unmanned Aerial Vehicle
USDA	U.S. Department of Agriculture
VIS	Visible
VNIR	Visible-Near Infrared
WI	Water Index

Chapter 1. Introduction

1.1 Importance of forest environments

Forests provide multiple benefits to the environment, people and wildlife. They shape the visual landscape, provide habitat for species that contribute to preserving biodiversity, maintain the water cycle and provide timber, as well as prevent land degradation and desertification (Joint Liaison Group, 2008; DEFRA and Forestry Commission, 2014). Forests are often called "green lungs" of the Earth as they make a vital contribution to the recycling of carbon dioxide from the atmosphere. Through sequestration they are able to reduce the amount of carbon dioxide in the atmosphere, absorbing around 9.53Gt of CO^2 per year (Solomon $et\ al.$, 2007). Inland forests are thought to reduce the frequency and magnitude of floods (Alila $et\ al.$, 2009; Tan-Soo $et\ al.$, 2016), whilst deforestation was shown to be a driver of soil erosion and consequent siltation of irrigation channels and agricultural fields (Bakoariniaina $et\ al.$, 2006; Minten and Randrianarisoa, 2012). Furthermore, especially in mountainous areas, woodlands provide protection from rock falls, debris flows and shallow landslides (Dorren $et\ al.$, 2004; Alila $et\ al.$, 2009). Forest environments are currently threatened by a number of factors, such as deforestation (Lewis $et\ al.$, 2015), drought (Millar and Stephenson, 2015), invasive species (Mack $et\ al.$, 2000), pests and pathogens (Wingfield $et\ al.$, 2015), air pollution (Mclaughlin, 1985), wildfire (Flannigan $et\ al.$, 2009), climate change (Ray $et\ al.$, 2010; Gauthier $et\ al.$, 2015) or unsustainable management (Suorsa $et\ al.$, 2003). Conservation of the forests is therefore imperative, as healthy trees are more stable and resilient to such hazards.

Healthy forests were conventionally described as those growing at their optimal capacity, unaffected by insects, diseases or wildfire (Kolb $et\ al.$, 1994). However, in the mid to late 20th century it has been recognised that natural disturbances were essential for the ecosystem, contributing to forest functioning and resilience (Raffa $et\ al.$, 2009). Current research focuses on developing the understanding of the severity of disturbance that can be tolerated before forest persistence is threatened (Millar and Stephenson, 2015). Monoculture plantation woodlands, such as those commonly grown in the UK, are particularly vulnerable to disturbance events. Relative species uniformity makes such stands highly susceptible to the native pests and diseases present in the natural forests, and increases their vulnerability to introduced pests and pathogens (Wingfield $et\ al.$, 2015). It is believed the future of planted forests will depend on the ability to detect and respond to the threat of biological invasions (Wingfield $et\ al.$, 2015).

1.2 Forest health and climate change in the UK

1.2.1 Direct climate change impacts

Tree growth and survival depends on edaphic and climatic conditions, which influence processes like photosynthesis and respiration. Thus changes in climate and weather conditions will inevitably influence forest health and growth (Thompson *et al.*, 2009). The climate globally is changing due to rising levels of greenhouse gases in the atmosphere, resulting from anthropogenic activities such as the burning of fossil fuels. The most important of these in terms of sheer volume is carbon dioxide. Its concentration in the atmosphere prior to industrialisation is estimated to have been approximately 270 ppm, which had risen up to a value of 391 ppm by 2011 (Broadmeadow and Ray, 2005; IPCC, 2013).

As a result, the Earth's climate has experienced a gradual warming with consequent changes to other variables such as rainfall, humidity and weather patterns. It is expected that over the coming century, temperature will increase by around 3°C at a global scale, whereas in the UK mean annual temperature is predicted to rise by up to 4.2°C by the 2080s, relative to 1961-1990 baseline (Murphy *et al.*, 2009; Christensen *et al.*, 2011). According to model simulations, a decrease in precipitation in the south of Europe is expected, particularly in the summer period, whilst over much of northern Europe an increase in precipitation is predicted (Blenkinsop and Fowler, 2007; Christensen and Christensen, 2007; Déqué *et al.*, 2007). It is suggested that, under the medium emissions scenario, rainfall over much of the UK will increase by up to 33% in winter months and decrease by as much as 40% in summer months by the 2080s, relative to the 1961-1990 baseline (Murphy *et al.*, 2009). Along with rising temperatures, the number of frost days in the UK is expected to sharply decrease; it is forecasted that by the 2080s the frequency of nights with temperature below or equal to 5°C will reduce from 15% to about 4% of all winter nights (Ray *et al.*, 2008).

Such climate change will have both direct and indirect effects on tree health and productivity. Since current carbon dioxide concentrations are not optimum for photosynthesis, it is expected that increased CO_2 emissions will enhance growth rates (Broadmeadow and Ray, 2005). Experiments conducted under elevated CO_2 concentrations of 475-600 ppm showed that leaf photosynthetic rates increased by an average of 40%, leading to a greater dry matter production both aboveground (by approximately 17%) and belowground (by more than 30%) (Taub, 2010). Warmer temperatures and the resulting lengthening of the growing season should increase the

productivity of trees, if water and nutrient availability do not become limiting factors (Ray *et al.*, 2010). However, substantial decreases in rainfall and increased temperatures over summer seasons are likely to lead to longer periods of drought stress on trees (Read *et al.*, 2009). Limited water availability can cause ring shake and drought crack in some species, leading to poor quality timber (Ray *et al.*, 2008; Read *et al.*, 2009). Such damage was, for example, encountered in 2003 in eastern Scotland within spruce forests, resulting in 14-20% mortality rate at some sites (Green and Duncan, 2009). Milder winters will accelerate the time of flushing, increasing the risk of late spring frost damage, which can significantly reduce productivity; in extreme circumstances, repeated frost injury can even result in mortality, particularly of young trees (Read *et al.*, 2009).

Higher winter rainfall will cause an increase in soil erosion and wetness, waterlogging and flooding throughout the UK (Ray *et al.*, 2010). Waterlogged soils rapidly become anaerobic as the supply of oxygen from the atmosphere is cut off by a very low rate of diffusion of oxygen through water. It can even make root systems of susceptible species cease to function and die (Fitter and Hay, 2001; Ray *et al.*, 2010). Such seasonally fluctuating water tables tend to reduce the depth of rooting, resulting in reduced tree stability. Limited root systems also restrict moisture availability, exacerbating summer water stress problems (Ray *et al.*, 2008; Read *et al.*, 2009).

1.2.2 Indirect climate change impacts

Climate change in the UK will also indirectly affect the distribution and abundance of forest insect pests and pathogens, as well as the severity of tree diseases (Ray *et al.*, 2008), as presented in Figure 1.1. The predicted temperature rise and longer growing season will generally favour insect population growth, by leading to faster insect development. It is suggested that the number of generations in a year (voltinism) for many insects will increase, giving the potential for semi-voltine insects to become uni-voltine, and uni-voltine insects to become multi-voltine (Ray *et al.*, 2008). Moreover, warmer winters will reduce insect mortality rates, allowing tree pests to extend their range (Ray *et al.*, 2010). Insect groups most likely to benefit from these changes are multi-voltine aphids, semi-voltine sawflies, weevils and lepidoptera, and most significantly semi-voltine bark beetles (Read *et al.*, 2009). Higher temperatures will not only increase the rate of population build up, but will also make stressed trees more vulnerable to attack (Ray *et al.*, 2008; Read *et al.*, 2009).

Climate change:

| Temperature rise | Change in rainfall pattern |

Direct effects:

| Longer growing season | Droughts | Waterlogging and flooding |

Indirect effects:

| Insect's faster development and lower mortality | Longer fungal pathogens activity | Increased tree vulnerability to attack | Increased pathogens propagation |
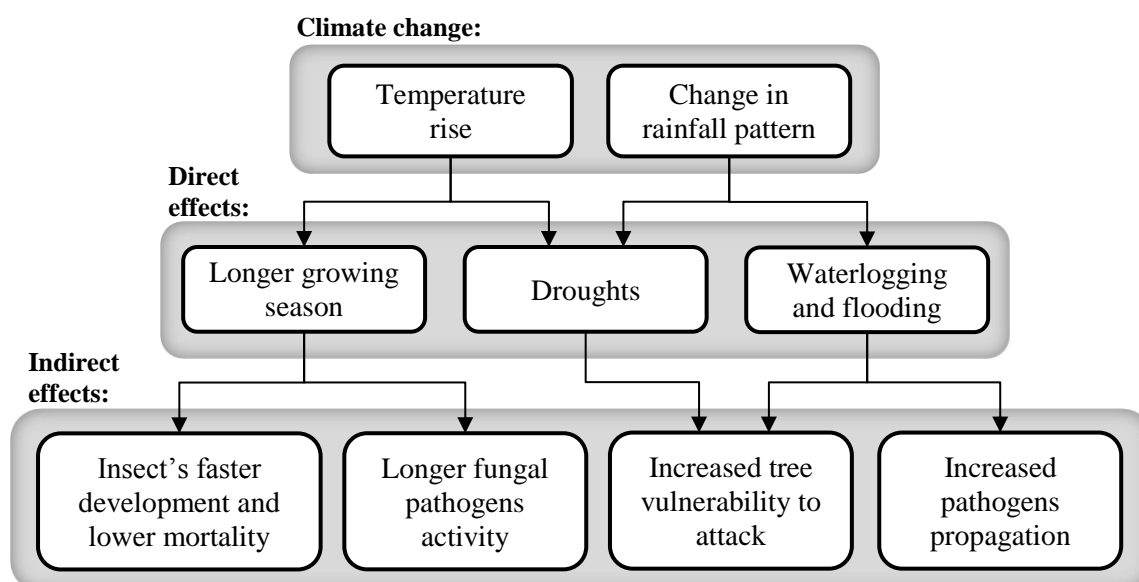
Figure 1.1: Climate change effects on forest insect pests and pathogens abundance.

Milder conditions will particularly benefit pathogens, such as *Dothistroma septosporum* (causing red band needle blight) and *Phytophthoras*, which thanks to temperatures closer to their optimum for growth and reproduction, will lengthen their periods of activity (Ray *et al.*, 2008). As *D. spetosporum* requires temperatures in the range of 12-18°C and high humidity for successful infection, warmer and wetter springs will favour its propagation and increase its potential to cause damage (Ray *et al.*, 2008). Similarly, most *Phytophthora* types require moist soil conditions or even periods of flooding for infection. These fungi principally attack roots, thus damage caused by them tends to be most visible over the summer, especially if trees experience drought stress (Brasier, 1999). Greater water table fluctuations, with occasional waterlogging, caused by changes in the pattern of rainfall will therefore significantly benefit the *Phytophthora* species (Broadmeadow and Ray, 2005).

It has been predicted that pests and pathogens currently distributed in the south of the UK may expand towards northern regions (Broadmeadow and Ray, 2005). Furthermore, changing climatic conditions will increase the risk of introduction of new 'exotic' pests and pathogens that previously were not able to survive in the UK (Ray *et al.*, 2008). International spread of invasive species is usually initiated by global trade of live plant material and timber, which allows them to pass natural barriers of their dispersal (Evans and Oszako, 2007). In fact, it is estimated that horticultural trade accounts for 90% of invasive introductions to the UK (Maynard and Allen, 2012).

Local movement of infected plant material also plays an important role in dispersal of pests and diseases. For instance, red band needle blight, caused by *D. septosporum*, can travel very long distances through movement of infected live plants and possibly seeds. Contaminated plant material has been a cause of multiple red band needle blight outbreaks in Scottish nurseries, which have had to be quarantined, and the stock destroyed. It is estimated that during an outbreak in 2010, the losses in just a single nursery exceeded £120,000 (HDC, 2011).

1.3 Impacts of tree diseases and pests on UK forestry

1.3.1 Overview of major diseases and their outbreaks

In recent years, various new pests and pathogens have established in the UK, posing significant risks to forests; these include several *Phytophthora* species, oak processionary moth (*Thaumetopoea processionea*), red band needle blight, Asian longhorn beetle (*Anoplophora glabripennis*) and ash dieback (Figure 1.2). Due to outbreaks of such pests and diseases UK forestry incurs costs annually of at least £130 million (Maynard and Allen, 2012).
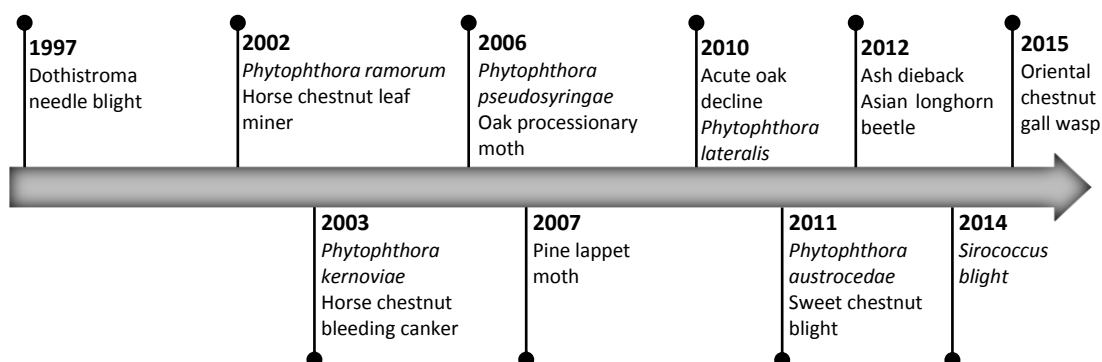
Figure 1.2: First outbreaks of major invasive pests and diseases in the UK over the past decade. The figure is based on data from Hendry (2013), Green *et al.* (2014) and Forestry Commission (2017).

The most severe epidemic within the UK so far, took place in the 1960s/70s, and was caused by the Dutch elm disease (*Ophiostoma novo-ulmi*). It faded primarily due to decimation of available host trees, resulting in death of over 30 million English elms (*Ulmus procera*) and drastic changes to landscapes. The disease is still present in the UK and continues to attack new elm trees emerging from the remaining rootstock (Maynard and Allen, 2012). Another serious disease is ash dieback, which is caused by *Chalara fraxinea*. Since it was first reported in Poland in 1992, it has caused widespread damage to ash (*Fraxinus* sp.) tree stock within continental Europe, mainly due to its rapid spread

and particularly destructive effect on young plants. *Chalara fraxinea* was first detected in the UK in 2012 in Buckinghamshire, and by 27th March 2013 the infection was confirmed at 440 sites across the whole of the UK (Forestry Commission Scotland, 2013b). Ash trees account for 5% of UK's woodland cover, and if infection was to follow similar rates as in Denmark, up to 72 million trees could ultimately be affected (Downing, 2012).

The oak processionary moth is a significant forest pest, whose larvae feed on the foliage of oak trees (*Quercus* sp.), and when abundant can cause complete defoliation. Repeated infestation can weaken the tree and make it more susceptible to other pests and pathogens, which may lead to oak decline and in some cases to its death (Forestry Commission, 2009). The establishment of oak processionary moth as a widespread breeding species in Britain would have major implications for forestry, horticulture and public health (Forestry Commission, 2009). Its larvae were found in the UK for the first time in 2006 at two sites in west London and are believed to have originated from imported semi-mature oak trees (Forestry Commission, 2009). Despite intensive treatment, including pesticide and pheromone trap use, as well as manual nest removal, the pest has continued to spread, with infections now present outside of London (Forest Research, 2017b).

Currently the most significant, in terms of potential damage, types of *Phytophthora* present in the UK are *P. ramorum*, and *P. kernoviae*. *P. ramorum*, more commonly known as 'sudden oak death', which is capable of causing serious damage to a wide range of plants (DEFRA, 2008). Even though *P. ramorum* rarely affects UK's native oaks (*Quercus petraea* and *Quercus robur*), it has other host species such as sweet chestnut (*Castanea sativa*), Holm oak (*Quercus ilex*) and larches (*Larix* sp.). A species that was found to be particularly vulnerable is Japanese larch (*Larix kaempferi*), widely used in commercial plantations. The pathogen can cause its death within one to two growing seasons, negatively affecting its economic and environmental value (Forestry Commission Scotland, 2013a). *Phytophthora kernoviae* is a related pathogen which affects similar plants to *P. ramorum* (DEFRA, 2008; Webber *et al.*, 2009).

One of the most recently introduced pests is the Asian longhorn beetle, an insect native to China and south eastern Asia. The most serious damage to trees is caused by its larvae, which develop under the bark and within the wood. If larvae feed in the vascular tissue, they lead to death of the overlying bark and may cause rapid wilting of leaves. However if they are mining in the heartwood, they weaken branches and trunks, making them susceptible to diseases and wind damage. Ongoing infestation can lead to death of

affected branches, development of dead tops on trees, or even death of whole trees (CSL, 2004). Asian longhorn beetle has a wide range of primary host trees. It is thus believed that if the Asian longhorn beetle established in the UK, it would cause extensive damage to both urban and forest trees (Forestry Commission, 2013).

1.3.2 Red band needle blight

Red band needle bight is a disease, caused by fungus *Dothistroma septosporum*, the detection of which is the focus of this thesis. It affects more than 60 species of pine, very rarely causing tree mortality (Ray et al., 2008). However, it significantly affects diameter and volume growth. Red band needle blight is characterised by yellow or tan spots that appear on the needles and turn reddish or brown-reddish (Bulman *et al.*, 2008). Within them, small, black, spore-containing fruit bodies are formed, which erupt during May-June (Figure 1.3) (HDC, 2011). The fungus is dispersed through movement of infected plant material, and atmospheric humidity, i.e. mists or moist winds. Infection usually starts in the lower parts of the crown on older foliage, and is most apparent in June and July prior to defoliation (Macdonald, 2011). Defoliation caused by *D. septosporum* can occur throughout the year; however, it is most noticeable between September and October, when the old needles that carried the infection are shed (Bulman *et al.*, 2008).
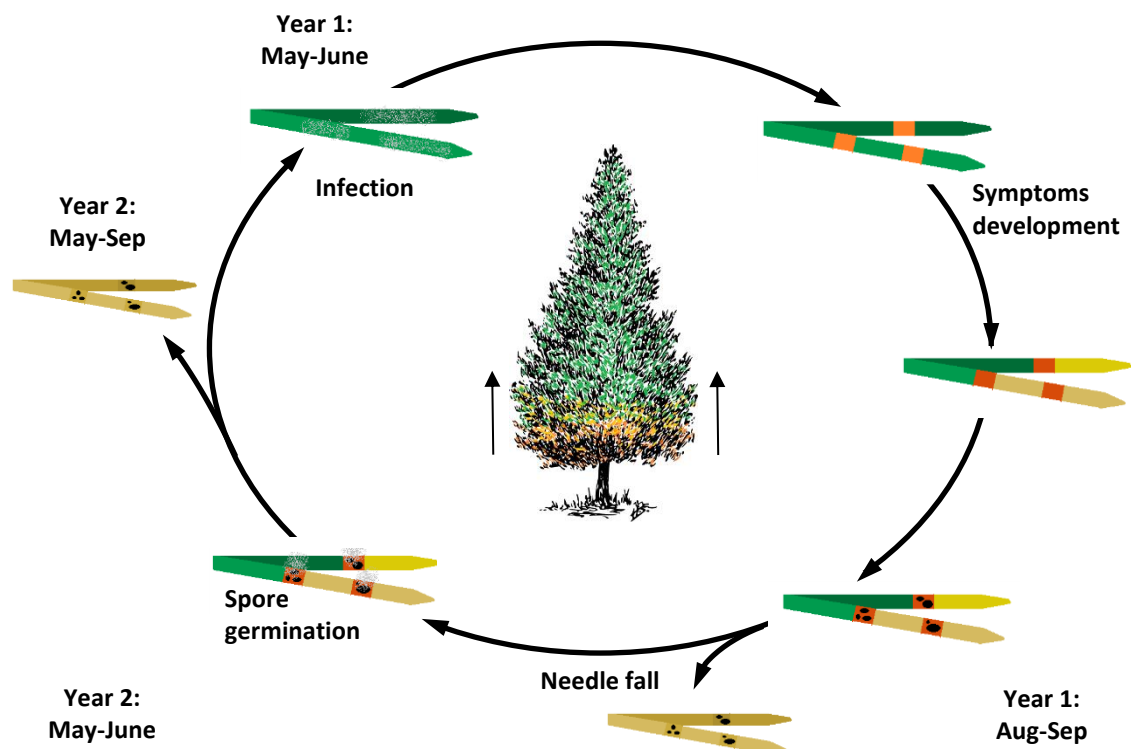
Figure 1.3: Diagrammatic life cycle of red band needle blight. Based on HDC (2011).

Red band needle blight has a worldwide distribution, and has been found in widely differing climates, such as Alaska and Jamaica (Bulman *et al.*, 2008). In the UK it was first reported on Corsican and ponderosa pines (*Pinus nigra* and *Pinus ponderosa*) in 1950s and 1960s in Dorset. In the late 1990s it started spreading significantly across the UK, causing serious damage to Corsican pine crops. By 2008, it had infected Scots and Lodgepole pines (*Pinus sylvestris* and *contorta*) in Scotland (Ray *et al.*, 2008). During a survey of the public forest estate, undertaken in 2006, *D. septosporum* was found within 70% of Corsican pine stands younger than 30 years. Further assessment of infected areas in 2009 revealed that 85% of measured stands had over 50% of needles infected (Forestry Commission, 2012). Additionally, according to assessments of East Anglia Forest District, the impact factor of the disease on Corsican pine stands, which is given as a combination of needle loss and crown infection, has almost doubled since it was first evaluated in 2003 (Forestry Commission, 2012). It was also assessed that in 2012, within Scotland alone, red band needle blight was present within circa 7,500 ha of Lodgepole pine, 3,300 ha Scots pine and 250 ha of Corsican pine (Forestry Commission, 2012). The rapid spread of *D. septosporum* in recent years is most likely due to availability of host trees, the fungus virulence, and increased movement of host material through plant and nursery trades (Macdonald, 2011). It is also believed that increased temperatures, and greater spring and summer rainfall may have optimised conditions for spore dispersal (Macdonald, 2011). The rate of spread of red band needle blight is particularly worrying as its preferred host species in Great Britain cover an area of approximately 363,000 ha, constituting 11.5% of the total forest cover (Figure 1.4) (Forestry Commission, 2016).

Red band needle blight can be controlled by breeding resistant planting stock, fungicide spraying and silvicultural interventions. The interventions can involve stand manipulations, such as thinning, pruning, respacing, brashing (removal of lower branches) or weeding (Brown, 2010). Stand manipulations decrease the amount of infected material (and therefore inoculum) and can improve the airflow within a stand, decreasing humidity levels and making the microclimate less favourable to the disease (Brown, 2010). Alternatively, copper-based fungicides could be used to suppress red band needle blight (Brown and Webber, 2008). However, as copper has been shown to build up in the soil of some horticultural crops, there are environmental concerns regarding the pollution of watercourses, which could arise from repeated applications of the fungicides (HDC, 2011). In the UK, currently no chemicals are registered for disease control in forests, but trials are ongoing (Brown and Webber, 2008).

	England	Wales	Scotland	Great Britain
⊞ Corsican Pine	40000	2000	3000	45000
⧄ Lodgepole pine	8000	4000	88000	100000
■ Scots pine	61000	3000	154000	218000
⊠ Total	109000	9000	245000	363000
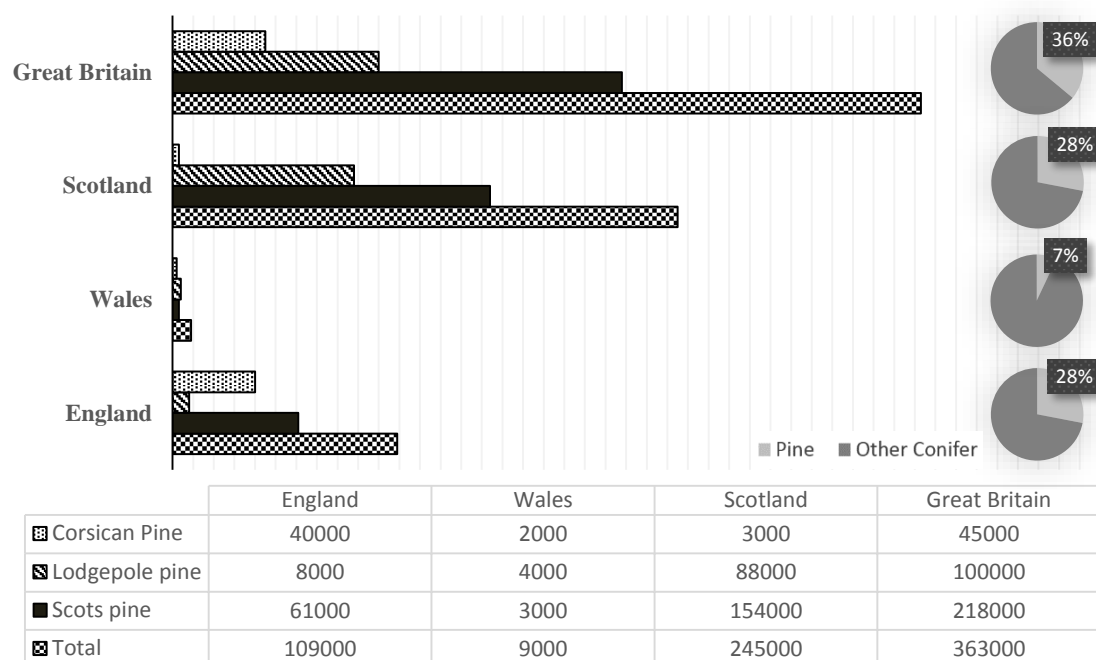
Figure 1.4: Planted areas, given in ha, of Corsican, Lodgepole and Scots pines, along with their contribution to overall area of conifer forests in Great Britain. Based on data from Forestry Commission (2016).

1.4 Forest health monitoring approaches in Great Britain

Between 1984 and 2006 Forest Research performed an annual survey of Great Britain's forest health, called the Forest Condition Survey. In 1985, it was coordinated with other forest condition monitoring programmes across Europe under a United Nations Economic Commission for Europe initiative (ICP-Forests), later known as "Level I" programme (Vanguelova *et al.*, 2007). The Forest Condition Survey involved an annual assessment of the condition of approximately 8400 trees of five species, located across the country in a network of 350 plots. Great Britain was initially divided into six regions, within which plots were established using a stratified sampling design. The plots for each tree species in all regions were chosen to display all possible combinations of three variables (altitude, rainfall, and sulphur deposition – the primary cause of acid rain) and of their levels (high and low) (Hendry, 2004).

The assessments carried out on individual trees included a number of variables, such as diameter at breast height, tree height and canopy closure. Additionally, the crown discolouration, as well as type and extent of biotic and abiotic damage present on the trees was visually assessed, and recorded. Another important variable was crown density, which gave an indirect evaluation of defoliation. The Forest Condition Survey not only

provided a national overview of forest health in Great Britain, but also contributed to the EU forest health monitoring programme (Hendry, 2004).

Although the Level I network provided accurate information on crown condition in Great Britain and Europe, it was unable to identify the cause of observed changes in forest condition. To overcome this issue, in 1994, a second monitoring network, the Intensive Monitoring Network or "Level II" network, was established. In Great Britain in 1995, ten long-term Level II intensive monitoring plots were established in oak, Sitka spruce (*Picea sitchensis*) and Scots pine plantations (Vanguelova *et al.*, 2007). Fourteen further plots in oak (2002, 2009), Scots pine (2002, 2009), beech (*Fagus* sp., 2002, 2009) and Norway spruce stands (*Picea abies*, 2002) were later established (Forest Research, 2017a). The plots were located across the country to ensure coverage of a broad range of climatic conditions and air pollution exposure levels (Figure 1.5) (Vanguelova *et al.*, 2007). Each plot covers an area of 0.25-0.3 ha and contains a permanent mensuration plot of 0.1 ha dedicated to tree growth measurements. Apart from tree growth and crown condition, a wide range of other variables, including foliar chemistry, litter fall, air quality and soil solution chemistry are assessed (Vanguelova *et al.*, 2007).

New infections by pests and diseases in woodlands and the wider environment are identified mainly through aerial surveillance. The infections are confirmed through ground level surveys of suspect sites (DEFRA and Forestry Commission, 2014). However, in the case of red band needle blight, the infection is often only visible from the aircraft in the advanced stages of the epidemic. There is therefore a need for a more robust method to map the extent and severity of the disease.

To complement the current infection detection efforts, ObservaTREE has developed a citizen-based system for early tree health warning. The project depends on groups of trained volunteers with technical expertise to record and verify instances of diseases (DEFRA and Forestry Commission, 2014). Furthermore, Forestry Commission has created an online tool called Tree Alert for the general public to report sightings of tree pests or diseases (Perez-Sierra, 2016).
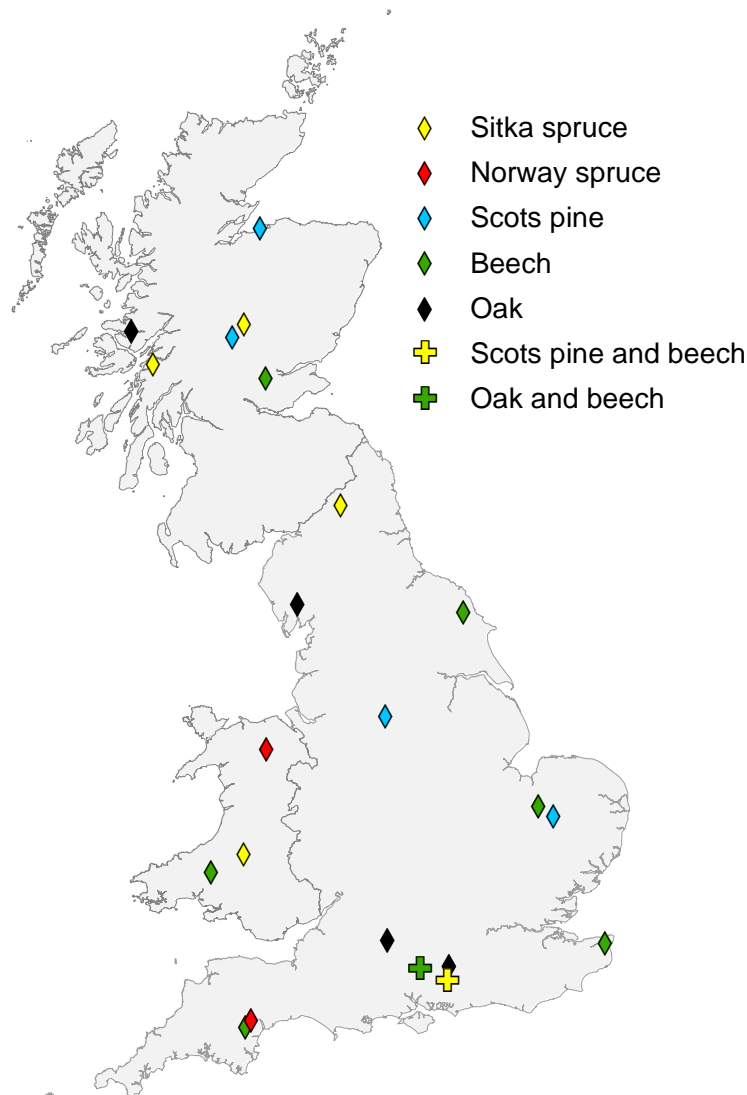
Figure 1.5: Location of Level II plots in Great Britain, based on Forest Research (2017a).

1.5 Remote sensing potential for forest disease monitoring

Timely detection of tree diseases is particularly important as timing is crucial for both limiting the damage to trees and treating the disease (Elmendorf *et al.*, 2000). Traditionally, monitoring is performed through field surveys, which is the most accurate approach, but normally also restricted to a limited number of plots across a country. It is widely considered that field surveys are expensive, labour-intensive, time-consuming, and thus unsuitable for monitoring large spatial extents of forest stands (Hendry, 2004; Lausch *et al.*, 2013). Remote sensing can potentially be a solution to this problem as it can provide better spatial coverage, shorter sampling intervals, and access to remote or restricted areas (Jyrki *et al.*, 2009). Moreover, as data are acquired in a digital form, their processing and integration with other data sources can be performed much faster. Another important advantage of remote sensing is that it utilises wavelength ranges not visible to

the human eye, which contain useful information on forest parameters, such as chlorophyll and water content (Malthus *et al.*, 2002). It is suggested that forest damage, such as crown discolouration and dieback, caused by some insects and diseases, is usually more visible from above the canopy (Ciesla, 2000).

Remote sensing technology has already been successfully used to monitor vegetation stress, wind throw, fire damage, as well as tree mortality due to pest infestation (Jackson *et al.*, 2000; Quintano *et al.*, 2011; Stagakis *et al.*, 2012; Fassnacht *et al.*, 2014). It has to be remembered though that remote sensing has its limitations. For example, in the case of dense forests composed of trees of different ages, smaller ones may be covered and only visible during field surveys (Lee and Cho, 2006). Additionally, algorithms used to retrieve vegetation properties may fail to produce reliable results, and thus have to be validated using field measurements (Jyrki *et al.*, 2009). For instance, the Normalised Difference Vegetation Index (NDVI) was found to saturate, and thus underestimate the vegetation cover in high biomass regions, e.g. the Amazon (Huete *et al.*, 2002). Nevertheless, it is considered that remote sensing could have an important role in forest health monitoring, and that further synergy with traditional methods is critical for adequate monitoring at the local, regional and national levels (Köhl *et al.*, 2006).

1.6 Thesis aim and scope

Red band needle blight is a disease which can cause severe damage to pine stands across the UK. Its growth is due to a combination of factors, such as suitable climatic conditions (now becoming even more favourable due to climate change), availability of suitable hosts (pines constitute 11% of total forest cover) and virulent fungal population. The disease has a particularly significant economic impact on plantation forests, having a dramatic effect on diameter and height growth of trees in heavily infected stands; for instance, in the UK preliminary studies showed a mean crown infection of 70% cause a 68% decrease in mean annual volume increment (Brown and Webber, 2008). Monitoring the spread and intensity of red band needle blight is complicated by the fact that the diseased trees are often only visible from the aircraft in the advanced stages of infection.

The aim of this research is to examine the ability to detect the severity of red band needle blight with different remote sensing technologies, and assess the potential for use of low-cost platforms and sensor fusion approaches for detection of the infection. For this purpose a range of remote sensing techniques and instrumentation is used. The main research questions are:

1) What are the physiological changes in trees occurring following infection, and how can they be detected using high spatial resolution remotely sensed data?
2) Can disease-induced temperature increase be detected in conifers using low-cost Unmanned Aerial Vehicle-borne (UAV) systems?
3) Can red band needle blight infection be detected using hyperspectral and LiDAR sensors?
4) Can integration of different high spatial resolution remotely sensed data improve detection of diseased forest stands?
5) Is there a potential to use low-cost platforms (i.e. UAVs) in forest studies, in particular for assessment of tree health status?

In order to address these research questions, a study based on four pine plantation stands in the Loch Lomond and the Trossachs National Park, Scotland, UK, which exhibited a range of red band needle blight infection levels was undertaken. The main objectives of this study and the resulting thesis are:

1) To successfully calibrate a low-cost thermal infrared camera for use in a UAV-borne survey, and test its performance in laboratory and outdoor conditions;
2) To assess the potential for using the calibrated low-cost thermal infrared sensor to investigate tree stress in coniferous species and examine the influence of data acquisition timing on the signal;
3) To investigate the spectral properties of diseased needles, derive the most distinctive disease indicators, and test their transferability to airborne imagery;
4) To examine canopy structural changes caused by the disease-induced defoliation; and,
5) To discuss the potential of integration of different remotely sensed data for improved detection of the disease, and the potential of low-cost platforms for assessment of tree health.

1.7 Thesis structure

Chapter 1 has provided an introduction to direct and indirect implications of climatic changes on forest health, and showed the need for more robust monitoring approaches. Finally, the main aim and objectives of this thesis have been introduced.

Chapter 2 provides a critical understanding of how common symptoms occurring during disease onset or infestation can be detected and quantified using remote sensing technologies.

Chapter 3 introduces the study area, and provides a summary of remote sensing data acquisition and the pre-processing steps, as well as a description of the methods used for acquiring accompanying field measurements.

Chapter 4 presents the calibration of the low-cost thermal infrared camera. Furthermore, it investigates the performance of the sensor in terms of retrieving accurate temperature readings in laboratory and field conditions.

Chapter 5 examines the use of the low-cost thermal infrared camera for analysing thermal properties of healthy and stressed trees. It covers two experiments performed on young larch trees with induced drought stress in a greenhouse setting, and on young pine plantation, infected with red band needle blight, using a UAV platform.

Chapter 6 investigates spectral characteristics of pine foliage affected by red band needle blight with help of leaf-level spectroscopic data.

Chapter 7 examines spectral characteristics of pine foliage affected by red band needle blight at a plot-level, utilising results from Chapter 6. Complementarily, it presents an investigation into forest structural parameters of the affected plots.

Chapter 8 summarises the findings and contribution of this research, discusses the potential for sensor fusion and use of low-cost platforms, and highlights further research needs.

Chapter 2. Literature review

2.1 Chapter overview

This chapter will provide a critical review of how common symptoms occurring during disease onset or infestation can be detected and quantified using remote sensing technologies. It will include an overview of methods used for retrieval of pigment concentration, Leaf Area Index (LAI), water content and stomatal conductance. Finally, a review of studies focused on the use of remote sensing for agricultural crops and forest health monitoring will be provided. The focus will be put on identification of disease/pest outbreak's extent using classification methods, and detection of their symptoms.

2.2 Common disease symptoms

Stresses induced by an invasion of insects or onset of disease manifest themselves in tree foliage, and may result in a variety of changes to plant's physiological processes, such as photosynthesis and respiration (Wulder and Franklin, 2003). The chemical composition of foliage has been found to be a major indicator of the disease onset, with photosynthetic pigments (chlorophyll *a*, chlorophyll *b* and carotenoids), nutrients (e.g. nitrogen) and carbon being the main chemical constituents (Wulder and Franklin, 2003). As pigments are integrally related to the physiological functioning of leaves, variations in their concentration may provide an indication on the plant's health (Sims and Gamon, 2002; le Maire *et al.*, 2004). Chlorophylls absorb radiation, which provides energy for photosynthesis, and transfer it into the photosynthetic system. Carotenoids (yellow pigments) can also contribute energy, however, their main role is to protect the reaction centres from excess light, avoiding damage to the leaf tissue (Sims and Gamon, 2002). When plants are subject to stress or undergoing leaf senescence, chlorophyll tends to decline more rapidly than carotenoids, making its concentration change more indicative of stress and phenological status. Along with the carotenoids content in leaves it also provides information on plants physiological status (Blackburn, 1998b; Sims and Gamon, 2002). Initially, during disease onset, the changes in pigments concentrations may be relatively small. However, as stress levels increase further, infected areas can experience the breakdown of pigments, disassembly of the photosynthetic apparatus and cell wall collapse, eventually causing necrosis (Blackburn, 1998b; Moshou *et al.*, 2012). Increasing necrosis can lead to reduction in leaf area due to severe loss of foliage (Wulder and Franklin, 2003).

Another common disease symptom occurring on the host plant is water shortage (Burdon, 1987). Most foliar, stem and root diseases alter the water relations of plants causing water deficit, which results from accelerated water loss (various foliar diseases), disruptions of transpiration (vascular wilt diseases) or damage to the root system (soil-borne diseases). Injury of root systems is often a result of declining assimilate translocation (transport of photosynthetic product from shoots) or root's necrosis induced by soil-borne pathogens, and may affect the mineral nutrients and water uptake (Burdon, 1987). Under moderate stress, stomatal closure and reduction in photosynthetic activity occurs, whilst with the onset of severe water stress, a general disruption of metabolism develops, which is signalled by high rates of respiration (Hopkins and Hüner, 2008). The closure of stomatal aperture is a defence mechanism that not only helps reduce water losses, but also prevents the entry of microbes and host tissue colonisation. It was also found to lead to increased leaf and plant temperature (Chaerle and Van Der Straeten, 2000; Moshou *et al.*, 2012; Montillet and Hirt, 2013). This is due to leaf temperature being primarily determined by the rate of transpiration, required for evaporative cooling of leaves (González-Dugo *et al.*, 2006). When a plant is under stress, stomatal closure can occur, leading to an increase in leaf and canopy temperature (Chaerle *et al.*, 1999a; Lindenthal *et al.*, 2005).

2.2.1 Spectral properties of healthy and diseased vegetation

Vegetation has distinctive spectral properties, which are primarily controlled by scattering and absorption characteristics of the leaf internal structure and biochemical components, such as photosynthetic pigments, nitrogen, water, cellulose and lignin (Govender *et al.*, 2009). Figure 2.1 shows a typical reflectance of healthy vegetation, obtained from a Lodgepole pine needles sample.

The spectral response of vegetation in the visible (VIS) part of electromagnetic spectrum, characterised by low reflectance and transmittance, is dominated by foliar pigments absorption. The absorbed energy is used by chloroplasts during photosynthesis to produce adenosine triphosphate, required to fuel plant maintenance and growth. The pigments which absorb visible energy in chloroplasts include chlorophylls, carotenoids such as β-carotene, and other accessory pigments. Foliar amounts of the main photosynthetic pigments chlorophyll *a*, chlorophyll *b* and the carotenoids are strongly related to the photosynthetic potential of vegetation, providing information on plant's condition and functioning (Blackburn, 2002). The chlorophylls are characterised by strong absorption of light in the blue and red parts of visible light, whilst carotenoids have their maximum absorption region in the blue part (Sims and Gamon, 2002). As pigments do not absorb

radiation at wavelengths above 700 nm, there is present a sharp change in leaf's absorption near this wavelength, leaving a high reflectance characterised by the water content and internal structure. This shift is called the red edge, and is considered a diagnostic feature of healthy vegetation (Eismann, 2012).
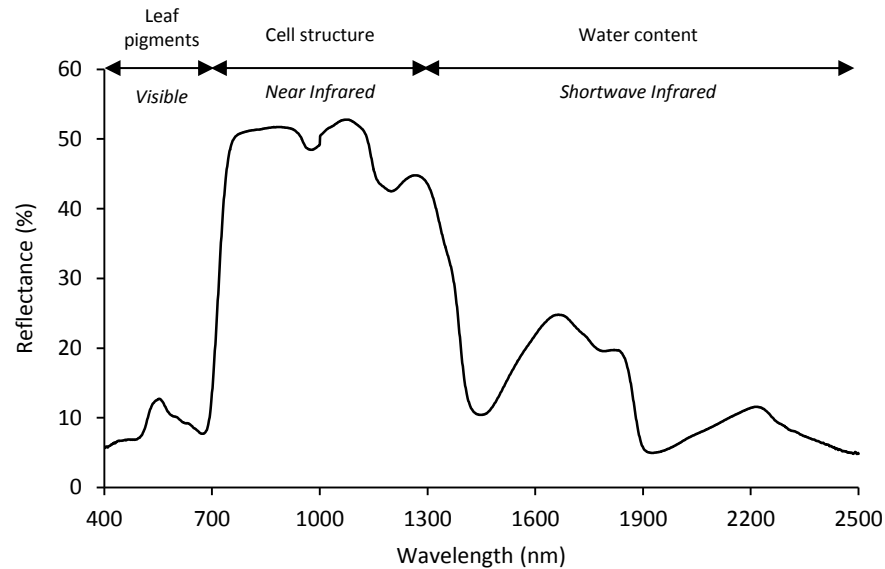
Figure 2.1: Typical spectral reflectance of vegetation in the optical region of the spectrum, as controlled by leaf pigments, cell structure and water content; obtained from a Lodgepole pine needles sample.

In the Near Infrared (NIR) region, vegetation response is characterised by high reflectance (40-50%), high transmittance and very low absorbance. Reflectance in this region is primarily caused by volume scattering within leaf structures, and is therefore influenced by the arrangement, size, and shape of cells, as well as by distribution of the air spaces within a leaf. As the transmitted energy may also be reflected by lower levels of the canopy, the total near infrared reflectance is not only determined by leaf structure, but also by the number of leaf layers in the canopy (Lillesand *et al.*, 2008; Eismann, 2012).

The spectral response of vegetation in the Shortwave Infrared (SWIR) region, is primarily governed by strong water absorption, but is also influenced by foliar contents such as cellulose, lignin, and pectin. Pure liquid water exhibits absorption peaks at 980, 1200, 1470 and 1940 nm, which can be observed as reflectance minima in Figure 2.1. Generally as water content increases, the reflectance in those regions decreases (Eismann, 2012).

Abiotic and biotic stresses interfere with photosynthesis and physical structure of vegetation, affecting the absorption of light and thus altering the reflectance spectrum of vegetation (Prabhakar *et al.*, 2012). Plant stress, like normal senescence, typically results in lower chlorophyll concentration that allows expression of β-carotene and xanthophylls. Spectrally, it results in broadening of the reflectance peak located near 550 nm. The broadening occurs towards longer wavelengths, increasing visible reflectance, and causing leaves to appear chlorotic (Pinter Jr. *et al.*, 2003). At the same time, with increasing stress, NIR reflectance decreases and the red edge begins to shift towards shorter wavelengths. In the case of senescent vegetation the red edge may disappear entirely (Pinter Jr. *et al.*, 2003). In the SWIR part of the spectrum, reflectance is controlled by water content, and is relatively low for vigorously growing vegetation. As the leaves dehydrate, the reflectance in this region increases (Eismann, 2012).

2.2.2 Structural changes in diseased forest canopies

Forest structure is dynamic and subject to change from one year to the next, or even within a single growing season. Most damage first appears as a change of colour of the forest canopy, and then as loss of needles. In the long term, it can often result in smaller growth and increased mortality, leading to loss of yield/timber (Ciesla, 2000). However, the severity and rate of defoliation varies greatly between different environmental stressors.

Defoliator insects damage forest trees by eating leaves or needles. The effects of most of them are negligible. However some (for instance sawflies) may cause a significant loss of canopy foliage. Infestation can increase susceptibility of affected trees to attack by other insects and pathogens, and sometimes even lead to tree mortality. When insect populations are at epidemic levels, the outbreak may cover vast areas, in which nearly every tree can be affected (Holsten *et al.*, 2008). If severe defoliation occurs early in the growing season, damaged broadleaf trees can typically refoliate during the same season, masking the actual defoliation (Ciesla, 2000). Conifer trees rarely refoliate following a severe defoliation due to a loss carbohydrate reserves, which are stored in leaves rather than in roots (Clancy *et al.*, 1995).

Wood boring insects, including moths and beetles, normally attack only freshly cut, injured, dying, or recently dead trees. In fact, they usually have a positive effect on their natural ecosystem, helping to break down woody debris, catalyse nutrient cycling and create structural diversity in forest stands. However, when host material is abundant and climatic conditions favourable, their populations may rapidly build up, successfully colonising neighbouring healthy trees (Brasier, 1999). Ongoing infestation can lead to

death of affected branches, development of dead tops on trees, or even death of whole trees (CSL, 2004). For instance, after twelve months of a mass attack of mountain pine beetles (*Dendroctonus ponderosae*) over 90% of the infested trees can have red needles (the red attack stage), and after three years most of them would have lost all needles (Wulder *et al.*, 2006).

In the case of foliar pathogenic infections, the defoliation is not as rapid. Following infection in conifer species, affected needles experience discolouration and fruiting bodies development. Usually only after completion of fungus development cycle and spore germination, the infected needles are shed. Depending on a pathogen, it may take from several months to 3 years. The process may be accelerated in a case of severe attack or if a highly susceptible tree species is affected. The defoliation in broadleaf tree species is usually not as evident, as the leaf pathogens usually overwinter in the fallen leaves to germinate and spread the infection in spring. However, if the attack is severe, a premature leaf fall may occur (Butin, 1995).

Root and butt rots of trees can cause significant mortality of mature trees, leading in long term to dramatic changes in forest structure and composition (Gilbert, 2002). For instance, *P. lateralis* is responsible for severe mortality of an endemic Port Orford cedar (*Chamaecyparis lawsoniana*) in California and Oregon (Hansen *et al.*, 2000). If not lethal, root rots can adversely reduce host growth, for example *Armillaria ostoyae* was found to reduce radial growth of Douglas fir by up to 60% (Bloomberg, 1989). Cankers, wilts and dieback diseases may cause similarly devastating effects, especially if non-native in the area (Gilbert, 2002). For instance, *P. ramorum* is responsible for widespread death of tanoak and other native tree species in California and Oregon, and it was found to cause death of Japanese larch trees within only one to two growing seasons (Kliejunas, 2010); the Dutch elm disease in the UK caused death of over 30 million English elms, and led to drastic changes in landscapes (Maynard and Allen, 2012).

2.3 Current remote sensing technologies

Currently remote sensing data can be obtained from a range of ground-based, airborne, and Earth-orbiting platforms (Figure 2.2) capable of acquiring data at different spatial, spectral and temporal resolutions (Köhl *et al.*, 2006). When selecting any of those platforms, trade-offs have to be made in terms of the spatial, spectral and temporal resolutions; cost of operation, extent of survey, and flexibility of the approach. For example, whilst UAVs and terrestrial instruments offer greater flexibility and acquire data at higher spatial resolution, they are unable to cover large spatial extents (Wulder and Franklin, 2003).
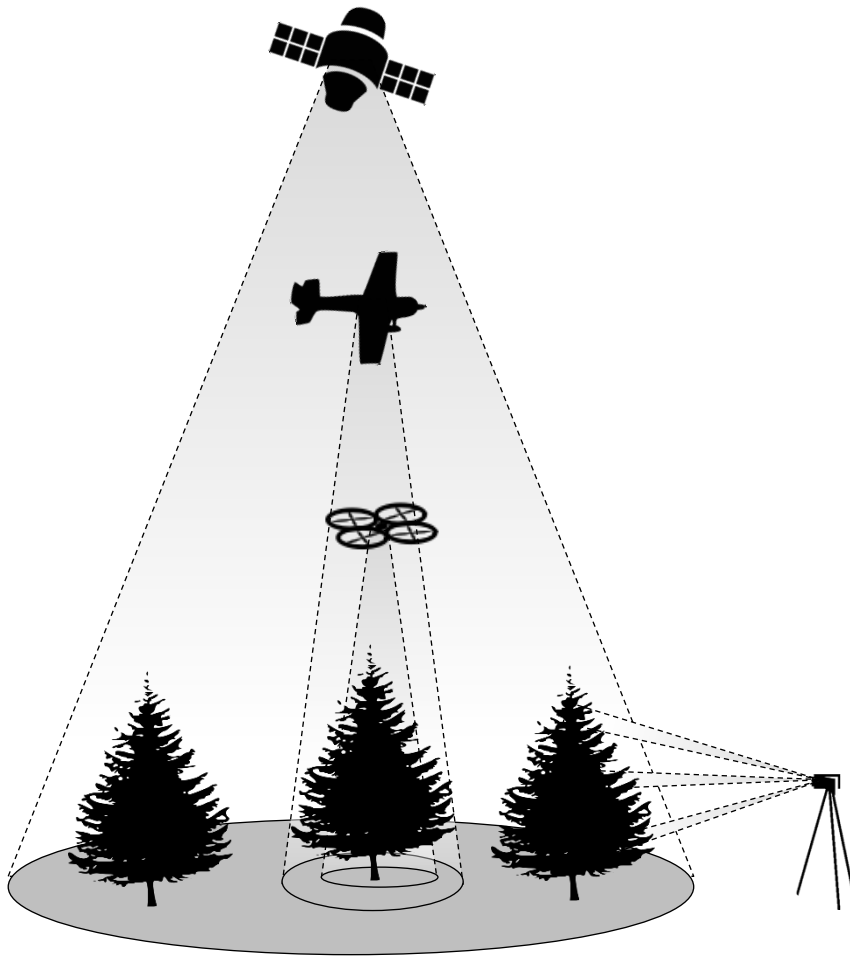
Figure 2.2: Scales of operation of spaceborne, airborne, UAV-borne and terrestrial remote sensing instruments. Based on van Leeuwen and Nieuwenhuis (2010).

Remote sensing data can be collected using passive and active systems. Passive optical sensors generally are used to provide information on the amount of foliage and the biochemical properties of vegetation, whilst active sensors are better suited to retrieve information on woody biomass and forest structure (Roberts *et al.*, 2007). For the purpose of conciseness, only optical, thermal and LiDAR sensors will be considered in this thesis.

Reviews on the use Synthetic Aperture Radar (SAR) for forestry applications are provided by Balzter (2001) and Koch (2010).

Passive optical instruments record energy that was reflected or emitted from the Earth's surface in the visible (400-700 nm), near infrared (700-1300 nm), and shortwave infrared (1300-2500 nm) regions of electromagnetic spectrum (Varshney and Arora, 2004). Panchromatic imaging systems detect radiation in a single channel within a broad wavelength range. Multispectral sensors record measurements of reflected radiation in relatively broad wavelength bands, whilst hyperspectral instruments acquire imagery across hundreds of very narrow and adjacent wavelength intervals, making observation of even subtle details in reflectance spectra possible (Lein, 2012a). Hyperspectral technology has been successfully used to retrieve chlorophyll content, water content and LAI (Haboudane *et al.*, 2004; Pu and Gong, 2004; Cheng *et al.*, 2008; Wang and Li, 2012). It has also been used to attempt retrieval of carotenoids content in plants (Blackburn, 1998a; Zarco-Tejada *et al.*, 2013; Yi *et al.*, 2014). The most commonly used methods for estimating those forest biophysical properties with hyperspectral imagery are spectral vegetation indices. Usually they are calculated as the ratio of two wavelengths, contrasting an absorbing feature with a non-absorbing reference feature (Huete, 2012). Retrieval of the aforementioned properties will be further covered in section 2.4.

Airborne LiDAR (light detection and ranging) is an active sensor that allows direct measurements of the three-dimensional distribution of the canopy and sub-canopy topography (Wulder and Franklin, 2003). In essence, LiDAR systems emit pulses of laser light (usually near infrared) and then record their return times. Distance between the sensor and a target surface is calculated using the elapsed time (time-of-flight systems) or phase difference (phase-shift systems) between the emitted and returned laser pulses (Lim *et al.*, 2003). There are two distinct LiDAR types: discrete return and full waveform (Figure 2.3). Discrete return systems record the occurrence of returns whose amplitude exceeds a noise threshold. In full waveform systems the returned laser energy is densely sampled over a short time interval to create a complete waveform of the backscattered laser pulse. This waveform describes intensity of the energy that was reflected back by different layers of the vegetation column encountered by the pulse (Wulder and Franklin, 2003). LiDAR has been widely used for multiple forestry applications, and due to its ability to record 3-dimensional information is currently considered an ideal remote sensing instrument to record structural information (Zheng and Moskal, 2009). Plant Area Index has been repeatedly retrieved using LiDAR in various forest types across the world

(Sasaki *et al.*, 2013; Moeser *et al.*, 2014; Tang *et al.*, 2014). Furthermore, LiDAR has been used to retrieve other parameters such as vertical foliage profile or canopy cover (Frazer *et al.*, 2005; Donoghue *et al.*, 2007), and also to delineate individual tree crowns (Wannasiri *et al.*, 2013).
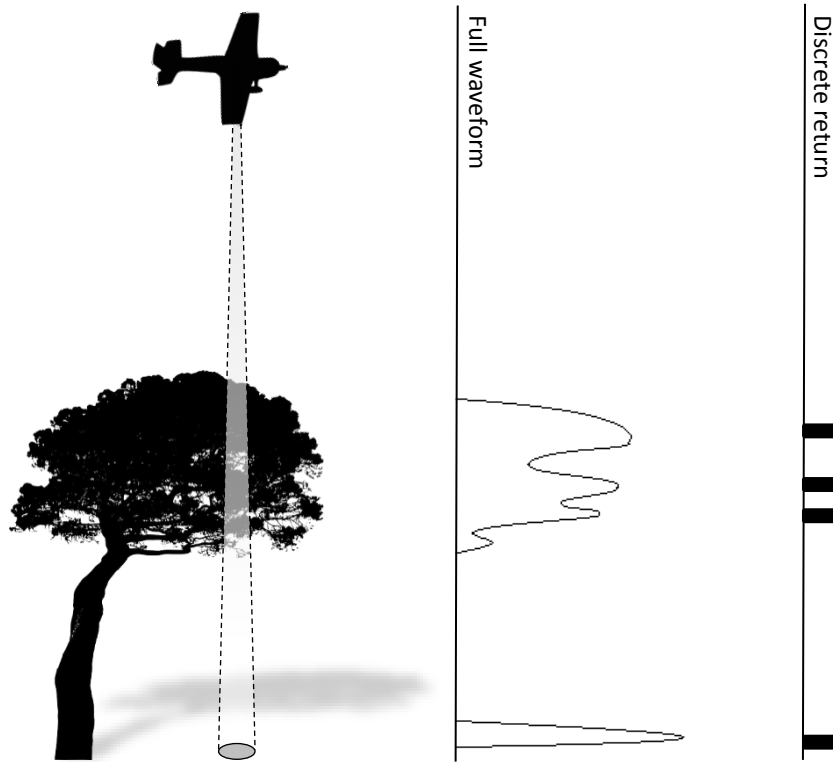
Figure 2.3: Graphical representation of discrete return and full waveform airborne laser measurements. Based on Lim *et al.* (2003).

The thermal part of the electromagnetic spectrum occupies wavelengths from 3 to 14 µm, but due to atmospheric absorption, only long-wave infrared (8-14 µm) region is utilised by thermography (Chaerle and Van Der Straeten, 2000; Lein, 2012b). Thermal sensors measure the radiant energy of surface features, which is quantified from the energy that was emitted by them. Emissivity of a surface (required for radiometric calibration) is defined as the ratio between energy radiated by a surface and energy that would have been radiated by a blackbody at the same temperature. Its value depends on several factors, which include the angle of measurement and wavelength; and can be acquired from generalised look-up tables (Lein, 2012b). Even though thermography is mainly known for its applications in human and animal medicine, it is also used for monitoring changes in the physiological state of plants (Chaerle and Van Der Straeten, 2000). Thermal sensors are known to be capable of estimating water content and stomatal conductance (Jones and Schofield, 2008). Stress factors change the thermal properties of plants, and consequently

influence emissions in the Thermal Infrared (TIR) band (Lee *et al.*, 2010). For instance, stress can induce stomatal closure leading to an increase in leaf and canopy temperature, which can often be detected at an early stage of infection by thermal imaging (Chaerle *et al.*, 1999a; Lindenthal *et al.*, 2005).

2.4 Remote sensing of forest biophysical properties

2.4.1 Photosynthetic pigments content

Chlorophyll retrieval indices are usually based on wavelengths neighbouring the red absorption maximum, which occurs at 660-680 nm (le Maire *et al.*, 2004). This is due to reflectance being sensitive to low concentration of chlorophyll in regions where the pigment absorption coefficients are high. At spectral regions with low absorption, reflectance is more sensitive to higher pigment's concentration (Blackburn, 2002). Therefore if chlorophyll indices were to be based on region of chlorophyll's maximum absorption, they would rapidly saturate even at low chlorophyll concentrations (Sims and Gamon, 2002). Blue wavelengths (440-490 nm) are generally not used for chlorophyll content estimation due to the overlap with carotenoids absorbance (Sims and Gamon, 2002).

Hyperspectral indices for estimating chlorophyll content at the leaf scale have been successfully developed, with strong relationships (i.e. $r^2 > 0.85$) recorded (Curran *et al.*, 1990; Blackburn, 1998a; Zarco-Tejada *et al.*, 2001). However most of the algorithms reported in the literature have been developed using leaf reflectance measurements for only a few tree species, and have not been checked if they can be widely applied. le Maire *et al.* (2004) provide a thorough review of over 60 chlorophyll indices, developed up to 2002, in which they were tested on leaves of different deciduous tree species. The authors found simple modified ratios of reflectance to produce best results. They also found indices based on simple reflectance combinations to perform considerably better than complicated indices based on derivatives.

Leaf carotenoid concentration retrieval is much more difficult due to the overlap with chlorophyll's absorption peak in the blue part of electromagnetic spectrum, and in most cases higher concentration of chlorophylls within leaves (Sims and Gamon, 2002). It has been attempted to estimate total leaf carotenoid content using reflectance measurements (e.g. Datt (1998)), however, Blackburn (1998b) showed that they were not capable of acquiring satisfactory results when applied to other datasets (i.e. average $r^2 = 0.25$). The use of reflectance indices for estimation of the ratio of carotenoids to chlorophylls has

proven more successful than retrieval of the absolute carotenoids content, with Peñuelas *et al.* (1995) and Merzlyak *et al.* (1999) recording $r^2 \geq 0.9$. Blackburn (1998b) achieved similar results (i.e. average $r^2 = 0.86$) applying already developed carotenoids to chlorophylls ratios to his dataset. Most of these ratio indices compare the reflectance in the region of the carotenoid absorption maximum (400-500 nm) with maximum chlorophyll absorption in the red region (Sims and Gamon, 2002).

Upscaling leaf measurements to the canopy level is difficult due to spatially complex forest structure and viewing geometry, which may differ with site and tree species (Zhang *et al.*, 2008). Additionally, canopy reflectance is strongly affected by other factors, such as distribution of pigments within the canopy, which tends to vary in time and space, the amount of leaf biomass and soil background (Curran *et al.*, 1990; Gitelson *et al.*, 2005). In remote sensing two approaches for estimating pigment concentration are commonly used: the empirical-statistical approach and the inversion of physically based leaf and canopy reflectance models. The empirical-statistical method is simple to use, and is based on correlations between optical indices and measurements of chlorophyll content (Zarco-Tejada *et al.*, 2001). However it does not account for canopy structure, which greatly affects canopy reflectance acquired by a sensor; plants with same canopy chlorophyll content can have different reflectance resulting from different canopy structure (Gitelson *et al.*, 2005).

The canopy structure's effect on spectral reflectance can be modelled with use of physically based canopy and leaf reflectance models, which describe the interactions of solar radiation with vegetation elements (Colombo *et al.*, 2008). The inversion of these models is often used to account for the effects of factors such as background reflectance, illumination geometry, and canopy architecture (Thomas *et al.*, 2007; Simic *et al.*, 2011). Radiative transfer models have proven to be useful for reducing effects of background and leaf area variability (Haboudane *et al.*, 2002; Zarco-Tejada *et al.*, 2004). They are computationally expensive, though, and the same unique solution can be achieved with different combinations of inputs (Baret *et al.*, 2007). The most popular models for retrieving biochemical and biophysical characteristics of vegetation are SAIL (Verhoef, 1984), PROSPECT (Jacquemoud and Baret, 1990) and PROSAIL (Baret *et al.*, 1992), which combines the previous two. PROSAIL describes the reflectance at a canopy level as a function of leaf biochemistry (parameterised with chlorophyll, water and dry matter content) and canopy structure (defined by LAI, leaf angle, distribution and relative size). More complex models, taking into account the heterogeneity of canopy structure, were

also developed; those include Discrete Anisotropic Radiative Transfer (DART) (Gastellu-Etchegorry *et al.*, 1996), Spreading of Photons for Radiation Interaction (SPRINT) (Goel and Thompson, 2000), Three-dimensional Forest Light Interaction (FLIGHT) (Kötz *et al.*, 2004), Forest Light Environmental Simulator (FLiES) (Kobayashi and Iwabuchi, 2008) and Invertible Forest Reflectance Model (INFORM) (Schlerf and Atzberger, 2006). An intercomparison of the radiative transfer models based on abstract and actual canopies can be found in Widlowski *et al.* (2013) and Widlowski *et al.* (2015).

2.4.2 Chlorophyll fluorescence

The energy absorbed by leaves can either be used for photosynthesis, dissipated as heat or reemitted as light - chlorophyll fluorescence. Chlorophyll fluorescence is produced by photosystems I and II, pigment-protein complexes participating in the initial stages of photosynthesis. When plants are experiencing stress or moderate to high irradiance, tissues increase heat production to dissipate excess energy, which tends to decrease fluorescence emission (Pedrós *et al.*, 2008). The main wavelengths found to be involved in the chlorophyll fluorescence release, when exposed to UV-a light, are located in the red region at 690 and 740 nm (Jones and Schofield, 2008). Fluorescence can be easily quantified in laboratory conditions by exposing leaf tissue to light of defined wavelength and then measuring at longer wavelengths the amount of re-emitted light. However, as the amount of chlorophyll fluorescence is very dependent on illumination conditions and leaf structure, it is only a relative measure, which needs to be normalised (Maxwell and Johnson, 2000). Furthermore, estimation of chlorophyll fluorescence from airborne and spaceborne sensors is complicated by the fact that the signal is strongly absorbed by the atmosphere, making differences inside absorption features less evident (Meroni *et al.*, 2009).

There are two main approaches used for remote quantification of chlorophyll fluorescence: reflectance-based and radiance-based. The former uses spectral reflectance, utilising spectral indices related to the effect of fluorescence. The latter uses the so-called Fraunhofer lines - narrow dark features of the solar and atmospheric spectrum, characterised by strong reduction of irradiance (Meroni *et al.*, 2009).

Optical indices used for fluorescence retrieval include reflectance ratios, derivatives and infilling indices, most commonly using wavelengths in the red edge region. The ratios generally use a set of two or three spectral bands, with at least one wavelength affected by fluorescence (Zarco-Tejada *et al.*, 2000; Dobrowski *et al.*, 2005). The second method uses derivatives of reflectance, which are said to enhance the effect of fluorescence and

enable the detection of subtle changes (Zarco-Tejada *et al.*, 2000; Zarco-Tejada *et al.*, 2003a). Zarco-Tejada *et al.* (2000), at canopy level, found derivative indices ($r^2 > 0.8$) to exhibit stronger correlation with fluorescence than optical ratio indices ($r^2 \leq 0.52$). They also found that the used derivative indices had a correlation with chlorophyll content. The last category of optical indices, the infilling indices, exploits Fraunhofer lines by measuring the height of the apparent reflectance peak – the infilling effect of fluorescence on reflectance (Pérez-Priego *et al.*, 2005). The magnitude of infilling depends on fluorescence intensity and Fraunhofer line depth, which in the O_2 bands is affected by the sun's position and air density. The use of this method is thus limited to a relative comparison of fluorescence measurements acquired under the same observation conditions (Meroni *et al.*, 2009). The use of spectral indices enables extraction of chlorophyll fluorescence from traditional remote sensing instruments. However, as several of the developed indices are also sensitive to absorption by pigments, the variations of reflectance may not only be due to fluorescence changes but also due to pigment concentration changes. These changes are linked to fluorescence, and their measurement is physiologically relevant, but they do not allow direct retrieval of fluorescence itself (Meroni *et al.*, 2009).

The radiance-based approaches for chlorophyll fluorescence retrieval exploit Fraunhofer lines, and allow for estimation of fluorescence in physical units (i.e. radiance units) when using radiometrically corrected data. For multispectral datasets there have been three methods developed that require two or three spectral channels near the investigated absorption line: Fraunhofer Line Depth (FLD), 3 bands FLD (3FLD) and corrected FLD (cFLD) (Theisen, 2002; Maier *et al.*, 2003; Gómez-Chova *et al.*, 2006; Moya *et al.*, 2007). For hyperspectral datasets other methods have been developed that make use of a set of contiguous channels covering the whole relevant spectral range: improved FLD (iFLD), extended FLD (eFLD), and Spectral Fitting Method (SFM) (Meroni and Colombo, 2006; Alonso *et al.*, 2007; Mazzoni, 2007; Alonso *et al.*, 2008). A detailed explanation of these techniques is provided by Meroni *et al.* (2009). Damm *et al.* (2011) assessed the fluorescence retrieval accuracy of FLD, 3FLD and iFLD methods under modelled variations of sensor properties. FLD was found to strongly overestimate the fluorescence signal, whilst iFLD appeared to be highly sensitive to noise, despite giving the best performance. 3FLD was concluded to be the best method among the three, offering a compromise between robustness and accuracy. Meroni *et al.* (2010) also found FLD to overestimate the fluorescence signal, and be less accurate than SFM approach under all considered noise configurations.

Estimation of chlorophyll fluorescence from airborne and satellite sensors is complicated by the fact that the signal is strongly absorbed by the atmosphere, making differences inside absorption features less evident (Meroni *et al.*, 2009). Maier (2001) proposed and patented a semi-empirical atmospheric correction method for the use of FLD at the O_2-A band, which uses non-fluorescing image pixels to determine radiance conditions on the ground and atmosphere's influence. This method was tested by Maier *et al.* (2003) on airborne hyperspectral dataset against ground based measurements, confirming that fluorescence light can be separated from reflected light if non-fluorescent objects are present in the image. Zarco-Tajeda *et al.* (2003) used this atmospheric correction method and applied the 3FLD methods to UAV-borne hyperspectral imagery of citrus orchards, recording R^2 of 0.67.

2.4.3 Stomatal conductance

Stomatal conductance of plants can principally be evaluated with thermal remote sensing instruments. This is due to leaf temperature being primarily determined by the rate of transpiration, responsible for evaporative cooling of leaves (González-Dugo *et al.*, 2006). When a plant is under stress, stomatal closure can occur, leading to an increase in leaf and canopy temperature (Chaerle *et al.*, 1999a; Lindenthal *et al.*, 2005). In controlled laboratory conditions, measuring the leaf temperature allows for straightforward quantification of stomatal conductance across the leaf surface (Omasa and Croxdale, 1992; Omasa and Takayama, 2003).

At a canopy level, the plant temperature is affected in a complex manner by environmental factors such as air temperature, humidity, radiation and wind speed, posing a problem for the use of thermal sensing (Leinonen *et al.*, 2006). Direct or indirect information about these factors are therefore required to estimate stomatal conductance with thermography. One method accounting for these is to use indices that involve the comparison of leaf temperature with appropriate reference temperatures (Idso *et al.*, 1981; Jones, 1999). Leinonen *et al.* (2006) proposed three main approaches for estimating stomatal conductance. Similar to Jones (1999), the first one uses dry and wet reference temperatures (representing zero and maximum transpiration rates), whilst the other two require either only dry reference surface or no references, with all necessary ancillary information obtained from meteorological instruments. Estimation of stomatal conductance depending solely on environmental data yields the highest error and the lowest prediction power due to difficulties in obtaining accurate estimate of the net radiation absorbed by the leaf. The use of reference surfaces eliminates the need for

radiation measurements increasing the accuracies. The most practical method showed to be the one using only the dry reference surface, complemented with air humidity measurements.

Another difficulty in evaluation of stomatal conductance at a canopy scale is that image pixels may include both leaf and soil. This may change the observed temperatures depending on vegetative ground cover, with increasing proportions of soil usually leading to higher temperatures. Two ground-based approaches have been developed to account for this, which could potentially be applied to airborne thermal imagery. In the first one, Jones *et al.* (2002) used wet and dry reference surfaces as thresholds for separating leaves from background. Performance of this approach, though, is limited by the choice of reference, which may affect not only the observed mean temperature, but also the frequency distribution of temperatures. Furthermore, if plant's stomata are widely open or closely shut, leaf temperatures may overlap with wet or dry reference, resulting in exclusion of some leaf pixels from the analysis. In contrast, Leinonen and Jones (2004) proposed the combined use of thermal and visible imagery, to separate vegetation from background, and measure the temperature variation of whole plants. However, this method largely depends on successful geo-referencing of the images, and accuracy of plant versus background classification. Nevertheless, it allowed for effective exclusion of background temperature using close-range photography.

Quantification of stomatal conductance, with use of thermal imagery acquired from ground-based or platform-mounted sensors, has been performed successfully across various environments (Jones, 1999; Leinonen *et al.*, 2006; Maes *et al.*, 2011; Reinert *et al.*, 2012). Yet, the use of airborne or satellite thermal imagery for stomatal conductance in woody plants remains unexploited, with only Berni *et al.* (2009a) and Calderón *et al.* (2013) reporting good correlations when using airborne and UAV-borne imagery in olive orchards.

2.4.4 Water content

Plant water content at the leaf and canopy levels is often evaluated with use of spectral reflectance bands and indices based on NIR, Mid Infrared (MIR) and SWIR parts of the electromagnetic spectrum (Govender *et al.*, 2009). Laboratory studies conducted on leaves suggested that reflectance at 1200 nm and within major water absorption features centred at 1450 and 1940 nm is particularly sensitive to water content of leaves (Thomas *et al.*, 1971; Goetz and Boardman, 1995). However, due to strong absorption of reflectance at 1450 and 1940 nm by water vapour, those regions are not suitable to use

with remote sensing systems (Goetz and Boardman, 1995). Regions of intermediate leaf water absorption near 1650 and 2200 nm, as well as regions of weak leaf water absorption near 970 and 1200 nm have proven to be more suitable for plant water content retrieval (Tucker, 1980; Peñuelas *et al.*, 1993; Goetz and Boardman, 1995; Gao, 1996).

When relating spectral reflectance with leaf water content, internal leaf structure poses the main issue. Along with leaf thickness, it changes scattering properties of leaves, causing variations in reflectance, which are unrelated to water content. Danson *et al.* (1992) showed, on a dataset of several species, that leaf structure variations have a major effect on a relationship between leaf reflectance and leaf water content. They also found that the first derivative of leaf reflectance at selected wavelengths is insensitive to structural variations of the leaf.

Leaf or vegetation water content is usually measured as Equivalent Water Thickness (EWT, the volume of water per unit leaf area), which can be retrieved using a range of remote sensing techniques, including radar, thermal and optical sensors. Several methods, relying on empirical or physical approaches, have been developed to detect changes in plant water status (Ceccato *et al.*, 2001; Colombo *et al.*, 2008). At leaf level, empirical relationships are usually formed based on correlations between measured leaf water content and laboratory reflectance measurements, which have shown strong relationships during EWT retrieval (Peñuelas *et al.*, 1993; Datt, 1998; Ceccato *et al.*, 2001; Curran *et al.*, 2001). Most commonly for EWT estimation, spectral vegetation indices combining two or more wavebands are employed. These are designed to normalise the variation in reflectance spectrum caused by the internal structure of a leaf (Danson and Bowyer, 2004).

At the canopy level, reflectance is additionally influenced by viewing geometry, atmospheric conditions, canopy structure, and soil/understorey vegetation reflectance (Huete *et al.*, 1985; Dawson *et al.*, 2003; Zarco-Tejada *et al.*, 2003b). Changes in leaf area and canopy architecture may mask water related features in the reflectance spectrum, and thus complicate retrieval of leaf water content (Cohen, 1991). Due to the difficulty in separating the contributions of leaf water content and of leaf area, empirical relationships based on spectral indices are often employed to retrieve the total canopy water content (EWT$_{canopy}$, the volume of water per unit ground area) (Serrano *et al.*, 2000; Colombo *et al.*, 2008). The use of double ratio spectral indices, utilising a vegetation index for water content retrieval and a vegetation index measuring canopy greenness and structural

parameters (for example NDWI/NDVI) may reduce the effect of canopy internal structure, and allow retrieval of leaf EWT at landscape level (Colombo *et al.*, 2008).

Another way to account for canopy architecture is to use radiative transfer and inversion models of a canopy. They allow estimation of leaf and canopy properties from remote sensing data, and were also shown to enable estimation of leaf EWT at landscape level (Jacquemoud *et al.*, 1995; Zarco-Tejada *et al.*, 2003b; Toomey and Vierling, 2006). It has to be noted though, that the estimation of canopy structural parameters and leaf water content at such scale, is further complicated by the amount and distribution of leaf absorbing material within the canopy (Colombo *et al.*, 2008). Thus some studies suggest using physical models to estimate the EWT_{canopy}, rather than leaf EWT (Fourty and Baret, 1998; Kötz *et al.*, 2004). Despite the aforementioned difficulties, vegetation water content at canopy level, using both empirical and physical methods, has been estimated across various ecosystems, including agricultural crops, savannah woodlands, shrubs, and forests (Gao and Goetzt, 1995; Jacquemoud *et al.*, 1995; Gao, 1996; Ustin *et al.*, 1998; Serrano *et al.*, 2000; Ceccato *et al.*, 2002). Colombo *et al.* (2008) investigated the applicability of different empirical and physical models in estimating canopy water content in a poplar plantation, and found both approaches effective for estimating EWT_{canopy}. The methods included vegetation spectral indices, double ratio spectral indices and inversion of the PROSPECT+SAILH canopy reflectance model.

Plant water content can also be evaluated through temperature measurements. As plants transpire, water loss through evaporative cooling reduces leaf temperature. Conversely, plants under water stress tend to transpire less, leading to an increase in leaf and canopy temperature (González-Dugo *et al.*, 2006). However, the fundamental difficulty in relating leaf temperature to water stress is that the relationship between transpiration rate and leaf water status varies between plant species. The so-called "isohydric" plants have tight stomatal control over leaf water potential, which causes their stomata to close under water stress; whereas, the "anisohydric" plants do not close their stomata unless the water deficit is severe (Tardieu and Simonneau, 1998). In practice, the distinction between these two strategies is often unclear, as contrasting behaviour was found even among different cultivars of the same species, e.g. poplar (Hinckley *et al.*, 1994) and grapevine (Lovisolo *et al.*, 2010).

At a canopy scale, image pixels may include both leaf and soil, which may affect the observed temperatures with varying effect (depending on vegetative ground cover). The plant temperature at canopy scale is also affected by a number of environmental factors,

such as air temperature, humidity, radiation and wind speed. These could be accounted for with methods proposed by Leinonen *et al.* (2006) and Jones (1999), as already described in section 2.4.3. Alternatively 'stress indices' could be used, which aim to normalise the results for environmental variation, and relate the temperature difference, between the canopy and air, to plant water deficit (Idso *et al.*, 1981; Jackson *et al.*, 1981; Mahan and Upchurch, 1988; Moran *et al.*, 1994). These indices have been widely and successfully applied to agricultural crops (Alderfasi and Nielsen, 2001; Erdem *et al.*, 2010; Taghvaeian *et al.*, 2014) and orchards (Berni *et al.*, 2009a; Calderón *et al.*, 2013; Gonzalez-Dugo *et al.*, 2014). The application of thermal imagery for plant water content retrieval or water stress detection in forest canopies, however, still remains an unexplored area.

2.4.5 Canopy leaf biomass

The canopy leaf biomass can be quantitatively measured through LAI, which is defined as one-sided area of green leaves per unit horizontal ground area. LAI is most commonly retrieved using optical sensors. This can be done through various techniques, which can be classified into two main groups: empirical retrieval methods, and physically-based retrieval methods. The empirical methods relate the ground-measured LAI values against observed spectral responses through linear or non-linear algorithmic techniques (e.g. vegetation indices), whilst the physically-based retrieval methods utilise the radiative transfer models (Delegido *et al.*, 2013).

The red-to-NIR spectral region has been demonstrated to be significantly related to LAI, and has successfully been applied to retrieve LAI values in agricultural environments, characterised by homogeneous canopy architecture (Liu *et al.*, 2004; Delegido *et al.*, 2013; Nguy-Robertson *et al.*, 2014). One of the most extensively used vegetation index utilising this region is NDVI, for which fairly strong, but site specific relationships with LAI were found across different vegetation types (Law and Waring, 1994; Cohen *et al.*, 2003; Wang *et al.*, 2005). However, when applied to forests, vegetation indices like NDVI start saturating, and are affected in varying degrees by understorey vegetation (Qi *et al.*, 2014). They were also found to be sensitive to the tree species composition; Chen *et al.* (2002) demonstrated that the differences between conifer and deciduous forest stands are distinctive, making it necessary to calibrate separate models for different forest types. Furthermore, Lee *et al.* (2004) showed that relationship between field-measured LAI and spectral reflectance is significantly different between the non-forested and forested sites, with SWIR region being important in forested areas. They also demonstrated that, for a

coniferous canopy, the SWIR region had stronger correlation with LAI than either the NIR or the red region. Several studies that used vegetation indices including SWIR bands, i.e. reduced simple ratio (RSR), proved more successful in reducing the background effect and increasing sensitivity (Brown *et al.*, 2000; Chen *et al.*, 2002; Stenberg *et al.*, 2004). Nevertheless, the regression relationships are site, time and species specific, making it difficult to apply them at a landscape or global level.

Physically-based models, describing the propagation of light in plant canopies, have the potential to be more widely applicable, and have been used with varying results (Eklundh *et al.*, 2001; Rautiainen, 2005; Ganguly *et al.*, 2012; Houborg *et al.*, 2015). The LAI values are retrieved through model inversion by minimising the differences between simulated and measured reflectance at all wavelengths (Kuusk and Nilson, 2000; Rautiainen, 2005). However, the accuracy of such LAI estimates depends on the ability to regularise measurement and model uncertainties; different combinations of model parameters can result in nearly identical spectra, and consequently non-unique solutions (Baret and Buis, 2008).

Leaf area index of forested areas has also been extracted utilising LiDAR technology, with methods similarly divided into empirical and physically-based approaches (Pearse *et al.*, 2017). LiDAR descriptive metrics such as height percentiles, descriptive statistics, and distributional statistics for return elevations capture underlying canopy properties related to LAI (Jensen *et al.*, 2008; Beets *et al.*, 2011; Pope and Treitz, 2013). In particular, metrics quantifying the rate of penetration of pulses through the canopy, which provide a measure of gap probability, have proven useful in both empirical and physically-based studies (Morsdorf *et al.*, 2006; Solberg, 2010; Peduzzi *et al.*, 2012). Canopy gap probability is non-linearly related to LAI through the Beer-Lambert law, which describes the extinction of light through the canopy (Monsi and Saeki, 1953; 2005). Strong relationships were found between LiDAR metrics and field measured LAI in a range of natural and mixed forest types (Riano *et al.*, 2004; Morsdorf *et al.*, 2006; Jensen *et al.*, 2008). Jensen *et al.* (2008) using LiDAR canopy metrics obtained R^2 of 0.86 and 0.69 in mountain conifer woodlands. Similar strong relationships were observed at different sites (Riano *et al.*, 2004; Morsdorf *et al.*, 2006; Griffin *et al.*, 2008; Peduzzi *et al.*, 2012; Pearse *et al.*, 2017).

2.5 Remote sensing detection of infected plants

Remote sensing technology was used to detect diseased vegetation as early as in 1920's, when Taubenhaus *et al.* (1929) used aerial photography for detection of cotton root rot. Nowadays, detection of plant stress is usually performed with the use of passive optical remote sensing from a variety of platforms, where discrimination between diseased and healthy vegetation depends on identifying differences in the reflected spectra.

Throughout the years, the use of remote sensing for disease detection has been primarily applied to agriculture applications. For instance, Mirik *et al.* (2011) using multispectral Landsat Thematic Mapper (TM) data successfully separated healthy and diseased wheat fields with maximum likelihood classifier method (classification accuracies of 89-99%), whilst Santoso *et al.* (2011) utilised high resolution QuickBird satellite image and six vegetation indices derived from VIS-NIR region to identify diseased oil palms (mapping accuracy of highly infected palms: 60-67%). Multispectral imagery was also successfully used on airborne platforms to identify the differences in growth pattern induced by tarnished bug infestation (Willers *et al.*, 1999; Willers *et al.*, 2005), monitor citrus greasy spot disease in citrus (Du *et al.*, 2008), determine severe infestations of rice sheath blight disease (Qin and Zhang, 2005), and detect late blight infection of tomato fields (Zhang *et al.*, 2005). Zhang *et al.* (2005) and Qin and Zhang (2005) also tried to discern early stages of the monitored diseases, which proved difficult with use of broad band imagery due to similar spectral response of healthy and diseased plants.

The development of hyperspectral sensors offered an increased spectral sensitivity and inclusion of the moisture sensitive bands. Hyperion satellite data was found to increase the capability of mapping orange rust disease on sugarcane in Australia, when compared to the use of VIS-NIR reflectance alone (Apan *et al.*, 2004). This is due to ability to detect substantial change in leaf water content or pigmentation of stressed crops through increase in reflectance in MIR bands and shift in the red-edge in NIR bands. Apan *et al.* (2004) also formulated new indices, namely Disease Water Stress Indices (DWSI), which proved superior in discriminating diseased sugarcane crops, and also allowed Dutta *et al.* (2006) for successful characterisation of disease severity in mustard crops (68% correlation with the disease score when using DWSI-3, which is a ratio of reflectance at 1660 and 680 nm). Zhang *et al.* (2002) and Zhang *et al.* (2003) utilised field spectroscopy measurements of late blight infected tomatoes at different disease stages (1- light symptoms to 4 – severe damage) to develop a spectra-based classification approach to identify the infection. Field samples indicated that the NIR region was much more

valuable than the visible range to detect crop disease (spectral reflectance difference of 1.19% in the VIS, and of 10% in the NIR region between healthy and stage 3 plants). Using the minimum noise fraction transformation and spectral angle mapping to process the hyperspectral airborne image, they successfully separated tomato plants at stage 3 or above from the healthy plants. However, high correlations between the healthy and lightly diseased (stage 1 and 2) plants were found, indicating difficulty in separating the categories.

Detection of diseased trees in forests is further complicated by spatially complex forest structure and viewing geometry, which may differ with sites and tree species (Zhang *et al.*, 2008). Most commonly the effects of disturbance events, such as insect or disease outbreaks, are characterised through the examination of a temporal sequence of images, allowing quantification of reflectance changes. Its main advantage is that a record of spectral reflectance change can be extracted to characterise both the magnitude and direction of physiological processes or disturbance events (Hostert *et al.*, 2003). Multi-temporal satellite-based remote sensing has long been used to detect insect-induced defoliation in both coniferous and broadleaved forests, including such insects as moths (Muchoney and Haack, 1994; Kharuk *et al.*, 2004; Babst *et al.*, 2010), budworms (Radeloff *et al.*, 1999; Franklin *et al.*, 2008), pine sawfly (Eklundh *et al.*, 2009), and others (Hall *et al.*, 2003; Fraser and Latifovic, 2005; Somers *et al.*, 2010). For example, the Enhanced Wetness Disturbance Index (EWDI), involving Tasselled cap transformation and differencing of the wetness band pre- and post-infestation, allowed Skakun *et al.* (2003) to map bark beetles damage with classification accuracy of 67% to 78% (based on Landsat TM data). The analysis of imagery from a number of years may further improve the detection accuracy, as an increased number of repeat observations allows characterisation and interpretation of the reflectance patterns before, during, and after the infestation/disease. For example, the analysis of three Landsat images of forest stands prior to disturbance, after gypsy moth defoliation and during refoliation, resulted in a stronger and less ambiguous signal of gypsy moth damage, and consequently an improved detection accuracy of infested areas (Hurley *et al.*, 2004).

While studies examining temporal sequences of imagery have shown potential for detecting forest disturbances, their main limitation for forest health monitoring is the risk of large or frequent gaps in the image sequence. This risk is particularly high for countries like the UK, where the cloud cover is prevalent throughout the year. Such data gaps can decrease the number of observations available to capture spectral trends, and possibly

affect their interpretation as fitted curves could misrepresent the true signal of disturbance events (Wilson and Sader, 2002; Jin and Sader, 2005). Furthermore, to identify individual diseased trees or monitor areas of fragmented forest cover, such as those typical for the UK, high spatial resolution is needed. However, such data is usually obtained with low temporal frequency, due to limitations of satellite revisit times and high costs of aerial imagery or acquisition from commercial satellites. Additionally, accurate and up-to-date information about the spatial distribution and intensity of infection is critical to allow effective planning and implementation of appropriate countermeasures, before irreversible damages and yield loss occur (Fassnacht *et al.*, 2014). Timely detection of tree diseases is thus particularly important as timing is crucial for both limiting the damage to trees and treating the disease (Elmendorf *et al.*, 2000). However, subtle changes in forest condition, such as foliage discolouration and defoliation, have proven difficult to detect and map (Royle and Lathrop, 1997; Radeloff *et al.*, 1999).

A number of studies have attempted early infection stage detection with varying results. Leckie *et al.* (2004), using airborne multispectral imagery, tried to detect various levels of laminated root rot infection, but experienced significant confusion between the healthy, lightly and moderately damaged classes. They also found a considerable amount of stressed trees unrelated to root disease activity classified as diseased. Pena and Altmann (2009) explored the suitability of vegetation indices derived from satellite hyperspectral data for identifying stress symptoms induced by the invasion of cypress aphid, and found some correlations (R^2 = 0.4-0.59) with two anthocyanin reflectance indices and the photochemical reflectance index. Kelly and Liu (2004) unsuccessfully attempted detection of trees affected by sudden oak death (SOD) in the pre-visual stage with multispectral airborne imagery by discerning trees undergoing moisture stress (an early disease symptom). Poor classification accuracy achieved in this study could have been an effect of using broad spectral bands, which combined narrow moisture stress-sensitive regions with broader stress-insensitive regions, decreasing the capability to detect moisture stress. Pontius *et al.* (2008) used a linear regression equation based on six known stress- and chlorophyll-sensitive indices (chosen through a mixed-stepwise linear regression) to predict ash decline on a continuous 0 to 10 scale. They reported R^2 of 71% and accuracy of decline detection within one class of 97%. However, this result should be treated with caution as this approach was based on a dataset with only five decline classes (2 to 6), and was not further tested on any independent dataset.

Pu *et al.* (2004) found a slight, yet statistically significant, spectral difference between leaf samples affected by sudden oak death and healthy leaves. It was also concluded that these would not allow detection of stressed trees when using a standard classification method. To utilise this finding, Pu *et al.* (2008) developed a multi-level classification (MLC) scheme consisting of four levels. Level 0 was used for classification of the entire study area, at Level 1 vegetated and non-vegetated areas were separated, at Level 2 these were subdivided into four vegetated (including an oak tree class) and four non-vegetated classes, and at Level 3 the oak class was subdivided into healthy and stressed trees. Using airborne hyperspectral imagery, they first extracted ten principal components (five from visible and five from NIR bands), and then applied the developed MLC to the dataset. This method yielded a producer's accuracy for stressed oaks of 73% at Level 3, and a joint producer's accuracy of 56% at Levels 2 and 3. This approach allowed differentiation of two oak health classes (unachievable at Level 0), indicating an increased spectral separability at the more detailed classification levels.

There has been more success in detecting green (pre-symptomatic) attack stage of bark beetles. Niemann *et al.* (2015) examined spectral properties of infected forest stands at pigment and water absorption features with use of airborne hyperspectral imagery. The authors derived continuum removed (CR) spectra for three health classes (healthy, green attack and red attack stages), and assessed their separability with SAM classifier. The analysis indicated high separation of the classes at the pigment absorption feature, and slightly lower one at the water absorption features, indicating that mapping pre-symptomatic stages of infection is possible. Fassnacht *et al.* (2014) used airborne hyperspectral imagery and a support vector machine classification approach to detect various degrees of pine beetle infestation and mortality. The tree mortality was classified with a producer's accuracy of 95%; separation of the early stages of beetle attack was also possible, but the producer's accuracy was reduced to 61%.

Adelabu *et al.* (2014) has shown that the inclusion of the red-edge band significantly increases capability of classifying insect defoliation levels. They used NDVI and the red-edge adaptation of NDVI to discern healthy, partly defoliated and refoliating (after severe defoliation) mopane trees (*Colophospermum mopane*) on satellite multispectral imagery. When the red-edge channel was included, the overall accuracy has increased from 51 to 83%, whilst detection accuracy of partially defoliated trees increased from 60 to 76%. Coops *et al.* (2003) also utilised the red-edge region of electromagnetic spectrum, whilst using airborne hyperspectral imagery for detecting *D. septosporum* infection

severity. By using the lower slope of the red-edge, Red-edge Vegetation Stress Index (RVSI) and "halo" sampling approach (which ignored each tree crown's brightest central pixels), they succeeded at detecting three severity levels of infection with an accuracy of over 70%.

2.6 Summary

The previous chapter highlighted the importance of detection and monitoring of forest insect pests and diseases in the light of changing climatic conditions. With traditional field surveys being unsuitable for monitoring large spatial extents of forest stands, remote sensing could significantly aid forest health monitoring as it provides better spatial coverage, shorter sampling intervals, and access to restricted areas. This chapter demonstrated how common symptoms occurring during disease onset or infestation can be detected and quantified using remote sensing technologies. Furthermore, it reviewed the use of remote sensing for identification of disease and pest outbreaks, which showed that only a limited number of studies, all utilising spectroscopy, investigated disease onsets in forest environments. There have only been two connected studies, on red band needle blight in Australia, examining the visible and near-infrared wavelength region. No further research examining the spectral characteristics of foliage affected by red band needle blight nor the transferability of the aforementioned methods to other species of pines or other climatic zones has been conducted. The use of LiDAR and thermal sensors for identification of disease-induced changes in forests has not been investigated either, leaving a major research gap. This research, therefore, examines the ability to detect the severity of red band needle blight using different remote sensing technologies, i.e. thermography, LiDAR and hyperspectral data.

Chapter 3. Data acquisition

3.1 Chapter overview

A range of remote sensing data and field measurements were collected specifically for this project. This chapter presents the study area, describes the available data sets and presents the methodology behind their acquisition. The field data were collected during two fieldwork campaigns. In summer 2014, the research plots were established, plot-level measurements were performed and a range of airborne data was collected. During a follow-up fieldwork campaign in August 2015, UAV-borne visible and thermal imagery was acquired, accompanied by destructive sampling and leaf spectroscopy measurements.

3.2 Pine plantations in the UK

The area of woodland in the UK is estimated to be 3.16 million hectares (13% of the total land area), around half of which comprises conifers. Pines are among the most commonly found conifer trees, with Scots pines accounting for 17%, Lodgepole pines for 8% and Corsican pines for 4% of the total conifer area. In 2016 there were 218, 100 and 40 thousand hectares of Scots, Lodgepole and Corsican pine woodland in total (Forestry Commission, 2016). The wood is widely used for roofing, flooring and other general building work, as well as for furniture production. Scots and Lodgepole pine plantations are most prevalent in Scotland (accounting for 71 and 88% of total UK area occupied by those species) (Forestry Commission, 2016). Due to this prevalence, this research focused on diseased single-species stands in Scotland.

3.3 Study area

The study was located in central Scotland in Queen Elizabeth II Forest Park, which lies within the Loch Lomond and the Trossachs National Park. The park is managed by the Forestry Commission and consists of 50,000 acres of commercial plantation forest and semi-natural woodland. Within the park, Scots pine (*Pinus sylvestris*) and Lodgepole pine (*Pinus contorta*) stands are infected with red band needle blight and exhibit various stages of physiological stress. Four study sites representing a range of red band needle blight infection levels were chosen in Scots and Lodgepole pine stands. The locations of the study area and each of the sampling plots are shown in Figure 3.2, whilst the main characteristics of all chosen plots are presented in Table 3.1. Plot A was initially established by Forest Research, with two trees instrumented with multi-depth sap flow sensors; though, the readings were not available at the time of the UAV-borne survey in 2015 due to equipment malfunction. Plot B was supposed to serve as a reference healthy

Scots pine site (average visible disease level of 0.6%), but in the end it was only used for leaf level water content measurements, being outside of the airborne data coverage. Plots C and D were located in Lodgepole pine stands with contrasting health statuses in terms of defoliation and the observed disease level. A further fifth plot in a mature Scots pine stand with trees instrumented by Forest Research was established, but as it was not covered by any of the data acquisitions, it is not listed.

3.4 Sampling plots establishment

Due to difficult terrain conditions and/or substantial wind throw damage within some of the plots, two sampling designs were used; as presented in Figure 3.1. Design I was used for plot B and C, whilst design II was used for plots A and D. Within each of the plots, positions of sampling trees (approximately 50 per plot) were measured with the aid of land surveying methods. A number of fixed base stations, which served as control points, were established in clear-cut areas using relative GNSS positioning. Each station was observed for a period of at least two hours with the logging rate of 15 seconds, and processed with nearby OS Net continuously operating reference stations (KILN, GLAS and LOGG – located 32, 36 and 70 km away). In some of the cases, 1 hour long observation periods were performed and processed against observations from already established points, providing a short baseline solution. Next, using the control points, stations suitable for detailing within sampling plots were established through resection. Tree locations were obtained by surveying the trunk positions.
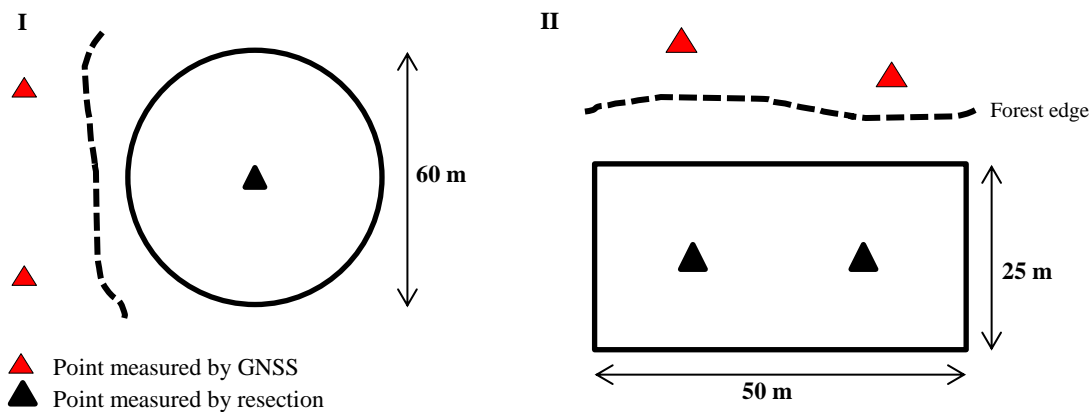
Figure 3.1: Schematic diagrams of the layouts of research plots.

Table 3.1: Main characteristics of sampling plots. Coordinates are given in WGS84.

Plot A

Location: 56° 11' 45.42"N   4° 23' 34.78"W

Elevation: 274 m

Planting year: 2003

Primary species: Scots pine

Average visible disease level: 59%

Average tree height: 4.5 m

Plot B

Location: 56° 11' 42.01"N   4° 23' 29.79"W

Elevation: 260 m

Planting year: 1940

Primary species: Scots pine

Average visible disease level: 0.6%

Average tree height: 23 m

Plot C

Location: 56° 08' 46.97"N   4° 28' 44.80"W

Elevation: 253 m

Planting year: 1965

Primary species: Lodgepole pine

Average visible disease level: 34%

Average tree height: 16 m

Plot D

Location: 56° 08' 20.17"N   4° 29' 31.91"W

Elevation: 321 m

Planting year: 1966

Primary species: Lodgepole pine

Average visible disease level: 15%

Average tree height: 15.5 m
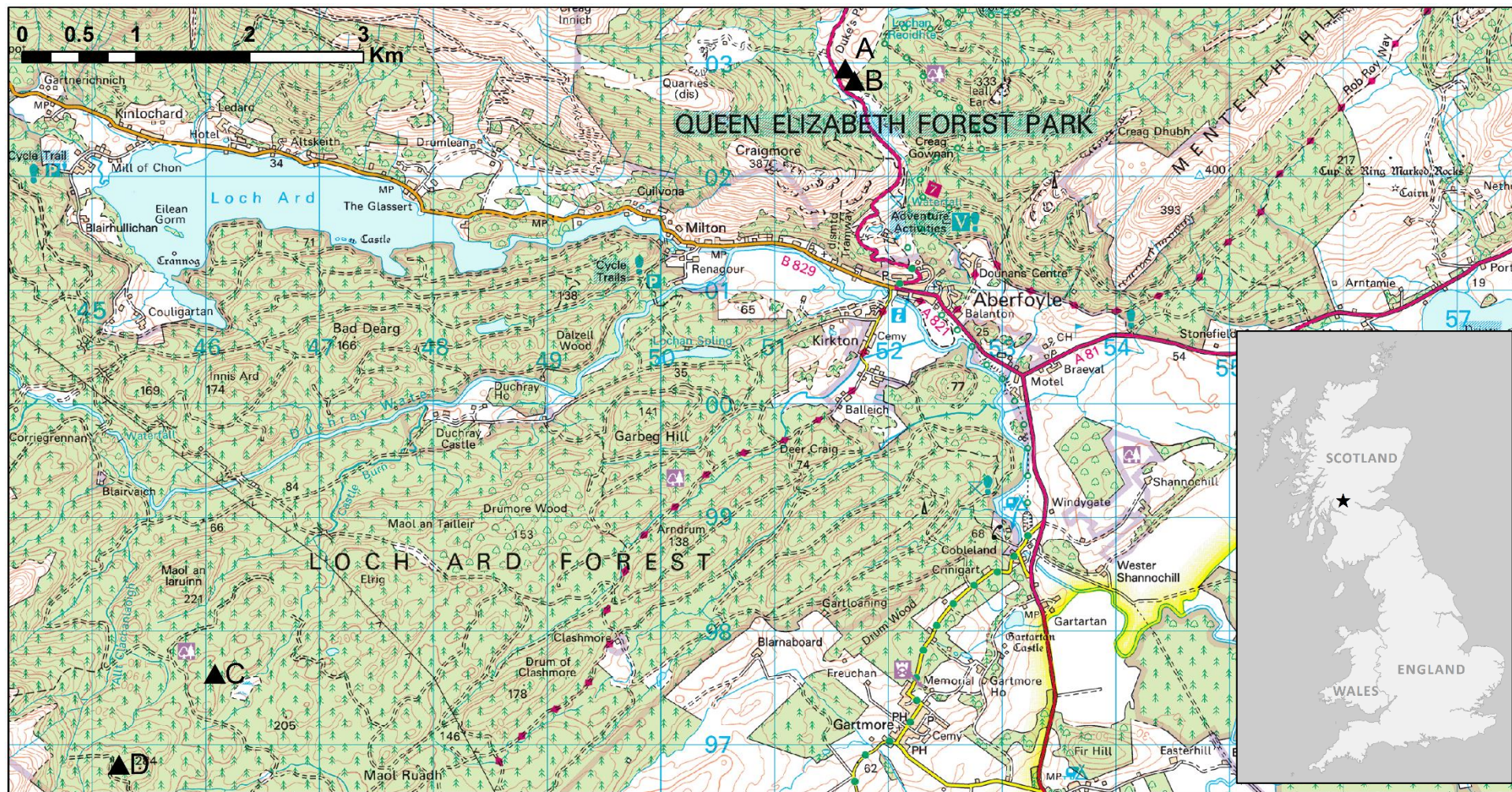
Figure 3.2: Location of the study area, and each of the sampling plots (triangles). Contains OS data © Crown copyright and database right 2017.

3.5 Plot-level measurements

Within each of the plots a number of structural measurements of sampling trees were performed. The measured variables were the diameter at breast height (DBH, at 135 cm), crown spread in the longest diameter and the diameter perpendicular to it (using densitometer and tape), and the height of the tree and of the lowest live foliage (using a vertex hypsometer). The height measurements were used to compute live crown depth and uncompacted live crown ratio. Live crown depth is determined as the distance between top live foliage and the lowest foliage on the lowest live twig (Schomaker *et al.*, 2007). All dieback, dead branches, as well as sprigs or leaves on the main stem below the lowest twig were excluded from the estimation. Uncompacted live crown ratio is defined as the tree's length with live foliage, relative to the tree height. The ratio is calculated by dividing the live crown depth by the actual tree height, and then multiplying by 100 to express the ratio as a percentage (Figure 3.3).
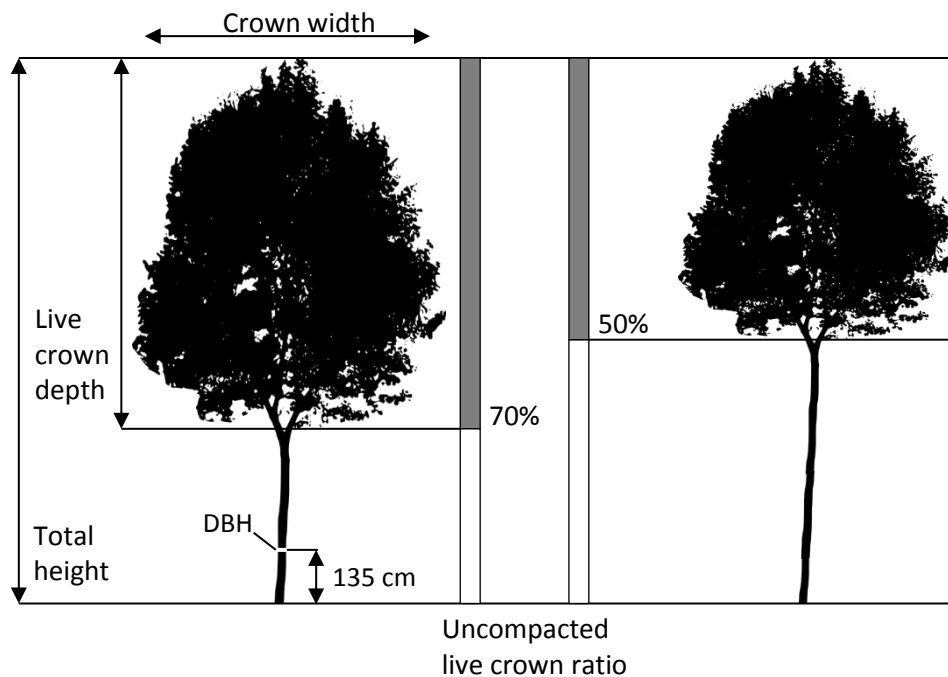
Figure 3.3: Summary of the performed tree structural measurements.

Another measured variable was the severity of red band needle blight infection, which was assessed with binoculars by estimating the proportion of infected to uninfected tree crown, following guidelines from Bulman *et al.* (2004). Infection level was expressed as percentage of total unsuppressed crown volume in 5% steps (i.e. 5, 10, 15 …), where a score of 20 indicates that 20% of the crown was diseased. In addition, a 1% score was given to trees where the disease was detectable at a trace level. Bare branches caused by needle loss, as well as sprigs or leaves on the main stem below the lowest twig were

excluded from the estimation. In case of plot A, infection levels were established with help of a hypsometer; further details are provided in Chapter 5 Section 4.1.

Soil water levels within the plots were measured to compare local conditions and rule out drought stress. The measurements were performed with a ML2x ThetaProbe soil moisture sensor at four locations in each of the plots. To avoid bias, any plants, scrape mulch or leaf litter were removed prior to measurements. A summary of all described measurements for plots A, C and D is presented in Table 3.2.

Table 3.2: Summary of measurements performed within sampling plots.

		A	C	D
Diameter at breast height (cm)	Min	4.5	14.3	15.7
	Max	11.6	49.7	40.7
	Avg	7.6	22.6	27.1
Average crown spread (m)	Min	1.6	0.8	1.8
	Max	3.15	6.4	5.4
	Avg	2.2	2.5	3.2
Tree height (m)	Min	3.5	10.4	7.9
	Max	9.8	21.6	22.6
	Avg	4.8	16.1	15.5
Uncompacted live crown ratio (%)	Min	77	11	44
	Max	100	85	99
	Avg	89	50	68
Disease level (%)	Min	25	0	0
	Max	80	90	60
	Avg	59	34	15
Soil moisture (%)	Avg	51	94	44

3.6 Destructive sampling

3.6.1 Leaf spectroscopy

Twenty of the surveyed trees from plot A were destructively sampled to perform leaf spectral measurements. Twigs from upper and lower canopy (chosen in a random manner with closed eyes) were harvested, and their needles combined to homogenise the samples. The foliage collected from the upper canopy predominantly constituted of green needles, whilst foliage from lower parts was composed of a mixture of green and partially discoloured needles. Upon collection, the samples were immediately put in sealable bags and placed on ice for later measurement. Maximum time between the collection and measurements was 7 hours. The spectral reflectance of the needles was measured using an ASD FieldSpec Pro spectroradiometer and a fibre optic contact probe with illumination source. The sample needles were closely aligned to minimise gaps and attached to a black

insulating background to form a continuous surface. The reflectance was then recorded with the probe tip orientated in the nadir position, perpendicular to the leaf surface, for a spectral range from 350 nm to 2500 nm, at a 1 nm spectral sampling interval. Between each measurement, a SpectralonTM reference panel (average reflectivity = 0.970) was measured. The processing procedures applied to leaf spectral measurements are described in Chapter 6, Section 4.

3.6.2 Leaf water content

Leaf samples from a number of surveyed trees (7, 5, 4 and 4 from plots A, B, C and D accordingly) were collected to perform water content measurements. In plot A, the needles were collected from twigs originating from different parts of the canopy (top, middle and bottom). In other plots the samples were obtained with aid of arborist sling-shot, which allows for sample retrieval from branches located up to 12 metres above the ground level. Homogenisation was achieved by composing samples with needles from different twigs. The collected needles were then immediately put in sealable bags to avoid moisture loss. In order to obtain leaf water content, the fresh weight of samples was recorded using an analytical balance (Tree HRB-103). The sample needles were then dried at 65°C in a circulation oven, until a constant weight was reached. Following this, the leaf gravimetric water content on dry (*GWC$_d$*) mass basis was calculated:

$$\text{GWC}_d = [(m_f - m_d)/m_d] * 100 \qquad (3.1)$$

where m_f is the fresh leaf mass and m_d is the oven dry leaf mass.

A weak negative correlation (-0.609, p=0.003) was found between the estimated disease level and the retrieved leaf water content (Figure 3.4). When the leaf measurements were divided into specie subgroups, a strong negative correlation was obtained for the Scots pine samples (-0.861, p<0.001), and no statistically significant correlation was found for the Lodgepole pine samples (0.043, p=0.913).
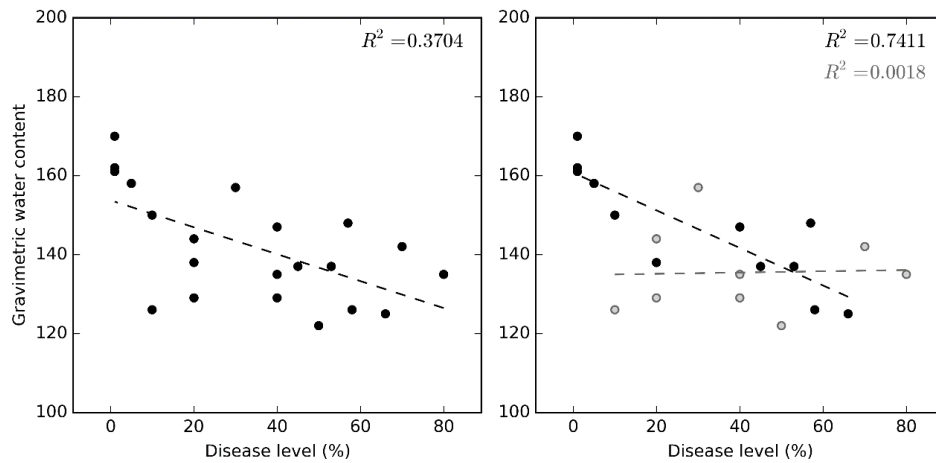
Figure 3.4: Relationship between the estimated disease level and leaf gravimetric water content for all samples (left), for Scots pine (right, black markers) and for Lodgepole pine (right, grey markers) samples only.

3.7 Airborne data collection and pre-processing

Airborne hyperspectral, discrete and full-waveform LiDAR data were collected specifically for this project by the Natural Environment Research Council (NERC) Airborne Research Facility (ARF). The datasets were acquired on the 7th of August 2014 between 15:30 and 16:30 GMT from an altitude of 1280 m, under scattered cloud cover. The sensors that were used for data collection were the Leica ALS50 Airborne Laser Scanner and the hyperspectral Aisa FENIX imager. Their specifications can be found in Table 3.4, whilst acquisition details are given in Table 3.3. Examples of the acquired airborne data are shown in Figure 3.5, Figure 3.6 and Figure 3.7.

Table 3.3: Details of the airborne remotely sensed data sets collected for the study.

Sensor	Resolution	Coverage:
AisaFENIX	448 spectral bands (383 – 2505 nm) Nominal spatial resolution: 2 m.	Plots C and D
LiDAR	8.4 points per m^2, recording first, second, third and last returns and intensity	Discrete: plots A, C, D Full-waveform: N/A

Table 3.4: Specifications of the airborne sensors used for this study.

SPECIM AisaFENIX:	
Sensor type	Dual channel hyperspectral sensor
Spectral range	VNIR 380-970 nm, SWIR 970 – 2500nm
Spectral resolution	VNIR 3.5 nm, SWIR 12 nm
Number of spectral bands	620
Instantaneous field of view	0.084°
Swath width	0.58 x altitude
Leica ALS50-II LiDAR	
Sensor type	Airborne laser scanner
Used operating mode	Full-waveform
Max field of view	75° *(full angle)
Beam divergence	0.22 mrad
Scan repetition rate	Up to 120 kHz
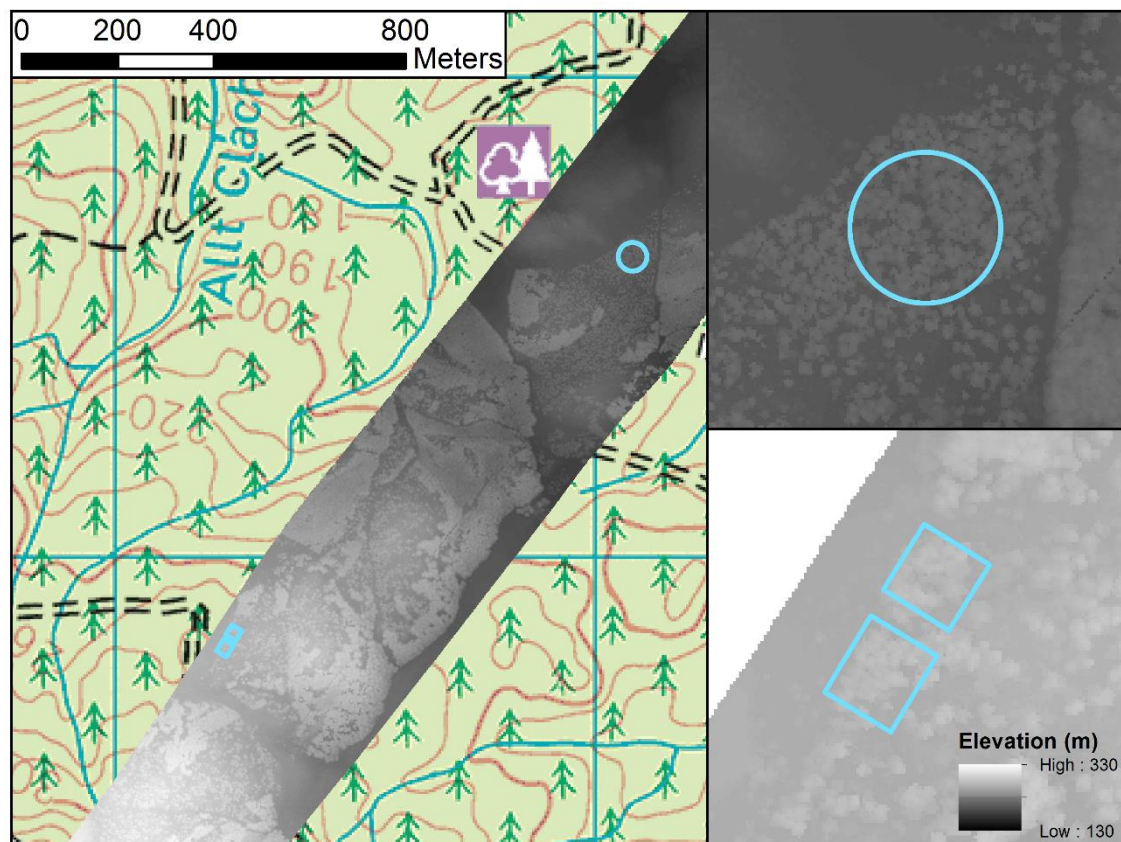
Figure 3.5: LiDAR-derived digital surface model for plots C (*top*) and D (*bottom*).
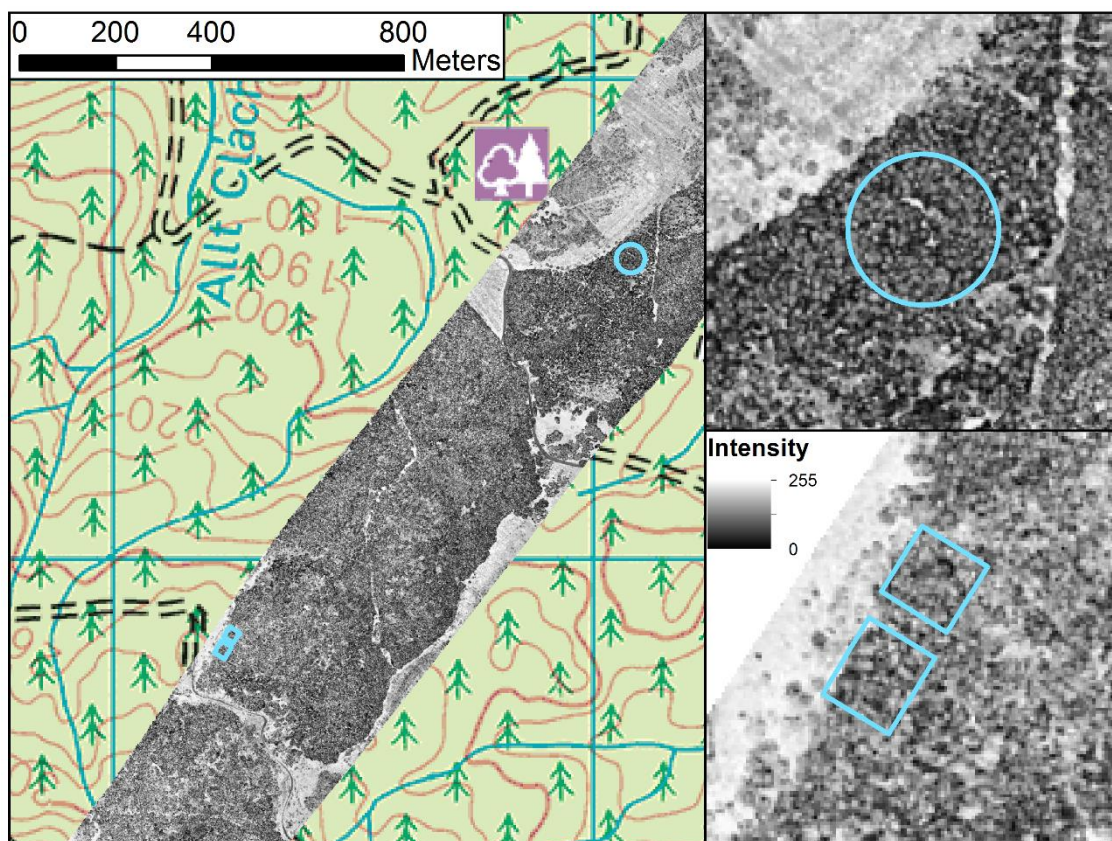
Figure 3.6: LiDAR intensity values for plots C (*top*) and D (*bottom*).
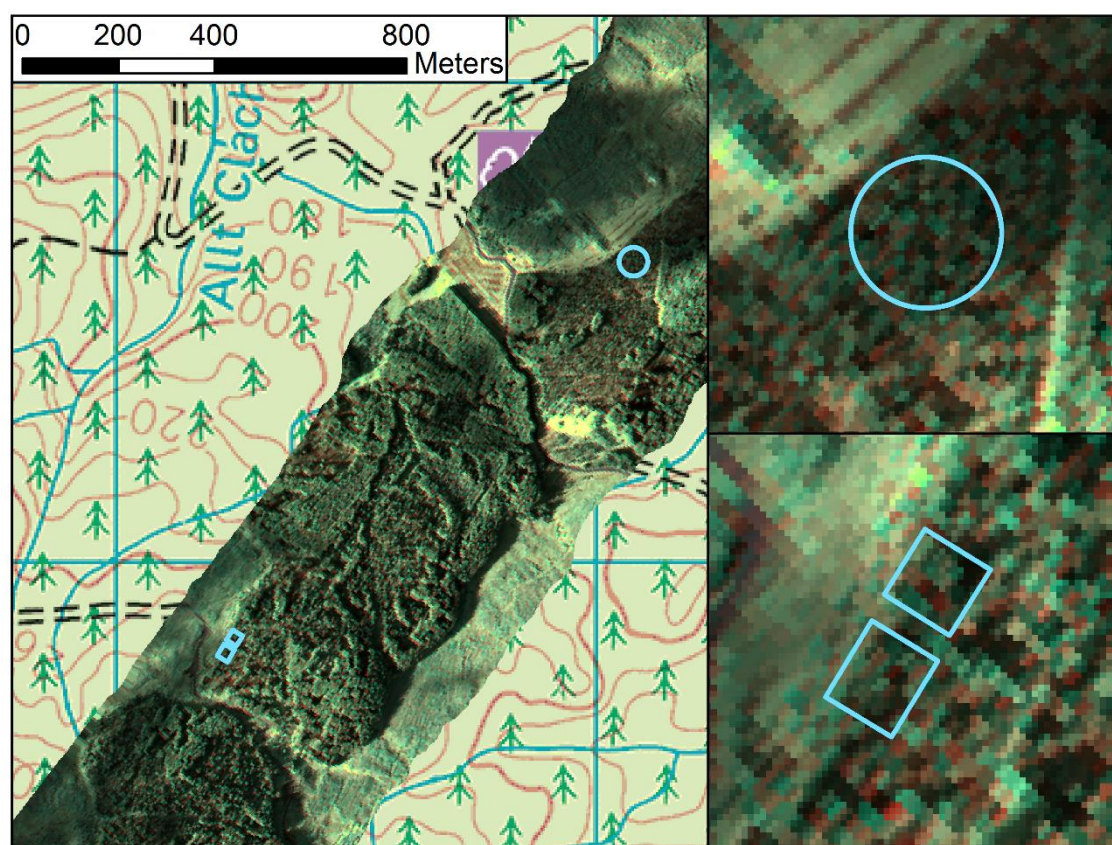
Figure 3.7: Hyperspectral imagery acquired for plots C (*top*) and D (*bottom*).

Hyperspectral imagery was delivered as Level 3 data (Figure 3.7) following a radiometric and atmospheric correction (projection: British National Grid). The atmospheric correction was performed in ATCOR4 version 7.0.3 using variable visibility. To reduce noise, the data were spectrally resampled prior to correction by averaging over 3 bands for VNIR and 2 for SWIR using a Gaussian response function. Due to high noise levels, the following ranges had to be removed: 615-633, 685-740 and 1060-1090 nm. A comparison of reflectance from the imagery with ground spectra collected using the ASD spectrometer is provided in Appendix A.

Pre-processing of the LiDAR point clouds at plot locations was performed in the FUSION software, developed by the U.S. Department of Agriculture (USDA) Forest Service (McGaughey, 2016). Digital elevation models (DEMs) of the plots were generated using ground points with a spatial resolution of 2 m. The ground returns were extracted from the point cloud using a filtering algorithm based on Kraus and Pfeifer (1998), with 40 iterations and a tolerance of 0.05 m. The algorithm uses an iterative process to create an average surface using all input points by calculating weights for every point based on its distance and direction to the surface. On the final iteration, all points lying within a specified distance of the final intermediate surface (tolerance) are considered bare-earth points. The final surface was then filtered to remove spikes (>45°) related to residual returns from vegetation. These DEMs were used to normalise LiDAR returns for differences in elevation. Using the normalised first return data, canopy height models (CHMs) with a spatial resolution of 1m and 0.5m were generated for each plot, assigning the elevation of the highest return within each grid cell (Figure 3.8). Any gaps in data were filled using a 3x3-window mean.
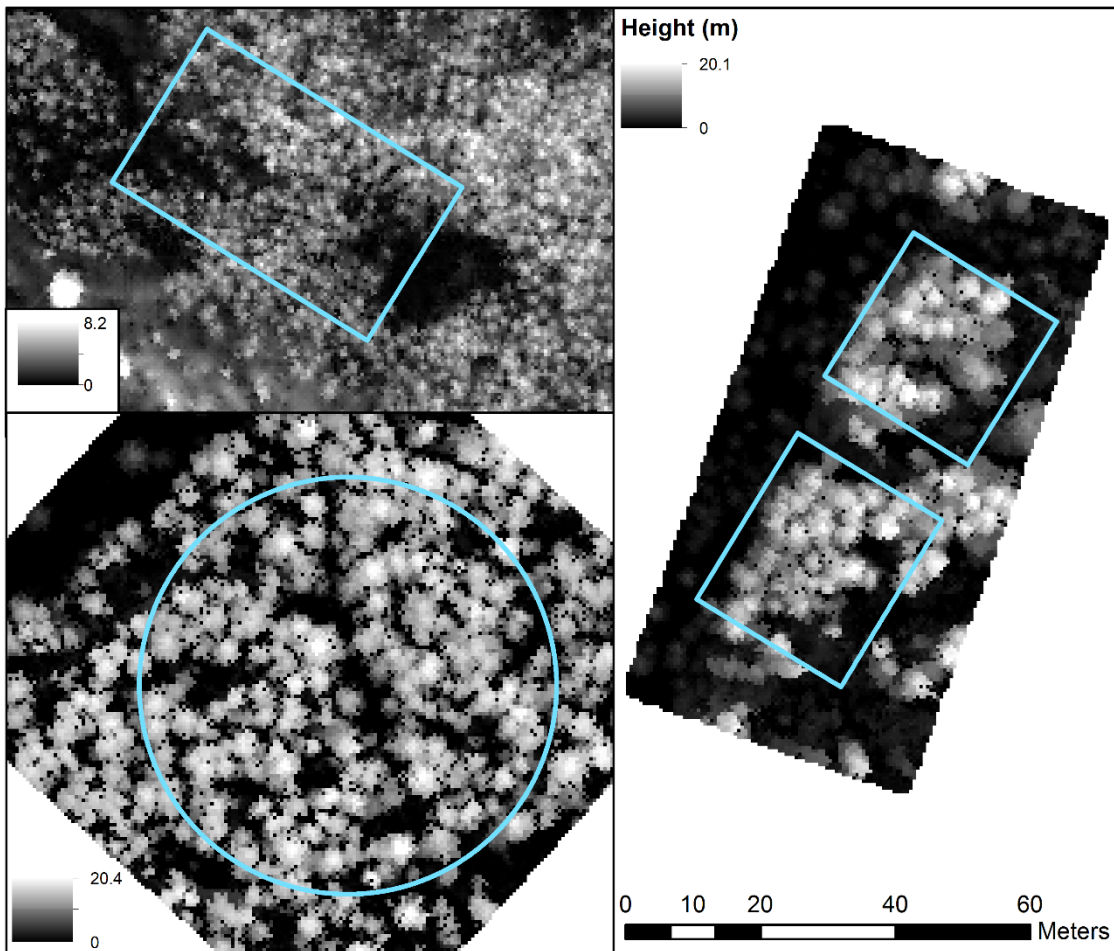
Figure 3.8: CHMs of plots A (*top*), C (*bottom*) and D (*right*).

3.8 UAV-borne data collection and pre-processing

The UAV used for this research was a DJI Phantom 2 Vision+ Quadcopter, which is a lightweight (1160g) aircraft with an integrated, wide-lens camera (with resolution of 14 Megapixels and recording field of view of 110 degrees). In August 2015, the quadcopter's camera was used to collect recordings of the plots, from which frames were extracted to serve as reference imagery. The resultant image overlap is shown in Appendix B. The extracted images were first corrected for lens distortion in Photoshop (version 18.0) using a universal distortion model provided by the DJI. The images were then used for orthophoto generation, complemented by the Structure from Motion (SfM) workflow. First, points visible on multiple photographs (tie points) were detected to enable multiple stereo-pair reconstruction; the image alignment step was undertaken in Agisoft PhotoScan (version 1.2).

Five ground control points (GCPs), circular targets established within each of the plots, were then utilised to scale and orientate the tie points into a fixed reference frame (OSGB36), and used as external constraints. In combination with the detected tie points, they allowed for the self-calibration of the bundle adjustment. Inclusion of GCPs not only allows for projecting the point cloud to a reference system, but also adds constraints, which can mitigate systematic errors in the DEM shape (James and Robson, 2014). The coordinates of GCPs were obtained through post processed kinematic (PPK) GNNS positioning technique. For this purpose a base GNNS receiver was positioned at a pre-established base station, with data logging interval of 1 second. The centre of each GCP was occupied with a rover receiver for a period of at least 3 minutes, with a data logging rate of 1 second. Following the bundle adjustment, dense point clouds were generated. Images were then aligned to create orthomosaics, using 3D meshes created from the dense point clouds. The settings used in the Photoscan's workflow are summarised in Table 3.5, whilst the derived orthomosaics are shown in Figure 3.9, Figure 3.10 and Figure 3.11. A short summary of survey details and the georeferencing accuracy is presented in Table 3.6; a more comprehensive report including GCP locations is provided in Appendix B.

Table 3.5: Settings used in the Photoscan's workflow for orthomosaic generation.

Task	Option	Setting
Align Photos	Accuracy:	High
	Pair selection:	Generic
	Key point limit:	100,000
	Tie point limit:	0
Optimise camera alignment	f, b1, b2, cx, cy, k1, k2, k3, p1, p2	
Build dense cloud	Quality:	Lowest
	Depth filtering:	Moderate
Build mesh	Surface type:	Height field
	Source data:	Dense point cloud
	Face count:	Moderate
	Interpolation	Enabled
Build orthomosaic	Surface:	Mesh
	Blending mode:	Mosaic

Specifically for this survey, the DJI quadcopter was modified in-house to carry a miniature longwave infrared camera (Optris® PI-450). This modification increased the take-off weight of the UAV by 600 g (to a total of 1760 g), and consequently limited the flight time to 6 minutes, allowing data collection in a safe manner only from a very limited area. On the 18th of August 2015, the aircraft was used to collect multiple thermal datasets in plot A. The camera characteristics and calibration are further discussed in Chapter 4, whilst the acquisition details and processing procedures for thermal imagery are described in Chapter 5, Section 4.

Table 3.6: Processing details and RMSE measures obtained for each plot. The error measures were estimated based on control points used in the processing.

Projection	Plot A	Plot C	Plot D
Number of images	607	352	291
Flying altitude (m)	69	62.2	71.3
Number of tie points	273 819	288 317	376 321
Ground resolution (cm/pixel)	5.32	4.55	5.52
Reprojection error (pixel)	0.776	0.924	1.190
Control points RMSE			
Planimetric error (cm)	3.420	20.768	14.664
Vertical error (cm)	4.205	1.042	0.401
Total error (cm)	5.420	20.794	14.670
Image error (pixel)	0.395	0.453	0.276

3.9 Summary

This chapter presented the study area and provided a summary of remote sensing and field data collected specifically for this project. An overview of performed leaf-level (water content and reflectance) and tree-level (structure and disease level) measurements was presented. Furthermore, the chapter detailed the pre-processing procedures applied to the airborne hyperspectral (atmospheric correction) and LiDAR data (creation of DEMs and CHMs), as well as to UAV-borne imagery (orthomosaic generation). The leaf spectroscopy, UAV-borne orthomosaics and airborne data presented in this chapter were used for hyperspectral analysis of diseased stands in Chapters 6 and 7, whilst UAV-borne thermal imagery was used to investigate the potential to detect disease-induced canopy temperature increase in Chapter 5.
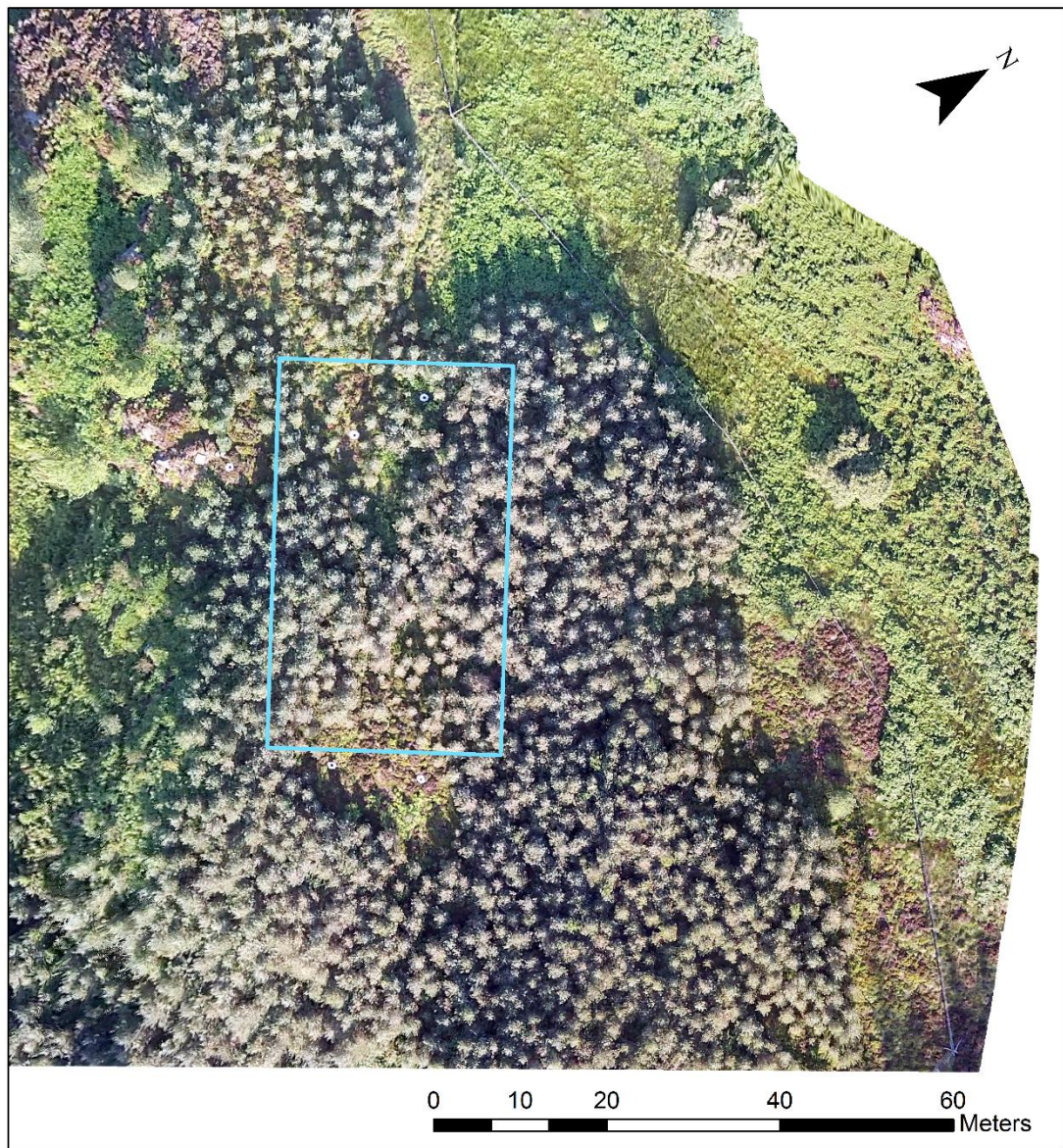
Figure 3.9: Orthomosaic of plot A (blue polygon) and the surroundings.
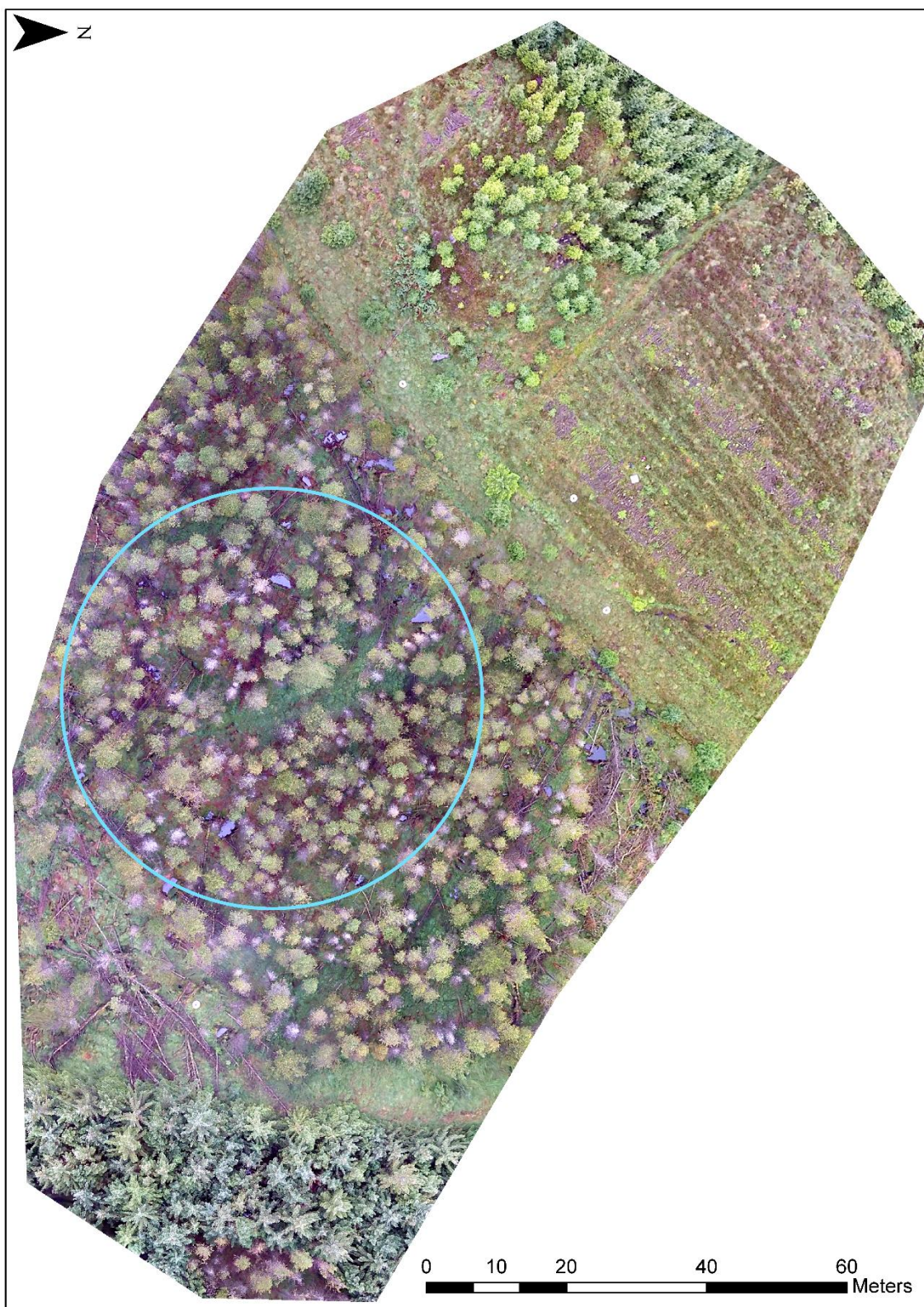
Figure 3.10: Orthomosaic of plot C (blue polygon) and the surroundings.

Figure 3.11: Orthomosaic of plot D (blue polygon) and the surroundings. Plot D was divided into two subplots due to wind throw damage.

Chapter 4. Thermal sensor characterisation

4.1 Chapter overview

This chapter investigates the performance of a low-cost thermal infrared camera developed for UAV systems in terms of providing radiometrically accurate temperature measurements. Firstly, theoretical principles of thermal imaging are explained. Then the performance of the thermal camera is inspected in laboratory conditions, resulting in a non-uniformity correction of the sensor's response. Furthermore, the stability of this calibration under changing camera temperatures is inspected, and a field-based investigation of camera performance (simulating flight conditions) is performed using a ground target, for which the retrieval of spectral emissivity values is also described within this chapter.

4.2 Theoretical background of thermal remote sensing

The thermal part of the electromagnetic spectrum occupies wavelengths from 3 to 14 µm; however, due to atmospheric absorption, only two regions are utilised by thermography: 3-5 µm and 8-14 µm (longwave infrared) (Lein, 2012b; Kuenzer and Dech, 2013). Within the 3-5 µm region, daytime TIR imagery can be slightly contaminated by reflected radiation. Therefore, more typically, the longwave infrared region is utilised, which is only affected by a narrow ozone absorption band (Kuenzer and Dech, 2013).

Thermal sensors measure the radiant energy of surface features, quantifying the emitted energy. Temperature readings recorded by such sensors are calculated by relating the measured radiant energy to the energy that would have been radiated by a blackbody source at the same temperature. A blackbody is a perfect hypothetical radiator that absorbs and re-emits all incident energy. The electromagnetic radiation emitted by a blackbody is described by Planck's blackbody radiation law, and for any given wavelength can be calculated from its temperature:

$$R_{BB}(T, \lambda) = \frac{2hc^2}{\lambda^5 (e^{hc/\lambda kT} - 1)} \qquad (4.1)$$

where R_{BB} is spectral radiant exitance, h is Planck's constant, c is speed of light, k is Boltzmann's constant, T is absolute temperature, and λ is wavelength.

The wavelength of maximum emittance and total amount of energy radiated by a blackbody depend on its temperature. The total emitted electromagnetic radiation is defined by Stefan-Boltzmann's law, whilst Wien's displacement law describes the

wavelength of maximum spectral radiant exitance. In essence, with increasing temperature of an object, the total amount of emitted radiation increases (in a non-linear way), and the maximum spectral radiant exitance shifts to shorter wavelengths (Kuenzer and Dech, 2013), as presented in Figure 4.1.
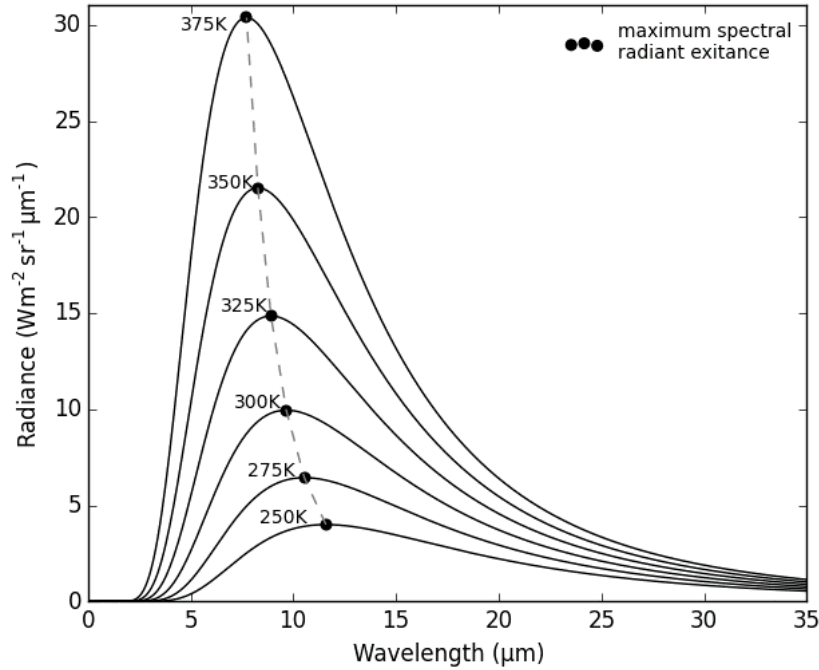
Figure 4.1: Blackbody radiation curves calculated for different selected temperatures.

Terrestrial surfaces would normally not act as blackbodies, emitting only a percentage of the radiance incident on them. The amount of infrared energy radiated by such surfaces can be described as a function of its kinetic (surface) temperature (T) and its spectral emissivity (ε). The emissivity of a material is the ratio of the radiant flux of this object (R_S) to the radiant flux of a blackbody (R_{BB}) at the same kinetic temperature:

$$\varepsilon(\lambda) = \frac{R_S(T,\lambda)}{R_{BB}(T,\lambda)} \qquad\qquad 4.2$$

Emissivity varies as a function of wavelength, but generally is not temperature dependent. It also varies with surface type, strongly depending on surface roughness. As a result, surface objects with the same kinetic temperature can have widely different radiant temperatures (Figure 4.2).
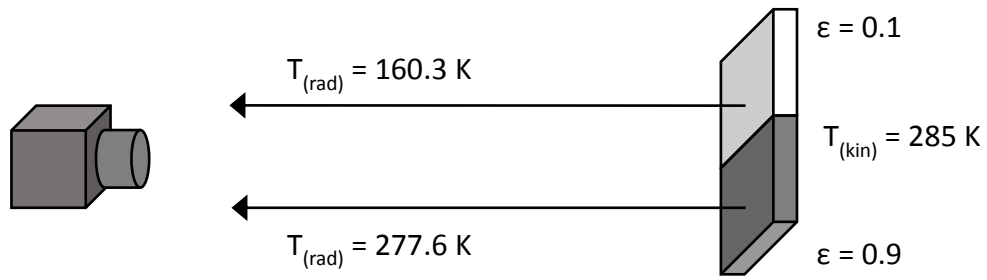
Figure 4.2: Impact of spectral emissivity on the radiant temperature, as recorded by a thermal infrared sensor. Based on Kuenzer and Dech (2013).

Using Kirchhoff's Law, the spectral emissivity of an object can also be predicted from its spectral reflectance (r):

$$\varepsilon(\lambda) = 1 - r(\lambda) \tag{4.3}$$

Consequently, highly reflective materials would have small emissivity values, absorbing and radiating small amounts of energy. On the contrary, surfaces with low reflectance would have high emissivity value. If the emissivity of an object is known, its radiant temperature can be converted to the kinetic temperature (utilising Stefan-Boltzmann's law and the definition of emissivity):

$$T_{(rad)} = \varepsilon^{(1/4)} * T_{(kin)} \tag{4.4}$$

4.3 Emissivity measurement principles

The emissivity value of a surface defines the amount of infrared energy radiated by it, and consequently influences a thermal sensor's temperature reading. Emissivity values range from 0 to 1, with the most efficient emitter being a blackbody ($\varepsilon = 1$). Objects whose emissivity is less than 1, but remains constant across all wavelengths, are called grey bodies. Some organic materials exhibit behaviour close to this; however, most objects, especially man-made materials, are selective radiators (also known as non-grey bodies). In effect, their emissivity is expressed as a function of wavelength, otherwise known as spectral emissivity (Smith, 2010).

Emissivity values of various substances and materials can be obtained from generalised tables. These would usually only provide the so-called total emissivity, which is the mean emissivity over all wavelengths at a given temperature, rather than spectral emissivity. Such tables should only be used as a guide, as the emissivity value can vary due to many factors, such as orientation of the material, nature of the surface (e.g. oxidised vs.

unoxidised), surface roughness, chemical composition and prior history (e.g. exposure to high temperature can change material properties) (Smith, 2010).

Emissivity can also be measured using indirect and direct techniques. Indirect methods mainly utilise Kirchhoff's Law to predict the spectral emissivity from the reflectivity and the transmissivity of a sample (Zhang *et al.*, 2015). Using direct measurement techniques emissivity is computed as a ratio of measured radiance values of a sample and a blackbody under the same conditions (e.g. temperature, wavelength and angle). Such methods would often employ a Fourier transform infrared (FTIR) spectrometer or a monochromator (Zhang *et al.*, 2015).

The core of FTIR spectrometers is the Michelson interferometer. It typically consists of a beam splitter and two perpendicular mirrors, one stationary and one movable. The incoming radiation is split in half into two different paths by the beam splitter towards the mirrors. The radiation is reflected, and recombined at the detector to produce an interference pattern. Measurements of the signal at multiple positions of the moving mirror are performed and recorded as a function of mirror position at discrete time intervals, generating an interferogram. A spectrum of energy intensity is then produced as a function of frequency (wavelength) by calculating the cosine Fourier transform of the interferogram. Figure 4.3 shows a schematic of the Michelson Interferometer.
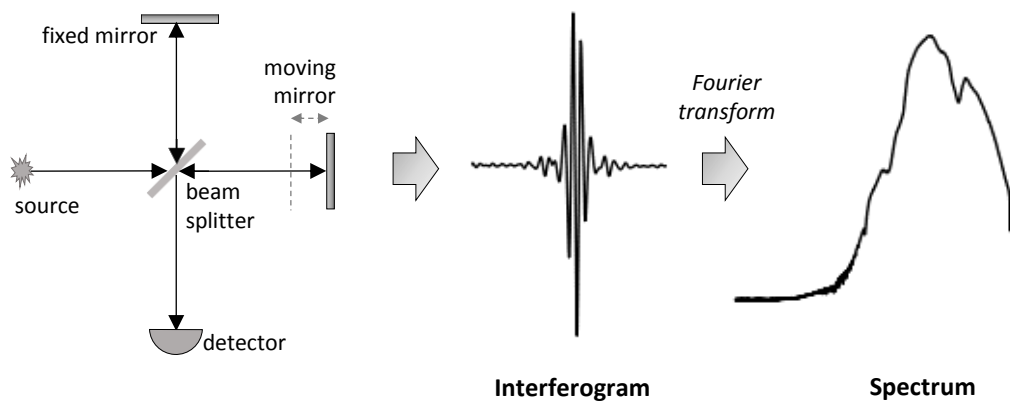
Figure 4.3: Schematic of the Michelson Interferometer, with an example interferogram and its corresponding single beam spectrum.

As radiation leaves the target surface, it interacts with the atmosphere and spectrometer elements, i.e. mirrors, beam splitters and lenses, before reaching the detector. The final measured spectrum of the surface is further affected by self-emission of these elements, as well as noise introduced by electronic parts of the system (filters and amplifiers). The

influence of each of these components cannot be theoretically modelled. Therefore, a calibration procedure has to be undertaken in order to determine the collective effect of these influences. The calibration process conventionally involves measuring spectra of reference radiation sources with known temperatures, typically blackbodies (Hecker *et al.*, 2013).

The radiance of the target can be described by a basic mathematical model as a function of the spectrum measured by the spectrometer:

$$R(\lambda) = G(\lambda)S(\lambda) + O(\lambda) \qquad 4.5$$

where R is spectral radiance emitted by target surface, G is spectral response (gain) of the sensor, S are digital numbers recorded by the sensor, O is spectral radiance emitted by sensor's internal parts (offset), and λ is wavelength. If the radiances of two blackbodies at different known temperatures ("cold" and "hot") are given by:

$$R_c = P(\lambda, T_c); R_h = P(\lambda, T_h) \qquad 4.6$$

where R_c and R_h are band-integrated "cold" and "hot" blackbody radiances, T_c and T_h are their temperatures, and P is Planck blackbody radiance, then by measuring image intensities, there is enough information to solve Equation 4.5 for gain (G) and offset (O) parameters:

$$G(\lambda) = \frac{R_h(\lambda) - R_c(\lambda)}{S_h(\lambda) - S_c(\lambda)} \; ; \; O(\lambda) = R_h(\lambda) - G\,S_h(\lambda) \qquad 4.7$$

The upwelling target radiance measured by a spectrometer is composed of both target thermal emission and reflected downwelling radiance (DWR). The DWR originates from the atmosphere above the sample, as well as radiance emissions from surrounding objects. Measurements of DWR, therefore, have to be taken using a diffusive reflective surface, typically using an InfraGold panel with emissivity < 0.1 (Hecker *et al.*, 2013). The radiance received by the FTIR spectrometer during the measurement of the gold plate can be then described as:

$$R_G(\lambda) = [\varepsilon_G(\lambda)R_{BB}(T_G, \lambda) + (1 - \varepsilon_G(\lambda))R_{DWR}(\lambda)]\tau_A(\lambda) + R_A(\lambda) \qquad 4.8$$

where R_G = radiance emitted by a gold plate, R_{BB} is radiance emitted by a blackbody at gold plate temperature, R_{DWR} is downwelling radiance, R_A is atmospheric radiance between the plate and spectrometer, τ_A is atmospheric transmission between the plate and spectrometer, ε_G is emissivity of gold plate, and T_G is temperature of gold plate. If

measurements are performed over a path shorter than 1 m, the atmospheric terms τ_A and R_A can be ignored, and the above equation can be rearranged to:

$$R_{DWR}(\lambda) = \frac{R_G(\lambda) - \varepsilon_G(\lambda) R_{BB}(T_G, \lambda)}{1 - \varepsilon_G(\lambda)} \qquad 4.9$$

The DWR subsequently has to be subtracted from upwelling target radiance to isolate target emission and obtain absolute emissivity:

$$\varepsilon_S(\lambda) = \frac{R(\lambda) - R_{DWR}(\lambda)}{R_{BB}(T_S, \lambda) - R_{DWR}(\lambda)} \qquad 4.10$$

Using these measurement principles, a number of LWIR spectral libraries have been created, which provide information on a wide variety of materials (e.g. Baldridge *et al.* (2009), Kerekes *et al.* (2008) and Kotthaus *et al.* (2014)). Most recently, Kotthaus *et al.* (2014) derived emissivity spectra of 74 samples of impervious surfaces and quantified measurement uncertainties for a setting with moderate temperatures (40-70°C). The spectra were measured with MIDAC M2000 series FTIR spectrometer; since the same instrument was used in this study it is assumed the findings are directly transferable. Kotthaus *et al.* (2014) showed that the two-blackbody method works best if the blackbody sources are set to temperatures closely bracketing the target's temperature, i.e. for the samples at 50-60°C, the blackbodies were set to temperatures of 40-45°C and 70°C. With such setting, the errors introduced by calibration remained small with mean bias error of 0.06 W m^{-2} μm^{-1} sr^{-1} between 8 and 14 μm. The calibration remained most stable for the 9-11 μm spectral region indicating a better signal-to-noise ratio in the centre of the LWIR region for the used temperatures. It was suggested the overall signal-to-noise ratio can be improved by heating the samples well above room temperature and by sampling the target spectral radiance multiple times. However, increasing the number of scans extends the measurement period during which the target's temperature must remain stable. It is vital to ensure a set of measurements is collected in a relatively short time period as incoming radiance and instrument response are assumed stable throughout this time.

4.4 Currently available camera technologies

There are two types of sensors that are typically used for thermal cameras: quantum detectors and thermal detectors. The former utilises photoconductive cells, and are based on quantum absorption phenomena in semiconductor material. The main advantage of quantum detectors is that they can have short (sub-nanosecond) response times and very high sensitivities. However, such detectors exhibit strong wavelength dependence and only operate efficiently when:

$$kT_d < h/\lambda \qquad\qquad 4.11$$

where k is Boltzmann's constant, h is Planck's constant, T_d is detector's temperature, and λ is wavelength of radiation to be detected. As a result, an external cooling system is required in order to reduce thermal generation of charge carriers and thermal noise. Typically for sensitive imaging in the mid- to far-infrared regions, quantum detectors would be operated at cryogenic temperatures [i.e. down to 77 K (liquid nitrogen) or 4 K (liquid helium)]. This need for deep cooling significantly limits their applications (Datskos and Lavrik, 2004; Luhmann *et al.*, 2013).

Thermal detectors produce an electrical response as an effect of a temperature change of the detector element. As they absorb IR radiation, the amount of produced heat varies, leading to a change in the electrical properties of the detector. These changes are then measured and transformed into intensity values. Thermal detectors tend to have slower response times and are less sensitive than quantum detectors, but do not need any cooling element. This makes them less expensive and more competitive, as well as allowing for miniaturisation of the sensor (Datskos and Lavrik, 2004; Luhmann *et al.*, 2013). Lack of a cooling system results in a low signal-to-noise ratio, but makes such sensors sufficiently lightweight for inclusion as part of an UAV payload. Uncooled thermal imagers are severely degraded by spatial non-uniformity noise, which is defined as spatially heterogeneous response of the camera to uniform incoming radiation (Holst, 1998). The non-uniformity noise has a fixed spatial structure, but its intensity varies over time due to instability in the camera temperature (Holst, 1998; Thomas *et al.*, 1999). It is particularly severe in microbolometer sensors because the infrared detector tends to drift over time; temperature variations result in a different thermal drift among the detector elements, exacerbating the effects of the non-uniformity (Grgic and Pusnik, 2011; Wolf *et al.*, 2016). Thermal imagers provide an internal system correcting for the drift and non-uniformity caused by the drift. However, as this system is located between the

detector and the optics (which are also imperfect), some non-uniformity across the image is expected to remain (Grgic and Pusnik, 2011).

4.5 Laboratory-based investigation of thermal camera performance

4.5.1 Equipment specifications and setup

The thermal sensor used for this study is a weight-optimised Optris® PI-450 longwave infrared camera, equipped with a 38° x 29° field-of-view lens and manual focus. It utilises uncooled microbolometers arranged into a Focal Plane Array (FPA) with optical resolution of 382 x 288 pixels. Microbolometer is a type of thermal detector, which is most extensively used in thermal cameras. Vanadium oxide and amorphous silicon are commonly used in its design as IR detecting materials. As IR energy strikes the microbolometer, the electrical resistance of its materials change. The change in resistance is probed by passing a current through the device and then used to produce a thermal image (Ostrower, 2006).

The Optris® PI-450 sensor operates in a spectral range of $7.5 - 13$ µm and a temperature range of $20 - 900°C$ (thermal sensitivity: 40 mK, accuracy: $\pm 2°C$ or $\pm 2\%$, whichever is larger). The camera's internal mechanical calibration device was set to flag in front of the detector every 12 seconds to correct for the thermal drift and non-uniformity caused by the drift. In-flight, the camera is operated through a miniaturised lightweight PC (with a Windows XP Professional operating system). The whole kit weighs 380 g, making it ideal for UAV-borne applications. Prior to such sensor use, its performance in obtaining reliable temperature measurements across the whole lens has to be determined. This is crucial for quantitative use of the camera, especially when applied to plant sciences, where differences in temperature are usually small.

The Optris® thermal camera was therefore calibrated in laboratory conditions against a thermally controlled flat plate blackbody radiation source (ISDC's IR-160, $\varepsilon_{BB} = 0.96$), ensuring the camera's field-of-view was fully covered by the blackbody (Figure 4.4). The emitter has a size of 12" x 12", temperature resolution of $0.1°C$ (calibration accuracy: $\pm 0.2°C$) with short and long-term stability of $\pm 0.2°C$ and $\pm 0.1°C$. It operates in the temperature range of ambient to $350°C$ and spectral range of $1 - 99$ µm. The blackbody source used in this study is heated by means of a resistive-heating element, which is designed to provide uniform heating of the entire surface area. To ensure even distribution of the power to the entire surface (that is proper uniformity), after each temperature setting change the system was given 30 minutes to stabilise before measurements were made.
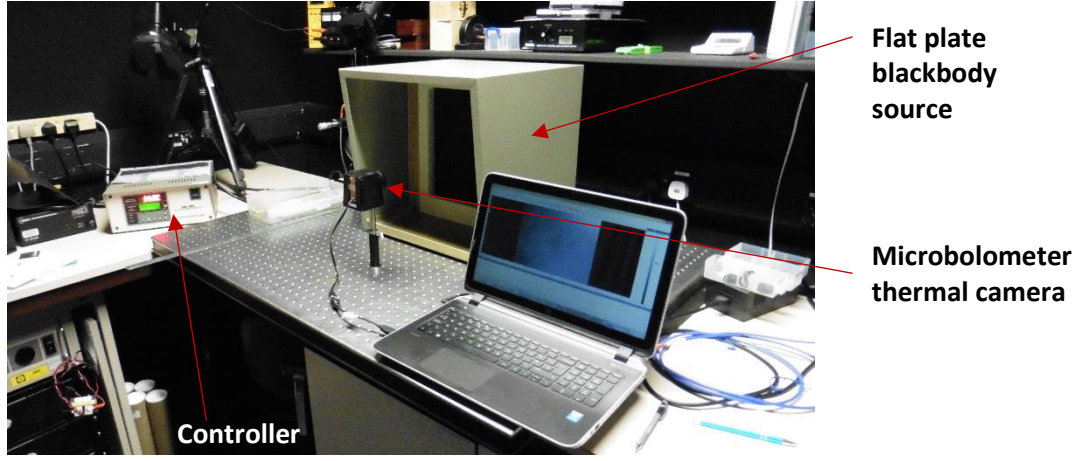
Figure 4.4: Equipment setup for camera calibration

4.5.2 Calibration process

Thermal cameras can be radiometrically corrected by quantitatively relating their output to source radiance or temperature. Typically, this would be performed by measuring the output digital numbers while the camera views one or more blackbody sources (Nugent *et al.*, 2013). In this study, the non-uniformity across the image was corrected using a two-point calibration technique, using Equation 4.5, where S is the digital number recorded by the sensor. The gain and offset parameters followed the same calculation process, utilising measurements of the spectral radiance emitted by the two blackbodies. Equation 4.6 was then adjusted to account for the emissivity of the blackbody source:

$$G = \frac{\varepsilon_{BB}R_h - \varepsilon_{BB}R_c}{S_h - S_c}; O = \varepsilon_{BB}R_h - GS_h \qquad 4.12$$

As equation 4.6 is sensitive to any non-linearity between the input radiance and output data, the average and pixel level sensor responses had to be linear in terms of emitted flux versus digitised flux over a range of temperatures at both image and pixel level. This was achieved by heating the blackbody to a wide range of temperatures (i.e. from 298.15 K to 333.15 K at 5 K increments), and recording the image intensities. The averages at each temperature step were calculated from 10 consecutive images, taken at 10 s intervals to account for variability of response over time. Images of the blackbody at 298.15 K to 333.15 K were then used to calculate the gain and the bias of each detector across the array. In order to check the effectiveness of the derived non-uniformity correction, the offset and gain matrices were applied to a temporal set of the imagery. The camera was set to store one raw image of a blackbody at 298.15 K (25.0°C) every minute over the course of 109 minutes. The kinetic temperature values acquired by the camera were

computed using an emissivity value for the blackbody of 0.96. Processing was performed in Python using self-written packages.

4.5.3 Experiment design

Calibration techniques based on the quantitative relationship between camera outputs and blackbody temperature assumes that the camera's response is time invariant, i.e. that an image of a scene taken at a later time can be calibrated to give a quantitative value. However, in the case of uncooled microbolometer imagers, the output depends on both the scene temperature and the FPA temperature. As such, their performance might vary with changes to the camera's temperature, since without thermal stabilisation, cameras might not maintain a stable radiometric calibration. Significant ambient temperature difference can cause the gain and offset of linear response of individual pixels to change. This effect is mostly due to temperature variations of the optics and FPA (Socolinsky *et al.*, 2003; Nugent *et al.*, 2013).

When deployed on a UAV platform, a camera would normally be subject to temperature change during the launch and altitude gain. According to the international standard atmosphere model (ISO 2533:1975, Standard Atmosphere), the air temperature decreases with altitude at a constant rate of 1.98°C/1000 ft. Based on this, for UAV operation at altitudes of 200 and 400 feet, the expected ambient temperature decrease would be 0.396°C and 0.792°C. The stability of the radiometric calibration with respect to changing ambient temperature was tested against a blackbody radiation source by altering the camera's temperature. For this purpose, several scenarios were tested, as summarised in Table 4.1. Sets 1 and 4 were acquired by cooling down the thermal sensor below the ambient in a walk-in cold room prior to the image acquisition. Set 3 was acquired by turning on an external heating source, raising the room's temperature. Sets 2 and 5 were control periods with relatively stable camera temperatures. The camera was then set to image the blackbody (heated to 25°C) at 10 second intervals, whilst its temperature was continuously monitored at 30 second interval with a thermocouple (attached to the camera's body). For each of the data sets, the rate of the camera temperature change (Tch_{cam}) was calculated at 60 second intervals. Temperature offset from true blackbody temperature (T_{off}) was retrieved for each image, and then resampled to the same 60 second intervals. Plots of the data series are provided in Appendix C.

Table 4.1: Summary of acquired data sets with camera treatment regimes.

Dataset	Treatment	Total camera temperature change	Average camera temperature change	Sample Length
Set 1: Cool1	Camera cooled down	6.97°C	0.21°C per min	34 minutes
Set 2: Stable1	None	0.74°C	0.02°C per min	34 minutes
Set 3: Warm1	Ambient temperature raised	4.94°C	0.12°C per min	42 minutes
Set 4: Cool2	Camera cooled down	8.09°C	0.28°C per min	29 minutes
Set 5: Stable2	None	0.73°C	0.02°C per min	38 minutes

Time series analysis was performed in order to determine whether camera temperature changes are affecting the reading accuracy (represented here as an offset from true temperature). Typically, to measure the relationship between two time series a cross-correlation function (CCF) of the two variables is examined. The CCF measures the degree of association between an explanatory variable and the dependent variable at various lags. However, as a time series is a set of consecutive samples collected over a time interval, it would normally contain some autocorrelations, inhibiting such analysis. If any of the series is highly autocorrelated, the CCF can be difficult to interpret and potentially misleading. If both of the time series are highly autocorrelated, the CCF can show high spurious correlation, even if the variables are not related (Yule, 1926; Cryer and Chan, 2008). Equally, any non-stationarities, such as drifts or trends over time would lead to misleading results. To account for these factors, the data sets were prewhitened. Prewhitening refers to the removal of autocorrelation from a time series. It is performed by transforming one of the series to white noise using a filter, which is then also applied to the other series. As prewhitening is a linear operation, any linear relationships between the original series are preserved (Cryer and Chan, 2008).

Prewhitening was performed using an Autoregressive Integrated Moving Average (ARIMA) model; further information on the procedure is provided in Appendix D. Initial ARIMA(p,d,q) models were chosen upon investigation of autocorrelation and partial autocorrelation functions of the input time series, i.e. camera temperature change series. These were adjusted to minimise the value of Akaike Information Criterion (AIC), which

is a measure of the relative quality of statistical models (Shumway and Stoffer, 2011). The final models were applied to the series containing offsets from true blackbody temperature. The modelling was performed with R version 3.2.2 and the 'forecast' package (Hyndman and Khandakar, 2008).

4.5.4 Camera performance in laboratory conditions

During camera calibration in laboratory settings, a significant temperature shift was observed over the course of the first 30 minutes, indicating a need for camera stabilisation prior to undertaking any imaging (Figure 4.5). Moreover, after the readings had stabilised, it was revealed that the sensor overestimated the blackbody's temperature by over 3.5 K throughout the imaging period.
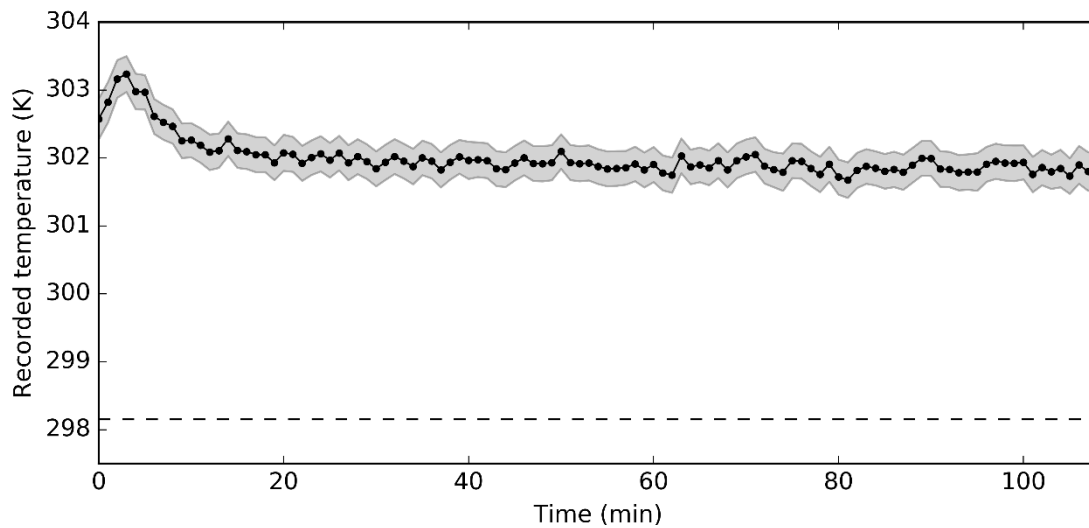
Figure 4.5: Mean image temperature of a blackbody at 298.15 K (dashed line), as recorded by the sensor over time. The temperature readings were adjusted for the blackbody's emissivity value ($\varepsilon_{BB} = 0.96$). Shaded areas represent one-sigma standard deviation. The initial spike (first 30 minutes) was due to the camera warming up period.

Further investigation of temperature readings at a pixel level showed a non-uniformity in the photo response of the detectors in the array; responses over time of 100 randomly selected sample pixels are presented in Figure 4.6. The temperature readings across the imagery varied significantly, with differences exceeding 2 K in some cases. The variation within the response across the imagery was initially assumed to have come from "vignetting" effect, which is the main optical artefact in cameras. It results in a darkening of the image at its periphery due to a transmission coefficient decreasing with increasing distance from the optical axis. However, in the case of the investigated camera no such

pattern was evident. Instead, an increase in recorded temperature value towards the right-hand side of the image was observed (Figure 4.7). The most problematic area was the upper right corner of the image, where offsets up to 5.2 K were recorded. This spatial pattern of offsets remained the same throughout the experiment. It is suspected the observed non-uniformity and temperature offset were probably caused by a joint effect of the imperfections of the optics and degradation of the calibration of the sensor.
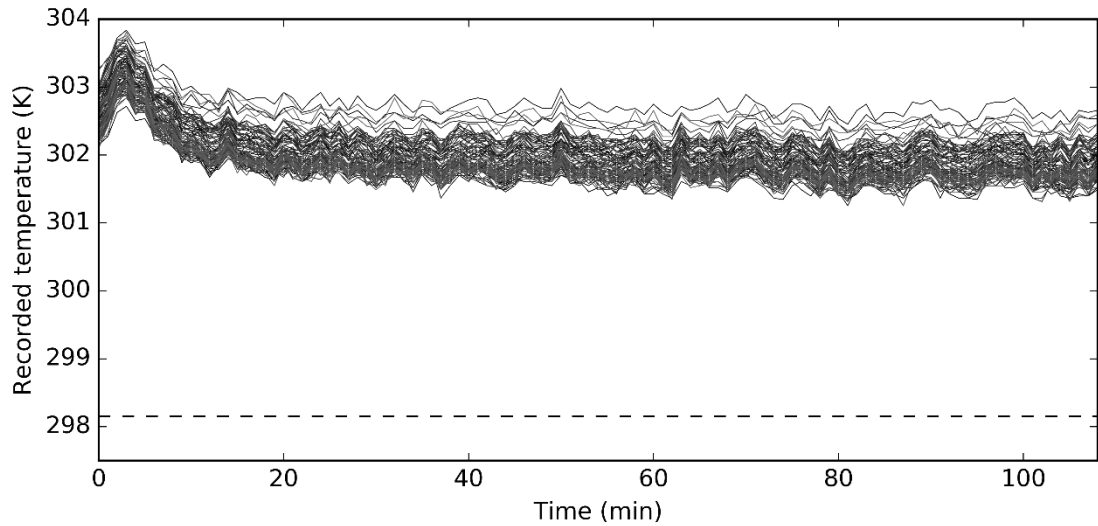
Figure 4.6: Temperature readings over time of a blackbody at 298.15 K (dashed line), as recorded by 100 randomly chosen pixels. The temperature readings were adjusted for the blackbody's emissivity value ($\varepsilon_{BB} = 0.96$). The initial spike in values (first 30 minutes) was due to the camera warming up period.
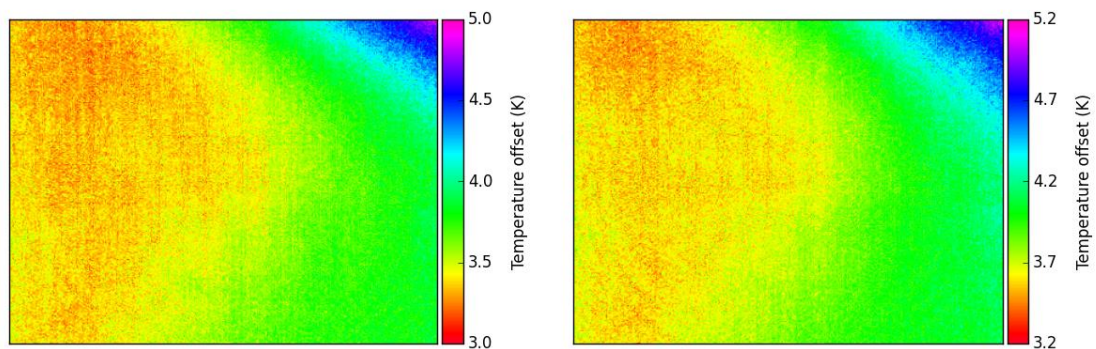
Figure 4.7: Recorded image offsets from the true temperature of the blackbody at minute 40 (*left*) and 80 (*right*).

4.5.5 Non-uniformity correction

Thermal images of the blackbody at a range of temperatures showed the average and pixel level sensor responses were linear in terms of emitted flux versus digitised flux over the measured temperature range at both image and pixel level. Highly significant linear relationships were found for both the mean values of the image ($R^2 = 0.99998$ at $p<0.001$) and for 100 randomly chosen pixels (R^2 ranging from 0.99996 to 0.99998 (Figure 4.8). Imagery of the blackbody at 298.15 K to 333.15 K were used to calculate the gain and the bias of each detector across the array. In order to minimise the observed temporal differences in temperature offsets recorded within each pixel, an average of ten pictures of the blackbody were used. The resultant gain and offset matrices were then used to calibrate all the detectors across the array so that they produced a radiometrically accurate and uniform reading at the reference temperatures, as presented in Figure 4.9.
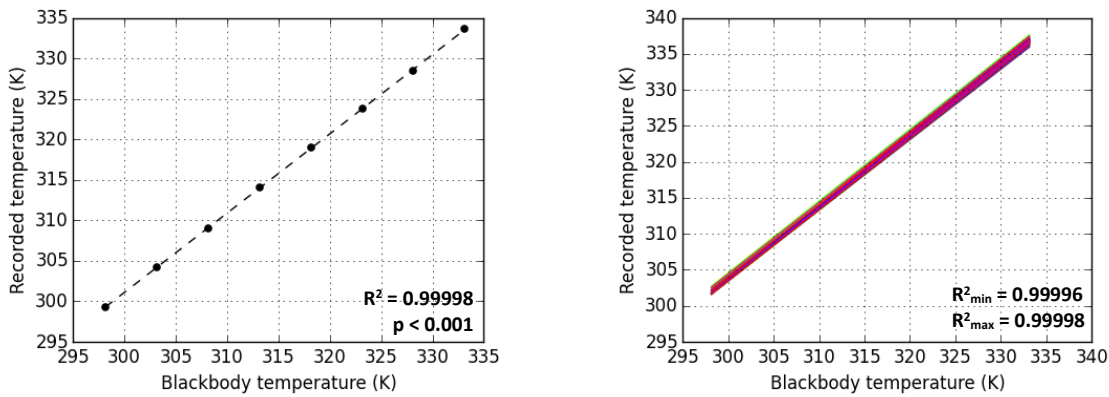
Figure 4.8: Average recorded image values of a blackbody heated to temperatures from 298.15 to 333.15 K at 5 K increments (*left*) and trend lines constructed from readings from 100 randomly chosen image pixels (*right*).
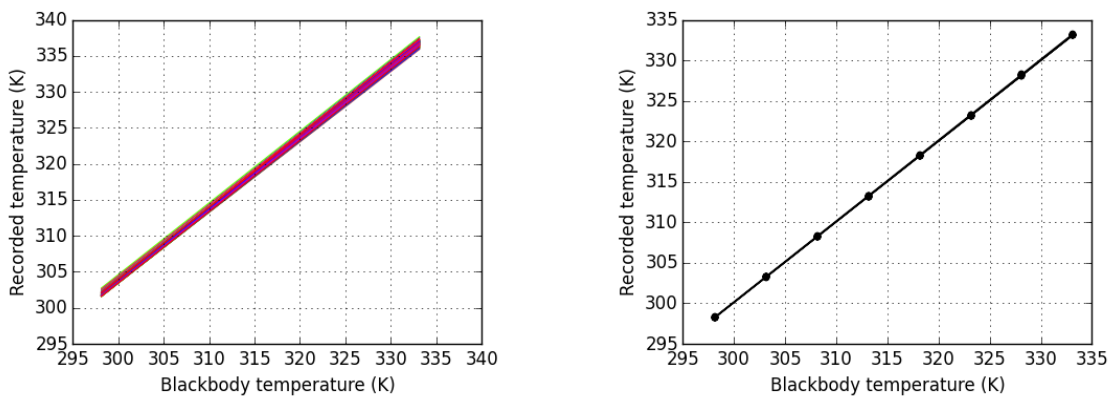
Figure 4.9: Trend lines constructed from readings from 100 randomly chosen image pixels of a blackbody heated to temperatures from 298.15 to 333.15 K at 5 K increments before (*left*) and after (*right*) applying the non-uniformity correction.

The derived non-uniformity correction accounted for the overestimation in the average temperature readings (Figure 4.10); the imagery was representing the actual blackbody temperature with maximum offsets of mean image temperature of 0.23 K (once sensor stabilisation was achieved). The variation in temperature readings across the imagery had also been minimised, with 95.4% (2σ) of the pixels falling within ± 0.14 K (average across the time series) of the mean temperature reading (Figure 4.11). The resultant gain and offset matrices were used to correct all acquired thermal imagery (the python processing script is provided in Appendix E). The validity of the derived calibration parameters was subsequently confirmed after six months on the same blackbody source, following a similar measurement set-up.
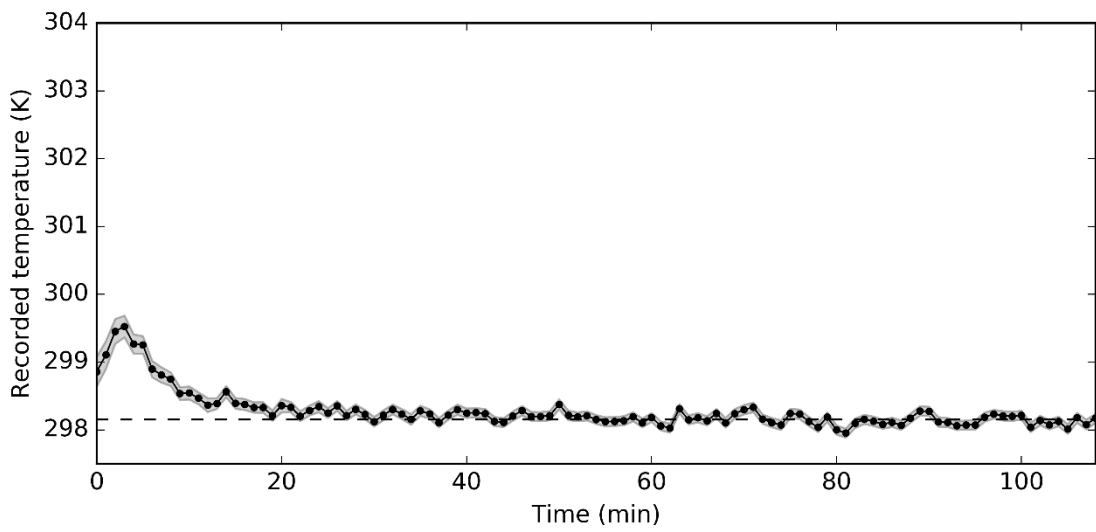
Figure 4.10: Corrected mean image temperature of a blackbody at 298.15 K (dashed line), as recorded by a camera over time. The temperature readings were adjusted for the blackbody's emissivity value (ε_{BB} = 0.96). Shaded areas represent one-sigma standard deviation. The initial spike (first 30 minutes) was due to the camera warming up period.
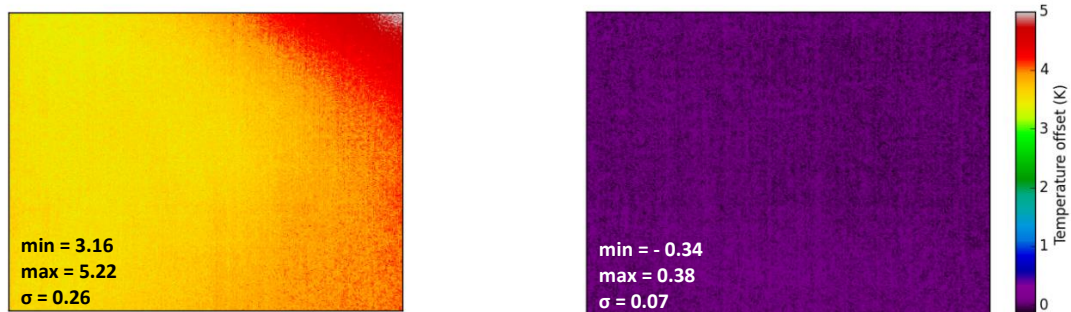
Figure 4.11: Recorded image offsets from the true temperature of the blackbody at minute 60, prior to (*left*) and after (*right*) applying corrections.

4.5.6 Sensitivity to changing FPA temperature

Figure 4.12 shows CCFs of stationarised non-prewhitened time series. The time series acquired under stable conditions showed no statistically significant cross-correlation, indicating that the camera temperature change and offsets from true blackbody temperature within those datasets are largely uncorrelated. For the other three datasets, the CCFs show significant correlation at multiple time lags; however, these could be spurious since most of the input series exhibited strong autocorrelation, and would therefore require prewhitening.
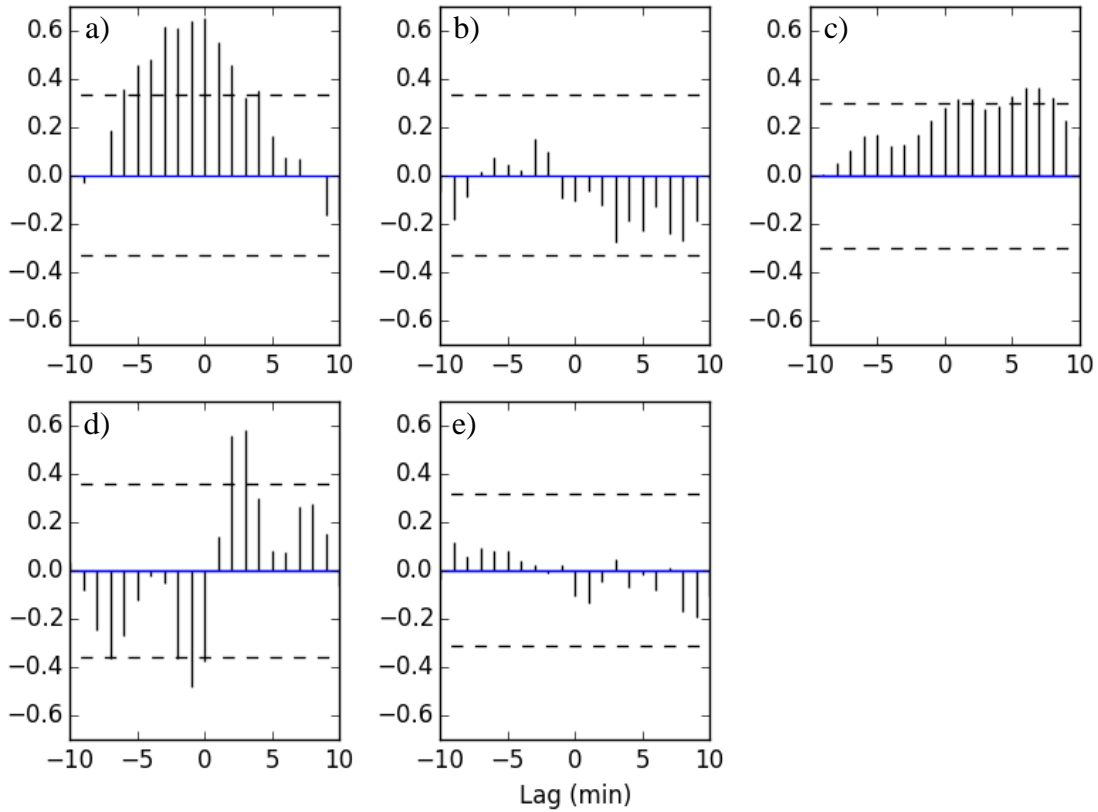
Figure 4.12: Cross-correlations between stationarised non-prewhitened T_{off} and Tch_{cam} series for a) Set1: Cool1, b) Set2: Stable1, c) Set3: Warm1, d) Set4: Cool2 and e) Set5: Stable2. Dashed lines indicate confidence threshold for $\alpha=0.05$.

Initial ARIMA models were chosen upon investigation of autocorrelation and partial autocorrelation functions of the input time series and adjusted to minimise the AIC value. The final models were applied to the series containing offsets from true blackbody temperature. The summary of fitted ARIMA models is presented in Table 4.2. No models were fitted to the datasets 2 and 3 since they did not show statistically significant correlation between the variables at any lag.

Table 4.2: Summary of ARIMA models fitted to Tch_{cam}.

Dataset	p	d	q	Coefficients	AIC	σ^2
Set 1: Cool1	1	0	0	AR1 = 0.8121	-197.1262	0.0002
Set 3: Warm1	2	1	2	AR1 = 0.9905 MA1 = -1.0788 AR2 = -0.8106 MA2 = 0.5230	-199.1376	0.0004
Set 4: Cool2	0	0	2	MA1 = 0.8603 MA2 = 0.5632	-103.1091	0.0016

After prewhitening of the time series, the CCFs of sets 1 and 3 were only significant at a single lag, at lag 4 (r = 0.46) in set 1 and at lag 2 (r = 0.44) in set 3 (Figure 4.13). In the case of dataset 4, there were 3 statistically significant lags: -2, 0 and 2 minutes (r_1 = -0.32, r_0 = -0.33, r_2 = 0.40). However, cross-correlations at lags -2 and 0 are only marginally significant ($\pm$ 0.30 confidence threshold for $\alpha = 0.05$, given by $1.96/\sqrt{n}$); considering the model was of considerably lower quality (based on AIC) they were likely to be false alarms. All three datasets suggest that the high rate of the camera temperature change leads temperature offset from true blackbody temperature, and has a positive influence on it. The time after which the temperature offset is affected is not consistent among the time series, i.e. set 1 – 4 minutes, set 3 and 4 – 2 minutes. No such effect is observed when camera temperature is changing gradually.
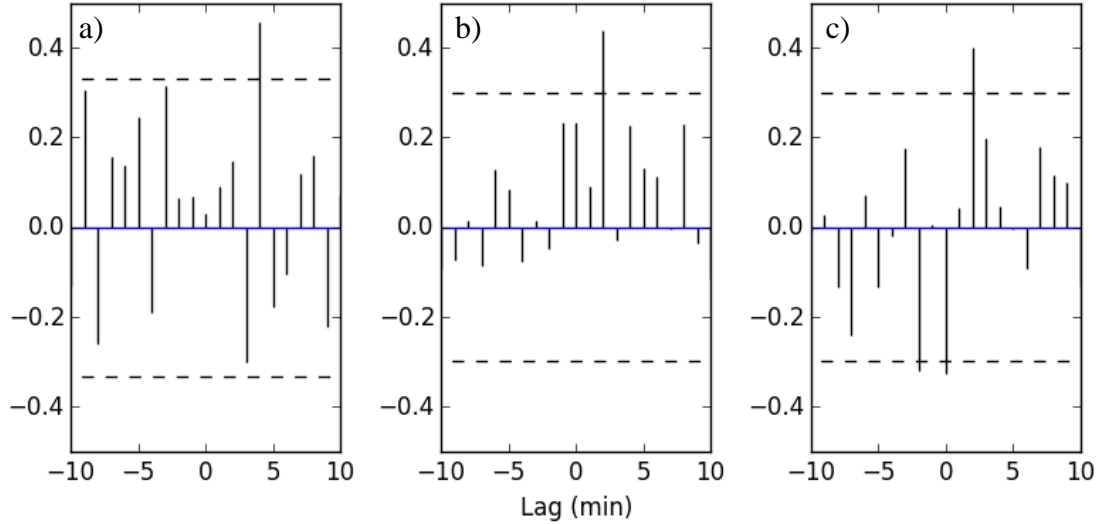
Figure 4.13: Cross-correlations between prewhitened T_{off} and Tch_{cam} series for a) Set1: Cool1, b) Set3: Warm1, and c) Set4: Cool2. Dashed lines indicate confidence threshold for α=0.05.

It can therefore be concluded that in order to ensure consistent temperature measurements with a microbolometer camera, thermal surveys should not be conducted within several minutes of rapid camera temperature change. Other studies have similarly demonstrated that the changes in the camera's operating temperature cause a corresponding change in the FPA's output level (Hoelter and Meyer, 1998; Nugent *et al.*, 2013). The output drift with environmental temperature creates two main problems: a need for an update of the temperature calibration coefficients and a reduction of the usable dynamic range for actual changes in scene temperature (Hoelter and Meyer, 1998). Within this experiment, the sensor was exposed to drastic temperature changes (up to 8.09°C difference from the ambient temperature), which normally would have not occurred in the field. Based on the international standard atmosphere model, for UAV operation at altitudes of 200 and 400 feet, the expected ambient temperature decrease would have only been 0.396 and 0.792°C. Consequently, the expected temperature change rate experienced during UAV launch can be assumed to be of similar level as in the datasets acquired under stable conditions, and therefore have no significant effect on the quality of thermal imagery.

4.6 Field-based investigation of thermal camera performance

4.6.1 Experiment design

Field-based tests of the microbolometer thermal camera were performed in order to test its capability to perform accurate temperature measurements of non-blackbody objects in an outdoor environment, using a high-emissivity target, constructed from carpet underlay foam. The camera's performance was tested at two distances to ensure that the response is consistent, independent of the imaging distance.

The camera was initially placed 25 metres, then 7 metres away from the target (as shown in Figure 4.14), set up perpendicular to the wind direction in order to simulate an in-flight movement of air in front of the lens. The camera was set to image at 1 second intervals over the course of 66 and then 31 minutes. The camera's FPA temperature was also monitored; readings were provided by the imaging software and recorded every 2 minutes. The FPA temperature varied between 18.5 and 21°C throughout the experiment (average temperature change 0.038°C per min). The target's temperature was measured with a type K thermocouple (accuracy of ± 2.2°C) attached to the bottom part of the target (placed inside to maximise the contact surface), and recorded at 2 seconds intervals. Additionally, the wind speed was measured at 5 minute intervals, whilst air temperature measurements were acquired from a nearby weather station, located within 500 metres.

Figure 4.14: Equipment setup for outdoor tests.

The target's temperature recorded by the camera, after accounting for the target's emissivity (retrieval is described in Section 4.6.2), was obtained as an average of 266 central pixels (14x19 pixel polygon, 25 metres distance) and 4400 central pixels (40x110 pixel polygon, 7 metres distance), and resampled to the thermocouple's measurement interval (2 seconds) for comparison. The standard deviations of temperature recorded within these polygons was also retrieved and resampled.

In order to determine whether any of the changing weather conditions had any significant effect on the accuracy of the camera's readings, the relationships between camera temperature change (Tch_{cam}) and differences in the target temperatures recorded by the camera and the thermocouple were investigated. For this purpose, the rate of FPA temperature change was calculated. Differences in the target temperatures (T_{diff}), as well as absolute differences in rates of target temperature change (Tch_{diff}), recorded by the camera and the thermocouple were resampled as averages of same intervals (2 minutes). To investigate possible relationships between these data sets, the time series were prewhitened according to the procedure outlined in Section 4.5.3. An ARIMA(0,0,1) model was fitted to the camera temperature change 25 m series, and then applied to the other series; no modelling was required for the 7 m series as no autocorrelations were found.

4.6.2 Target's emissivity retrieval

The MIDAC M2000 series Fourier transform infrared (FTIR) spectrometer was used to perform TIR spectral emissivity measurements. It is equipped with a mercury cadmium telluride sensor and zinc selenide optics, offering a spectral range of ~1.5 – 15.4 µm and a selectable resolution of 32 – 0.5 cm^{-1}. For this study the spectroradiometer was set to perform 8 scans with 16 background scans at 2 cm^{-1} resolution. For spectrometer calibration purposes, a blackbody system built by Electron Systems was utilised, which consists of three blackbodies ($\varepsilon = 0.96$), two of which were set to 15°C and 60°C. Calibration measurements of the blackbodies along with downwelling (DWR) measurements were performed at regular intervals to account for changes in background radiance and spectrometer temperature. The DWR measurements were acquired using a diffusive gold highly reflective surface (InfraGold panel), with a reported emissivity of less than 0.06. Surface temperature of the gold panel and samples were measured using a contact thermocouple. All measurements were performed from a distance of approximately 30 cm, thus no atmospheric correction was required. The equipment setup is presented in Figure 4.15, whilst processing scripts developed for emissivity retrieval are provided in Appendix F and Appendix G.
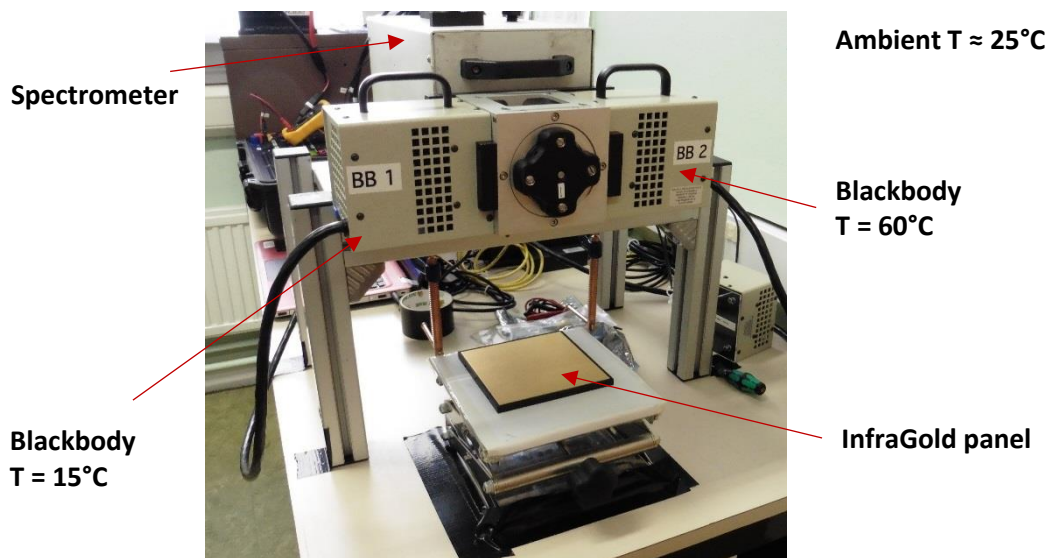
Figure 4.15: Equipment setup for FTIR measurements.

The first trial involved collection of target spectra, with samples remaining at ambient temperature. However, in this laboratory setting, the measured DWR was particularly high, resulting from radiance emissions from the ceiling and walls at ambient temperature. In effect the DWR cancelled out the upwelling target radiance, precluding retrieval of emissivity values. To avoid influences from surrounding objects,

measurements could potentially be undertaken in the field under a clear ('cold' at IR wavelengths) sky. However, the presence of many low clouds could result in sky temperatures equal to ambient temperatures on the ground, and consequently high DWR (Hecker *et al.*, 2013).

In the absence of favourable weather conditions (i.e. cloudless sky), it was decided to instead ensure that the upwelling target radiance was higher than the DWR during the lab measurements. This can be achieved by heating up samples above the ambient temperature. For this purpose, the samples were placed between two metal plates and heated up in a convection oven set to 40°C prior to measurements (Figure 4.16). Metal plates were used to avoid rapid heat dissipation during transportation of samples. Immediately prior to measurements the top plate was removed, and then multiple target spectra were collected. During the measurement, the target was at 29.9 to 30.5°C, whilst the gold panel remained at temperatures from 27.8 to 28°C.

The target was at a temperature close to the ambient temperature, which may have resulted in a relatively low signal-to-noise ratio. Increasing the sample temperature further was not possible as it could change the properties of the target (i.e. through melting) and due to fast heat dissipation from the target's surface. Kotthaus *et al.* (2014) suggested the overall signal-to-noise ratio can also be improved by increasing the number of times the target spectral radiance is sampled. However, as incoming radiance and instrument response are assumed stable during the measurement period, a set of measurements has to be collected in a relatively short time period. As the target's temperature was changing relatively dynamically, the number of scans collected during one measurement could not be further increased. Instead, to improve the signal-to-noise ratio, multiple spectral measurements were performed and integrated.

In total 8 spectral measurements of the black target were used to obtain absolute emissivity. The acquired spectra were radiometrically calibrated by utilising the measurements of two blackbodies at known temperatures, and then accounted for DWR present throughout the experiment. The absolute spectral emissivities of the target retrieved for each measurement are presented in Figure 4.16. The black target's emissivity within the camera's spectral range, i.e. 7.5 to 13 μm, varied from 0.89 to 0.98 ($\sigma = 0.02$), with a spike at 8.08 μm. For further use, the retrieved spectral emissivity of the target was integrated into a single value, denoted as total emissivity, of 0.92.
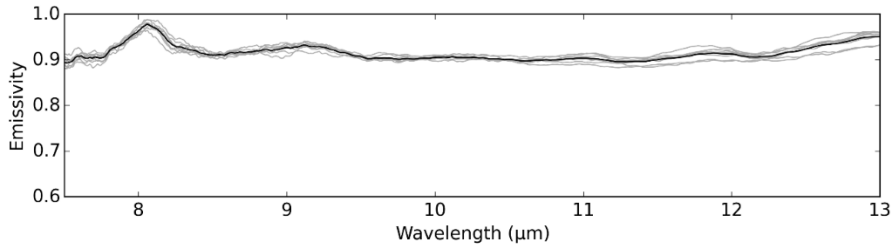
Figure 4.16: Target sample preparation: heating up in a convection oven between two metal plates (*left*), setup immediately prior to FTIR measurements (*right*), and average absolute spectral emissivity (black) of the target retrieved from eight spectral measurements (grey).

The USGS (Kokaly *et al.*, 2017), ASTER (Baldridge *et al.*, 2009) and SLUM (Kotthaus *et al.*, 2014) spectral libraries were explored to identify spectrally similar surfaces. The closest match was provided by a black roofing tile consisting of clay-based ceramics (SLUM library reference number R007, Figure 4.17). Both materials had similarly high spectral emissivity throughout the spectrum, with highest values recorded around 8 μm. Although some differences in the shape were present, the total emissivity in the 8-13 μm region was identical for both materials ($\varepsilon = 0.92$).
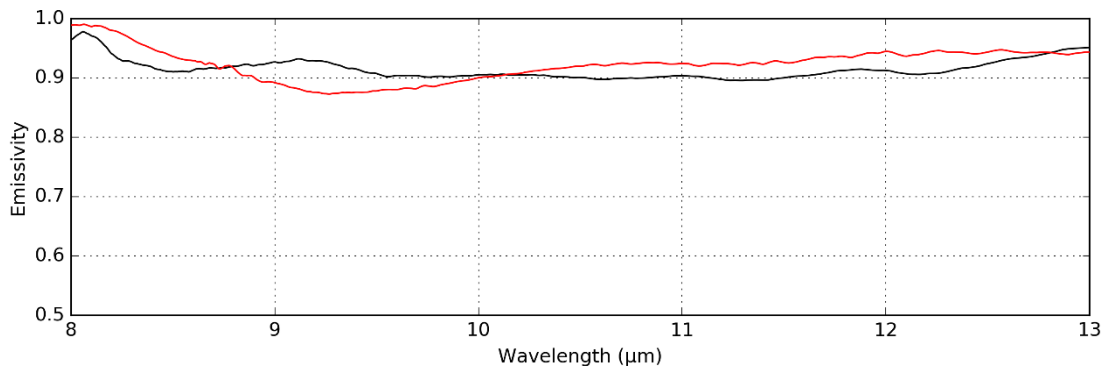
Figure 4.17: Absolute emissivity of a black roofing tile (red, SLUM R007 - Kokaly *et al.* (2017)) and average absolute spectral emissivity of the black target (black).

4.6.3 Camera readings against thermocouple measurements

The calibrated image temperature throughout the experiment was consistently higher than the recorded thermocouple values for both investigated distances (Figure 4.19 and Figure 4.20). On average the difference between the image and thermocouple readings was 1.39°C (min = 0.50°C, max = 2.94°C at 25 m) with standard deviation of 0.43°C, and 1.04°C (min = 0.33°C, max = 1.64°C at 7 m) with standard deviation of 0.25°C. Nevertheless, most of the retrieved image temperatures (around 98%) remained within the accuracy threshold of this type of a thermocouple. This suggests that obtaining absolute temperatures of non-blackbody objects can be accurately performed with the microbolometer cameras, providing the emissivity of surfaces is accurately known.

The variation in the target's surface temperature throughout time was also well reflected by the thermal imagery. The temporal patterns of computed temperature change between consecutive measurements obtained from the thermocouple and images were well aligned; the average RMSE for the 25 m dataset was 0.045°C with minimum and maximum absolute difference values of 0.000 and 0.202°C, whilst for 7 m the average RMSE was 0.031°C with minimum and maximum absolute difference values of 0.000 and 0.109°C. The RMSE for 25 m dataset is significantly higher; however this is due to contribution of higher error values observed during the periods of abrupt surface temperature changes occurring during this test (i.e. RMSE = 0.055°C until minute 35, and RMSE = 0.031°C past minute 35). These discrepancies might be caused by the different nature of the measurements; the image values reflect temperature of a large area of the target, whilst the thermocouple is a point measurement. Excluding this period, no significant differences in temperature accuracies retrieved from different distances were observed.

4.6.4 Camera's performance and weather conditions

The air temperature throughout the trial remained fairly consistent, varying between 16.3 and 17.2°C, whilst the speed of wind and gusts ranged from 3.8 to 9.3 mph, and 5.9 to 17.7 mph. These wind speeds covered the typical range under which rotary-wing UAVs would normally be operated. As presented, under such conditions thermal images produce an accurate representation of the target's thermal state (Figure 4.19 and Figure 4.20).

It appeared that within the period of a higher wind speed, i.e. in 25 m dataset until minute 35, the absolute differences between rates of temperature changes recorded by the camera and the thermocouple were elevated. This could potentially be attributed to an increased convective heat loss, i.e. moving air removing radiated heat, leading to accelerated

cooling of the target. Such change might not be uniform throughout the target surface, which could have been reflected in the form of increased discrepancies between thermocouple and image temperatures.

The pattern of retrieved standard deviations of image temperatures supports this hypothesis. The standard deviations in recorded temperatures are significantly higher within this period, potentially signifying non-uniformity in temperature change throughout the target surface. Alternatively, such accelerated cooling might have affected the camera lens, modifying the camera temperature and causing higher errors in image readings; this possibility is further investigated in the next section.

4.6.5 Camera's performance and FPA temperature

The CCFs between camera temperature change and differences in the target temperatures between the camera and thermocouple are shown in Figure 4.18 a-b, whilst CCFs between camera temperature change and absolute differences in rates of target temperature change are presented in Figure 4.18 c-d. There is no statistically significant correlation between Tch_{cam} and T_{diff}, nor between Tch_{cam} and Tch_{diff}, indicating that the change in camera temperature throughout the experiment had no effect on the accuracy of the thermal imagery. This is in accordance with results from the laboratory-based tests, confirming that image quality from such cameras is not compromised by changing FPA temperature, as long as they are operated under gradually changing conditions.
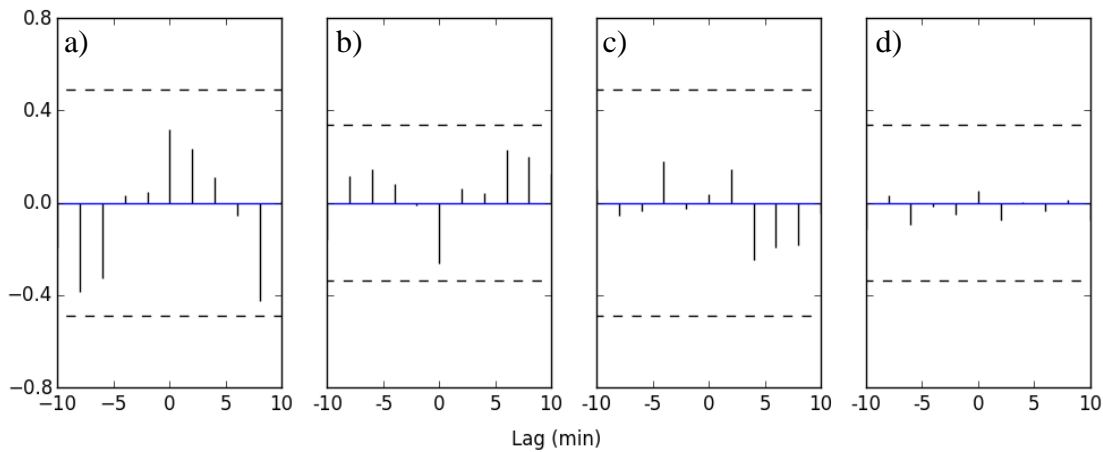
Figure 4.18: Cross-correlations between Tch_{cam} and T_{diff} at a) 7 m and b) 25 m (prewhitened), and between Tch_{cam} and Tch_{diff} at c) 7 m and d) 25 m (prewhitened). Dashed lines indicate confidence threshold for $\alpha=0.05$.
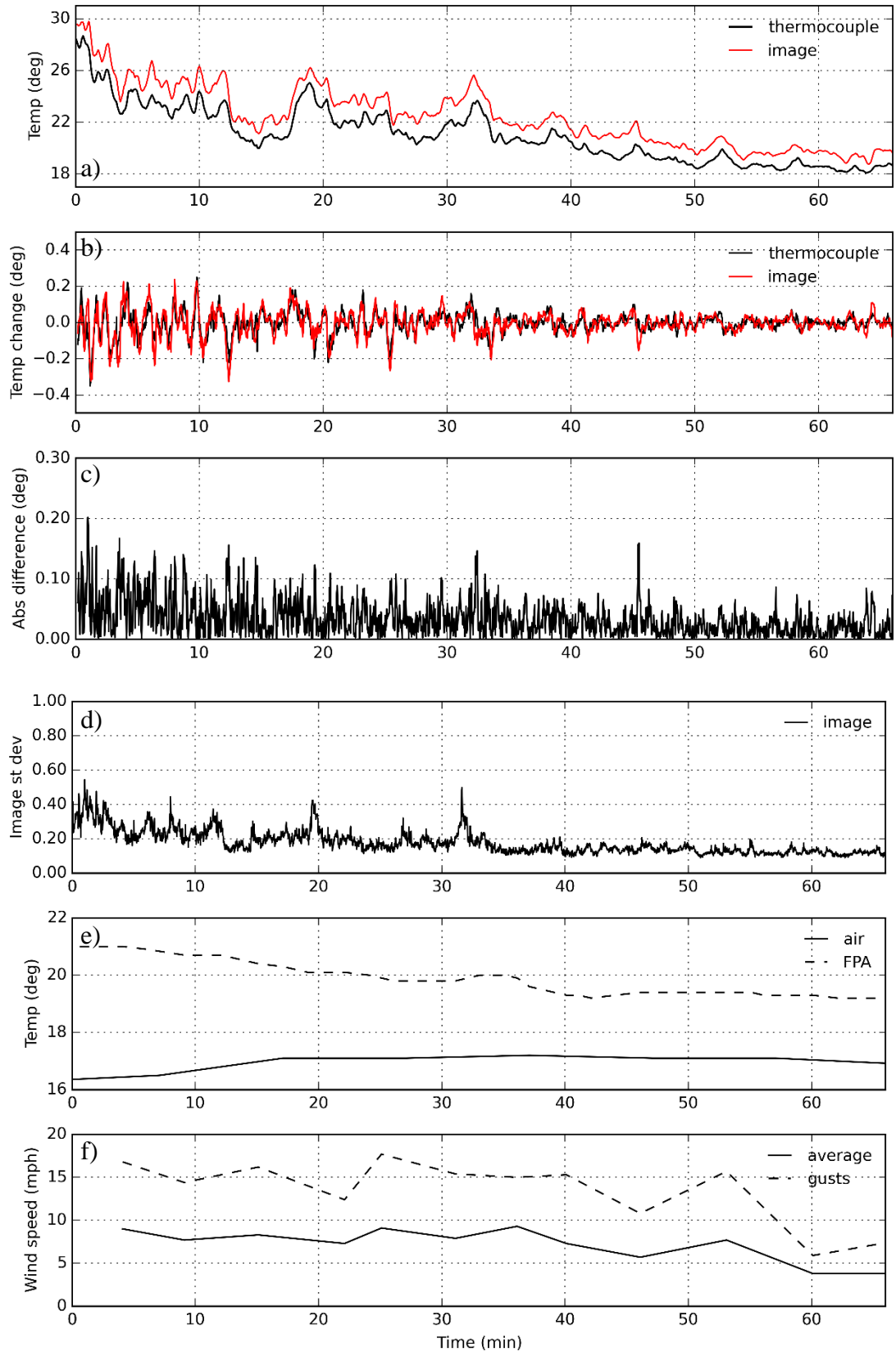
Figure 4.19: a) Retrieved image and thermocouple temperature measurement of the target at 25 m distance. b) Rates of temperature changes recorded by the camera and the thermocouple, c) and their absolute differences. d) Recorded image standard deviation. e-f) FPA temperature and weather conditions throughout the experiment.
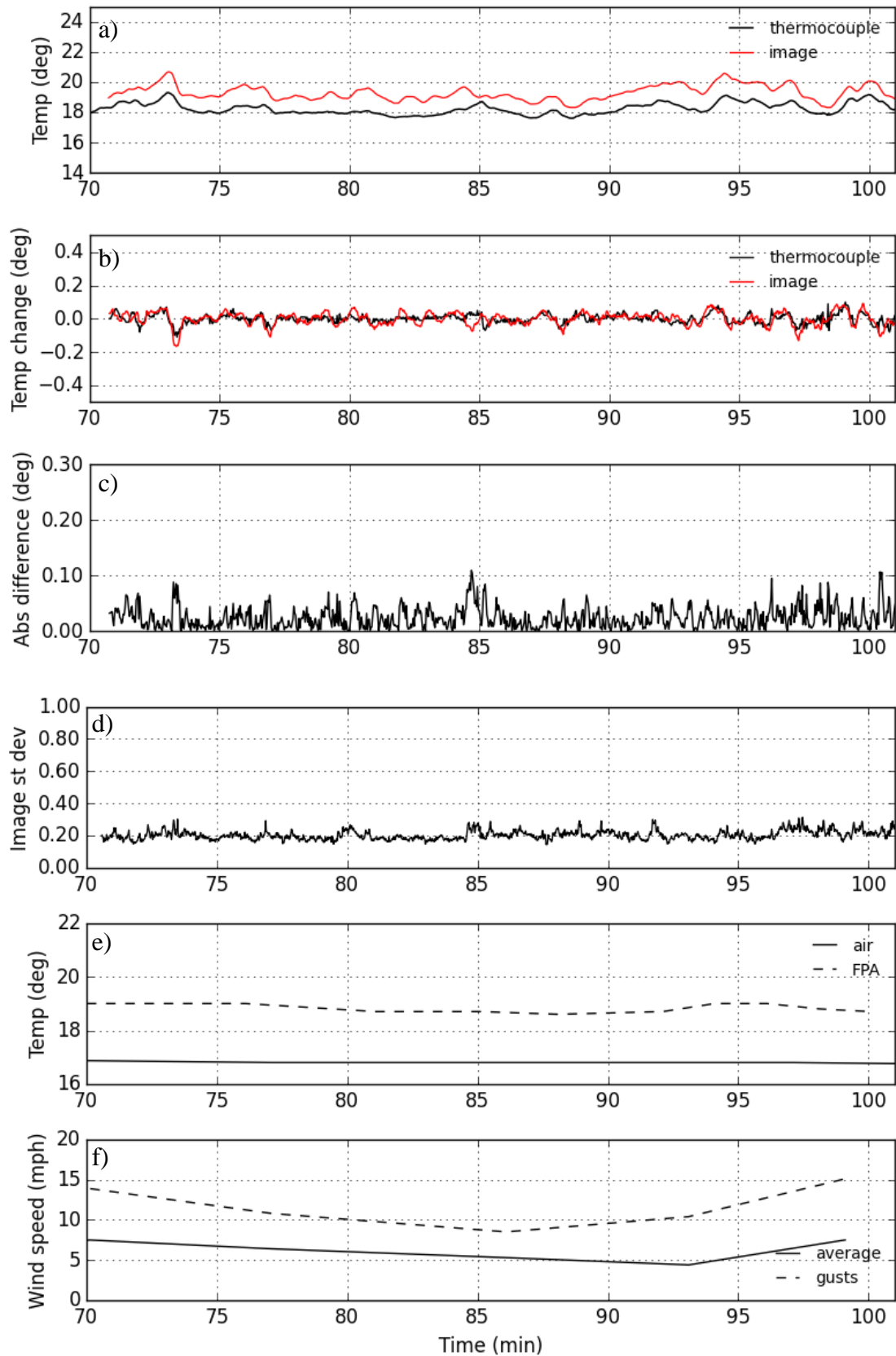
Figure 4.20: a) Retrieved image and thermocouple temperature measurement of the target at 7 m distance. b) Rates of temperature changes recorded by the camera and the thermocouple, c) and their absolute differences. d) Recorded image standard deviation. e-f) FPA temperature and weather conditions throughout the experiment.

4.7 Chapter summary

This chapter investigated the performance of a miniature low-cost microbolometer FPA thermal infrared camera developed for UAV-borne applications. Initially, camera calibration was performed revealing a significant overestimation of the temperature readings and a non-uniformity across the imagery. These effects have been minimised with a two-point calibration technique, using imagery of a blackbody at two distinct and known temperatures. Furthermore, temporal changes in the sensor response have been observed, indicating a need for stabilisation (i.e. 30 minutes waiting time prior to use).

The main issue with using uncooled microbolometer imagers is that their performance might vary with changes to the camera's temperature, since without thermal stabilisation, cameras might not maintain a stable radiometric calibration. Laboratory tests suggested that a rapid camera's rapid temperature change is reflected in future images, but no such effect was observed when the temperature was changing gradually. The expected temperature change rate experienced during UAV launch and altitude gain, based on the international standard atmosphere model, would therefore have no significant effect on the quality of thermal imagery. However, it should be ensured that thermal surveys are not conducted within several minutes of any rapid camera temperature change to obtain consistent temperature measurements.

Further field-based experiment showed that obtaining absolute temperatures of non-blackbody objects can be accurately performed with the microbolometer cameras under a typical UAV operation wind speed range, providing the emissivity of surfaces is accurately known. The variation in the target's surface temperature throughout time was also well reflected by the thermal imagery. Furthermore, this experiment showed that the gradual change in camera temperature throughout the experiment had no effect on the accuracy of the thermal imagery; this is in accordance with results from the laboratory-based test.

Chapter 5. Thermal analysis of tree stress

5.1 Chapter overview

This chapter investigates the use a low-cost thermal infrared camera for analysing thermal properties of healthy and stressed trees. The camera is used for two separate experiments, one terrestrial and one UAV-borne. The former was performed in a greenhouse on young larch trees, with induced drought stress to investigate the potential for temporal analysis of canopy temperature. Furthermore, the vertical temperature distribution within the canopy in healthy and stressed larch trees was examined. The latter experiment was performed on young pine plantation (plot A, see Figure 3.2) and investigatef the use of UAV-borne thermal imagery for detecting disease-induced canopy temperature increase at different times during a day.

5.2 Introduction

Leaf temperature is primarily determined by the rate of transpiration. As plants transpire, water loss through evaporative cooling reduces leaf temperature (González-Dugo *et al.*, 2006). Conversely, plants under water stress tend to transpire less due to stomatal closure, leading to an increase in leaf and canopy temperature and reduction in photosynthetic activity (Jones, 1999). Therefore, leaf temperature can be an indicator of water availability. With the onset of severe water stress, a general disruption of metabolism develops, which is signalled by high rates of respiration. The closure of stomatal apertures is a defence mechanism, which not only helps reduce water losses, but also prevents the entry of microbes and host tissue colonisation. The resultant increase in leaf and canopy temperature can often be detected by thermal imaging at the leaf level at an early stage of infection (Chaerle *et al.*, 1999a; Lindenthal *et al.*, 2005).

In agriculture, much work has been done on relating leaf temperature to water stress. At canopy level, several methods utilising knowledge on environmental factors (such as air temperature, humidity, radiation and wind speed) were developed to estimate stomatal conductance and water content using thermography (Jackson *et al.*, 1981; Jones, 1999; Leinonen *et al.*, 2006). As an alternative, thermal 'stress indices' were created, aiming to normalise the results for environmental variation. Canopy temperature depression (CTD) is the most straightforward of the indices; it normalises canopy temperature with reference to air temperature, and is calculated as $T_{canopy} - T_{air}$ (Idso *et al.*, 1981). However, it depends on weather conditions, and thus can only be used in climates where weather conditions vary little between consecutive days (Keener and Kircher, 1983). The crop

water stress index (CWSI) is a drought stress index, which introduces a non-water-stressed baseline (representing a crop transpiring at a maximal rate) and a non-transpiring upper baseline (representing a dry crop with closed stomata) (Idso *et al.*, 1981; Jackson *et al.*, 1981). There are different approaches for calculation of CWSI, namely analytical, empirical and direct; a review of these approaches can be found in Maes and Steppe (2012). Similarly, the stomatal conductance indices (Ig and I3) utilise "wet" and "dry" reference surfaces to reduce the sensitivity to environmental variations (Jones, 1999).

The thermal stress indices have been widely and successfully applied to agricultural crops (Alderfasi and Nielsen, 2001; Erdem *et al.*, 2010; Taghvaeian *et al.*, 2014). Yet, the use of thermography for investigation of water stress in trees has been predominantly limited to orchards (Berni *et al.*, 2009a; Gonzalez-Dugo *et al.*, 2012; Ballester *et al.*, 2013). Using thermal imagery, noticeable differences in canopy temperature between treatments of persimmon trees were detected, whilst in citrus the relationship between crown temperature and plant water stress differed in each experimental season (Ballester *et al.*, 2013). Within a heterogeneous olive orchard, good correlation between estimated and field-measured canopy conductance values was achieved by Berni *et al.* (2009a). Similarly, the CWSI, modelled for water-deficient and well-irrigated olive trees, correlated well with the measured water potential, as well as the canopy conductance (Berni *et al.*, 2009a). Relationships between canopy temperature, and stomatal conductance and water potential, were also found in almond trees (Gonzalez-Dugo *et al.*, 2012); furthermore, it was suggested that the intra-crown temperature variability could also be used for water stress detection.

In forestry, thermography has so far been used to analyse drought tolerance of several deciduous tree species in a mixed forest stand (Scherrer *et al.*, 2011) and of Scots pine seedlings from different provenances (Seidel *et al.*, 2016), to assist forest planning in light of changing climatic conditions. Scherrer *et al.* (2011) recorded noticeable differences between investigated species, ranking them according to their resistance. With ongoing drought, they also observed a divergence in mean relative (to air) canopy temperature readings between 'dry' and 'moist' sites, but could not attribute them to differences in soil water potential. Grant *et al.* (2010), using thermal imagery, monitored leaf physiology of cork oak under varying water regimes (80, 100 and 120% of natural precipitation). Following a year of treatment, the well-watered leaves were significantly cooler than those with natural or reduced precipitation levels. On a larger scale, a monthly forest vulnerability index was derived for a range of forest types by subtracting normalised

monthly water balance from normalised MODIS land surface temperature (Mildrexler *et al.*, 2016). Nevertheless, the application of thermography to investigate stress in forest species, especially conifers, requires further exploration to assess its feasibility as a reliable monitoring technique. Conifers represent particularly challenging targets for remote sensing analysis, mainly due to their structural features, for example, narrow needle leaves. With the exception of Kim *et al.* (2016) and Seidel *et al.* (2016), thermography of conifer trees still remains almost unreported in the literature; therefore, the investigation of stress responses in the temperature domain is largely lacking. In Kim *et al.* (2016), the daily and sub-daily mean canopy temperatures extracted from uncorrected imagery were shown to be related to climatic and soil variables, but the retrieved canopy temperatures were not validated against ground measurements. Seidel *et al.* (2016) used thermocouples attached to needles to derive their apparent emissivity, but did not utilise them in further measurements.

The main challenge for using thermal remote sensing approaches for forest health monitoring arises from the need for high spatial resolution data to identify individual trees or to monitor areas of fragmented forest cover. Newly emerging technologies, such as small unmanned aerial vehicles (UAVs) could significantly aid in provision of the required data. This chapter investigates whether a low-cost miniature thermal camera, destined to be used on a UAV platform, is capable of providing reliable canopy temperature measurements of conifers. For this purpose, the temporal change and spatial variation of canopy temperature in conifer trees is monitored in a greenhouse setting. The terrestrial experiment explores whether there is a distinction in whole canopy temperature between control and drought-stressed trees, assessing the potential of low-cost thermography for investigating tree stress in conifers. The drought-stressed trees were used as a proxy for diseased plants experiencing alterations to the water relations, a common disease symptom occurring on the host plants. Furthermore, the chapter investigates the use of UAV-borne thermal imagery for detecting disease-induced canopy temperature increase, and explores the influence of the imaging time on the performance.

5.3 Terrestrial analysis

5.3.1 Plant preparation and experiment design

Twenty specimens of potted two-year-old Japanese larch trees were selected and kept throughout 2016 in an indoor growth room made of glass. The plants were divided into control and drought-stressed groups in August 2016, and subsequently watered at 2-3 days intervals, with a reduced amount provided to the drought group. In control trees the soil moisture content was kept between 50 and 80%, whilst in the drought stress group this was constrained between 10 and 30%. The air temperature within the room was set to 16°C, and for the last month prior to acquiring imagery, temperatures varied between 16 and 22°C as on warm days the cooling system could not retain a constant low temperature.

Two separate pairs of structurally similar trees in terms of number of branches (one treated, one control) were selected for the experiments conducted on 7th and 10th of October 2016, during which the Optris PI-450 thermal camera was used to take images. The first trial involved a moderately stressed tree, whilst the second used a mildly stressed tree; soil moisture measurements (using CS650 soil water content reflectometer) prior to commencing imaging showed 7% and 33% moisture levels for the drought-stressed trees, 48% and 63% for the control trees. The tree stress status was based on the soil moisture measurements and the visual examination of the canopies. The difference in soil moisture between equivalent trees in the two experiments was assumed to be caused by different tree sizes, hence different water consumption.

The experiments were performed in a greenhouse to utilise sunlight; additional light sources were also used to ensure plants were undergoing photosynthesis. Two lamps (400 Watt high pressure sodium system) were attached to the roof of the greenhouse approximately one meter from top of the plants, pointing downwards, directly towards the trees. In this set-up, any shadowing of the lower parts of the trees was only expected to come from overhead branches. In order to minimise the effects of wall reflectance, immediate surroundings were covered with a uniform, non-reflective black paper. A small calibration target, constructed from high-emissivity carpet underlay foam, was placed alongside the plants.

Direct temperature measurements were performed with type K welded tip fast response thermocouple sensors (conductor diameter of 0.315 mm, accuracy of $\pm\,2.2°C$). Each plant had a thermocouple wrapped inside of needle clumps in the upper and lower part of the foliage. The thermocouples were not firmly attached to needles to avoid causing mechanical damage. Thermocouples were also used to monitor the temperature of the air and the calibration target. The full experimental set-up is presented in Figure 5.1. The experiments were undertaken in southern Scotland at 12.00 and 14.00 local time on 7th and 10th of October 2016. In the case of the first experiment, the plants were initially imaged under natural light conditions; the experiment lasted 60 minutes, with lamps turned on between minute 8 and 55. Weather conditions remained consistent, with a thick cloud cover obstructing the sun. The second experiment lasted 47 minutes and was performed with the lamps on; on that day, the conditions were variable, with intermittent sunshine and moving, thick clouds. The thermal camera was placed approximately 1.5 m away from the plants and acquired imagery at approximately 1-minute intervals. The emissivity of the canopy foliage was assumed to be 0.95 (average leaf emissivity value reported by Jones (2004), based on a range of plant species).

Figure 5.1: Experiment 1 set-up with calibration target on the right; thermocouples were wrapped inside of needle clumps, as shown on the insets.

5.3.2 Image processing

The first step of image processing was the application of corrections derived in Chapter 4 to all acquired thermal imagery. Following this step, the emissivity values of the calibration target and of the canopy foliage were accounted for, resulting in two sets of imagery for further processing.

The signal reaching the thermal camera is composed of target radiance, but also of background radiance. Background radiance is variable in time, and in indoor environments, with emissions from walls, ceiling and other surrounding objects, can introduce a significant error to analysis. In order to account for changes in background radiance throughout the experiments, the calibration target was used. For each of the acquired images, the target's centre 3500 pixels were used to retrieve an average target temperature value, which was compared against the thermocouple measurements. The differences between image and thermocouple readings of the target surface were then subtracted from the camera readings to normalise them for the changes in the background radiance levels.

Following the correction and prior to further analysis, background masks were created by means of temperature thresholding. For each of the experiments, the image with highest plant-to-background temperature contrast (defined as the temperature difference between central part of the stressed canopy and of the background in top part of the image) was used. Based on this image, ten temperature thresholds, one for each set of 25 image rows, were manually chosen to separate plant foliage from the surroundings. The choice of thresholds was aided by comparison with visible imagery, which allowed the number of mixed pixels located at the edges of the canopy to be minimised. Multiple thresholds were required for accurate separation as both the temperature of the background and of the plants depended on the distance from the heat source. The derived masks allowed for extraction of canopy pixels, as presented in Figure 5.2. To ensure that the selection of canopy pixels was consistent throughout the experiments, the same masks were applied to all imagery within each of the datasets. Furthermore, for a qualitative comparison between plants, a second mask (low canopy volume mask) was created excluding image rows in which either of the trees in each of the experiments had a limited foliage; such rows were likely to be affected by mixed pixels (containing the response from both the canopy and the background). Any image row constituting of less than 30 canopy pixels was therefore masked (the resultant mask in shown in Figure 5.2).
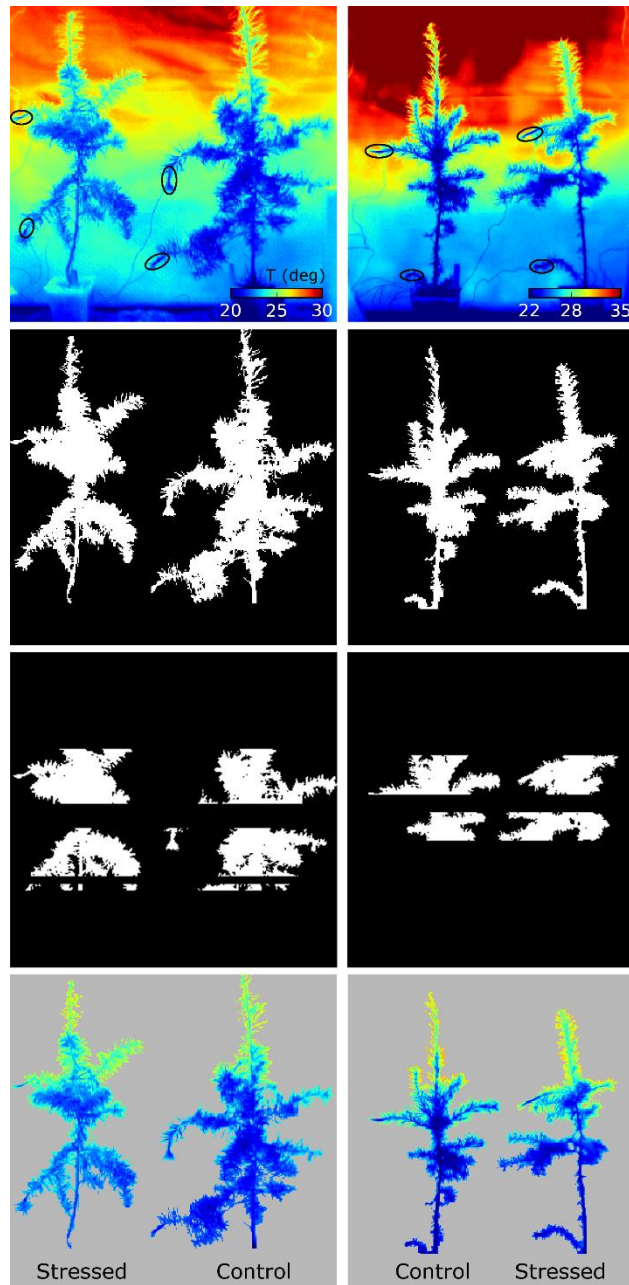
Figure 5.2: Canopy pixel extraction for the first (*left*) and the second (*right*) experiment, showing original thermal image, the canopy mask, the low canopy volume mask, and extracted canopy pixels. Black circles indicate regions, where thermocouples were placed.

Another point of interest was the vertical distribution of temperature within the canopies, and how this changed over time. To analyse this, average foliage temperature values for each image row were computed. To minimise large variations in readings between consecutive rows and aid the interpretation, the readings retrieved from all images were smoothed first using Kaiser window smoothing (Kaiser, 1966), which offers a flexible

window that can be modified depending on the application. A window size of 11 and a beta parameter of 4 were used (Figure 5.3).
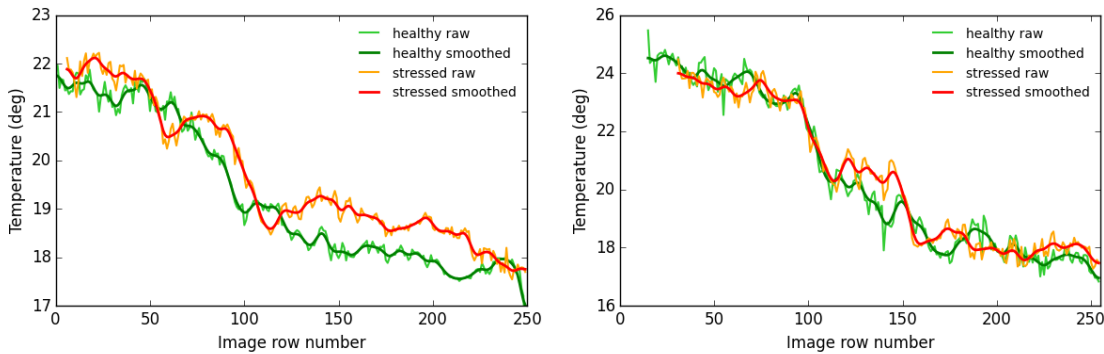
Figure 5.3: Smoothing procedure for the 1st (*left*) and 2nd (*right*) experiment.

Lastly, average canopy temperature values (excluding rows of low volume, i.e. constituting of less than 30 pixels) were calculated for each image to compare the thermal response of control and stressed plants over time. The significance of the difference between the canopy temperature means at each time stamp was tested using Welch's unequal variance t-test (Welch, 1938) at 0.01 confidence level (h0 = the true difference in means is equal to zero, null hypothesis rejected at $p \leq 0.01$). To provide an indication of the variation of temperature within the canopies, standard deviation was calculated.

5.3.3 Changes in background radiation inside the greenhouse

At the beginning of the first experiment, undertaken under cloudy weather conditions, the difference between the calibration panel thermocouple and image measurements was around 2°C (Figure 5.4). Upon the turning on of an additional light source, a substantial increase in background radiance was observed (change of 1.4°C). Throughout the rest of the experiment, the background radiance influence remained constant as shown by the differences between the image and thermocouple measurements. Furthermore, the standard deviation of the target pixels remained at the same low level, showing a consistent response from the whole investigated area of the target.

During the second experiment, the measurements were much more variable (Figure 5.4); this was due to changing weather conditions, i.e. moving cloud cover. Occasional periods of sunshine increased the shortwave radiation inside the greenhouse leading to an increase in temperature of the air and surfaces. Consequently, the longwave background radiation emitted by surrounding objects increased (causing differences between the image and thermocouple measurements up to 6°C). This influence can also be observed in the image standard deviation value of the target, which almost doubled. Otherwise, prior to clouds

clearing, the difference between image and thermocouple values remained at the same level as in experiment 1 (around 2.5°C, apart from a single spike caused by a brief sunshine period).
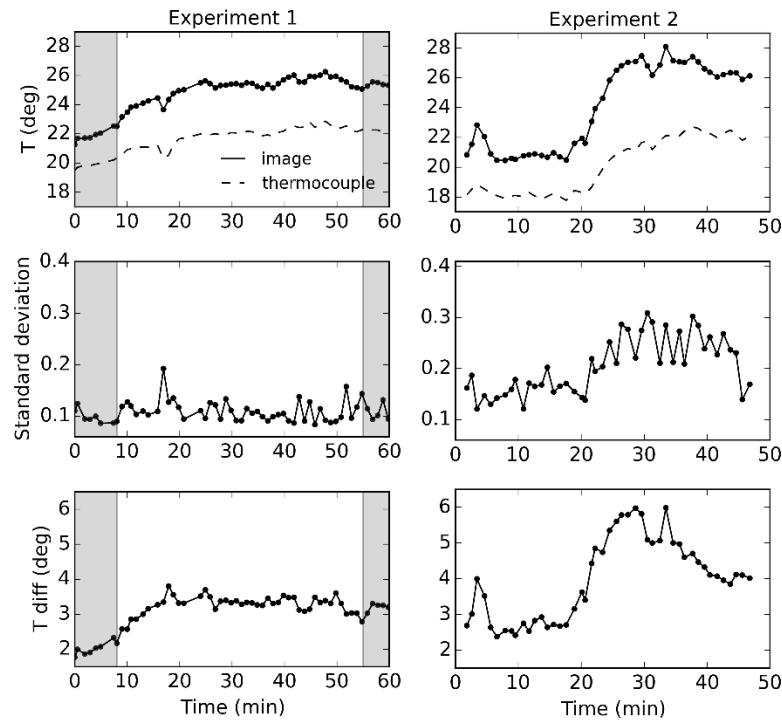
Figure 5.4: Retrieved image and thermocouple temperature measurement of the calibration target with corresponding differences between the two and image standard deviations. Shaded areas indicate times at which the additional light sources were turned off.

The results above demonstrate that image readings were significantly affected by the large variations in background radiance emitted from surrounding objects, in particular in the second experiment. If left unaccounted for, these changes would inhibit temporal analysis of the datasets.

5.3.4 Thermocouple and image measurements of trees over time

During the first experiment, air temperature inside of the greenhouse was stable until the additional light source was turned on. Afterwards, a substantial, yet steady, increase in air temperature from 21 to around 24°C was observed. Thermocouples attached to different parts of the canopies showed different rates of temperature increase (Figure 5.5). At the beginning of the experiment, all measurements were close together, showing barely any difference in temperature readings. However, with additional radiation, readings started to separate, with higher increases recorded for upper sections of the trees.

Throughout the second trial, the air temperature varied more as a result of moving cloud cover. Intermittent sunshine caused temperature spikes, whilst partial cloud clearing led to a drastic ambient temperature increase from 20 to 25°C. In this experiment, from the beginning, there was a clear difference between the upper and lower parts of the canopies. However, there were no considerable differences between the mildly stressed and the control plant occurred until after minute 30, when readings from the canopy top separated. The upper parts of the canopies were located closer to the light source, and consequently were receiving more direct radiation, leading to a steeper increase in the temperature when compared to the lower parts. Within the first experiment, there were visible differences in temperature readings between the control and stressed canopies, the second being warmer. However, those observations cannot be conclusive, as the differences could have been caused by the distribution of the thermocouples on trees, e.g. placement at uneven distance from the light source. The thermocouple measurements were, therefore, primarily used for validating thermal camera readings and assessing the performance of the normalisation for the background radiance.
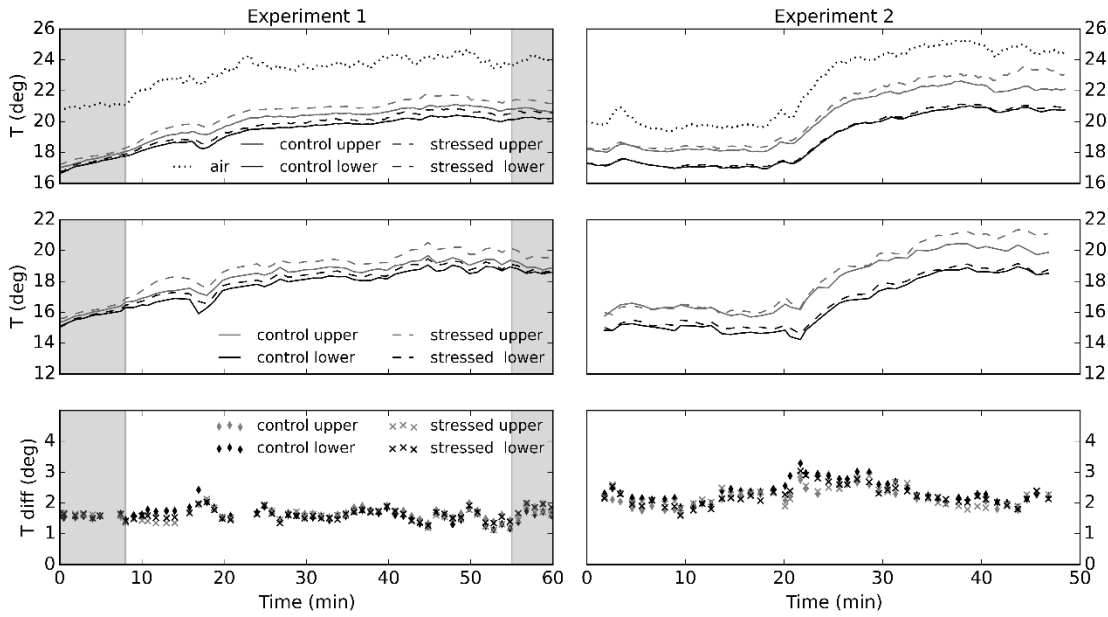
Figure 5.5: Temperature readings acquired by the thermocouples (top) and the thermal camera (middle) for the lower and upper parts of tree crowns, with differences between the two (bottom). The first experiment involved a moderately, whilst the second a mildly stressed tree. Shaded areas indicate times at which the additional light sources were turned off.

The thermocouple measurements were compared to the image readings, extracted from the corresponding regions. The differences between the temperatures recorded by the thermocouples and the camera were calculated (with image temperatures subtracted from the thermocouple measurements), and are shown in Figure 7. In the first experiment, image temperature extracted for each thermocouple location were on average different by 1.64°C, which is within the thermocouple accuracy threshold of $\pm$ 2.2°C. However, the temperature values acquired for the second experiment marginally exceeded the threshold with average difference of 2.26°C. The image canopy temperature readings were normalised for changes in background radiance levels, which allowed minimisation of the temporal variability of measurements. The standard deviation of the offsets from the thermocouple readings was reduced from 0.46 to 0.20°C in the first experiment and from 1.00 to 0.32°C in the second experiment.

5.3.5 Vertical distribution of canopy temperature

The temporal and vertical variation in canopy temperature extracted from the imagery, alongside pixel count histograms, for both experiments is shown in Figure 5.6. For all of the trees, the upper parts of the canopies were considerably warmer than the lower parts. The difference increased as time went by, caused by an input of additional shortwave radiation and consequent warming up of the room. This effect was probably mainly caused by the proximity to the light (and consequently heat) source and limited foliage of the tree top. In canopy parts characterised by very low volume, the temperature was higher, which is particularly evident in the transition from a single tree leader to sections with branches. For example, for the control tree in the second experiment the difference amounts to about 4°C. The higher temperature in the areas of scarce foliage is likely to have been caused by inclusion of mixed pixels, containing readings from both the canopy and background. Despite attempts to exclude all mixed pixels during the masking stage, some may have remained and contributed to higher temperature measurements. Therefore, for comparison between the plants, the low canopy volume mask was applied prior to further analysis.
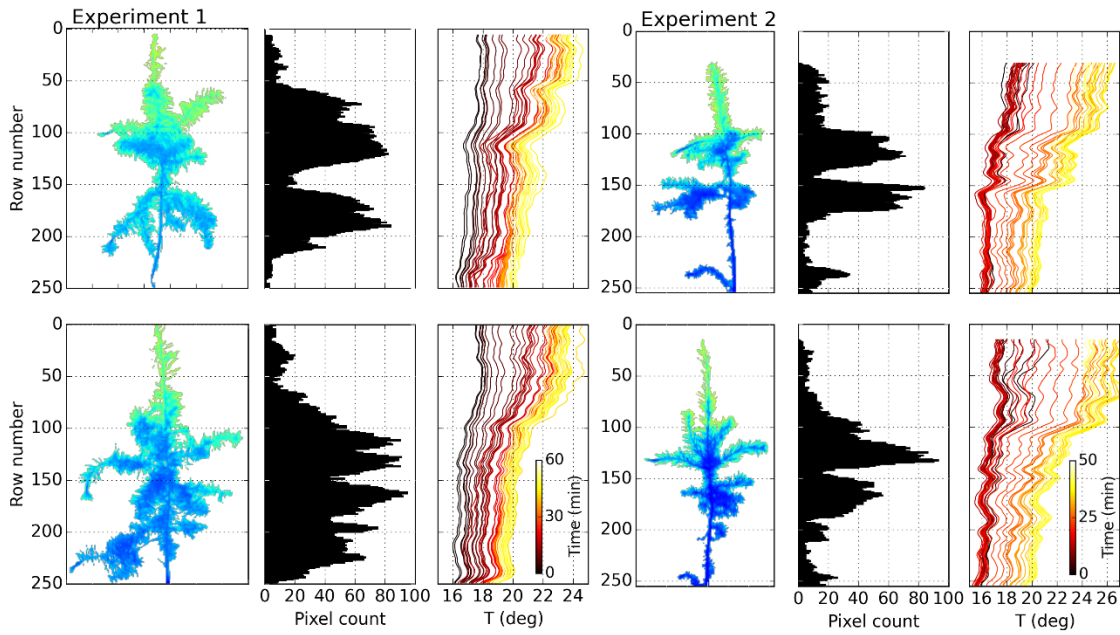
Figure 5.6: Vertical distribution of canopy temperature over time, retrieved from thermal imagery, for stressed (*top*) and control (*bottom*) plants.

For all remaining rows, the temperature differences between the stressed and control plants were computed and are shown in Figure 5.7. In experiment 1, the control tree was colder than the stressed tree in most image rows, and this difference was further accentuated over time. The only region where the stressed plant was colder were rows 110-120, most likely an artefact of structural differences; within this region, the stressed plant consists of multiple branches clumped closely together, whilst the control plant has limited foliage. Conversely, in experiment 2, the temperature differences between the trees seemed to be dictated primarily by structural variances across the canopies, rather than stress; lower temperatures were recorded in rows of high foliage volume, and foliage clumping around the main stem.
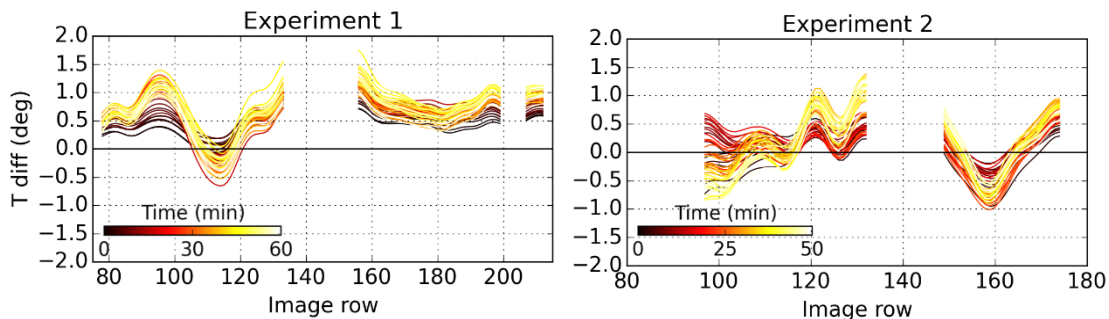
Figure 5.7: Temperature difference between control and healthy plants calculated from average derived for each image row.

5.3.6 Differences in thermal response of control and stressed plants

To further explore the thermal response of control and stressed plants over time, average canopy temperature values were calculated for each image. Utilising the low canopy volume mask, mean, median and standard deviation values of the rest of the pixels were computed. The mean and median response over time, alongside the difference in mean temperatures between stressed and control plants for both experiments are shown in Figure 5.8 and Figure 5.9.
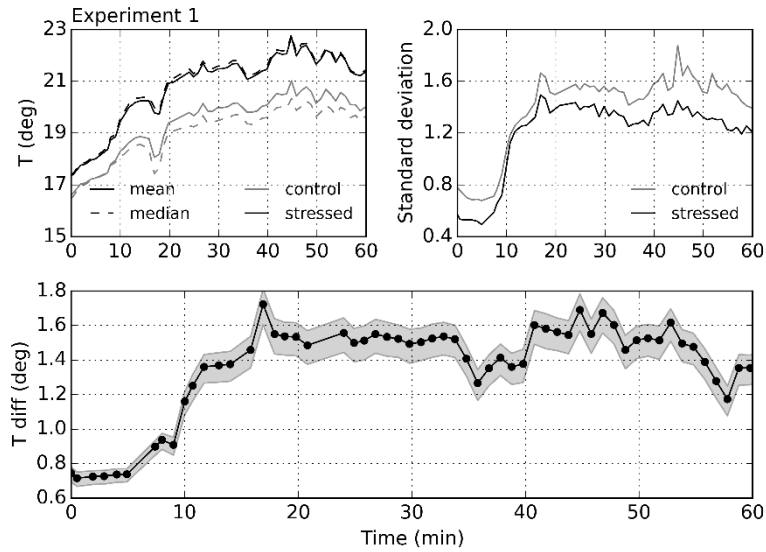
Figure 5.8: Mean and median temperature values over time for plants, alongside standard deviation (*top*); difference in mean temperatures between stressed and control plants with 99% confidence intervals derived with Welch's t-test (*bottom*). If confidence interval overlaps Tdiff = 0°C, the temperature means are not significantly different at the given confidence level.

In the first experiment, the mean and median values for the moderately stressed plant were the same, indicating symmetric distribution of temperature values across the canopy. However, for the control tree, the distribution became skewed upon the turning on of lamps (turned on between minute 8 and 55) – the mean was greater than the median, whilst interquartile range by minute 20 increased by 0.54°C (as opposed to 0.45°C for the stressed plant). This suggests that the canopies responded to the change in environmental conditions in a different manner; the stressed plant warmed up fairly uniformly, whilst the control canopy only showed high levels of temperature change in its upper part. As a result, the overall temperature difference between the trees drastically increased after the additional light source was turned on, i.e. from 0.75°C to 1.5°C. This difference started declining again after the lamps were turned off. Nevertheless, the difference in standard

deviation over time between the two plants remained at the same level of approximately 0.2°C, despite the sudden increase (by around 0.8°C) when the additional light source was turned on. Welch's t-test showed that the difference between the canopy temperature means was statistically significant throughout the whole experiment, even under low illumination conditions.

Throughout the second experiment, despite slightly different canopy structure and volume distribution, the mean and median temperature values of the plants were nearly identical. The standard deviation of both plants increased significantly by around 1.1°C, with greater differences between the upper and lower canopy caused by the occasional periods of sunshine increasing the amount of shortwave radiation and air temperature inside of the greenhouse. However, the mild stress, under which the plant was put, did not exhibit itself in statistically significant differences in canopy temperature; the overall temperature difference between the trees continuously oscillated around 0°C, notwithstanding drastic environmental change in radiance and ambient temperature (Figure 5.9).
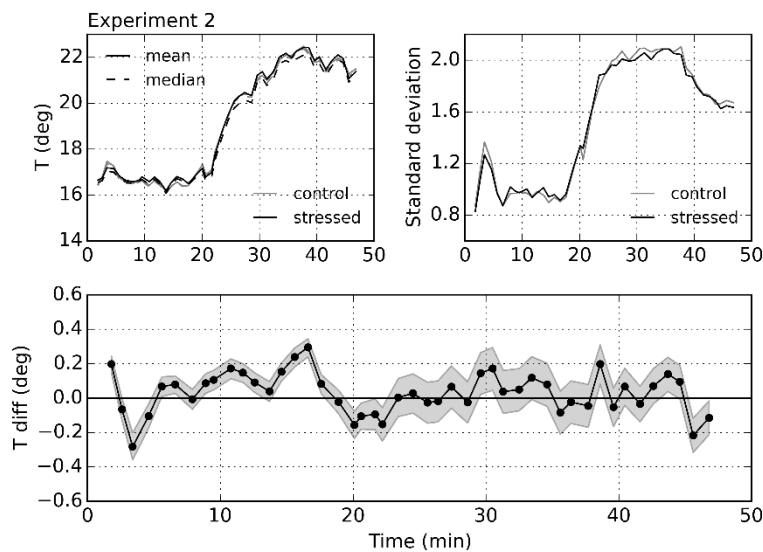
Figure 5.9: Mean and median temperature values over time for plants, alongside standard deviation (*top*); difference in mean temperatures between stressed and control plants with 99% confidence intervals derived with Welch's t-test (*bottom*). If confidence interval overlaps $T_{diff} = 0$°C, the temperature means are not significantly different at the given confidence level.

5.4 UAV-borne analysis

5.4.1 Experiment design

This research was based in plot A, planted with Scots pine in 2003; within this plot, the positions of 60 sample trees were surveyed. The sampled trees were chosen through a cluster sampling approach based on visibility from the detailing stations established within the plot (see Section 3.4). The tree heights varied between 2.9 and 6.3 m, whilst the disease level ranged from 25 to 80%. Infection level was expressed as percentage of total unsuppressed crown volume; corresponding heights needed for the calculation (Figure 5.10) were measured using a hypsometer.
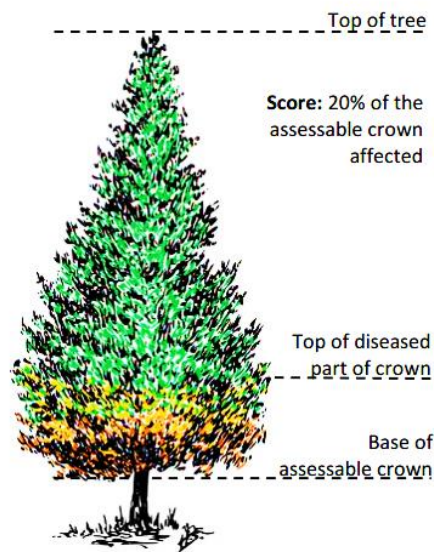
Figure 5.10: Diagram showing the procedure for estimation of red band needle blight infection levels, based on guidelines from Bulman *et al.* (2004).

The UAV used for this research was a DJI Phantom 2 Vision+ Quadcopter, which is a lightweight (1160g) aircraft with an integrated, wide-lens camera (resolution of 14 Megapixels). Specifically for this survey, the quadcopter was modified in-house to carry the thermal camera. This modification increased the take-off weight of the UAV by 600 g (to a total of 1760 g), and consequently limited the flight time to 6 minutes, allowing data collection in a safe manner only from a very limited area. On the 18th of August 2015, the aircraft was used to collect multiple thermal data acquisitions. The main interest was to determine whether the sensitivity of thermography in detecting stressed plants might be affected by the outside conditions, such as radiation levels. Therefore, to examine the influence of timing and atmospheric conditions on the signal, the flights took place at different times of the day. In total six flights were performed at 10:15, 11:10,

12:10, 13:15, 15:10 and 16:50 (GMT) at an altitude of 230 ft (60 m). During the flights, the cloud conditions were monitored; other weather measurements, i.e. the temperature, wind speed, atmospheric pressure and humidity, were retrieved from the nearest weather station in Port of Menteith (located 7 km away at 39 m altitude, reference: IUNITEDK106).

Creation of an orthomosaic from the thermal imagery (using SfM approach) was attempted, but proved infeasible. The poor optical resolution of the camera (382 x 288 pixels) and lack of contrasting features within the environment inhibited detection of a large enough number of tie points for creation of an accurate surface. Thus, from each flight a single photograph with nadir viewing angle, containing all the survey trees was chosen and used for further processing. The emissivity of the canopy foliage was assumed to be 0.98 (whole plant emissivity value reported by Jones (2004)).

5.4.2 Image processing

Geometric correction of the UAV-borne datasets was achieved by registration to the canopy height model derived from LiDAR. A local maximum filter was then developed to identify treetops within the canopy height model, and aid a manual "tree to tree" registration of thermal imagery. All but one of the images were georeferenced using a second order polynomial transformation (Table 5.1). The forward RMSE was between 0.10 to 0.30 pixel (mean of 0.20), whilst the average output cell size ranged from 0.138 to 0.172 m (mean of 0.153 m).

Tree canopies of the surveyed trees were manually delineated, and are shown in Figure 5.12. The areas that could have been directly influenced by the understorey vegetation, i.e. canopy edges, were excluded by using a buffer of at least two pixels.

Table 5.1: Georeferencing summary based on tree tops used as GCPs.

Flight	Time	Points	Transformation	Forward RMSE (pixel)	Cell size (m)
1	10:15	82	2nd order	0.3005	0.145
2	11:10	26	1st order	0.1746	0.170
3	12:10	18	2nd order	0.1040	0.148
4	13:15	48	2nd order	0.1720	0.138
5	15:10	20	2nd order	0.1732	0.145
6	16:50	44	2nd order	0.2958	0.172
			Average:	0.2034	0.153
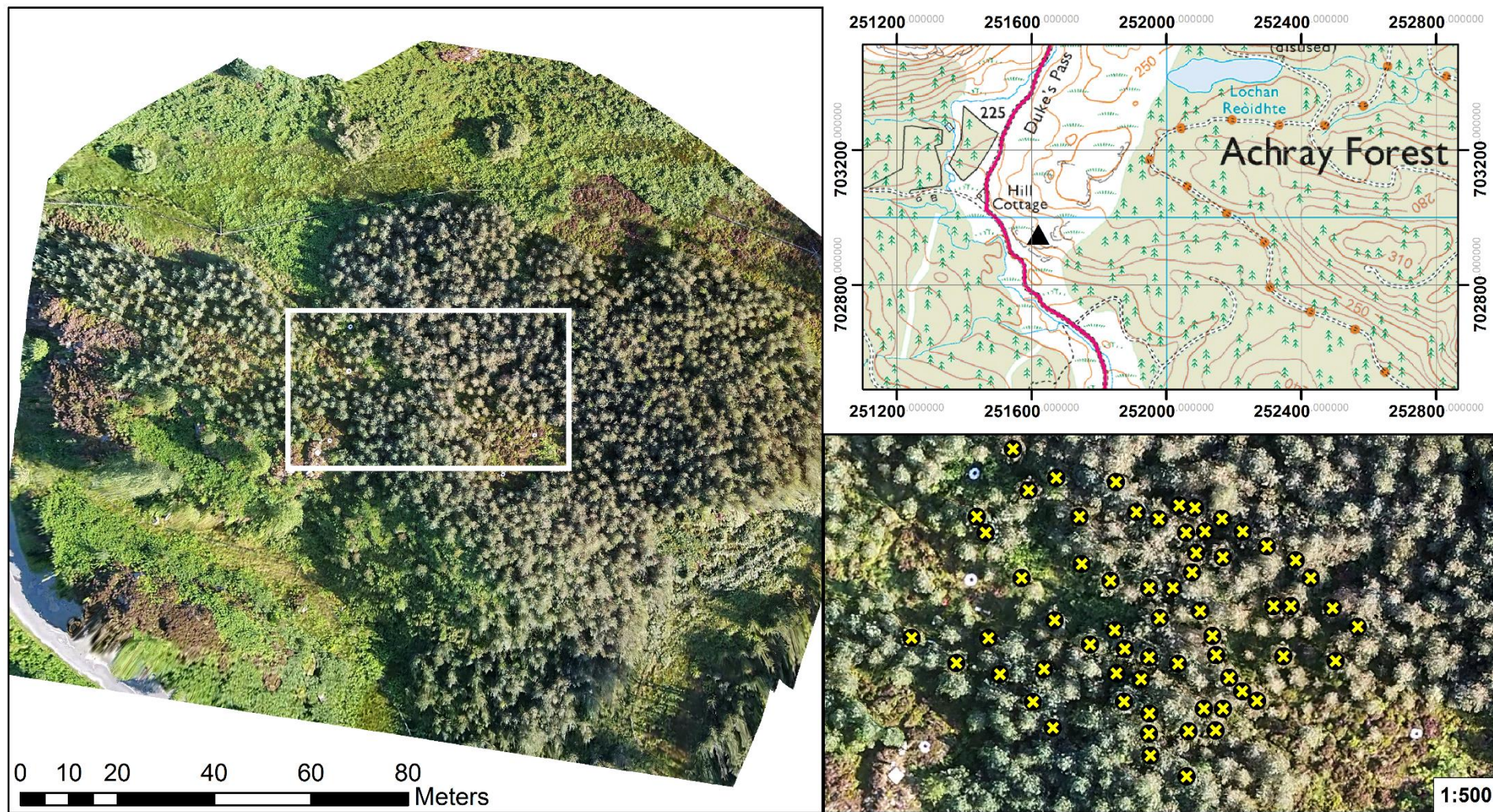
Figure 5.11: Locations of the test trees, marked on a UAV-borne orthophoto. Contains OS data © Crown copyright and database right 2017.
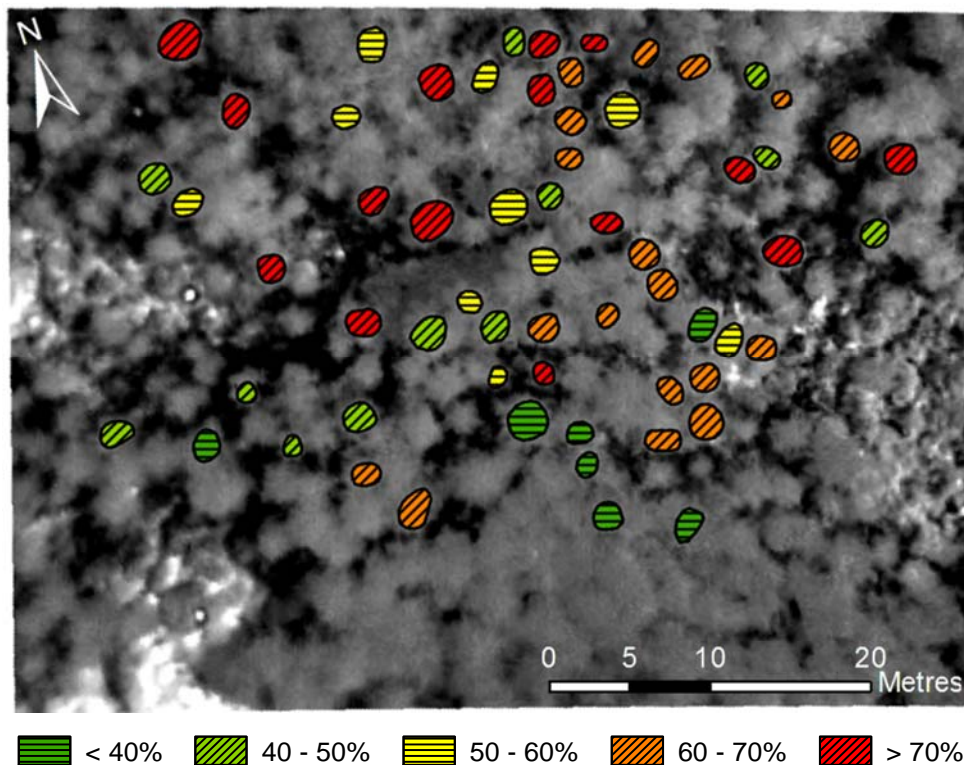
Figure 5.12: Delineated tree crowns with their disease levels (Flight 1 at 10:15).

The canopy sizes of the surveyed trees varied greatly; the number of pixels constituting tree polygons ranged from 86 to 366, with vast majority falling between 175 and 200 pixels (Figure 5.13). There were no patterns in terms of the tree size and the disease level. However, spatially, the least diseased trees were located to the south of the plot, whilst the most diseased ones were predominately located in the northern part. Such spatial differences are most probably caused by the dispersion mechanism of the disease. The fungus is dispersed through movement of atmospheric humidity, i.e. mists or moist winds, which makes the closest trees more vulnerable to attack. The site was characterised by poor tree condition, which is reflected by the significant left skewness of the disease level data (Figure 5.13); the measurements most commonly fell within the 60-70% infection range. Furthermore, there were no entirely healthy trees within the surveyed sample, and only 7 that had a relatively small (<40%) disease level.

The delineated polygons were used to extract average temperature and the standard deviations for each canopy. Scatter plots and Pearson's correlation coefficient were used to examine the relationship between these and the estimated disease levels.
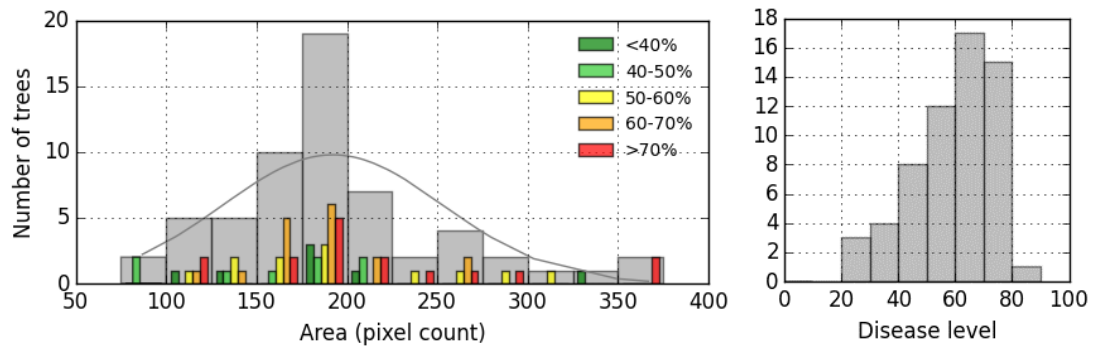
Figure 5.13: Histograms showing canopy polygon areas according to infection levels.

The thermal response of a tree can be affected by its structure, as well as the amount of live foliage. Inclusion of Lidar metrics could therefore account for structural differences between trees, and help explain the observed variations in canopy temperature. Furthermore, as one of red band needle blight's symptoms is defoliation, structural metrics could potentially identify differences in the amount of lost foliage. The airborne LiDAR dataset was used to calculate multiple structural metrics: height percentiles (p5, p25, p50, p75 and p90) normalised to canopy extents, skewness, kurtosis, standard deviation, coefficient of variation, as well as maximum, mean and median heights. The manually-delineated polygons created for canopy temperature extraction were used to extract LiDAR points for each of the trees. These points, excluding those below a cut-off height of 0.3 m (understorey vegetation), were then used to calculate the canopy metrics.

Partial least squares regression (PLSR) was performed on all extracted LiDAR and canopy temperature metrics to investigate whether inclusion of structural measures could improve the observed relationships with tree disease levels. The analysis was performed in R using the "pls" package (Mevik and Wehrens, 2007). PLSR is a dimension reduction technique, whose main advantage is that it was designed for situations when there are many, possibly correlated, predictor variables, and relatively few samples. PLSR was shown to be robust with regard to several data inadequacies (such as skewness or multicollinearity of the indicators) (Cassel *et al.*, 1999). A leave-one-out cross-validation (LOOCV) strategy was used to select the number of principal components and to prevent over-fitting. The coefficient of determination (R^2) and root mean squared error of prediction (RMSEP) were used to evaluate the model's performance.

5.4.3 Canopy temperature and disease progress

The extracted mean canopy temperature values and the associated standard deviations were compared against the estimated disease levels; the resultant scatterplots for each flight are shown in Figure 5.14 and Figure 5.15.
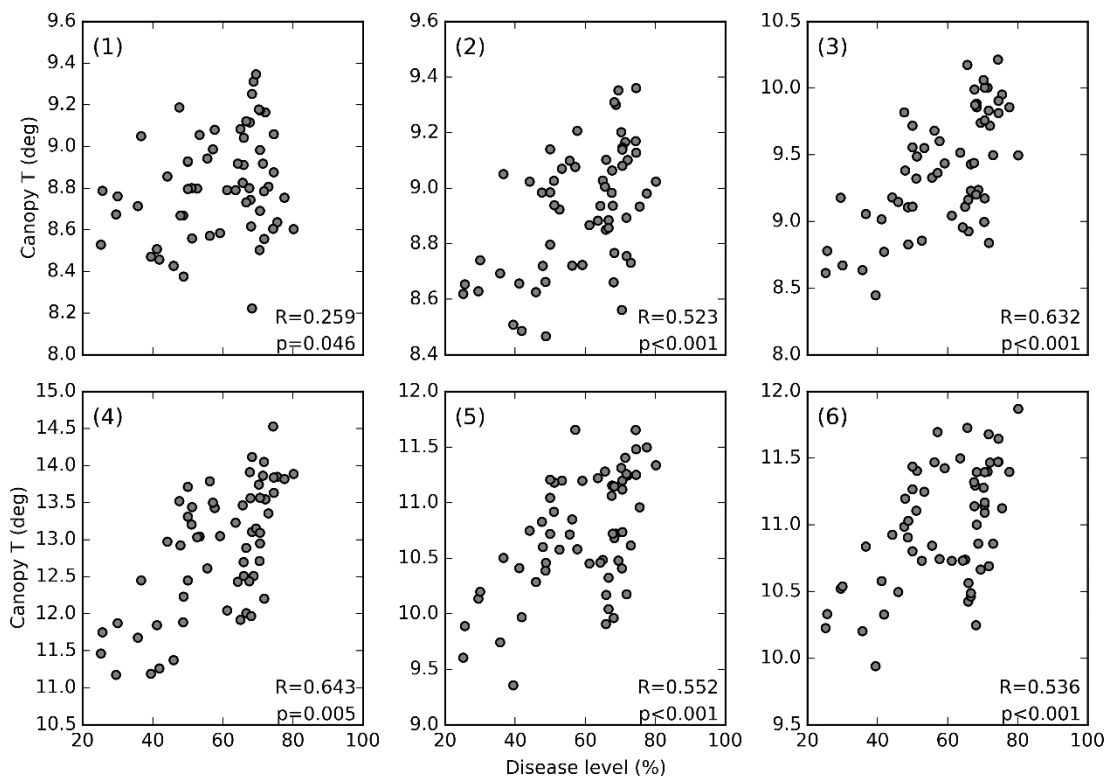
Figure 5.14: Scatterplots presenting the retrieved mean canopy temperature values against the estimated disease levels at different flight times (flights 1 - 6).

The Pearson's correlation coefficients acquired varied considerably between the flights. In the first flight, no significant relationship was found between the canopy temperature and the disease level. However, in the case of the other flights there was a significant correlation ranging from 52 to 64%, with best correlation (above 60%) achieved with the imagery taken during the third and fourth flight. Weak relationships (33 to 36%) were found between the standard deviations of the canopy temperature and the estimated disease levels. Similarly, the best correlation was achieved during the third and fourth flight.
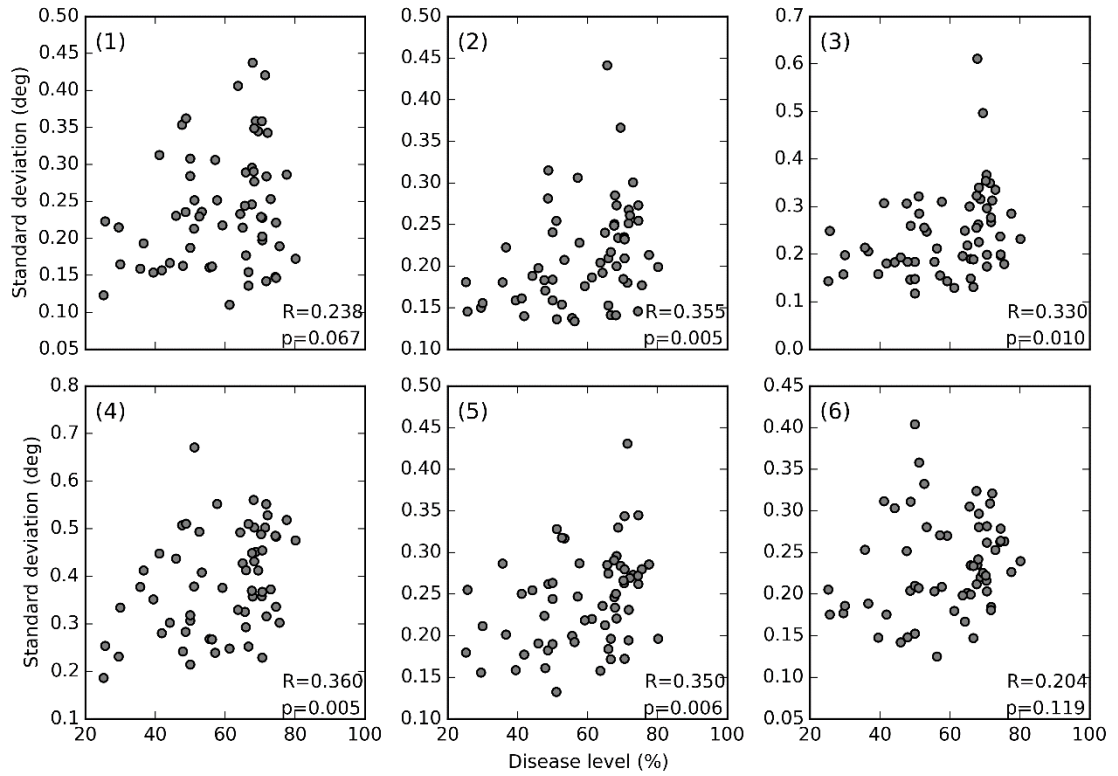
Figure 5.15: Scatterplots presenting the standard deviation of the retrieved canopy temperature against the estimated disease levels at different flight times (flights 1 - 6).

The temperature measurements from the first two flights were clustered together, the difference between the maximum and minimum temperature value was only 1.13 and 0.90°C (standard deviation σ = 0.25 and 0.22). With time, the tree canopies warmed up and the temperature measurements spread out. The highest temperatures, and also the highest ranges, were recorded for flight 4, with a range of 3.38°C (σ = 0.84). The canopy temperatures during flights 5 and 6 were considerably lower, and the difference between the maximum and minimum value equated to 2.32 and 1.94°C (σ = 0.53 and 0.45). Similar values were also recorded for flight 3: range of 1.78°C (σ = 0.44). However, higher ranges did not necessarily yield higher correlations.

5.4.4 Inclusion of structural metrics

PLSR was performed on all extracted LiDAR and canopy temperature metrics using the LOOCV approach to select the number of principal components. The cross-validation results suggested the use of four (flights 2-5) and three (flight 6) components, based on minimisation of the RMSEP (Figure 5.16). Using the identified optimum component numbers, the PLSR models were designed for each of the flights. The retrieved normalised regression coefficients for the models are presented in Figure 5.17. As anticipated, the variable with highest effect on the models was the average canopy

temperature, followed in almost all cases by the standard deviation of canopy temperature. Other variables, which were repeatedly highlighted were kurtosis, p5, p75 and p95. Kurtosis is a statistical term indicating the extent of peakedness/flatness of a distribution curve. Consequently, kurtosis of point cloud density distribution is a metric describing the vertical stratification of canopy vegetation; lower values characterised by flatter curves would indicate that the vegetation is dispersed more broadly across a wider vertical range. Two scenarios for final PLSR models were considered: 1) regression based only on temperature measures and 2) regression including kurtosis, p5, p75 and p95. The summary of performance of the regressions is presented in Table 5.2, whilst RMSEP values and variable loadings for each regression component are available in Appendix H.

Table 5.2: Results of regression against the estimated disease levels. Three approaches were tested: 1) linear regression of canopy temperature, 2) partial least squares regression of canopy temperature and standard deviation of canopy temperature (PLSR1), and 3) partial least squares regression of canopy temperature, standard deviation of canopy temperature and selected LiDAR metrics - kurtosis, p5, p75 and p95 (PLSR2).

Flight	Regression	Number of components	RMSEP (%)	R^2 (%)
	Canopy temperature	n/a	n/a	27.35
2	PLSR1	1	12.04	31.23
	PLSR2	3	12.48	34.72
	Canopy temperature	n/a	n/a	39.94
3	PLSR1	2	11.21	41.03
	PLSR2	2	11.65	41.93
	Canopy temperature	n/a	n/a	41.34
4	PLSR1	2	10.98	44.26
	PLSR2	3	11.93	46.57
	Canopy temperature	n/a	n/a	30.47
5	PLSR1	2	12.01	32.62
	PLSR2	3	12.58	35.15
	Canopy temperature	n/a	n/a	28.73
6	PLSR1	2	12.40	28.70
	PLSR2	2	12.92	30.01
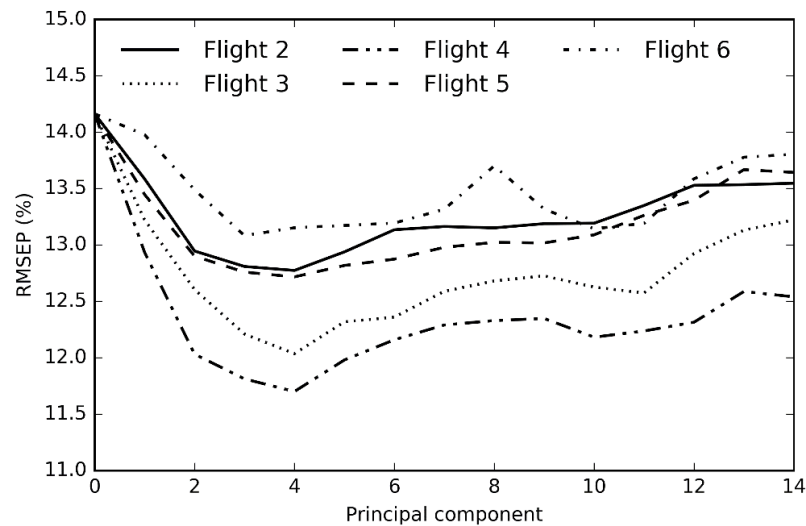
Figure 5.16: Cross-validated RMSEP curves for each of the flights.

The inclusion of standard deviation of canopy temperature in regression (PLSR1), in most cases, improved the observed relationships by +1.09% (flight 3) to +3.88% (flight 2); a minimal decrease of -0.03% was reported for flight 6. Incorporation of LiDAR metrics (PLSR2) provided further slight improvement between +0.9% (flight 3) and +3.49% (flight2). However, a worsening of the RMSEP values was observed for PLSR2, suggesting an increase in differences between values predicted by the regression model and the observed values (by 0.44-0.95%).

5.4.5 Influence of imaging time on the signal

The flights were performed at different times of the day, as well as slightly different weather conditions, as presented in Figure 5.19. The temperature throughout the day was slowly rising from 17.5°C at 10 am, peaked after 3 pm (23.4°C), and then slowly declined to 19.9°C at 5 pm. The wind followed a similar pattern – lowest values were recorded in the morning, then the speed peaked at 12 (for gusts) and 1 pm (for average speed), followed by a decline. There was a further increase in wind speed towards the evening recorded. On the other hand, the humidity in the morning was 57%, then declined to 40% at 12 pm, remained at similar level until 3 pm, and then rose again to 61% at 5 pm. The atmospheric pressure levels did not vary much (between 1013.1 and 1017.2 hPa), and thus were not included on the graphs. The sunshine conditions throughout the day varied greatly (Figure 5.18). The morning (10 am, during flight 1) was hazy, with a thin but uniform layer of clouds (cirrostratus). Throughout the day, the clouds were quickly thinning, bringing bright sunshine in between moving cloud cover (cirrus types) for the

3rd and 4th flight. Before 3 pm the high-altitude clouds thickened, and greater amounts of lower altitude clouds formed.
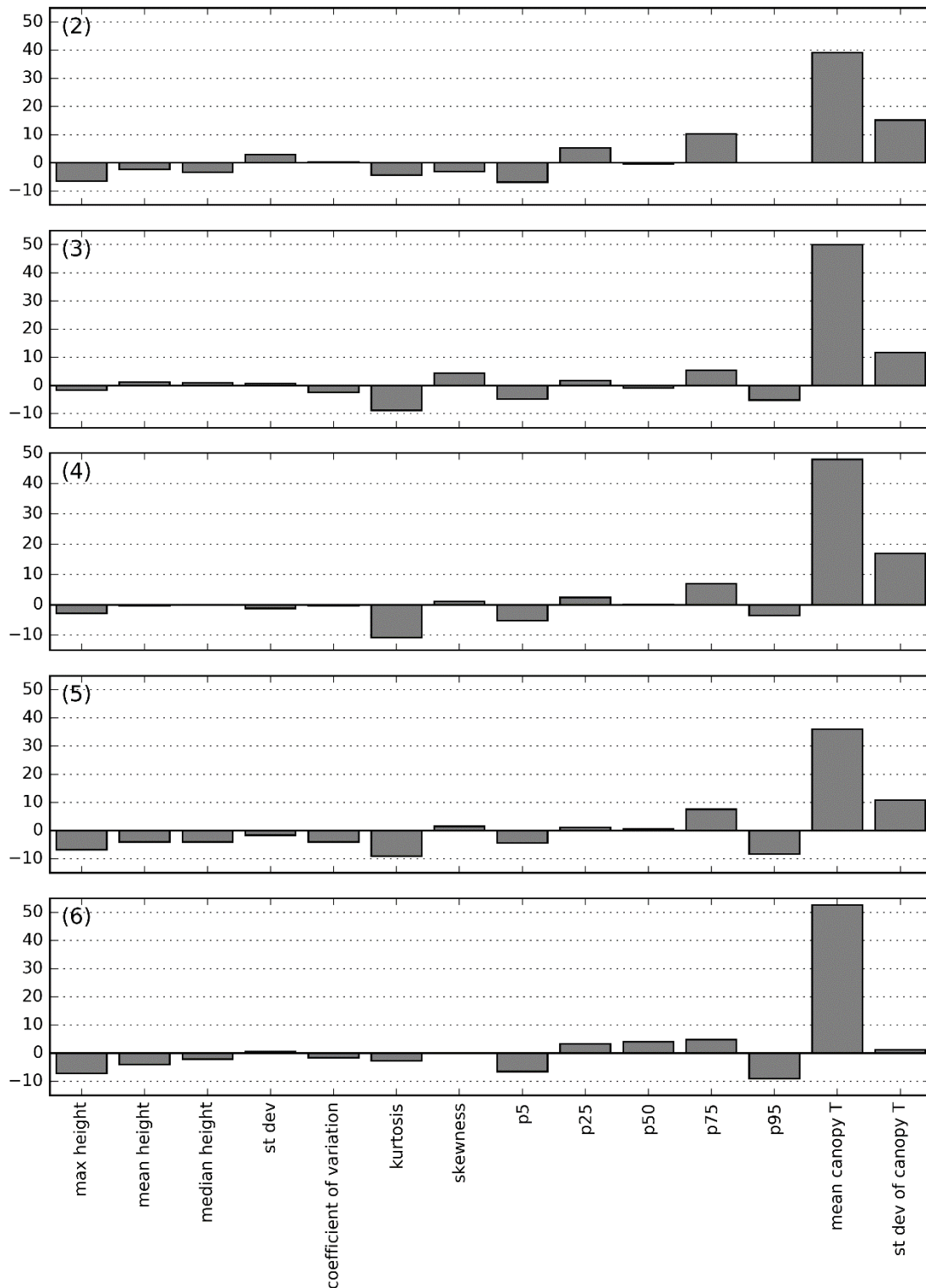
Figure 5.17: Regression coefficients obtained for partial least squares regression (flights 2-6). The coefficients were normalised so their absolute sum equals 100.
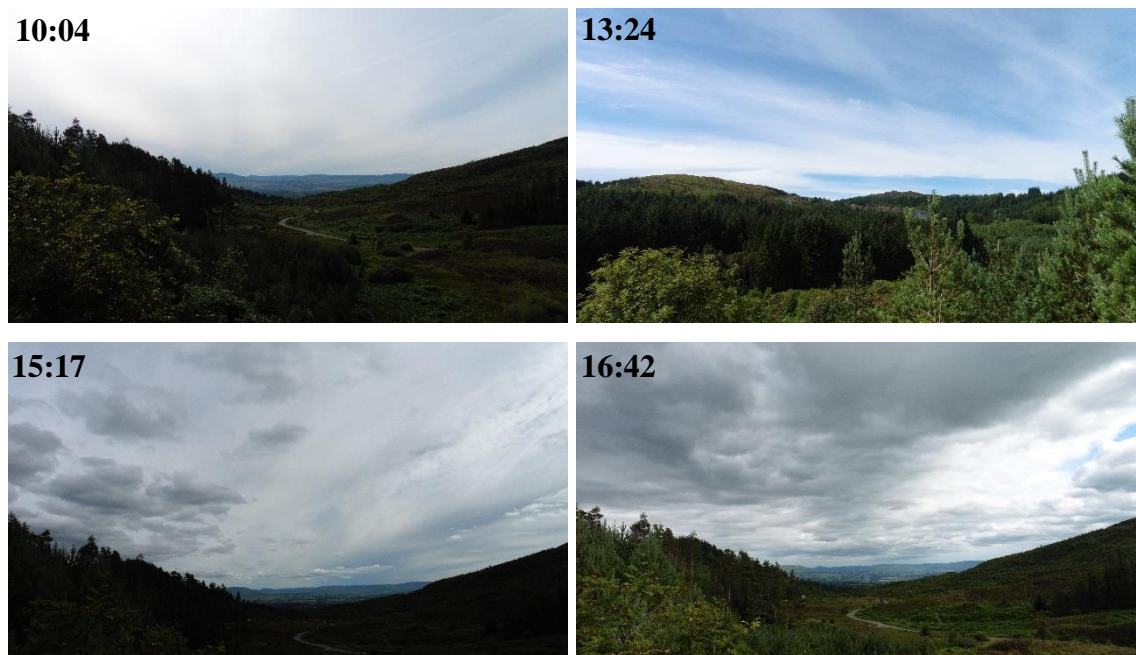
Figure 5.18: Cloud conditions throughout the survey. Times are given in GMT.

Figure 5.19 shows progression in terms of retrieved correlation score over time. There was no significant correlation in the early morning, which was followed by a steep rise, plateauing around 12 – 1 pm, then a small decrease towards the late afternoon. The highest correlations were present around the time of the solar noon (i.e. 1 pm), when the stomata are expected to be most active (Jones, 1992). However, other environmental conditions were very likely to have contributed as well.

Evapotranspiration is influenced by incoming solar radiation and aerodynamic effects dependent on wind, humidity, and temperature. The relative humidity of the air surrounding the plant has a direct influence on transpiration of plants, based on the difference between leaf and air vapour pressure. Decreasing relative humidity would therefore accelerate a plant's rate of transpiration (under normal circumstances) (Spellman, 2014). In the case of wind, with increasing speed, normally an increase in transpiration is observed. This is due to the increased movement of the air being related to relative humidity of the air surrounding the leaf; with wind present, the more saturated air close to the leaf would be replaced by drier air (Spellman, 2014). In theory, the weather conditions favouring increased transpiration rates should accentuate the differences between the trees, as stomata of the stressed plants would be closed to prevent the loss of water, which in turn should lead to an increase in leaf and canopy temperature.
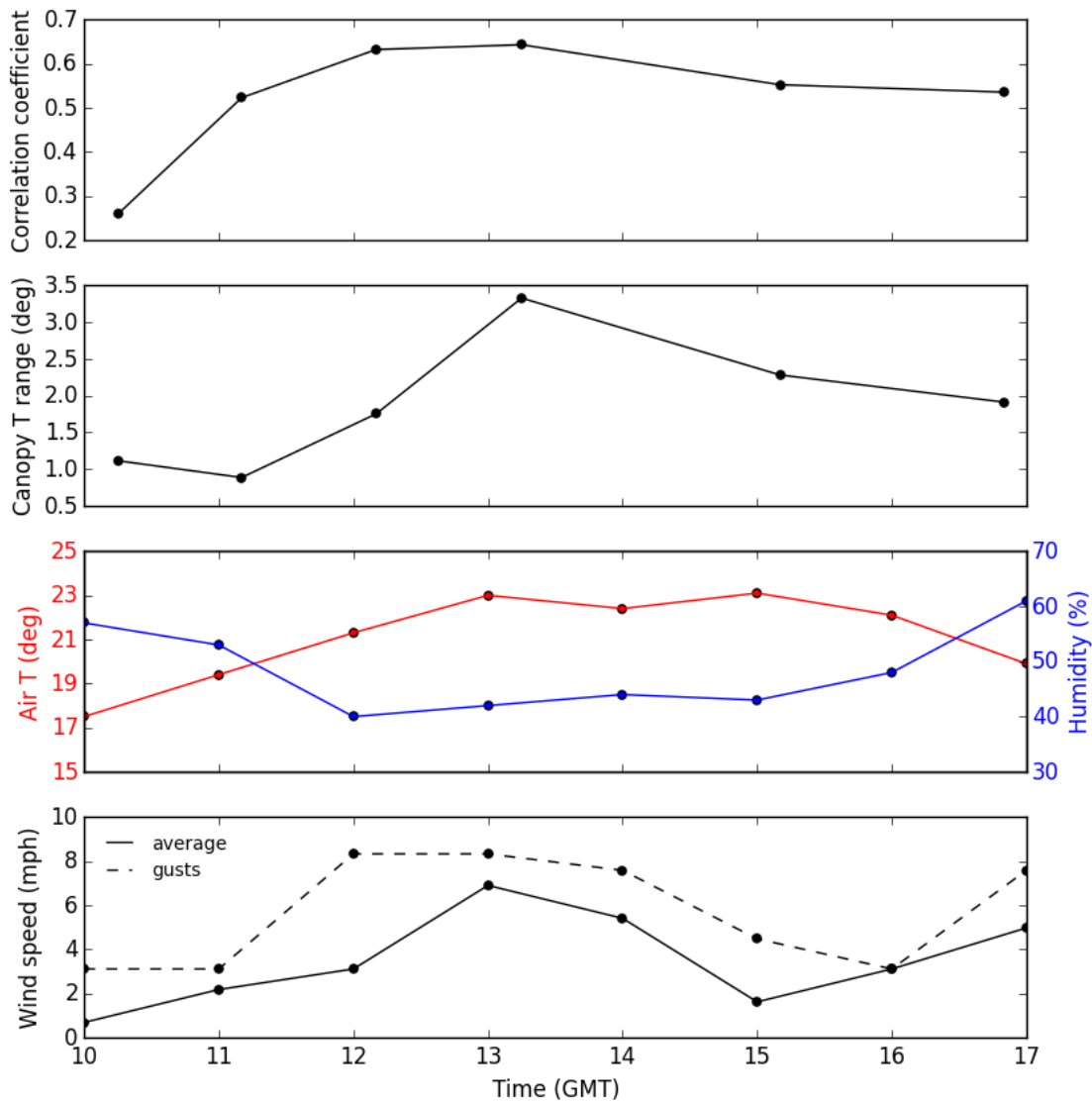
Figure 5.19: Achieved correlation coefficient of mean canopy temperature values against the estimated disease levels (*top*), range of retrieved mean canopy temperatures, calculated as the difference between maximum and minimum value (*middle*) and weather conditions (*bottom*) at different flight times.

This is partially reflected by this study. In the early morning imagery, due to a uniform layer of clouds, the photosynthesis was expected to be limited, making the separation of trees impossible. As the clouds started thinning and light intensity increased, the rate of the light-dependent reaction, and therefore photosynthesis, increased. The highest correlations with disease levels were achieved for times when the intermittent sunshine was present (12 and 1 pm). The range of observed temperatures was greatest at 1 pm, the solar noon, time when stomata would normally be most active. At this time, the air temperature and the average wind speed were highest, very likely contributing to the result. With reappearance of clouds in the afternoon, the tree canopies started cooling,

and the temperature differences between the trees decreased, resulting in lower correlation coefficients. This coincided with a decrease of the wind speed, which probably led to a decrease in transpiration.

5.5 Discussion

The greenhouse experiments showed that the thermal camera, following calibration and a basic normalisation for background radiation, is capable of monitoring temporal temperature change in conifer tree foliage. A significant non-uniformity was found across the camera's field of view with differences exceeding 2°C in some cases. In thermography of plants, where differences in temperature are usually small, such non-uniformity, if left unaccounted for, might significantly affect the results when measurements originating from different pixels are compared. For ground-based applications, the relative temperature change within the same pixels may still be investigated, such as in Kim *et al.* (2016), providing pixel level sensor responses are linear in terms of emitted flux versus digitised flux over a range of desired temperatures, since the same error in the estimation of absolute temperature would persist. Following the non-uniformity correction, the spatial variation of canopy temperature was well characterised, showing that thermal imagery can provide a reliable means for thermal analysis of conifers. Nevertheless, it was not possible to fully determine the accuracy of retrieval of absolute canopy temperature values, as the readings for one of the experiments marginally exceeded the typical type K thermocouple accuracy threshold of ± 2.2°C. A high uncertainty was introduced into thermocouple measurements, preventing absolute validation of the camera readings. Due to foliage type, to avoid causing mechanical damage, the thermocouples were not firmly attached to needles, and instead, they were wrapped inside needle clumps. It is therefore likely that the thermocouple measurements were not only affected by the needle surface temperature, but also, to some degree, by the surrounding air temperature. Nevertheless, even though absolute temperature values could not be fully ascertained, the background correction did normalise the camera readings over time. The differences between all thermocouples and image values were relatively stable throughout the experiments (exhibiting standard deviation of temperature offsets of 0.20°C in the first experiment and 0.32°C in the second experiment). The camera effectively monitored the temperature trend over time for all thermocouple locations, and recorded temperature differences between the different locations. The canopy temperature could otherwise be measured using thermo-radiometers. However, these return an aggregation of temperature measurements for an area, the extent of which depends on the view angle and

distance from the canopy (Gomez-Candon *et al.*, 2016); in this study, point measurement was more appropriate for validation of the intra-crown temperature variation.

For a more accurate correction of the background radiation, at least two different calibration targets of known emissivity and surface temperature would have to be utilised. With temperature readings from at least two targets (ideally colder and hotter than the measured object, i.e. plants) radiometric calibration coefficients could be calculated based on a linear regression, which would allow brightness temperature (as measured by the camera) to be related to the actual surface temperature. Initially a diamond diffusion foil was utilised as the second target, which proved infeasible due to strong directional dependence of its emissivity. In a UAV survey setting, the same approach based on an empirical line correction can be used, with at least three contrasting ground targets, whose temperatures are continuously being monitored. Inclusion of a third target not only provides redundancy, but also allows assessment of the quality of fit between recorded and actual temperatures. To retrieve the calibration coefficients, the deployed targets would normally be imaged at the beginning and the end of the survey (Santesteban *et al.*, 2017), although additional mid-flight calibrations (Gomez-Candon *et al.*, 2016) may be preferred on longer flights or if weather conditions are rapidly changing. Using the empirical line calibration method, Gomez-Candon *et al.* (2016) reported R^2 value of 0.768 in linear regression of apple tree canopy temperature measurements from calibrated thermal imagery and from radio-thermometers positioned 1.2 m above top of the tops of the canopies. Alternatively, surface temperatures may be obtained using radiative transfer equation, such as MODTRAN (Berk *et al.*, 1999), as demonstrated by Berni *et al.* (2009b), who observed a reduction in RMSE of target temperature measurements from 3.44K to 0.89K following the correction.

Within the greenhouse experiment, spatio-temporal analysis of the imagery provided an insight into thermal properties of the plants. In parts of the canopy characterised by very low volume the temperature was considerably higher. The higher temperature in the areas of scarce foliage is likely to have been caused by inclusion of mixed pixels, containing readings from both the canopy and background. Those areas could also potentially have closed stomata as a result of increased insulation and transpiration, leading to an increase in temperature. Potentially, larger proportion of trunk pixels also had an influence on the retrieved mean temperature; Kim *et al.* (2016) showed there is a consistent difference between leaves and trunks in ponderosa pines, especially during the afternoon, with the latter being warmer. After exclusion of the areas with minimal foliage, very mild stress

did not exhibit itself, despite drastic changes in ambient temperature and radiance levels; the temperature readings for both the stressed and control plant were closely related throughout the whole test (experiment 2). However, with higher stress levels (experiment 1), there was a clear distinction between the two plants, which then doubled after the additional light source was turned on. The observed increase in temperature as a response to plant water stress is in accordance with many previous studies (Jackson *et al.*, 1981; Grant *et al.*, 2010; Gonzalez-Dugo *et al.*, 2012). An increase in tree crown temperature was also observed in the investigated pines with increasing disease severity. Statistically significant positive correlations were found for most data acquisitions (R in the range of 0.52 to 0.64). This temperature increase can be related to the needle damage symptoms caused by the disease, i.e. loss of cellular integrity, necrosis, and eventual desiccation (Stone *et al.*, 2003). A significant correlation between the leaf water content of the Scots pine trees and the disease level was found (-0.861 at p<0.001, as shown in Chapter 3). Leaf-level studies reported an increase in temperature of the infected foliage, coinciding with the appearance of chlorotic and necrotic tissues (Chaerle *et al.*, 1999b; Lindenthal *et al.*, 2005). At a larger scale, elevated surface temperature were detected in spruce forest decayed under bark beetle (Hais and Kučera, 2008) and in olive tree crowns affected by *Verticillium* wilt (Calderón *et al.*, 2013).

The variations in canopy temperature are highly dependent on environmental factors. In a ponderosa pine forest, the thermal dynamics were shown to be mainly controlled by air temperature, water vapour and radiation (Kim *et al.*, 2016). Here, similarly, the increase in canopy temperature was dictated by the increased radiation levels and ambient temperature. In the greenhouse experiment, it was also observed that the plants warmed up in different manners – the moderately stressed plant fairly uniformly, whilst the control canopy exhibited lower levels of temperature change in its lower canopy. From the physiological point of view, the increase in temperature difference between the two trees would be caused by the different response of the plants to the additional radiation. A stressed plant would have its stomata closed to prevent the loss of water through transpiration, also preventing the entry of carbon dioxide into the leaves and disrupting the photosynthesis (Jones, 1999). This could explain the observed fairly uniform increase in temperature across the canopy, appearing to be mostly dependent on the change in ambient temperature. In contrast, with random distribution of foliage in a control canopy, the leaf response may vary depending on their shade history – some leaves upon illumination will have their stomata open, others after some time of illumination may still keep their stomata closed (Fereres *et al.*, 2003; Gonzalez-Dugo *et al.*, 2012).

In the case of UAV-borne survey, the differences between differently diseased trees were most accentuated at the time of solar noon (correlation of 0.64 and temperature range of 3.38°C), when the radiation levels were highest. At this time, the air temperature and the average wind speed were greatest, and thus very likely contributed to the result. It was therefore concluded UAV-borne thermal surveys investigating tree stress should be performed at the time of maximum evaporative demand. Maximum evaporative demand is normally expected to occur in the early afternoon (Phillips *et al.*, 1997), when air temperatures are driven by peak radiation. However, other environmental factors, such as humidity or wind speed, have also been shown to also affect the evaporative demand, and consequently temperature at a canopy level (Leinonen *et al.*, 2006). The question remains how they may influence the ability to distinguish stressed plants, in particular in countries with moderate air temperatures year-round, such as Scotland. Such guidance might help with planning UAV-borne campaigns utilising low-cost sensors, by identification of best acquisition times, when temperature differences between plants are expected to be greatest.

The standard deviation of the crown temperature was suggested to be an indicator of stress by some (Fuchs, 1990; Gonzalez-Dugo *et al.*, 2012). Fuchs (1990) on a simulated cotton canopy demonstrated that water stress, apart from increasing crown temperature, widens the range of temperature variation within the canopy. This is due to leaf orientation playing a great role in the energy budget, especially when stomata are closed. In more stressed canopies greater variation in temperatures may be detected due to the change in leaf angle resulting from wilting. Gonzalez-Dugo *et al.* (2012) observed that the variability of canopy temperature increased during the early stages of water stress, and diminished when the stress became more severe. No such trend was observed within the greenhouse study; with mild stress, there was no difference between the trees, whilst with the onset of moderate stress, the control plant exhibited minimally higher intra-crown temperature variability. As this indicator is attributed to the change in leaf orientation upon onset of stress, the effect on conifers is expected be none or very minimal. In grapevines, the intra-crown variations in temperature were not impacted by water status either, a supposed effect of the non-random distribution of leaf angles in the canopies (Grant *et al.*, 2007; Moller *et al.*, 2007). However, in the UAV-borne survey, the standard deviation of the crown temperature exhibited weak, but significant correlation (R = 0.330-0.360) with the estimated disease levels for four of the data acquisitions. This could potentially be caused by the effect of diseased foliage on the canopy's temperature heterogeneity. Most foliar, stem and root diseases alter the water relations of plants

causing water deficit, which results from accelerated water loss (various foliar diseases), disruptions of transpiration (vascular wilt diseases) or damage to the root system (soil-borne diseases) (Burdon, 1987). At leaf level, the development of visual infection symptoms is generally accompanied by a change in surface temperature. Diseases causing an increased water loss due to processes such as cuticle damage or changes in underlying leaf cell membrane permeability, have been found to lead to temperature decrease in the affected parts, whilst temperature increase was reported for diseases causing stomatal closure as a result of decreased xylem water flow or the release of certain closure-inducing chemicals (Chaerle *et al.*, 1999b; Chaerle and Van Der Straeten, 2000; Chaerle *et al.*, 2004; Lindenthal *et al.*, 2005; Berdugo *et al.*, 2014; Prashar and Jones, 2014). For instance, localised hot spots at the sites of infection, which resulted in increased heterogeneity of the temperature distribution, were reported on leaves affected by such diseases as powdery mildew (Berdugo *et al.*, 2014), downy mildew (Lindenthal *et al.*, 2005) and tobacco mosaic virus (Chaerle *et al.*, 2004). The main limitation of using the standard deviation as an indicator is that the variation in canopy temperature is affected by external conditions. During both experiments shown here, the standard deviation of canopy temperature varied through time. The larch trees exhibited a steep increase upon the turn on of additional light source. Similarly, the highest standard deviations of canopy temperature in the pine plantation were recorded at the time of highest radiation, suggesting this indicator could only allow for a relative comparison between trees investigated under same conditions. Gonzalez-Dugo *et al.* (2012) also recognised that the intra-crown temperature variability cannot be clearly compared without taking absolute canopy temperature into account.

The approaches presented for the direct investigation of canopy temperature can only be applied in a relative mode, comparing plants imaged under exactly the same conditions (in practice that means plants located within the same image). This is due to leaf and canopy temperature being dependent on air temperature, humidity, wind speed and absorbed net radiation (Jones and Schofield, 2008). Thermal stress indices have been most commonly used to overcome this problem, normalising the results for environmental variation, and allowing for multi-spatial and/or multi-temporal comparison. The most commonly used stress indices include the CTD (shown to be adversely affected by weather conditions (Maes and Steppe, 2012)), CWSI and Ig. CWSI and Ig have been shown not be influenced by the amount of incoming shortwave radiation and vapour pressure deficit; however, they are affected by air temperature and wind speed (Maes and Steppe, 2012). Optimal conditions, based on modelled discriminative power, for

application of those indices include high air temperature, incoming shortwave radiation and vapour pressure deficit and low wind speed (Maes and Steppe, 2012).

It was hypothesised that the inclusion of Lidar metrics in the analysis could account for structural differences between trees and improve the observed relationship. Furthermore, as one of red band needle blight's symptoms is defoliation, structural metrics could potentially detect the differences in the amount of lost foliage. However, only a slight improvement (between +0.9% and +3.49%) was observed when height percentiles and kurtosis were included in the partial least squares regression. The defoliation within the plot was minimal and the uncompacted live crown ratio varied between 77 and 100%, and may therefore be undetectable with Lidar.

A key limitation in the UAV-borne survey is lack of healthy trees within the plantation plot. Since all of the trees are to some degree stressed, they do not photosynthesise to their full potential, and the functioning of their stomata is hampered. Inclusion of healthy trees in a survey, such as this one, could therefore provide a better baseline for comparison. The use of the top height the disease has reached to estimate the percentage of the suppressed tree crown does give an indication of the infection level. However, it is not an ideal metric, as the disease can spread in a non-uniform manner within a tree crown, and with different intensities. This could be one of the reasons for a wide scatter of measurements within the dataset. Nevertheless, this study shows that there is an identifiable difference in thermal response between the trees with different infection levels, which is most evident at high solar radiation levels. The applications of thermography have been limited due to restricted medium-resolution satellite sensors, providing pixel resolutions of 90-120 m, being only suitable for regional scales. Airborne thermography provides spatial resolutions that allows the detection of isolated tree crowns, but the surveys are normally expensive and logistically complex. The use of miniature thermal cameras on UAV platforms is a new alternative, offering very high resolution (sub-metre) imagery at a fraction of the cost, allowing not only for extraction of individual crown temperatures, but also for investigation of the inter-crown temperature variability.

5.6 Chapter summary

With the development of UAVs, high spatial resolution data has become more accessible than ever before. Furthermore, UAVs can help in bridging the gap between ground surveys and other more traditional remote sensing platforms. However, their main constraint is the limited payload they offer, requiring the use of miniature sensors. This

study investigated whether a low-cost miniature thermal camera, destined to be used on a UAV platform, is capable of providing reliable canopy temperature measurements of conifers. The greenhouse experiments showed that the thermal camera, following a basic normalisation for background radiation, is capable of monitoring both the spatial and temporal variation of canopy temperature. The thermal imagery can, therefore, provide a reliable way for relative thermal analysis of plants, despite not retrieving absolute canopy temperature values. Furthermore, there was a clear distinction in canopy temperature between the investigated healthy and the moderately stressed tree, showing the potential of low-cost thermography for investigating stress in conifers. An increase in tree crown temperature was also observed in the investigated pines with increasing disease severity, with statistically significant correlations found for most data acquisitions. However, a change in environmental conditions altered the magnitude of the observed responses. Rising radiation level and ambient temperature led to an increase in the difference between the average canopy temperatures in the terrestrial analysis, whilst in the UAV-borne test the strongest correlations were observed at times with high solar radiation levels. The performance of thermography when applied to conifer stress investigation may therefore depend on environmental conditions under which the data is acquired. Research in a fully controlled environment could quantify the influence of different environmental factors, and define conditions under which thermal imagery can be used most effectively in different climates. Such guidance might help with planning UAV-borne campaigns utilising low-cost sensors by identification of best acquisition times, when temperature differences between plants are expected to be greatest.

Chapter 6. Hyperspectral analysis of stress at leaf level

6.1 Chapter overview

This chapter investigates spectral characteristics of pine foliage affected by red band needle blight. Leaf-level spectroscopic data obtained from green and partially chlorotic needles are used to identify best spectral regions for detecting the infection. Three approaches for spectra analysis were investigated: spectral indices, derivative metrics and continuum removal analysis. The results informed airborne hyperspectral analysis of diseased pine plantation sites (Chapter 7).

6.2 Introduction

Vegetation has distinctive spectral properties, which are primarily controlled by scattering and absorption characteristics of the leaf internal structure and biochemical components, such as photosynthetic pigments, nitrogen, water, cellulose and lignin (Govender *et al.*, 2009). Much research has been done on relating the leaf reflectance with photosynthetic pigments (Curran *et al.*, 1990; Blackburn, 1998a; Zarco-Tejada *et al.*, 2001; Sims and Gamon, 2002) and water status (Peñuelas *et al.*, 1993; Datt, 1998; Ceccato *et al.*, 2001; Curran *et al.*, 2001), which can provide an indication of the physiological status of plants. The variations in the visible and near-infrared region of the electromagnetic spectrum are mainly used to detect changes in the condition of vegetation, especially to evaluate alterations in photosynthetic activity of plants and in pigments concentrations (Vogelmann *et al.*, 1993; Penuelas and Filella, 1998; Leckie *et al.*, 2004; Zarco-Tejada *et al.*, 2009; Behmann *et al.*, 2014). In particular the red-edge region (690 − 740 nm) was found to provide early indications of plant stress or disease onset (Penuelas and Filella, 1998; Wilson *et al.*, 1998; Carter and Knapp, 2001; Stone *et al.*, 2001). Changes in leaf water content, especially related to stress caused by drought, would normally be detected utilising the shortwave infrared region (Ceccato *et al.*, 2002; Fensholt and Sandholt, 2003; Eitel *et al.*, 2006; de Jong *et al.*, 2012).

Red band needle blight infection usually starts in the lower parts of the tree on older foliage and spreads upward. Early symptoms consist of small chlorotic lesions on needles, which (if conditions are appropriate for the fungus) enlarge and turn reddish or brown-reddish. The tissue distal to the lesion then desiccates, progressively turning pale green to tan or brown. The complex series of damage symptoms, which occur as the disease progresses involves initial chlorosis, production of red and brown metabolites, rapid loss of cellular integrity, cellular necrosis, and eventual desiccation (Stone *et al.*,

2003). The amount of damage caused by red band needle blight is usually assessed based on the visual estimate of these symptoms.

Stone *et al.* (2003) investigated spectral properties of Monterey pine (*Pinus radiata*) needles infected by red band needle blight (divided into five damage categories) over the visible and near-infrared wavelength region (400–1000 nm). Even though they found the shoulder of the near-infrared region near 760 nm to yield the greatest difference in reflectance, the most sensitive wavelengths were observed in the 680–690 nm region, followed by wavelengths near 760 and 550 nm. The reflectance indices which were shown to best correlate with needle damage were a simple ratio 709/691 nm (r = − 0.739, p < 0.001) and an index based on the upper slope of the red edge (r = − 0.730, p < 0.001). Based on this study, Coops *et al.* (2003) utilised the red-edge region of electromagnetic spectrum for detecting red band needle blight infection severity in a Monterey pine plantation located in Australia using airborne hyperspectral imagery. Three indices showed significant correlations with disease severity scores: the lower and upper slope of the red-edge and Red-edge Vegetation Stress Index (RVSI), among which the upper slope of the red-edge showed highest discriminating power. With the use of "halo" sampling approach (which ignored each tree crown's brightest central pixels), they could successfully detect three severity levels of infection with an accuracy of over 70%.

There have been no further studies examining the spectral characteristics of foliage affected by red band needle blight, nor the transferability of the aforementioned methods to other species of pines or other climatic zones. The changes in shape of the spectrum, which can be characterised using derivative or continuum removal analysis, and their potential diagnostic power have not been explored either. The aim of this chapter is to identify best spectral regions and methods for detecting red band needle blight infection. For this purpose, three approaches for spectra analysis were investigated: spectral indices, derivative indices and derivative analysis. The results were used to inform airborne hyperspectral analysis covered in Chapter 7.

6.3 Common techniques for spectrum analysis

6.3.1 Spectral indices

Spectral vegetation indices are mathematical combinations of two or more different spectral bands designed to enhance the vegetation properties and to overcome the spectrum variability introduced by e.g. atmospheric conditions. They have been widely used to retrieve various forest biophysical parameters such as chlorophyll content. Vegetation indices, most commonly, utilise bands in the red and NIR region of the electromagnetic spectrum, corresponding to the chlorophyll absorption well and the region of higher reflectance caused by intracellular scattering (NIR). Such band placement allows detection of the red-edge feature of vegetation spectra. Indices combining those bands are usually related to biomass, canopy structure, and LAI. Among them, by far the most well-known and widely used is NDVI (Tucker, 1979), which has been employed to e.g. retrieve various vegetation parameters such as LAI (Law and Waring, 1994; Cohen *et al.*, 2003; Wang *et al.*, 2005), detect defoliation (Adelabu *et al.*, 2014; Olsson *et al.*, 2016), investigate the responses of vegetation to regional and global climate change (Piao *et al.*, 2006; Shen *et al.*, 2014) or to monitor plant phenology (Reed *et al.*, 1994; Jeganathan *et al.*, 2014). The wavelengths neighbouring the red absorption maximum would usually be used for chlorophyll retrieval (le Maire *et al.*, 2004), whilst indices based on green band were found to be indicators of active chlorophyll production, which is related to the leaf nitrogen concentration (Gitelson *et al.*, 1996a; Lelong *et al.*, 2008). Bands in the visible range have also been used to study short-term changes in photosynthetic efficiency, e.g. with Photochemical Reflectance Index (PRI) (Gamon *et al.*, 1992). PRI is sensitive to the epoxidation state of the xanthophyll cycle pigments and to photosynthetic efficiency, serving as an indicator of water stress (Peguero-Pina *et al.*, 2008; Zarco-Tejada *et al.*, 2009), whilst indices including bands in the MIR and SWIR region of the spectrum were shown to be sensitive to water content in plant tissues (Govender *et al.*, 2009).

6.3.2 Derivative analysis

A spectral derivative shows the rate of a spectrum's change relative to the wavelength. As it does not depend on the magnitude of the signal, it allows the analysis of spectrum's shape and rapid identification of inflection points, as well as reflectance minima and maxima (Tsai and Philpot, 1998). Furthermore, derivatives have been considered effective in compressing the effect of illumination variations (Tsai and Philpot, 1998), differentiating overlapping signatures and reducing background noise (Demetriades-Shah *et al.*, 1990). The second order derivative was found to be especially useful in eliminating the soil background, under the assumption of the spectral reflectance of most soils being an approximately linear function of wavelength (Demetriades-Shah *et al.*, 1990).

First and second order derivative spectra can be computed using a finite divided difference approximation algorithm with a finite band separation as follows (Tsai and Philpot, 1998):

$$\rho'(\lambda_i) = \frac{\rho(\lambda_{i+1}) - \rho(\lambda_{i-1})}{\Delta\lambda} \tag{6.1}$$

$$\rho''(\lambda_i) = \frac{\rho'(\lambda_{i+1}) - \rho'(\lambda_{i-1})}{\Delta\lambda} = \frac{\rho(\lambda_{i+1}) - 2\rho(\lambda_i) + \rho(\lambda_{i-1})}{\Delta\lambda^2} \tag{6.2}$$

where ρ is reflectance, ρ' and p'' are first and second derivatives, λ is wavelength and $\Delta\lambda$ is wavelength interval between λ_{i+1} and λ_{i-1}. Spectral derivatives are sensitive to the signal-to-noise ratio of hyperspectral data; minimising random noise e.g. through spectral smoothing is therefore imperative for meaningful analysis (Tsai and Philpot, 1998). Progressive differentiation will increase the sensitivity to the noise and other small variations in the reflectance spectra. Lower order spectral derivatives, being less susceptible, are therefore considered more suitable for operational remote sensing (Cloutis, 1996).

Derivative analysis in remote sensing of vegetation is most commonly used to investigate the movements in the position of the red-edge (identified as the location of the maximum first derivative spectrum). The shift in the red-edge position has been associated with a range of factors, such as chlorophyll concentrations (Curran *et al.*, 1990; Filella and Penuelas, 1994; Gitelson *et al.*, 1996b; Blackburn, 1998a), foliar nitrogen (Mutanga and Skidmore, 2007; Liu *et al.*, 2011) and LAI (Filella and Penuelas, 1994; Danson and Plummer, 1995; Ruiliang *et al.*, 2003). A range of other features related to vegetation parameters have also been identified from derivatives, such as the amplitude, area and

slope of the red-edge (Filella and Penuelas, 1994; Mutanga and Skidmore, 2007) or characteristics of the green reflectance peak (Penuelas *et al.*, 1994; Shaw *et al.*, 1998).

6.3.3 Continuum removal

Continuum removal (CR) is a reflectance spectrum normalisation method, which allows isolation and comparison of individual absorption features, emphasising their location and depth. The continuum is an estimate of the absorption present in the spectrum due to other processes. Typically, the continuum line is an upper convex hull (envelope) connecting the spectrum's local maxima (Figure 6.1); it represents the background absorption onto which other absorption features are superimposed.
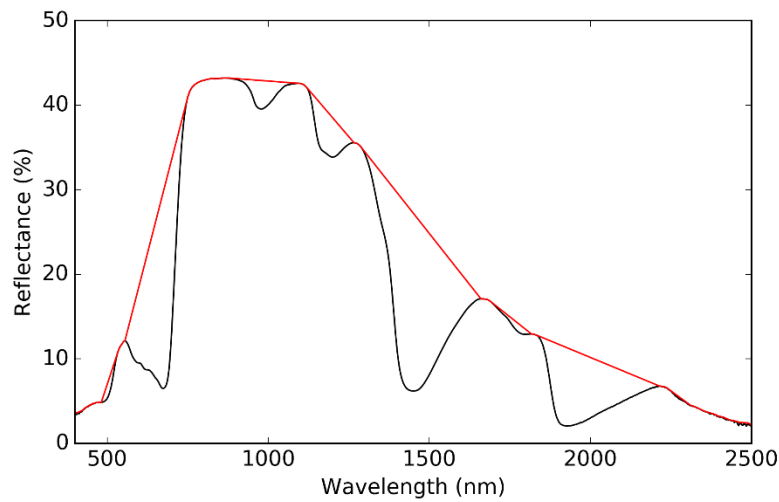
Figure 6.1: Continuum line (red) of an example vegetation spectrum.

The continuum-removed spectra are then derived through division of the original reflectance value for each waveband in the absorption feature by the corresponding values of the continuum line (Clark and Roush, 1984):

$$CR_{(\lambda i)} = \frac{R_{(\lambda i)}}{R_{c(\lambda i)}} \tag{6.3}$$

where CR is continuum-removed reflectance value, R is original reflectance value, R_c is convex hull continuum line value and λ is wavelength. The band depth (BD) at each wavelength in the absorption feature can then be calculated from the continuum-removed reflectance by (Clark and Roush, 1984):

$$BD_{(\lambda i)} = 1 - CR_{(\lambda i)} \tag{6.4}$$

Several metrics can be extracted for each absorption feature to characterise its shape, such as the band centre position, depth, width, slope or area; the key features are shown in

Figure 6.2. The band centre position is the wavelength position of minimum adjusted reflectance of an absorption feature, whilst the absorption depth is the depth of feature minimum relative to the continuum line. The width is defined as the full width of the absorption feature at half the band depth, abbreviated as FWHD. The area of the absorption curve, as well as of the left and right wings can be calculated using an integral method:

$$A = \int_{\lambda_{start}}^{\lambda_{end}} CR_{(\lambda i)} \; ; \; AL = \int_{\lambda_{start}}^{\lambda_{BDmax}} CR_{(\lambda i)} \; ; \; AR = \int_{\lambda_{BD_{max}}}^{\lambda_{end}} CR_{(\lambda i)} \qquad (6.5)$$

where: A is area of an absorption feature, AL and AR are areas of the left and right wings of an absorption feature, λ_{start} and λ_{end} are absorption feature's start and end points, λ_{BDmax} is position of an absorption feature's centre. Further to that, the symmetry and slope of an absorption feature can be calculated with:

$$S = \frac{AL}{AR} \; ; \; K = \frac{R_{(\lambda end)} - R_{(\lambda start)}}{\lambda_{end} - \lambda_{start}} \qquad (6.6)$$

where S is symmetry of an absorption feature and K is slope of an absorption feature. A further normalisation by scaling features to equal depth at the band centre can be performed to minimise the influences of residual atmosphere absorptions, soil background and leaf water content. The normalised band depth (NBD) can be calculated by dividing the band depth at each wavelength by the maximum band depth for that absorption feature (Kokaly and Clark, 1999):

$$NBD_{(\lambda i)} = \frac{BD_{(\lambda i)}}{BD_{max}} \qquad (6.7)$$

Continuum removal analysis of vegetation spectra has been used over the years to estimate concentrations of various foliar biochemicals (such as nitrogen, lignin, cellulose or chlorophyll) through investigation of the plant absorption features (Kokaly and Clark, 1999; Curran *et al.*, 2001; Malenovsky *et al.*, 2006; Malenovsky *et al.*, 2013). It has also been utilised to discriminate vegetation types in different environments (Kokaly *et al.*, 2003; Schmidt and Skidmore, 2003; Buchhorn *et al.*, 2013) and, in recent years, to investigate plants responses to stress (Sanches *et al.*, 2014; Niemann *et al.*, 2015; Gotze *et al.*, 2016; Lugassi *et al.*, 2017). The 680nm chlorophyll absorption feature was used by Sanches *et al.* (2014) to detect stressed grass and soybean plants, and by Niemann *et al.* (2015) for separation of trees in three stages of bark beetle attack (i.e. healthy, pre-visual green and red attack). Gotze *et al.* (2016) found the band depth at continuum removal spectrum at 1725nm to show a significant relationship with heavy metal load, whilst

Lugassi *et al.* (2017) used the water absorption feature centred at 1940nm to predict chlorine content in crop leaves.
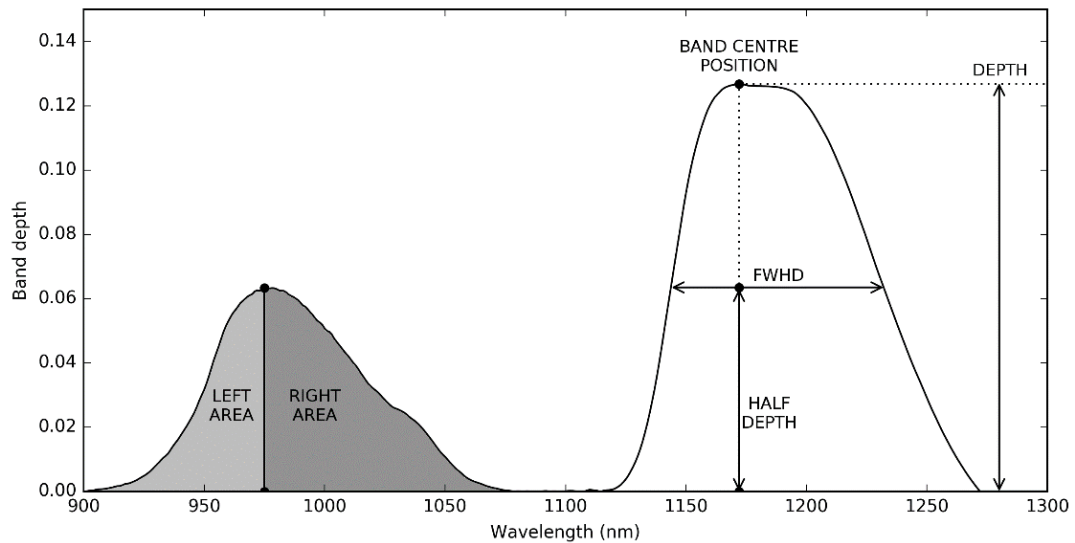
Figure 6.2: The illustration of commonly retrieved continuum removal metrics: left area, right area, band centre positions, depth and full-width half-depth (FWHD).

6.4 Experiment design

Upper and lower canopy of surveyed trees in plot A were destructively sampled to perform spectral measurements. Sampled twigs from fully-sunlit branches were chosen in a random manner, whilst homogenisation was achieved by combining needles from different twigs for each sample. In total 40 samples were collected from 20 trees with disease level ranging from 25 to 80% (mean = 59%). The foliage samples from the upper canopy parts predominantly constituted of green needles, whilst samples from lower parts were composed of a mixture of green and partially discoloured needles. The procedures for spectral reflectance measurements of the acquired spectra are provided in Chapter 3 Section 6.1.

6.5 Spectra processing

Prior to analysis, all measured spectra were calibrated for true reflectance of the white panel (%R = radiance from sample / radiance from reference panel x 100), and smoothed using the Savitzky-Golay Spline method (Savitzky and Golay, 1964) with a window size of 10 band separations. Sensitivity analysis in the VIS to SWIR regions was performed to identify wavelengths most responsive to differences between the samples collected from the upper and lower (partially chlorotic) canopy parts. A reflectance difference curve (Carter, 1991) was computed by subtracting the mean reflectance obtained from the lower

canopy samples from the mean of the upper canopy spectra. A relative change in reflectance was then calculated by dividing this difference by the mean reflectance of the upper canopy. The nonparametric Mann-Whitney U test was performed at each spectral channel to compare the between class differences in spectral response.

To investigate the shape of the spectra the first and second order derivatives were calculated using a finite divided difference approximation algorithm. The maxima and minima in first order derivative represent inflection points of slopes in the spectra. Reflectance peaks are represented by a negative value in the second derivative, whilst absorption troughs yield a positive value (Hugenin and Jones, 1986). The amplitudes and wavelength positions of potential diagnostic features, i.e. peaks and troughs, were extracted for each order. Boxplots were produced for the features extracted from the upper and lower canopy spectra to examine their variation between samples. The Mann-Whitney U (MWU) test was applied to the potential derivative spectra diagnostic features to assess the separability of the upper and lower canopy parts. Discriminant function analysis was used to identify derivative variables best highlighting differences between the top and bottom parts of the canopy, with features that did not show significant separation between group means excluded. Wilks's lambda parameter values, provided by the analysis, indicate the importance of the independent variable to the discriminant function - the smaller the value, the higher the importance.

Continuum analysis was also performed to investigate variation in the shapes of the absorption features. Based on the derivative analysis, four absorption features were selected, centred near 500, 680, 980 and 1170 nm. The end points used to derive the continuum lines, summarised in Table 6.1, were chosen such that the whole feature of interest was included. The continuum-removed reflectance and the band depth were then computed for each point within the absorption features. Metrics extracted for each absorption feature included the band centre, depth, total area, left and right area, absorption feature symmetry, slope and FWHD. The Mann-Whitney U test was used to compare the band-depth spectra on a band to band basis and assess separability of the continuum removal metrics.

Table 6.1: Continua end points of the absorption features used in this study with average locations of band centres calculated from the upper and lower canopy parts.

Absorption feature (nm)	Continuum line start (nm)	Band centre (nm)	Continuum line end (nm)
500	450	498	550
680	550	677	750
980	900	978	1100
1170	1100	1175	1280

To fully utilise the availability of hyperspectral data in narrow spectral channels, band ratios and normalised difference indices for each band combination between 450 and 2500 nm were computed (giving a total 4 204 550 narrow band pairs), including a number of commonly used indices shown in Table 6.2. Average values of the derived indices were used to calculate the absolute difference between the upper and lower canopy. The Mann-Whitney U test was then used to assess the separability of the upper and lower canopy parts at each band combination, restricting further investigation to indices showing significance at 0.05 confidence level. Discriminant function analysis with leave-one-out cross-validation method was utilised to help identify best indices. Further to that, a number of other commonly used indices were computed and tested; these are summarised in Table 6.3. All possible band combinations were examined for each index.

The best performing metrics were used to check if presymptomatic detection of the disease in needles is possible by comparing the measures retrieved for upper canopy with estimated tree disease levels. Processing of data shown in this chapter was performed in R (with help of *hsdar* package developed for management, analysis and simulation of hyperspectral data by Lehnert *et al.* (2016)). The *hsdar* package was used to retrieve CR and derivative spectra. Complementary packages were written to perform the sensitivity analysis, statistical testing and retrieval of CR and derivative metrics, as well as of spectral indices.

Table 6.2: Simple ratio and normalised difference vegetation indices tested in this study with formulation and authorship. R_λ is the reflectance at wavelength λ; G, R, NIR and SWIR are the reflectance for green, red, near-infrared and shortwave infrared bands, respectively.

Index	Equation	Reference
Green Normalised Difference Vegetative Index	GNDVI = (NIR − G)/(NIR + G)	(Gitelson *et al.*, 1996a)
Normalised Difference SWIR Index	NDSWIR = (839nm - 1693nm)/(839nm + 1693nm)	(Gerard *et al.*, 2003)
Normalised Difference Vegetation Index	NDVI = (NIR − R)/(NIR + R)	(Tucker, 1979)
Normalised Difference Water Index	NDWI = (NIR − SWIR)/(NIR + SWIR)	(Gao and Goetzt, 1995)
Normalised Green Red Difference Index	NGRDI = (G - R)/(G + R)	(Tucker, 1979)
Photochemical Reflectance Index	PRI = (570nm−531nm)/(570nm+531nm)	(Gamon *et al.*, 1997)
Simple ratio	SR = 800/675	(Jordan, 1969)
Water Index	WI = 900/970	(Penuelas *et al.*, 1996)
709/691	709/691	(Stone *et al.*, 2003)

Table 6.3: Commonly used vegetation indices tested in this study with formulation and authorship. R_λ is the reflectance at wavelength λ; B, R and NIR are the reflectance for blue, red, red edge and near-infrared bands, respectively.

Index	Equation	Reference
Disease water stress index	$DWSI = (R_{802}+R_{547})/(R_{1657}+R_{682})$	(Apan *et al.*, 2004)
Enhanced Vegetation Index	$EVI = 2.5[(NIR - R)/(NIR + 6*R - 7.5*B + 1)]$	(Huete *et al.*, 2002)
Enhanced Vegetation Index 2	$EVI2 = 2.5[(NIR - R)/(NIR + 2.4*R + 1)]$	(Jiang *et al.*, 2008)
Modified simple ratio	$mSR = (R_{800}/R_{670} -1)/(R_{800}/R_{670}+1)^{0.5}$	(Chen, 1996)
Modified Triangular Vegetation Index 1	$MTVI1 = 1.2(1.2*(R_{800}-R_{550})-2.5(R_{670}-R_{550}))$	(Haboudane *et al.*, 2004)
Modified Triangular Vegetation Index 2	$MTVI2 = 1.5\{[1.2(R_{800}-R_{550})-2.5(R_{670}-R_{550})]/$ $SQRT[(2*R_{800}+1)^2-(6*R_{800}-5*SQRT[R_{670}])-0.5]\}$	(Haboudane *et al.*, 2004)
Red-edge Stress Vegetation Index	$RVSI = (R_{718}+R_{748})/2-R_{733}$	(Merton, 1999)
Renormalised Difference Vegetation Index	$RDVI = (NIR-R)/(NIR+R)^{0.5}$	(Roujean and Breon, 1995)
Triangular Vegetation Index	$TVI = 0.5[120(R_{750}-R_{550})-200(R_{670}-R_{550})]$	(Broge and Leblanc, 2001)
WI/NDVI	WI/NDVI	(Penuelas *et al.*, 1997)

6.6 Spectra analysis

6.6.1 Sensitivity

The mean reflectance curves of the upper and lower canopy samples show a clear difference between the spectra (Figure 6.3). A general decrease of reflectance in the NIR region, and an increase in the SWIR region is present for the lower canopy spectra. Further to that an increase in red reflectance is observed. Mann-Whitney U test confirmed that the populations of the two classes were significantly different throughout the majority of the investigated spectral range that is between 520-566 nm, 616-930 nm, and 1378-2500 nm.
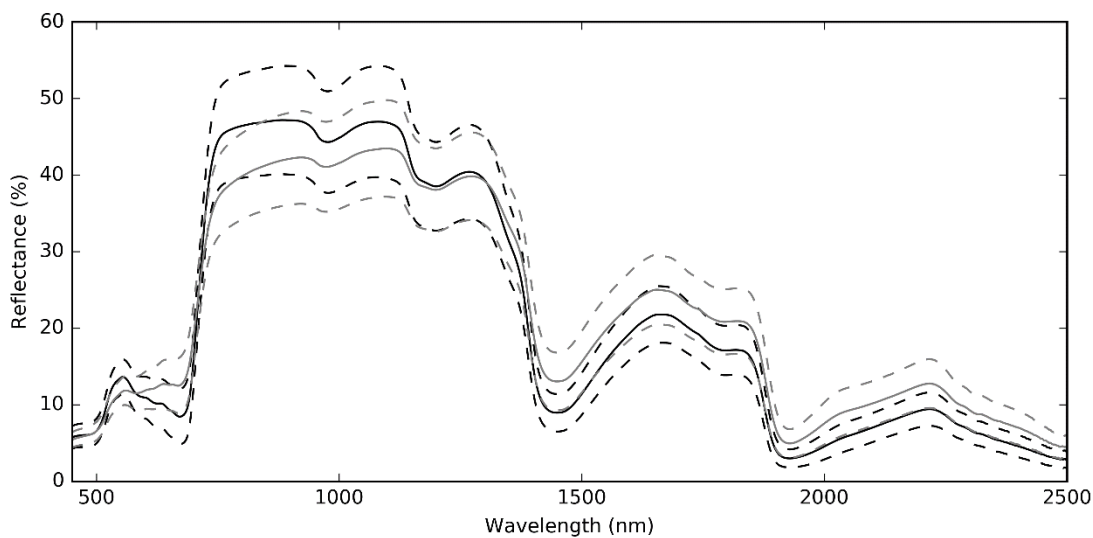
Figure 6.3: Mean reflectance spectra for the upper (black) and lower (grey) canopy parts. Dashed lines represent 1σ standard deviation.

The reflectance difference curve, presented in Figure 6.4, shows the magnitude of change in reflectance between the mean upper and lower canopy spectra. The largest difference occurred within the upper slope of the red edge; the local minimum of -7.5% was located at 756 nm. Other significant peaks occurred in the lower slope of the red edge (+4.6% at 689 nm) and in the green absorption region (-2% at 543 nm). In the SWIR region, the difference between spectra remained fairly consistent (mean = +3.2%, σ = 0.6%), with two minor peaks at 1403 nm (+4.6%) and 1870 nm (+4.3%).

The spectral curve representing the relative change in reflectance (Figure 6.4) shows regions with highest responsivity. In the VIS-NIR part of the spectrum, similar regions were shown to be sensitive; however, their relative importance differed. The highest relative change in reflectance was observed in the lower slope of the red edge (+50% at

680 nm). The local minima were located at 545 nm (-16.8%) and at 750 nm (-17.0%). In the SWIR region, two major local maxima were present in the water absorption features at 1450 nm (+45.8%) and at 1907 nm (+61.3%). Significant differences, increasing with the wavelength, were also observed in between the two peaks (relative change of around +20%) and past the second peak (relative change of around +35-50%).
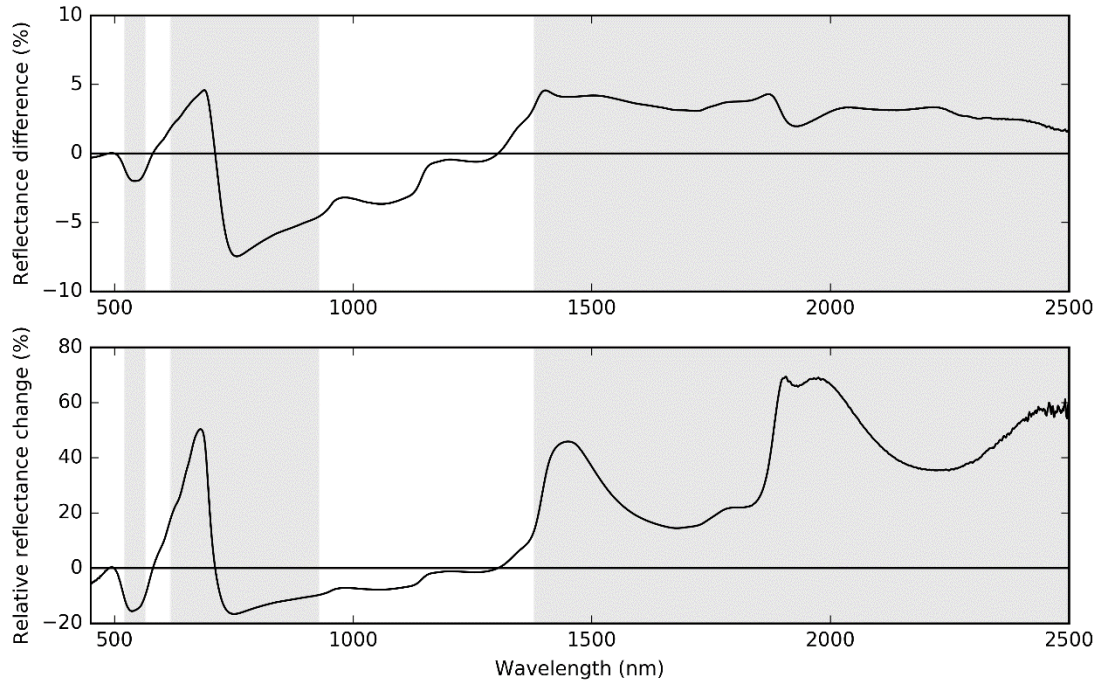
Figure 6.4: Absolute reflectance difference (top) and relative reflectance change (bottom) between the mean upper and lower canopy parts. Shaded regions represent wavelengths at which the two populations are significantly different according to Mann-Whitney U test at 0.05 confidence level.

6.6.2 Derivative analysis

The first and second order derivatives of the averaged spectra of upper and lower canopy samples are shown in Figure 6.5. The value at the red-edge inflection point (dRE, maximum value of the first derivative between 650 and 750 nm) is considerably higher for upper canopy parts, suggesting a steeper red-edge. Similarly, a more prominent peak in the first derivative corresponding to the slope of the green reflectance peak (dGE, around 525 nm) can be observed. Following this are negative values, which can be attributed to a decrease in the spectral reflectance between the green and red wavelengths (dG, 550 to 590 nm), with little change in reflectance exhibited by the lower part of the canopy. In the NIR and SWIR regions, four other inflection points attributed to water absorption features can be identified around 950 ($dNIR_{min(900:1000)}$), 1140

($dNIR_{min(1100:1200)}$), 1390 ($dSWIR_{min(1300:1500)}$) and 1880 nm. The magnitude at the first three of those features is visibly greater for upper canopy parts.

A peak in the second derivative between 670 and 700nm represents the minima of the red absorption feature (ddRE), whilst a trough in the region between 700 and 750 nm corresponds to the reflectance peak in the spectra at the start of the NIR region ($ddNIR_{min(650:750)}$). Both of those features are more distinctive in the upper canopy spectra. Further peaks and troughs attributed to the presence of water absorption features can be located between 1100 and 1200 nm ($ddNIR_{min(1100:1200)}$ and $ddNIR_{max(1100:1200)}$), 1300 and 1500 nm ($ddSWIR_{max}$), 1800 and 2000 nm, some of which are again more prominent in the upper canopy spectra. Furthermore, the green reflectance peak of vegetation can be identified in the second derivative by the presence of negative values in the 500 to 550 nm range, with a deeper trough evident for the upper canopy.

Based on the derivative spectra, fifteen features, described in Table 6.4, were selected for further analysis. The distribution of values of each of those features extracted for the upper and lower canopy parts are shown in Figure 6.6. Most of the first and second derivative variables showed to be significantly different between the groups (based on Mann-Whitney U test at 0.05 confidence level); the exceptions were $dSWIR_{min1300:1500}$ and $ddNIR_{min(1100:1200)}$. The REP appeared to be shifted towards shorter wavelengths in the lower canopy; such changes in the position of the red edge were found to be related with plant stress (Hoque and Hutzler, 1992; Carter and Knapp, 2001; Liu *et al.*, 2015). In this group the REP had a wider distribution, which could potentially be caused by a different degree of infection level in canopies. Mann-Whitney U test indicated that locations of the REP were marginally different between the lower and upper canopy parts (p=0.046). The location of the peak in the second derivative corresponding to the minima of the red absorption feature ($\lambda ddRE$) also showed a marginal significance (p = 0.041). A shift towards shorter wavelengths in the lower canopy part is evident, though an overlap in the confidence intervals of the groups is present. The only positional feature that differentiated well between the groups (p < 0.001), with was the location of the trough in the 1850-1950 nm region of the first derivative, with a shift towards longer wavelengths.
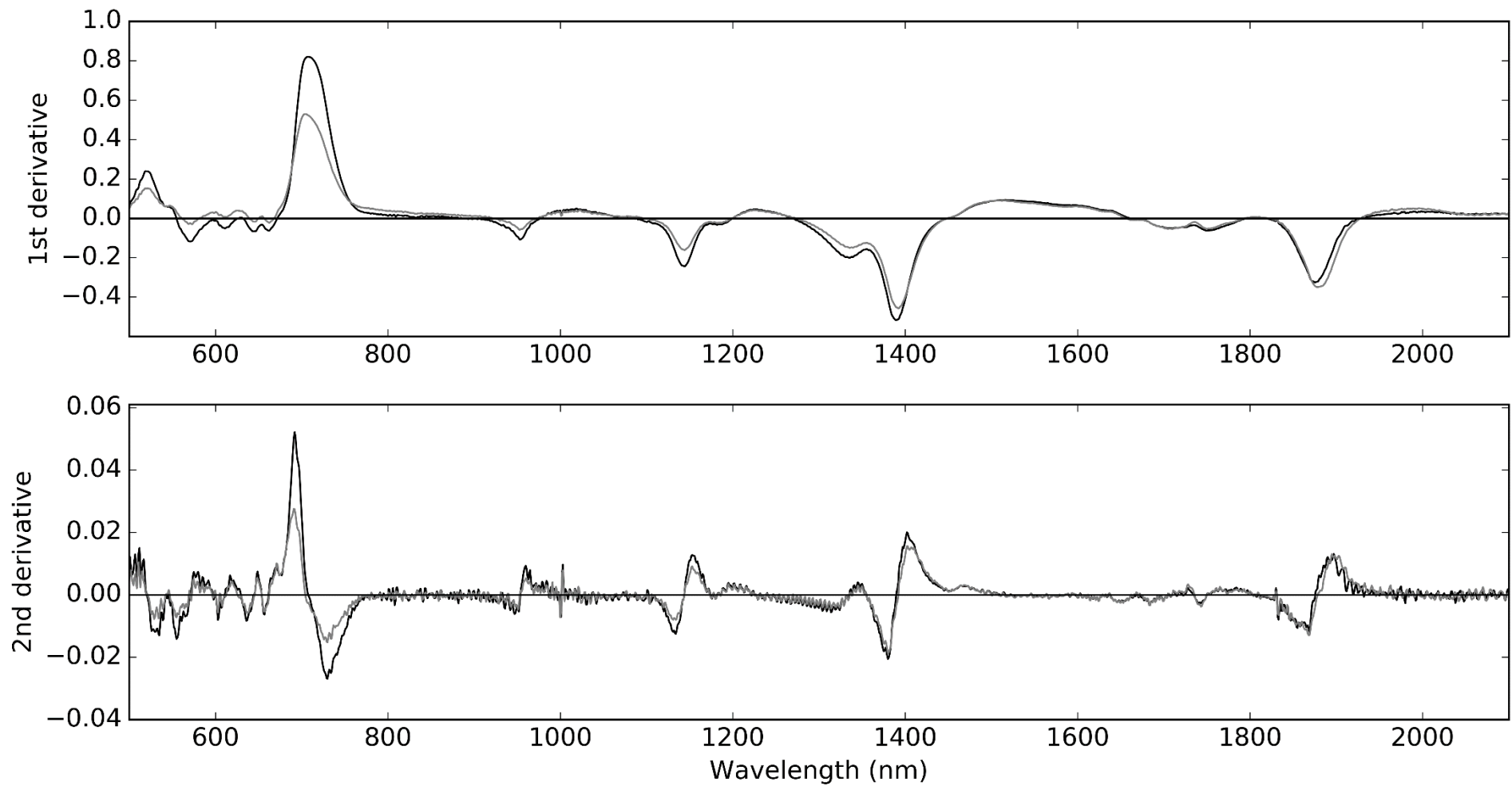
Figure 6.5: First and second order derivatives of averaged spectra for the upper (black) and lower (grey) canopy samples.
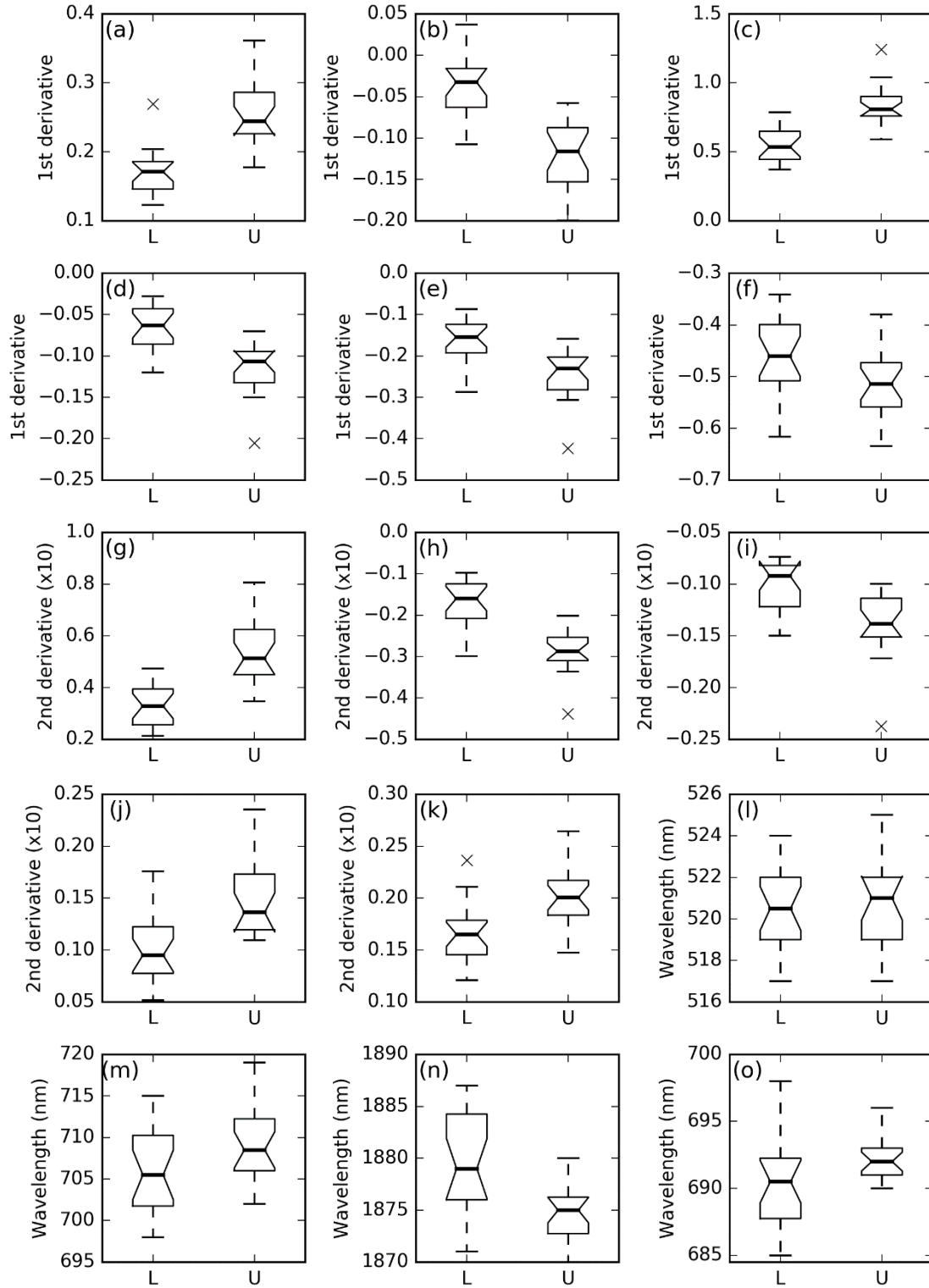
Figure 6.6: Box-and-whisker plots of the extracted derivative values and locations for lower (L) and upper (U) canopy parts: (a) dGE, (b) dG, (c) dRE, (d) $dNIR_{min(900:1000)}$, (e) $dNIR_{min(1100:1200)}$, (f) $dSWIR_{min(1300:1500)}$, (g) ddRE, (h) $ddNIR_{min(650:750)}$, (i) $ddNIR_{min(1100:1200)}$, (j) $ddNIR_{max(1100:1200)}$, (k) $ddSWIR_{max}$, (l) λdGE, (m) λdRE, (n) $\lambda ddSWIR_{min(1850:1950)}$ (o) $\lambda ddRE$. Outliers are shown as crosses, lines represent the 25th percentile, median and 75th percentile, whilst whiskers extend to a maximum of 1.5 times the interquartile range. Notches represent 95% confidence intervals about the median.

Table 6.4: Features extracted from the derivative spectra.

Feature	Order of derivative	Wavelength region	Description
dGE	1st	500-550	maximum derivative value
dG	1st	550-600	minimum derivative value
dRE	1st	650-750	maximum derivative value
$dNIR_{min(900:1000)}$	1st	900-1000	minimum derivative value
$dNIR_{min(1100:1200)}$	1st	1100-1200	minimum derivative value
$dSWIR_{min(1300:1500)}$	1st	1300-1500	minimum derivative value
ddRE	2nd	650-750	maximum derivative value
$ddNIR_{min(650:750)}$	2nd	650-750	minimum derivative value
$ddNIR_{min(1100:1200)}$	2nd	1100-1200	minimum derivative value
$ddNIR_{max(1100:1200)}$	2nd	1100-1200	maximum derivative value
$ddSWIR_{max}$	2nd	1300-1500	maximum derivative value
λdGE	1st	500-550	wavelength of dGE
λdRE	1st	650-750	wavelength of dRE
$\lambda dSWIR_{min(1850:1950)}$	1st	1850-1950	wavelength of minimum derivative value in 1850-1950 nm
$\lambda ddRE$	2nd	650-750	wavelength of ddRE

The features that did not show significant separation between group means ($dSWIR_{min(1300:1500)}$, $ddNIR_{min(1100:1200)}$ and λdGE) were excluded from the discriminant function analysis, whose outputs are summarised in Table 6.5. Wilks's lambda parameter values indicate the importance of the independent variable to the discriminant function - the smaller the value, the higher the importance. Derivative features located in the visible and the red edge region of the spectrum had the highest discriminative power (Wilks' Lambda values ranging from 0.437 to 0.482), with second derivative variables having slightly lower importance. A discriminant function based on all statistically significant features minimised the Wilk's Lambda value to 0.288, but also significantly worsened

the overall performance of the function (average accuracy of 80%) when compared to a single feature approach. Basing the analysis on five best features from the visible and the red edge region lowered the Wilk's Lambda value to 0.356, achieving overall accuracy of 85%.

Table 6.5: Tests of equality of group means with discriminant function analysis outputs. Function performance in terms of overall accuracy is assessed by Leave-one-out cross-validation (LOOCV) method. The structure matrix values of the discriminant functions (annotated here as variable loadings) indicate the relative importance of the predictor, showing the correlations of each variable with the given discriminant function. Dashes indicate variables excluded from the analysis.

Feature	Wilk's lambda	Sign.	Chi-square	LOOCV score	Variable loading	Variable loading
dGE	0.461	.000	29.030	90.0%	0.688	-0.804
dG	0.437	.000	31.019	90.0%	-0.722	0.844
dRE	0.453	.000	29.733	87.5%	0.700	-0.818
$dNIR_{min(900:1000)}$	0.558	.000	21.903	80.0%	-0.567	-
$dNIR_{min(1100:1200)}$	0.636	.000	16.955	75.0%	-0.481	-
ddRE	0.475	.000	27.922	85.0%	0.669	-0.782
$ddNIR_{min(650:750)}$	0.482	.000	27.375	82.5%	-0.660	0.771
$ddNIR_{max(1100:1200)}$	0.658	.000	15.694	67.5%	0.459	-
$ddSWIR_{max}$	0.704	.000	13.144	77.5%	0.412	-
λdRE	0.879	.028	4.823	57.5%	0.236	-
$\lambda dSWIR_{min(1850:1950)}$	0.672	.000	14.896	77.5%	-0.444	-
$\lambda ddRE$	0.938	.121	2.403	70.0%	-	-

Wilk's lambda:	0.288	0.356
Chi-square:	40.444	36.651
LOOCV score:	80.0%	85.0%

6.6.3 Continuum removal

The upper parts of the canopy exhibited consistently deeper band depths in all investigated absorption features (Figure 6.7). The most notable decrease of 34% in maximum band depth was recorded for the first NIR feature, followed by the chlorophyll absorption regions – decreases of 30% (450-550 nm) and 28% (550-750 nm) – and the second NIR feature with a decrease of 25%.

A significant difference in the band depth between the upper and lower canopy was present throughout most of the wavelengths; based on Mann-Whitney U test, performed on a band-to-band basis at 0.05 confidence level, measurements at the following spectral ranges were found to be significantly different: 454-528 nm, 553-744 nm, 912-1047 nm, and 1125-1258 nm.
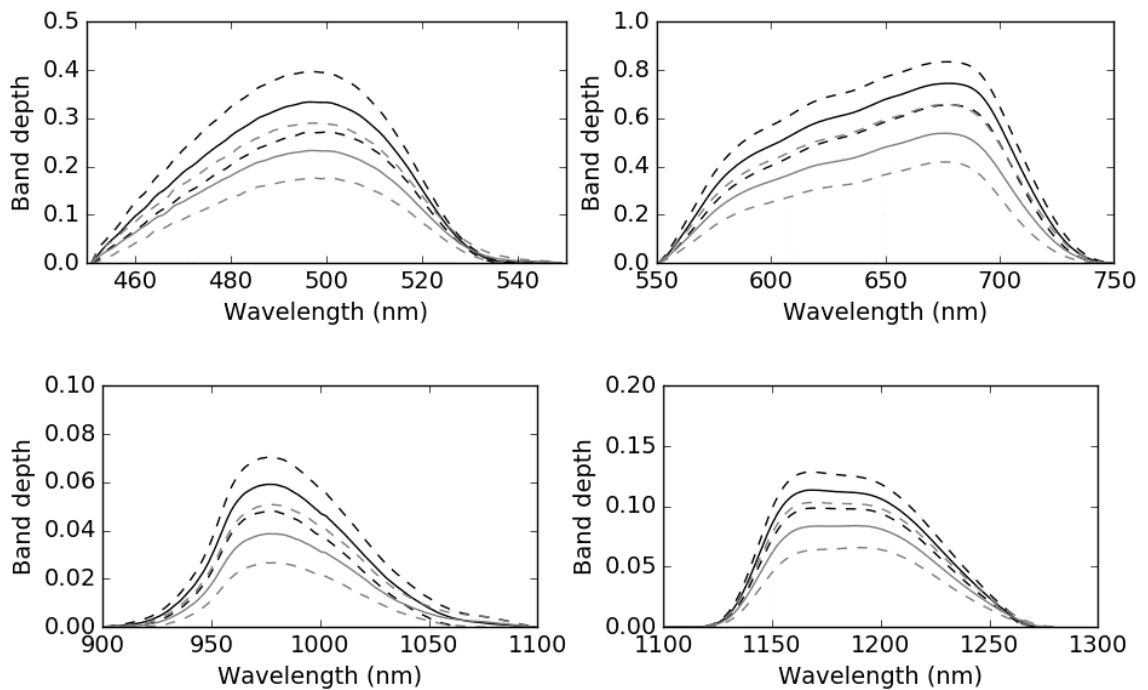
Figure 6.7: Mean band depth profiles of the chlorophyll (top: GE and RE) and NIR (bottom: NIR$_{min(900:1000)}$ and NIR$_{min(1100:1200)}$) absorption features for the upper (black) and lower (grey) canopy parts. Dashed lines represent 1σ standard deviation.

No changes in the symmetry or the width of features at half depth were observed. However, a number of other continuum removal metrics were found to be significantly different between the upper and lower canopy classes, such as the slope and absorption feature's area, which in here is directly related to the depth (Table 6.6 and Table 6.7). A 2-nm shift in the band centre towards shorter wavelengths was also detected for the lower canopy parts in the second chlorophyll absorption feature.

Table 6.6: Continuum removal metrics extracted for the 450-550 and 550-750 nm absorption features, combined with results of Mann-Whitney U test performed at 0.05 confidence level.

Metric	LOWER (450-550 nm)			UPPER (450-550 nm)			MWU test p value	LOWER (550-750 nm)			UPPER (550-750 nm)			MWU test p value
	mean	median	Std	mean	median	std		mean	median	std	mean	median	std	
Depth	0.235	0.232	0.059	0.336	0.338	0.065	<0.001	0.538	0.532	0.122	0.745	0.764	0.092	<0.001
Centre	497.35	497.00	2.519	498.00	498.00	1.92	0.293	675.95	676.00	1.43	677.65	677.50	1.60	0.002
Area	11.678	11.445	2.994	16.605	16.516	3.306	<0.001	61.271	56.889	15.866	88.120	90.315	13.228	<0.001
Left area	6.430	6.205	1.556	9.661	9.536	2.188	<0.001	43.542	41.021	11.103	63.149	65.381	9.777	<0.001
Right area	5.248	5.195	1.572	6.944	7.007	1.277	0.001	17.729	16.039	4.874	24.971	25.463	3.586	<0.001
Symmetry	0.579	0.590	0.037	0.555	0.548	0.042	0.030	0.711	0.711	0.014	0.716	0.719	0.010	0.213
FWHD	50.65	51.00	1.27	50.65	51.00	0.93	1.000	123.35	124.00	8.18	128.30	127.50	5.17	0.086
Slope	0.061	0.059	0.013	0.078	0.076	0.013	<0.001	0.127	0.128	0.023	0.154	0.148	0.026	0.002

Table 6.7: Continuum removal metrics extracted for the 900-1100 and 1100-1280 nm absorption features, combined with results of Mann-Whitney U test performed at 0.05 confidence level.

Metric	LOWER (900-1100 nm)			UPPER (900-1100 nm)			MWU test p value	LOWER (1100-1280 nm)			UPPER (1100-1280 nm)			MWU test p value
	mean	median	std	mean	median	std		mean	median	std	mean	median	std	
Depth	0.039	0.042	0.012	0.059	0.058	0.011	<0.001	0.085	0.087	0.019	0.114	0.113	0.015	<0.001
Centre	978.10	978.00	2.10	976.90	977.00	1.59	0.052	1179.20	1171.50	11.82	1170.75	1168.50	6.96	0.020
Area	2.888	2.859	1.011	4.421	4.346	0.997	<0.001	7.532	7.530	1.751	9.991	9.905	1.278	<0.001
Left area	1.116	1.159	0.403	1.724	1.709	0.367	<0.001	2.829	2.730	0.579	3.100	2.934	0.605	0.160
Right area	1.772	1.787	0.629	2.698	2.703	0.654	<0.001	4.703	4.945	1.782	6.891	6.901	1.279	<0.001
Symmetry	0.386	0.384	0.037	0.392	0.391	0.027	0.317	0.394	0.320	0.116	0.313	0.289	0.071	0.028
FWHD	69.10	69.50	3.61	70.10	70.00	2.63	0.478	88.20	88.00	2.59	88.10	88.00	1.52	0.774
Slope	0.007	0.007	0.005	-0.002	-0.002	0.005	<0.001	-0.020	-0.022	0.009	-0.036	-0.035	0.009	<0.001

Discriminant function analysis was performed on all significantly different continuum removal metrics; the summary of outputs is provided in Table 6.8. Among the best predictors in each absorption feature were band depths, ranging in Wilk's lambda value from 0.507 to 0.590. The absorption feature, which yielded highest discriminative power for its metrics was the second chlorophyll absorption feature, showing high importance of this region. Based on a single metric approach, the accuracies and the Wilk's lambda values were worse than those achieved by the derivate metrics. The overall accuracies ranged from 70% for the band centre of the second chlorophyll feature to 80% for slope of the first chlorophyll and the NIR features.

Stepwise discriminant analysis (SDA) was used to identify the most useful features to separate the upper and lower canopy (and therefore partially chlorotic from healthier foliage). Features showing good separation were assumed to have a potential for detecting foliage affected by red band needle blight. SDA builds a group membership prediction model, at each step evaluating all input variables to establish their contribution to the discrimination between classes. The parameter with the highest discriminatory power is then included in the model. Three metrics were included in the final discriminant function: the depth of second chlorophyll feature, slope and right area of the first chlorophyll absorption region (Wilks' lambda = 0.349, chi-square = 38.445, accuracy = 82.5%). The inclusion of right area of the first chlorophyll absorption region in the final stage provided a minimal improvement to the Wilk's lambda parameter (from 0.395, chi-square = 34.400), but also caused a 5% drop in the overall accuracy. At the second step of the analysis, the centre of the first chlorophyll absorption feature was identified as another potential input variable. Substitution of the right area of the first chlorophyll absorption with this metric yielded a slight improvement to the function (Wilks' lambda = 0.353, chi-square = 38.027, accuracy = 85%). With SDA based on a single absorption feature, the second chlorophyll feature provided highest discriminative power with the depth and the band centre metrics selected (Wilks' lambda = 0.442, chi-square = 30.229, accuracy = 85%). Second in performance was the first NIR absorption feature, with the depth and the slope metrics selected (Wilks' lambda = 0.480, chi-square = 27.156, accuracy = 77.5%).

Table 6.8: Tests of equality of group means combined with discriminant function analysis outputs. The performance of the discriminate functions is provided by overall accuracy achieved through Leave-one-out cross-validation (LOOCV) method. Dashes indicate metrics which were excluded from the analysis based on their insignificance (assessed with the Mann-Whitney U test performed at 0.05 confidence level).

	450-550 nm				550-750 nm				900-1100 nm				1100-1280 nm			
	Wilks lambda	Significance	Chi-square	LOOCV	Wilks lambda	Significance	Chi-square	LOOCV	Wilks lambda	Significance	Chi-square	LOOCV	Wilks lambda	Significance	Chi-square	LOOCV
Depth	0.590	0.000	19.779	77.5%	0.507	0.000	25.448	75.0%	0.565	0.000	21.385	75.0%	0.573	0.000	20.913	77.5%
Centre	-	-	-	-	0.752	0.001	10.702	70.0%	-	-	-	-	0.834	0.009	6.829	65.0%
Area	0.609	0.000	24.407	77.5%	0.529	0.000	23.853	77.5%	0.619	0.000	17.957	72.5%	0.596	0.000	19.382	75.0%
L area	0.567	0.000	21.248	77.5%	0.520	0.000	24.550	77.5%	0.604	0.000	18.901	75.0%	-	-	-	-
R area	0.731	0.001	11.775	77.5%	0.570	0.000	21.064	77.5%	0.646	0.000	16.381	72.5%	0.656	0.000	15.801	77.5%
Symmetry	0.911	0.061	-	-	-	-	-	-	-	-	-	-	0.843	0.011	6.414	65.0%
Slope	0.705	0.000	13.107	80.0%	0.759	0.001	10.349	72.5%	0.544	0.000	22.814	80.0%	0.569	0.000	21.175	80.0%

6.6.4 Spectral indices

The differences between averages for the upper and lower canopy part values of ratios and normalised difference indices computed for each band combination are shown in Figure 6.8a. The difference between the canopy parts in most of calculated band ratios ranged from 0 to 1, with the highest of up to 8.3 recorded in ratios combining 700-1400 nm with 1900-2000 or 2400-2500 nm. In case of normalised difference indices the patterns were more variable, with differences ranging from 0 to 0.3. Highest differences were located at ratios pairing 500-580 nm (G) with 650-700 nm, 1400-1500 nm, and 1900-2100 nm, whilst lowest were generally found for adjacent wavelengths, but also when 450-600 nm and 720-1350 nm, and several other narrow bands were paired. The Mann-Whitney U test was used to assess the separability of the upper and lower canopy part, performed at 0.05 confidence level. Significant differences were found for vast majority of the computed indices (Figure 6.8b).

Discriminant function analysis was performed on all significantly different band ratios and normalised difference indices; a graphical summary of outputs is presented in Figure 6.8c, whilst Table 6.9 shows results for commonly used broad-band indices investigated as part of the analysis. Most of band ratios and normalised difference indices yielded accuracies above 60% (mean of 78% for band ratios and 77% for normalised difference indices). Among the most successful (up to 90%) were those ratioing blue and green regions over SWIR water absorption bands (around 1450, 1950 and 2500 nm). Other regions, combinations of which produced high accuracies, included red and green (80-87.5%), red and blue (77.5-87.5%) wavelengths, as well as pairings of 750-780 and 780-900 nm (80-90%). The 709/691 ratio identified by Stone et al. (2003) achieved 80%.

Similar spectral regions were identified by the discriminant function analysis for normalised difference indices. Blue and green regions against SWIR water absorption bands yielded accuracies of 70-87.5%, red and blue 72.5-87.5%, red and green (corresponding to NGRDI) 75-90%, 750-780 and 780-900 nm 80-90%. Furthermore, combinations of SWIR bands, and a pairing of SWIR and NIR regions (corresponding to NDWI) were found to perform well (75-85% for 1550-1850 and 2100-2300 nm, 75-87.5% for 1500-1800 and 850-1350 nm). The combination of NIR and red spectral regions, used in NDVI, achieved accuracies in the range of 70-80%.

Promising band ratios and normalised difference indices were located in spectral regions highlighted by the sensitivity analysis. A significant increase in the red and SWIR, and a decrease in the green and short NIR part of the spectrum for the more diseased needles

was found, which is reflected in the results of this analysis. Similarly, combinations of wavelengths at which the disease did not cause a significant change in reflectance value (e.g. 450-519 nm and 931-1377 nm) yielded low accuracies for both band ratios and normalised difference indices, leading to strong similarities in the final results of the two approaches (Figure 6.8c).

Table 6.9: Accuracy levels achieved (using leave-one-out cross-validation method) by the discriminant function analysis performed on simple ratio and normalised difference vegetation indices. The separation of the upper and lower canopy parts was tested using Mann-Whitney U test. The graphical summary of outputs is provided in Appendix I.

Vegetation index	Spectral regions	Mann-Whitney U test ($p < 0.05$)	LOOCV accuracy (%)
GNDVI	G, NIR	Passed at 30% of bands	57.5-72.5
NDSWIR	NIR, SWIR	Passed	77.5
NDVI	R, NIR	Passed at all bands	70.0 – 80.0
NDWI	NIR, SWIR	Passed at all bands	70.0 – 85.0
NGRDI	G, R	Passed at all bands	75.0 – 90.0
PRI	G	Passed	77.5
SR	R, NIR	Passed	80.0
WI	NIR	Passed	80.0
709/691	R, NIR	Passed	80.0

The accuracy levels acquired by other investigated vegetation indices for all possible band combinations are presented in Table 6.10; the graphical summary of outputs is provided in Appendix I. All of the indices showed good performance at discriminating the more diseased from healthier foliage, with the best being EVI (77.5 – 87.5%), followed by MTVI1 (87.5%) and WI/NDVI (72.5 – 82.5%). The accuracy of RDVI varied greatly depending on band placement. Worst results were achieved when shorter red bands were paired with longer NIR bands (55-70% for 620-640 and 1150-1300 nm), whilst best when longer red bands were paired with shorter NIR bands (77.5-82.5% for 660-700 and 760-

880 nm). All of the preselected narrow-band indices achieved high accuracies, with MTVI1 performing best (87.5%), and PRI and NDSWIR poorest (77.5%).
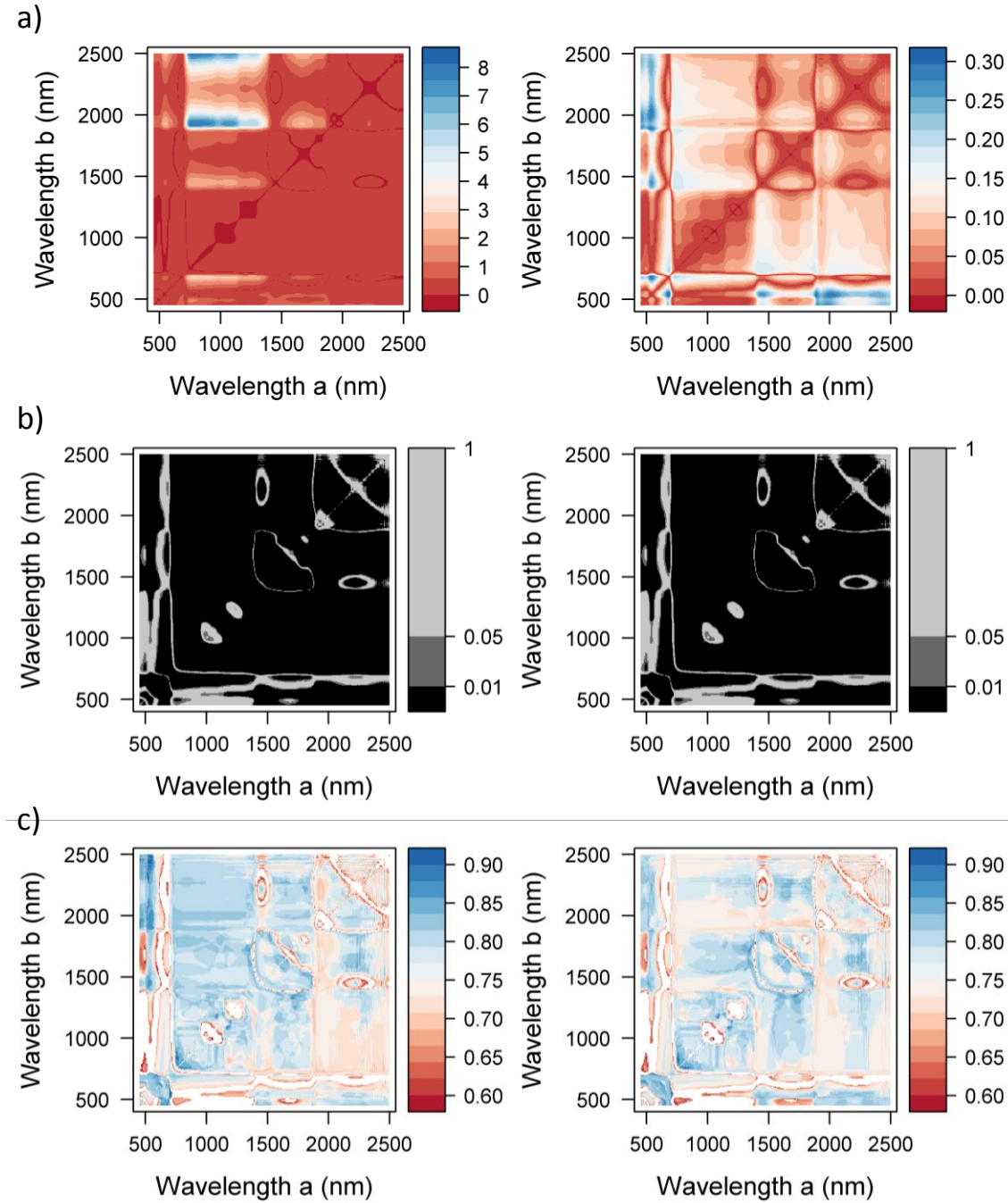
Figure 6.8: a) Absolute differences between the top and bottom canopy part calculated for band ratios ((λa/λb), left) and normalised difference indices ((λb − λa) / (λb + λa), right), b) the Mann-Whitney U test p-values, testing the separation of the top and bottom canopy parts, and c) accuracy levels achieved by the discriminant function analysis. The accuracy levels were retrieved through leave-one-out cross-validation method. Areas yielding success rate below 60% were masked.

Table 6.10: Accuracy levels achieved (using leave-one-out cross-validation method) by the discriminant function analysis performed on a number of vegetation indices. The separation of the upper and lower canopy parts was tested using Mann-Whitney U test.

Vegetation index	Spectral regions	Mann-Whitney U test ($p < 0.05$)	LOOCV accuracy (%)
DWSI	R, NIR, SWIR	Passed	82.5
EVI	B, R, NIR	Passed at all bands	77.5 – 87.5
EVI2	R, NIR	Passed at all bands	70.0 – 80.0
mSR	R, NIR	Passed	80.0
MTVI1	G, R, NIR	Passed	87.5
MTVI2	G, R, NIR	Passed	80.0
RDVI	R, NIR	Passed at >99% of bands	55.0 – 82.5
RVSI	NIR	Passed	85.0
TVI	G, NIR	Passed	80.0
WI/NDVI	R, NIR	Passed at all bands	72.5 – 82.5

6.6.5 Spectral features and disease level

The best performing indices and derivative metrics were chosen for a comparison of the values extracted from spectra of the entirely green foliage (upper canopy) with estimated tree disease levels. No significant or marginally insignificant correlations were found for any of the measures (Table 6.11), suggesting detection of the disease in presymptomatic foliage might not be possible.

Table 6.11: Achieved correlation coefficients (with the associated p values) of the investigated upper canopy metrics compared against the estimated tree disease levels.

Metric	Correlation (p value)	Metric	Correlation (p value)
EVI	-0.144-0.206 (0.383-0.100)	dGE	-0.005 (0.983)
NDVI	-0.278-0.059 (0.234-0.806)	dG	-0.061 (0.798)
NDWI	0.024-0.379 (0.010-0.920)	dRE	0.092 (0.701)
NGRDI	-0.267- -0.073 (0.256-0.759)	DWSI	0.160 (0.503)
RDVI	-0.401- -0.108 (0.080-0.651)	MTVI1	-0.092 (0.701)
WI/NDVI	0.132-0.372 (0.106-0.579)	PRI	-0.065 (0.784)
RDVI	-0.401- -0.108 (0.080-0.651)	RVSI	0.023 (0.923)

6.7 Comparison of approaches

The study investigated three different approaches to spectra analysis, namely derivatives, continuum removal and vegetation indices. All of the investigated methods highlighted the green, red and NIR parts of the electromagnetic spectrum as the most promising for identifying red band needle blight infection. The choice of bands followed the results of the sensitivity analysis performed in the VIS-NIR region; a significant increase of the reflectance in the red, and a decrease in the green and short NIR part of the spectrum for the more diseased needles was present, whilst the blue wavebands were unaffected. The local maxima and minima were found at 545 nm (-16.8%), 680 nm (+50%) and 750 nm (-17.0%). Pairings of SWIR and NIR regions (corresponding to NDWI) were also found to perform well, which is related to water content within leaves. A significant increase in the reflectance was found throughout the SWIR wavelengths, with two major local maxima present in the water absorption features at 1450 nm (+45.8%) and at 1907 nm (+61.3%).

No biochemical data was available to ensure the observed spectral changes were directly caused by the changing concentrations of photosynthetic pigments and water content. Nevertheless, the reflectance changes were in accordance with typical symptoms caused by an onset of stress, expected to be exhibited by needles affected by red band needle

blight as well (that is chlorosis and decreasing water content). The most predominant pigment within leaves, and consequently the one with greatest influence on reflectance within the visible spectrum is chlorophyll, which absorbs light in the blue and red parts of the electromagnetic spectrum (Sims and Gamon, 2002). The increase in the red wavelengths would normally be linked with its decreasing level, whilst the blue range is affected less severely due to a shared absorption with caretonoids, which tend to be present at higher concentrations when vegetation is under stress (Sims and Gamon, 2002; Mahlein *et al.*, 2013). Lower chlorophyll concentration also allows expression of β-carotene and xanthophylls, which results in broadening of the reflectance peak located near 550 nm (Pinter Jr. *et al.*, 2003). Similar spectral response in the VIS-NIR region to the one reported here was observed by Stone *et al.* (2003), who performed analysis of foliage affected by red band needle blight; sensitivity maxima were located in the green, red, and at the start of the NIR region as well (near 550, 680-691 and 760 nm). In contrast to NIR region, in the SWIR part of the spectrum, low reflectance is observed in healthy leaves due to increased water absorption. The water content of leaves, therefore largely influences the shape of the spectrum in this region, with increased reflectance observed in dehydrated leaves (Eismann, 2012).

Discriminant function analysis was used to test the performance of each of the derived shape metrics and vegetation indices at separating the upper (with green foliage) and lower (with partially discoloured foliage) canopy parts. The achieved accuracy levels are summarised in a graphic form in Figure 6.9.

The derivative metrics yielded a broad range of accuracies, from 57.5% for the red edge position to 90%, with best performing metrics being based on derivative values in the green and red regions, as well as the NIR plateau. The shift of the red edge towards shorter wavelengths was related with plant stress (Hoque and Hutzler, 1992; Carter and Knapp, 2001; Liu *et al.*, 2015), but in this study the REP was shown to be only marginally different between the samples, and consequently a poor discriminator. During the continuum removal analysis, similar parts of the electromagnetic spectrum were found to yield the best performance, i.e. the two chlorophyll absorption features in the green and red regions, followed by the water feature located on the NIR plateau. However, the retrieved shape metrics on average performed poorer, with accuracy levels between 65 and 80%, suggesting the use of derivatives would be more appropriate for detecting the infection.
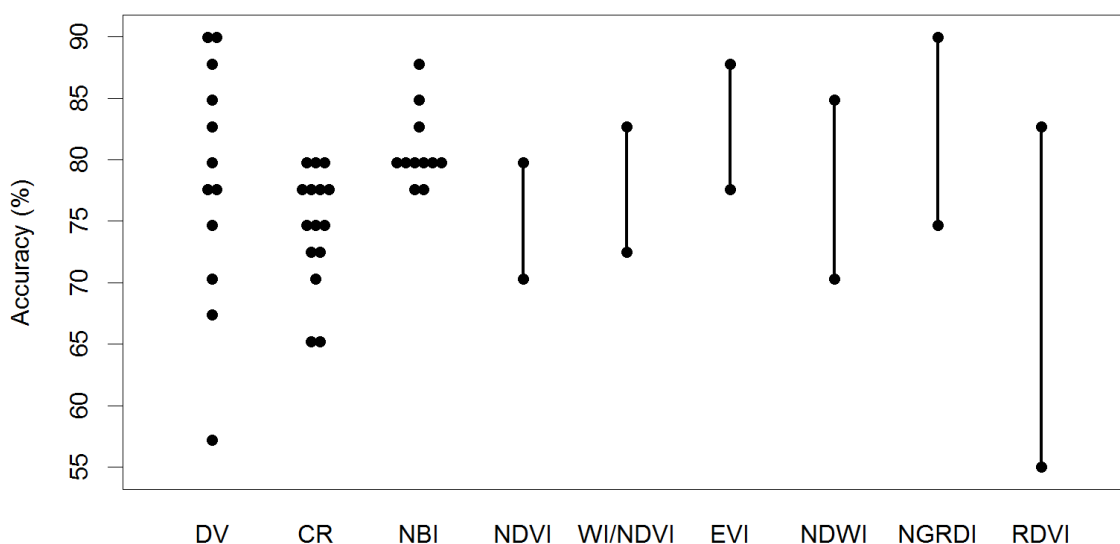
Figure 6.9: Accuracy levels achieved by investigated derivative metrics (DV), continuum removal metrics (CR), narrow-band indices (NBI), and selected broad-band indices. Accuracy scores of broad-band indices are shown as ranges.

In general, the vegetation indices showed the most varied performance, dependent on the band placement. The most commonly used broad-band index, NDVI, was among the poorest (70-80%); combining it with WI to form WI/NDVI only led to a marginal improvement (by 2.5%). EVI with the inclusion of blue band yielded a considerably higher accuracy (77.5 − 87.5%). The best index was found to be NGRDI (up to 90%), combining green and NIR regions. NDWI, which is sensitive to water content within the leaf also showed promising results. The performance of RDVI strongly depended on the choice of wavelengths, and as such it was considered unreliable. Narrow-band indices showed a more consistent performance, with all of them exceeding 75% success rate. Furthermore, the vegetation indices found combinations of blue and green wavelengths with SWIR water absorption bands to yield high accuracies. However, those bands are not normally available in the field and airborne spectra due to attenuation of the signal in those regions caused by strong atmospheric water absorption.

As the detection of red band needle blight is complicated by the fact the infection starts in the lower canopy, which is often obscured from view, the upper canopy spectra were investigated to check if presymptomatic detection of the disease in needles is possible. A comparison was made between metrics retrieved for the upper canopy spectra (green foliage) and the estimated tree disease levels, but no significant correlations were found. In a similar study, Stone et al. (2003) divided red band needle blight needle samples into six damage categories based on the proportion of needle length that was non-green.

Highly significant correlations between the damage categories and vegetation indices were found, with the healthy green needle category exhibiting very little variation. Although no such categorisation was investigated in this thesis, the study by Stone et al. (2003) and results of this chapter suggest the ability to detect red band needle blight in foliage appears to be dependent on the development of visual symptoms.

6.8 Conclusions

Leaf spectroscopy of green and partially chlorotic needles affected by red band needle blight was performed to identify the best spectral regions for detecting the infection. Three approaches for spectra analysis were investigated: spectral indices, derivative-based metrics and continuum removal analysis, all of which highlighted the green, red and NIR parts of the electromagnetic spectrum as the most promising. Among the derivative metrics performing best at separating the spectral response of the two sample groups, the best were based on first order derivative values retrieved in the green to red-edge region (leave-one-out cross validation accuracy of 87.5–90%). Broad-band indices showed varied performance sensitive to band placement, whilst all of the 11 investigated narrow-band vegetation indices showed a more consistent performance, exceeding 75% success rate. Therefore, for airborne hyperspectral analysis of infected plot stands, only the derivatives metrics, the tested narrow-band indices, a selection of broad-band indices (EVI, NDWI, and NGRDI) and best performing band ratios were considered. Furthermore, based on analysis performed on the green foliage spectra, it seems that the ability to detect red band needle blight is dependent on the development of visual symptoms.

Chapter 7. Plot-level analysis of tree stress

7.1 Chapter overview

This chapter investigates spectral characteristics of pine foliage affected by red band needle blight at a plot-level. The results from leaf spectroscopy presented in Chapter 6 were used to inform airborne hyperspectral analysis of affected Lodgepole pine plantation sites. Complementarily, airborne LiDAR data was utilised to retrieve forest structural parameters.

7.2 Introduction

Hyperspectral imagery is most commonly used to detect changes in the condition of vegetation by identifying the variations in the visible and near-infrared region of the electromagnetic spectrum. An overview of hyperspectral analysis of stress in vegetation, alongside descriptions of spectrum analysis methods are provided in Chapter 6. Apart from changes in spectral response, defoliation is another key symptom of most stress factors and damage agents, including red band needle blight. Structural parameters, such as those retrieved from LiDAR data, could therefore provide vital information for monitoring forest health.

LiDAR sensors directly measure the 3D distribution of vegetation, providing highly accurate measures of canopy structure. They have been successfully used in forestry for numerous applications at tree, stand and landscape level. Among the forest attributes successfully derived using small-footprint airborne laser scanning are canopy height and closure, biomass, leaf area index and tree species (Holmgren *et al.*, 2003; Naesset *et al.*, 2004; Donoghue *et al.*, 2007; Solberg, 2010). Conventionally LiDAR data are investigated at a plot level, and among the most commonly used metrics are the height-measures, which include minimum, mean, median and maximum heights, but also percentiles of the returns. The height percentiles characterise the point distribution by calculation of heights under which a certain percentage of points fall (typically at 10% intervals) (Wulder *et al.*, 2008), and are related to a number of forest attributes (Naesset *et al.*, 2004). Other LiDAR metrics measure the variability of height, which can provide an indication of local heterogeneity (Frazer *et al.*, 2005; Donoghue *et al.*, 2007); those include the height's standard deviation, coefficient of variation, kurtosis and skewness. The coefficient of variation summarises the relative dispersion of the returns, and is calculated as a ratio of the standard deviation and average height. As the coefficient is directly associated with LiDAR penetration rate, dense forest canopies are expected to

exhibit smaller variation rates than thinner stands (Donoghue *et al.*, 2007). Furthermore, the percent of ground returns can be calculated, which provides a measure of the canopy density, and has been shown to aid in characterisation of the forest structure, estimation of timber volume and identification of wind damage (Holmgren *et al.*, 2003; Donoghue *et al.*, 2007). LiDAR metrics can also be retrieved at an individual tree level if high resolution data are available. Various algorithms have been developed and successfully applied to identify tree crown structures and retrieve additional metrics, such as crown area and canopy volume. A comprehensive review of tree segmentation and shape reconstruction approaches is provided in Koch *et al.* (2014).

LiDAR metrics have been used to inspect forest damage caused by such agents as mountain pine beetle (Coops *et al.*, 2009), pine sawfly (Solberg *et al.*, 2006; Kantola *et al.*, 2013) and moose (Melin *et al.*, 2016). Solberg *et al.* (2006) detected pine sawfly defoliation in terms of estimated LAI changes using multi-temporal laser scanning acquisitions. Based on single data acquisition, Melin *et al.* (2016) investigated damage caused by moose browsing in severely affected pine seedlings. Differences were found in the vertical distribution and intensity of the laser echoes. Furthermore, the defoliation resulted in a higher number of ground returns in the browsed areas. Coops *et al.* (2009) also found the total number and vertical distribution of LiDAR returns to be distinctive among plots with different stages of the mountain pine beetle attack. Potential capabilities of full-waveform LiDAR were shown by Shendryk *et al.* (2016), who were able to successfully classify tree health in terms of crown dieback in an eucalypt forest. The most successful metrics were based on pulse width and intensity, although an improvement in overall classification was achieved when spectral indices were incorporated.

Most of the highlighted studies investigated canopy structural changes following highly disruptive events, i.e. severe defoliation caused by infestation. Apart from Shendryk *et al.* (2016), no consideration was given to long-term loss of foliage caused by other agents. The question of how the canopy structural metrics are affected following a long-term exposure to disease infection still remains open.

This chapter reports on the transferability of spectrum analysis approaches, which were deemed promising for detecting red band needle blight infection during the leaf spectral analysis (Chapter 6) to an airborne survey. Furthermore, it investigates the potential of a number of LiDAR-derived structural metrics for detection of changes in the canopy resulting from the defoliation induced by red band needle blight.

7.3 Experiment design

The experiment was based in plots C and D, located 1.2 km apart, which were planted with Lodgepole pines in 1965 and 1966. The trees in both plots had similar heights, but differed vastly in terms of their canopies. The assessed disease levels were considerably higher (by almost 20%) in plot C, whilst the average uncompacted live crown ratio of trees (measured using a hypsometer) was smaller by 20%. Furthermore, plot C was characterised by much higher soil moisture content, with areas of standing water, creating favourable conditions for red band needle blight to flourish. As such, the plots provided a suitable field sample to test the approaches, which were found to be responsive to red band needle blight infection during the analysis of leaf spectroscopic measurements.

A comparative study was performed on the signatures retrieved for each plot from the airborne hyperspectral data and the metrics retrieved from LiDAR data. The hyperspectral analysis was restricted to the derivative metrics, previously tested narrow-band indices and a selection of broad-band indices (EVI, NDWI and NGRDI). To ensure only canopy pixels were taken into account, a segmentation of the trees was performed using the discrete return LiDAR dataset. Details regarding the airborne hyperspectral and LiDAR data collection and pre-processing are provided in Chapter 3 Section 7.

7.4 Data Processing

Processing of hyperspectral data shown in this chapter was performed using R (with hsdar developed by Lehnert *et al.* (2016) and self-written packages) and ENVI. LiDAR point clouds were processed using R, FUSION (software developed by the USDA Forest Service (McGaughey, 2016)) and ArcGIS.

7.4.1 Tree tops detection

The LiDAR CHM data were used to derive a tree top product; Figure 7.1 shows the overall processing of the CHM data. Two approaches were tested and compared for this purpose: a watershed-based algorithm and a local maximum filter.

The former approach is based on a segmentation algorithm proposed by Vincent and Soille (1991). The algorithm is based on immersion process analogy, in which the water filling process is simulated. Watershed edges are established, as the basins are progressively flooded and join with "water" from adjacent basins, producing a 2d approximation of the tree crown shape. When applied to trees, the CHM is inverted, turning tree crowns or clumps of multiple crowns into basins. The minimum of each of the segmented basins is assumed to correspond to a tree top. Using this approach potential

tree tops and crown polygons were extracted (step 1). The second approach uses a fixed-width moving window to search for maximum values in a CHM, which are assumed to represent tree tops. Three sizes of circular windows were tested with radiuses of 0.5, 0.75 and 1 m, with the best performing one used in subsequent processing (step 2).
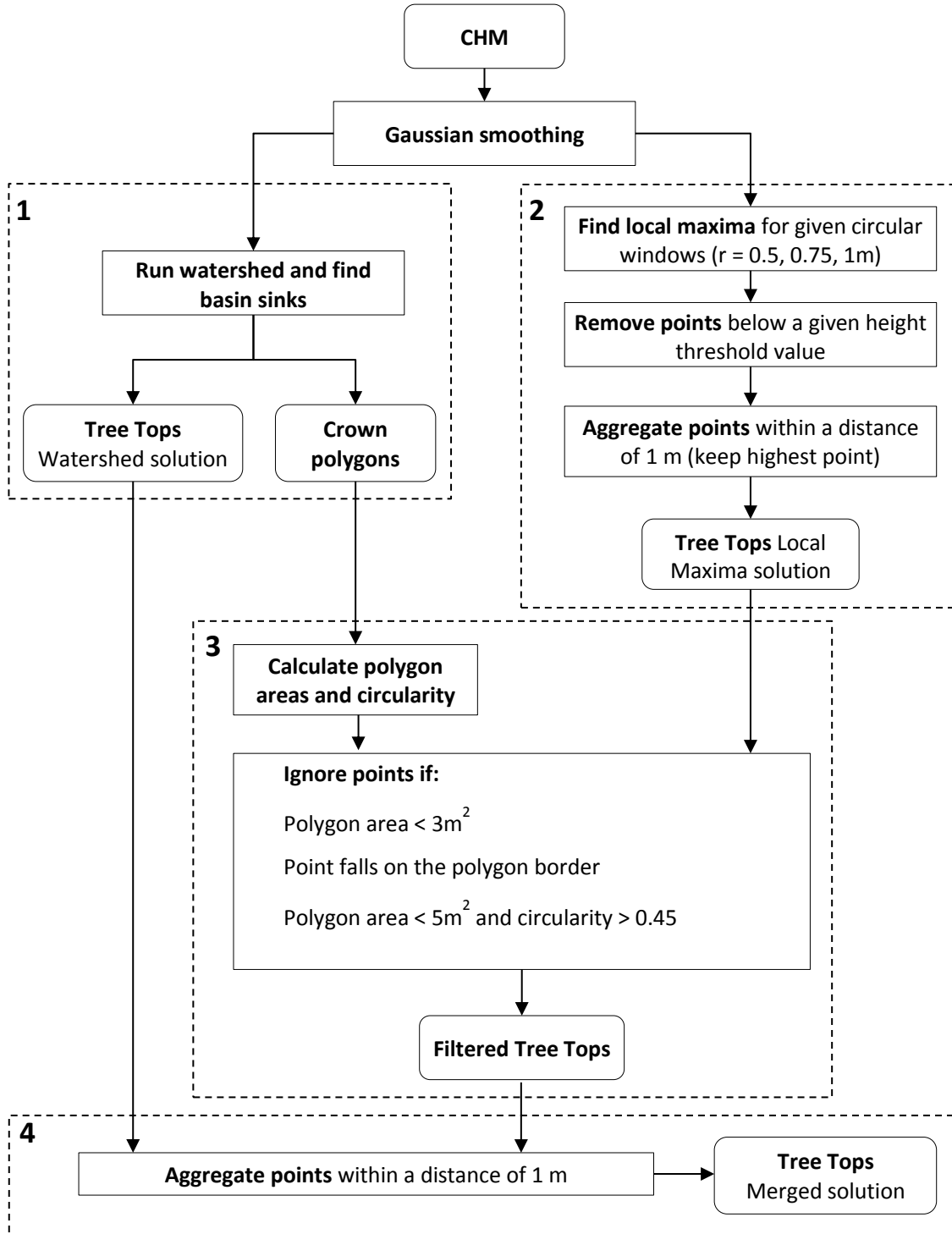
Figure 7.1: Flowchart of the LiDAR processing steps for tree tops extraction.

The outputs of the two approaches were combined to provide a merged solution. Due to the nature of the watershed algorithm, it was expected to provide the most precise (in

terms of low commission errors), but also a largely under-segmented canopy product, turning not only individual tree crowns but also clumps of multiple crowns into basins (Koch *et al.*, 2014). Based on this assumption, the points identified by the watershed algorithm were assumed to represent the true treetop locations of main trees.

Utilising watershed polygons three conditions were imposed to select supplementary tree tops from the local maxima approach (step 3). The points were rejected if they fell on a crown border or if they were located within a polygon smaller than 3 m^2, which is the minimum crown size identified in the field measurements. Furthermore, a circularity condition was imposed, based on an assumption that a coniferous tree crown is circular, whereas a cluster of trees is less circular. The circularity was computed as follows (Wolf and Heipke, 2007):

$$C = \frac{A}{\pi r^2} \tag{7.1}$$

where C is circularity of the polygon, A is area of the polygon, r is the largest distance between the centre of gravity and the polygon border. Points located within crown polygons smaller than 5 m^2 were considered the most likely to constitute individual trees if their circularity value was ≥0.45. The threshold value was chosen based upon investigation of the data. All of the points falling within larger polygons were accepted as potential tree tops.

The filtered local maxima treetop product was then merged with the watershed solution (step 4). All points falling within a distance of 1 m, which is smaller than an expected crown size (average measured crown spreads for plots C and D were 2.5 and 3.2 m), were aggregated, i.e. the watershed solution was retained.

The extracted locations were validated against reference tree positions; these were manually digitised with aid of the UAV-borne orthomosaics, and are shown in Figure 7.2 with the extent of boundaries of the areas processed. In case of plot C, there were no natural cut-off boundaries, which could be used to limit the processing extent. Therefore, a number of peripheral trees were included to aid in accurate segmentation of individual trees within the plots. The reconstructions of peripheral trees are likely to be contaminated by other canopy points, which were left after clipping the LiDAR dataset, and as such were not considered in the final analysis.
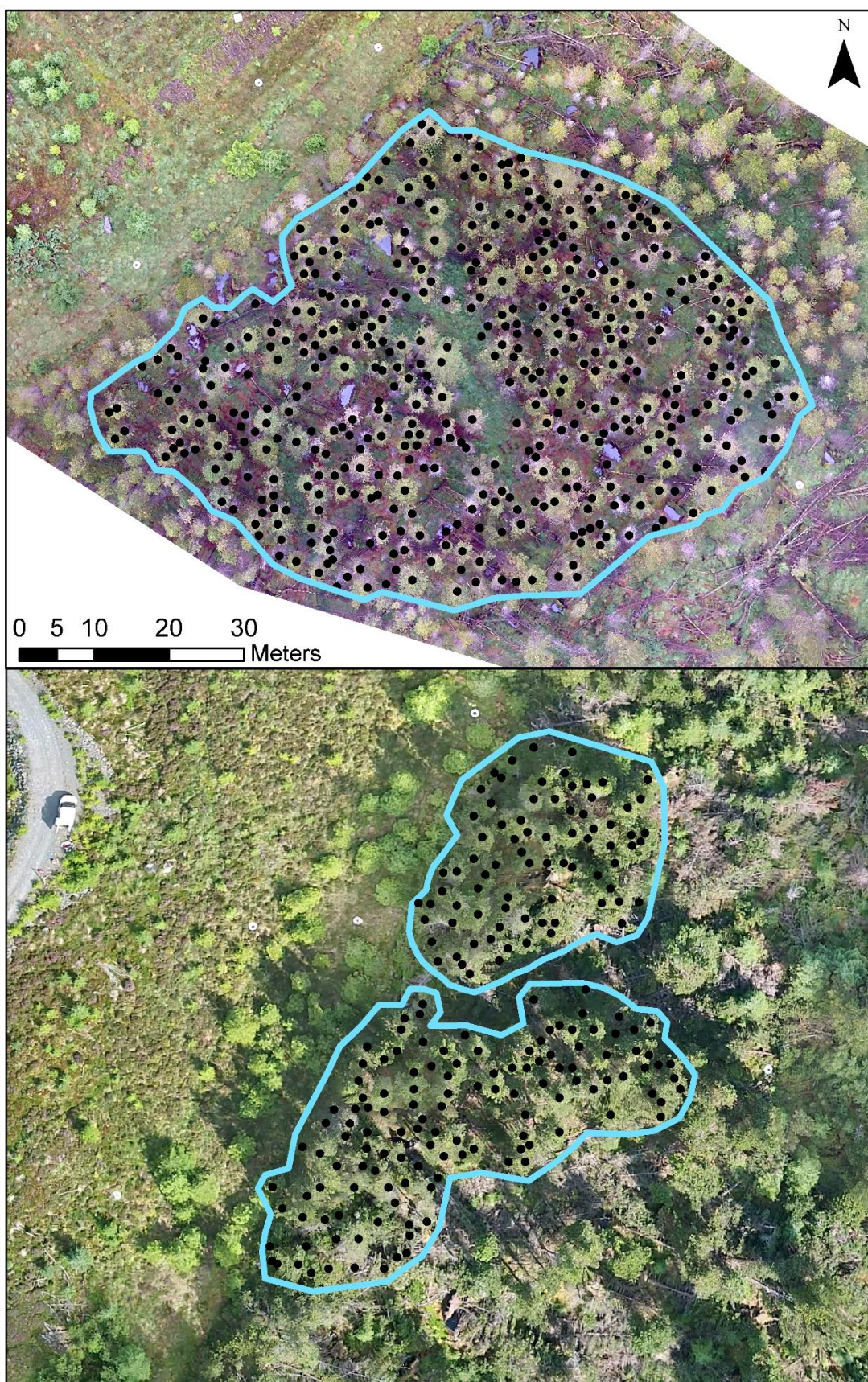
Figure 7.2: Processing extents for plots C (top) and D (bottom) with positions of manually identified trees used for validation. Background: UAV orthomosaics.

In total, 460 and 207 trees were identified in plots C and D respectively using the orthomosaics. Planar Euclidean distances were computed between the reference points and closest detected treetop to assess the accuracy of the algorithms. A match was only recognised if the distance did not exceed 1 m. To assess the performance of the algorithms the number of true positives (TP) representing correctly detected trees, false positives (FP) representing incorrectly detected trees and false negatives (FN) representing undetected trees were used to derive three statistical measures (Mann and Lacke, 2010):

- recall, measuring the proportion of observed treetops which were identified (TP/ (TP + FN)),
- precision, measuring the proportion of the detected treetops, which were correctly identified (TP/ (TP + FP)),
- f1-score, defined as the harmonic mean of the above (2TP/(2TP+FP+FN)).

7.4.2 Tree segmentation

The treetop product was used to perform a segmentation of individual trees in the plots using a k-means Euclidean distance clustering approach (Figure 7.3). The k-means clustering algorithm is an iterative process, which aims to minimise the inter-cluster variance, defined as the overall sum of distances of the points to the cluster centroids. Gupta *et al.* (2010) suggested the squared error function can be minimised further by scaling down the height values of the normalised raw points and seed points, allowing more precise clusters to be produced, with regard to tree crown shape. The clusters were created using the extracted tree top positions for initial centroids without and with scaling down the height (by 0.5 and 0.25). All LiDAR data points below 2 m (i.e. the expected height of lower foliage, as measured in the field) were filtered out before the processing.
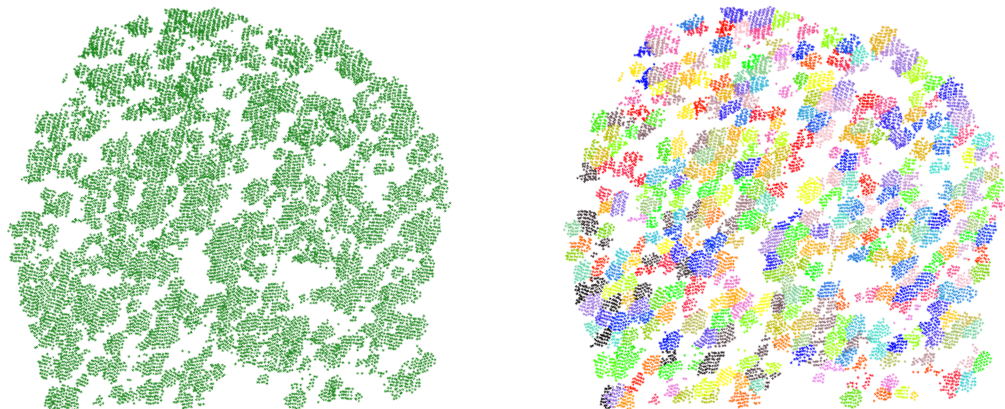
Figure 7.3: Individual tree segmentation example of plot C LiDAR point cloud using the k-means Euclidean distance clustering with 0.25 height scaling.

The shapes of individual tree crowns were reconstructed by means of the convex hull, corresponding to an outer boundary of a triangulation of the input points (Figure 7.4). The quality of reconstruction was assessed visually in terms of the 3-dimensional shape and by comparing canopy extents with orthomosaics. Additional validation was provided by relating the field-measured and LiDAR-derived tree heights.
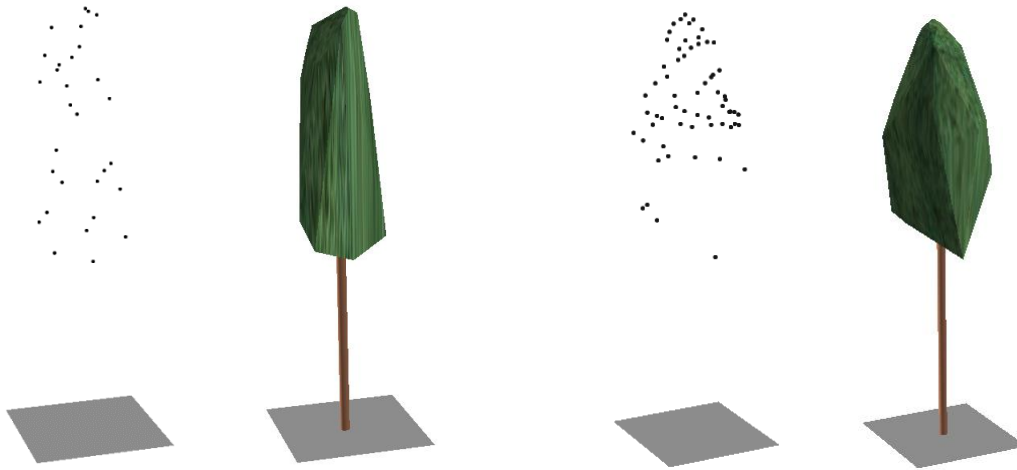
Figure 7.4: Segmented point clouds of two sample trees (*left*) and their convex hull crown reconstructions (*right*).

7.4.3 LiDAR metrics retrieval

Using the segmented LiDAR point clouds, a number of metrics describing canopy structure were calculated for each of the identified trees. The metrics included: (i) selected height measures, i.e. height percentiles (p5, p10, p25, p50, p75, p90 and p95), maximum, minimum, mean and median height (h_{max}, h_{min}, h_{mean}, h_{med}), (ii) measures of height variability, i.e. height's coefficient of variation, standard deviation, kurtosis and skewness (h_{cov}, h_{sd}, h_{kur}, h_{ske}), (iii) percent of ground returns, (iv) canopy volume (C_{vol}) and (v) canopy area (C_a). The area and volume were calculated utilising 2D and 3D convex hulls of the segmented point clouds. In order to analyse vertical distribution of points within the canopy, independently of the tree height, the heights of points were rescaled to a range between 0 and 1, with 0 representing the bottom and 1 representing the top of a given canopy. All height-based LiDAR metrics were derived using those normalised point clouds.

Boxplots and bean plots were produced to examine the structural variation within and between the plots. The Mann Whitney U test was used to assess the separability of the LiDAR measures, whilst stepwise discriminant function analysis was used to identify variables best detecting differences; the metrics were then compared against the estimated disease levels within plot C, which offered a wider range of infection levels than plot D.

7.4.4 Hyperspectral signatures extraction

The segmented trees were used to restrict hyperspectral analysis to tree canopies. For this purpose, two masks were created from the 2D canopy extents. The first mask excluded pixels with ≤50% tree cover, whilst the second mask, additionally, retained only those pixels which coincided with one of the detected tree tops. The spectra from plots C and D were extracted using both masks; in total 368 and 207 pixels were extracted with first mask, 298 and 160 with the second. The applied masks are shown in Appendix J.

For each pixel, the narrow-band indices defined in Chapter 6 Section 5 (excluding RVSI and TVI, for which required spectral bands were unavailable), as well as a selection of broad-band indices (EVI, NDWI and NGRDI) and band ratios were computed. All possible band combinations were examined for each broad-band index. Due to gaps within the spectra, derivative analysis was restricted to dG and dGE metrics. The Mann-Whitney U test (performed at 0.05 confidence level) was used to assess the separability of the spectra between the plots for each index and metric, with features that did not show significant separation between group means excluded from further investigation. Discriminant function analysis using leave-one-out cross-validation was then utilised to help identify best predictors, for which boxplots were produced to examine the variation between the plots. The most promising features were then compared against the estimated disease levels within plot C.

7.5 Results

7.5.1 Canopy top detection and tree segmentation

The accuracy assessment results for the individual treetop detection are shown in Table 7.1. In the case of the local maximum filter approach, smaller windows were shown to perform better, with f-1 scores of 0.84 and 0.88 for 0.5 m window as opposed to 0.75 and 0.67 for 1 m window. However, although the number of detected treetops was significantly improved (the recall increased from 61 to 86% in plot C and from 51 to 83% in plot D), some areas experienced over-segmentation. In plot C, the decrease in precision relative to 1 m window approach (-17%) was particularly evident, with 79 incorrectly detected trees for a 0.5 m window size instead of 1 m. The watershed algorithm achieved minimally higher accuracies than the 1 m window (f-score of 0.82 for plot C and 0.71 for plot D). However, it had a poor recall (69 and 55%), as the algorithm, due to its nature, is likely to produce groupings of multiple trees. The combination of the treetop products retrieved by the watershed algorithm and the 0.5 m local maximum filter performed best, achieving f1-scores of 0.89. This approach produced the most consistent results, retaining high recall (84% in both plots), whilst improving the precision, especially in the more densely-vegetated plot C (to 96%).

The combined tree top solution was used to perform segmentation of individual trees. The 3D and 2D convex hulls of the resultant clusters, representing canopy extents, are shown in Figure 7.5 and Figure 7.6. It is evident that the normal k-means algorithm failed to separate the clusters of points in forest conditions. There was a considerable amount of confusion in the horizontal plane, with tree foliage being divided into multiple canopies along the vertical axis, which is demonstrated as overlapping of the 2D convex hulls. When the height value of the datasets and respective seed points was scaled down before initialisation of the algorithm, better partitioning of the data and cluster formation was achieved. The 3D shape of the segmented crowns was considerably different, and closer to the expected silhouettes of pines. The improvement in pattern classification is particularly evident upon inspection of the 2D convex hulls, with resultant polygons of the 0.25 height scaling outlining the canopy crowns visible on the orthomosaic most accurately; these were used for mask creation to extract hyperspectral signatures.

Table 7.1: Accuracy assessment of individual tree detection based on the watershed and local maxima methods. True positives (TP) represent correctly detected trees, false positives (FP) represent incorrectly detected trees and false negatives (FN) represent undetected trees.

Area	Method	Number of detected trees					Recall (%)	Precision (%)	f1-score
		LiDAR	UAV reference	TP	FP	FN			
Plot C	Watershed	322	460	319	3	141	69	99	0.82
Plot C	Local maxima 1 m	280	460	279	1	181	61	100	0.75
Plot C	Local maxima 0.75 m	472	460	390	82	70	85	83	0.84
Plot C	Local maxima 0.5 m	473	460	394	79	66	86	83	0.84
Plot C	Watershed & Local maxima 0.5 m	402	460	385	17	75	84	96	0.89
Plot D	Watershed	114	207	114	0	93	55	100	0.71
Plot D	Local maxima 1 m	105	207	105	0	102	51	100	0.67
Plot D	Local maxima 0.75 m	184	207	171	13	36	83	93	0.87
Plot D	Local maxima 0.5 m	185	207	172	13	35	83	93	0.88
Plot D	Watershed & Local maxima 0.5 m	182	207	173	9	34	84	95	0.89
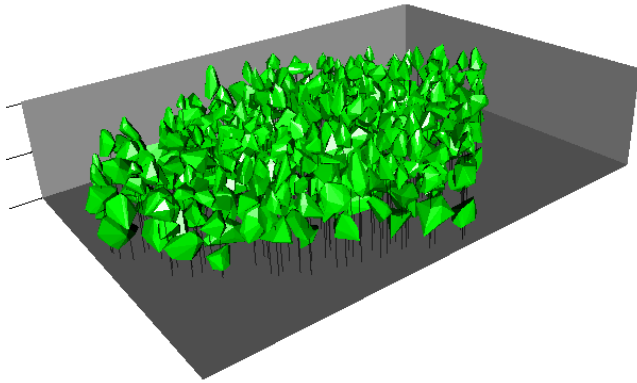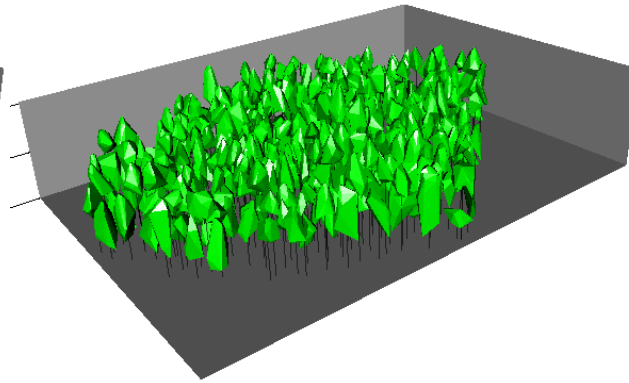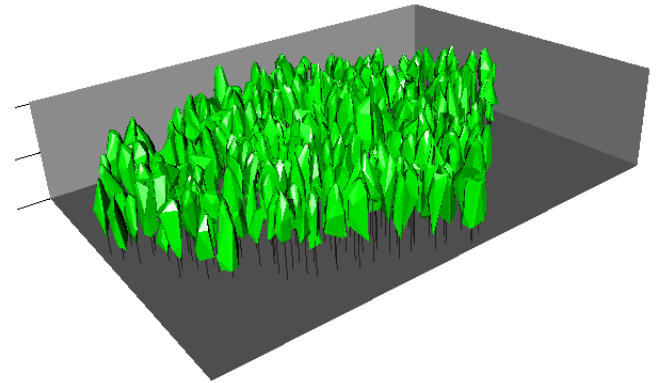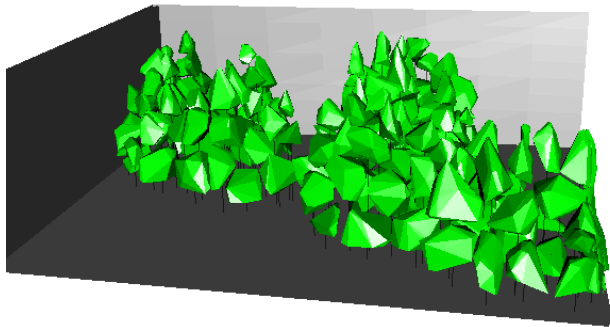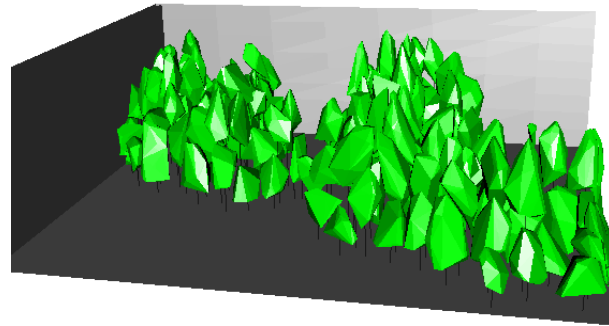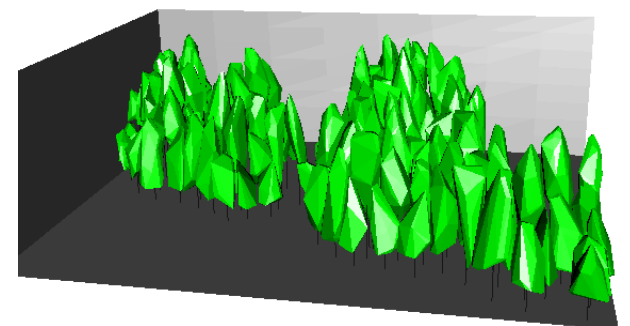
Figure 7.5: 3D convex hulls of the canopies segmented in plots C (top) and D (bottom). The segmentation was achieved using the k-means clustering algorithm with different height scaling (s = 1, 0.5 and 0.25).
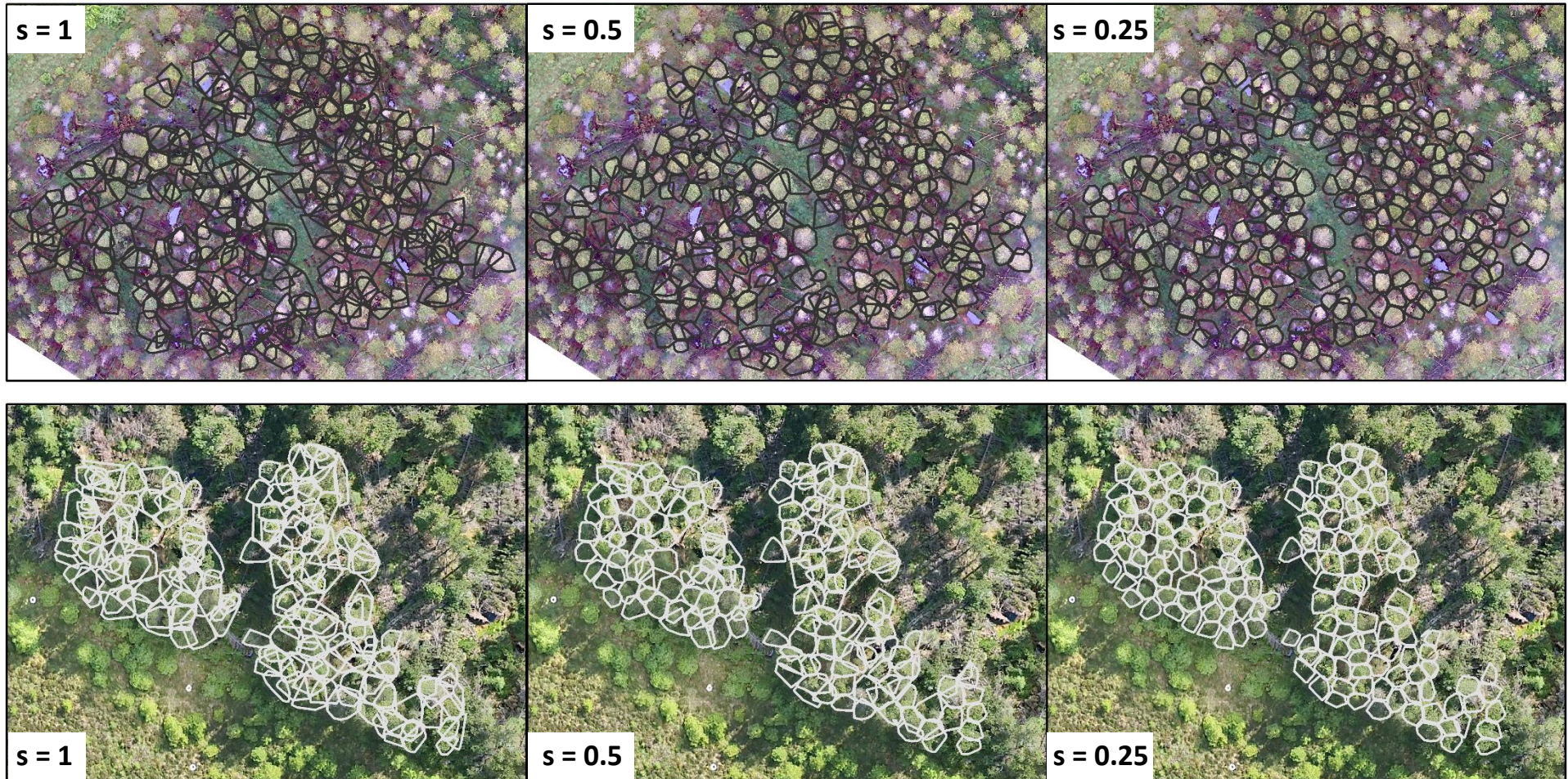
Figure 7.6: 2D convex hulls of the canopies segmented in plots C (top) and D (bottom). The segmentation was achieved using the k-means clustering algorithm with different height scaling (s = 1, 0.5 and 0.25). Background: UAV orthomosaic.

Further validation for canopy segmentation was provided through examination of the relationship between tree heights measured in the field and maximum heights extracted from the LiDAR data (Figure 7.7). The derived heights correlated well with field measurements, achieving Pearson correlation coefficients of 0.9319 ($p < 0.001$) for both of the plots. On average, the LiDAR canopy tops were lower than those measured in the field by 0.54 m in plot C (σ=0.72) and by 0.84 m in plot D (σ=1.48). Comparable slight general underestimation of tree height was reported by other studies (Edson and Wing, 2011; Kaartinen *et al.*, 2012); the tree tops are frequently missed by LiDAR return as the probability of a laser pulse intercepting the apex of a tree crown is relatively small (Zimble *et al.*, 2003).
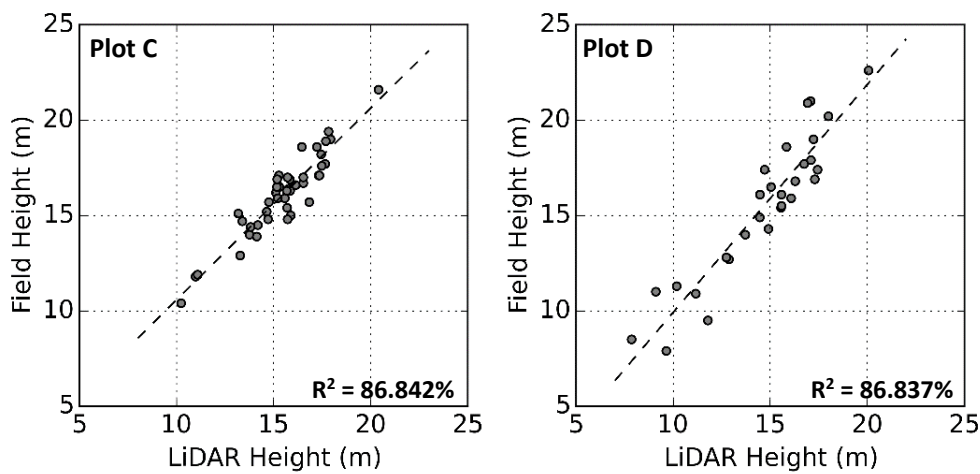
Figure 7.7: Relationship between tree heights extracted from LiDAR data and tree heights measured in the field using a hypsometer for plots C (left) and D (right).

7.5.2 LiDAR metrics

The LiDAR metrics (Figure 7.8) showed that the trees located within plot C were taller than trees in plot D (on average by 2.1 m) with the bottom of the canopy starting higher (on average by 1.2 m), which was expected considering plot C was one year older. In both plots the retrieved canopy areas were very similar (mean difference of 0.56 m^2), whilst canopy volumes were nearly identical (mean difference of 0.54 m^3) (Figure 7.8). The convex hull analysis outputs indicated that the investigated trees in both plots had nearly identical extents of tree canopies. The analysis was therefore focused on the vertical distribution of points within the canopy, which could provide an indication of the spread of the foliage and the bottom-up defoliation, characteristic for red band needle blight.
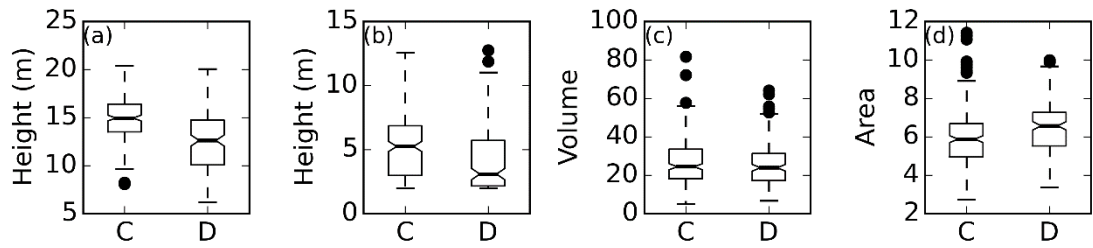
Figure 7.8: Box-and-whisker plots of the maximum (a) and minimum (b) height, canopy volume in m³ (c) and area in m² (d) for plots C and D. Outliers are shown as dots, lines represent the 25th percentile, median and 75th percentile, whilst whiskers extend to a maximum of 1.5 times the interquartile range. Notches represent 95% confidence intervals about the median.

Many of the retrieved height-based LiDAR metrics yielded similar response in both plots (Figure 7.9). Significant differences were found in the mean height and skewness. Both of the plots were characterised by higher density of points in the upper canopy, but the proportions were more shifted in the case of plot C – average skewness of -0.70 as opposed to -0.24 observed in plot D. The clearest difference was found in the percentage of ground returns within the canopy extents. Within plot C, which is more diseased and defoliated, more laser pulses were reaching the ground, and consequently fewer pulses hit the vegetation layer; the average percentage of ground returns was 31 and 18% for plots C and D.

The height percentiles, presented in Figure 7.10 as bean plots, confirmed the different inter-canopy distribution of returns between study areas. The trees in plot C had significantly fewer echoes coming from the lower part of the canopy; the distributions showed a significantly different shape in that part (5th and 10th percentile), whilst a nearly identical shape was present in the top parts (90th and 95th percentile). This distribution, alongside higher penetration through the vegetation layers (illustrated by the percentage of ground returns) suggests lower foliage density in the lower canopy of trees in plot C, which is expected to had been caused by red band needle blight defoliation; plot C was characterised by higher disease level and lower (by almost 20%) uncompacted live crown ratio. The biggest difference in the normalised height percentiles was found at the 25th and 50th percentile (average difference of 0.1). The height percentiles, alongside the percentage of ground returns could potentially serve as diagnostic features for detecting the defoliation.
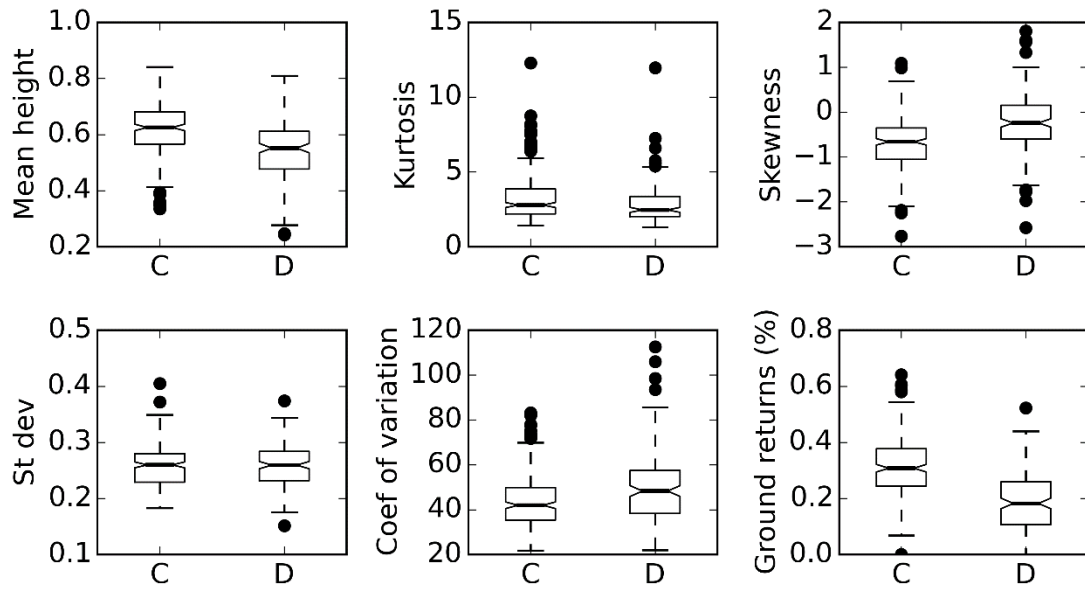
Figure 7.9: Box-and-whisker plots of the LiDAR metrics retrieved from canopy points normalised to the canopy height extent. Outliers are shown as dots, lines represent the 25th percentile, median and 75th percentile, whilst whiskers extend to a maximum of 1.5 times the interquartile range. Notches represent 95% confidence intervals about the median.
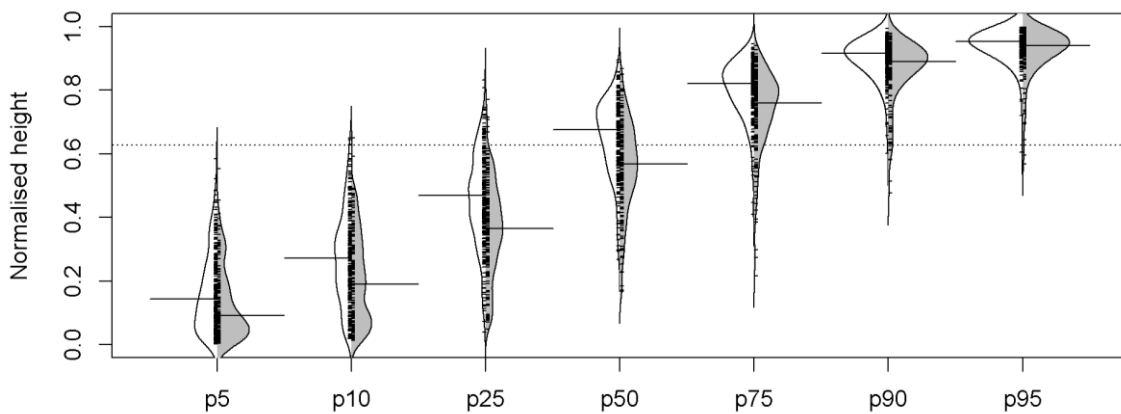
Figure 7.10: Bean plots of normalised height percentiles for trees in plot C (white) and plot D (grey), showing their distribution as a density shape with median value marked as a long black line. One-dimensional scatter plots are shown as short horizontal lines; each line represents a data point.

All metrics but one, standard deviation of height, proved to be significantly different between the plots (based on Mann-Whitney U test at 0.05 confidence level). However, because of the significant overlap, as shown in the box plots, the metrics performed poorly at discriminating the more diseased trees in plot C from the significantly healthier trees in plot D (Table 7.2). The only measure, which had a good discriminative power was the percentage of ground returns within the canopy extents, with accuracy of 72.6%. The second best with score of 62.6% were the mean and the 50th percentile. Stepwise discriminant analysis identified the percentage of ground returns and the 50th percentile as the most useful features for separation. Analysis based on those two features yielded an accuracy of 79.4%.

Table 7.2: Accuracy levels achieved (using a leave-one-out cross-validation method) by the discriminant function analysis performed on LiDAR metrics. The separation between plots C and D was tested using Mann-Whitney U test.

LiDAR metric	Mann-Whitney U test p value	LOOCV accuracy (%)
h_{mean}	<0.001	62.6
h_{sd}	0.771	-
h_{cov}	<0.001	55.9
h_{kur}	0.007	50.0
h_{ske}	<0.001	61.6
p5	0.001	49.8
p10	<0.001	59.9
p25	<0.001	58.7
p50	<0.001	62.6
p75	<0.001	60.4
p90	<0.001	55.4
p95	0.007	53.8
Ground returns	<0.001	72.6

7.5.3 Hyperspectral analysis

The mean reflectance spectra for each of the plots are presented in Figure 7.11. Utilising information only from the apexes of the canopies as opposed to all pixels with >50% cover led to very minimal changes in the spectra; the variations in standard deviation were also negligible. This suggests the clustering algorithm allowed for an effective segmentation of trees and exclusion of ground pixels. Similarly to leaf spectroscopy, a general decrease in reflectance of the NIR and green regions was present for the plot with higher disease intensity (plot C). For both plots, the response in the SWIR region was very similar, with only one clear difference in the longer wavelength water absorption feature (1800 to 2000 nm).
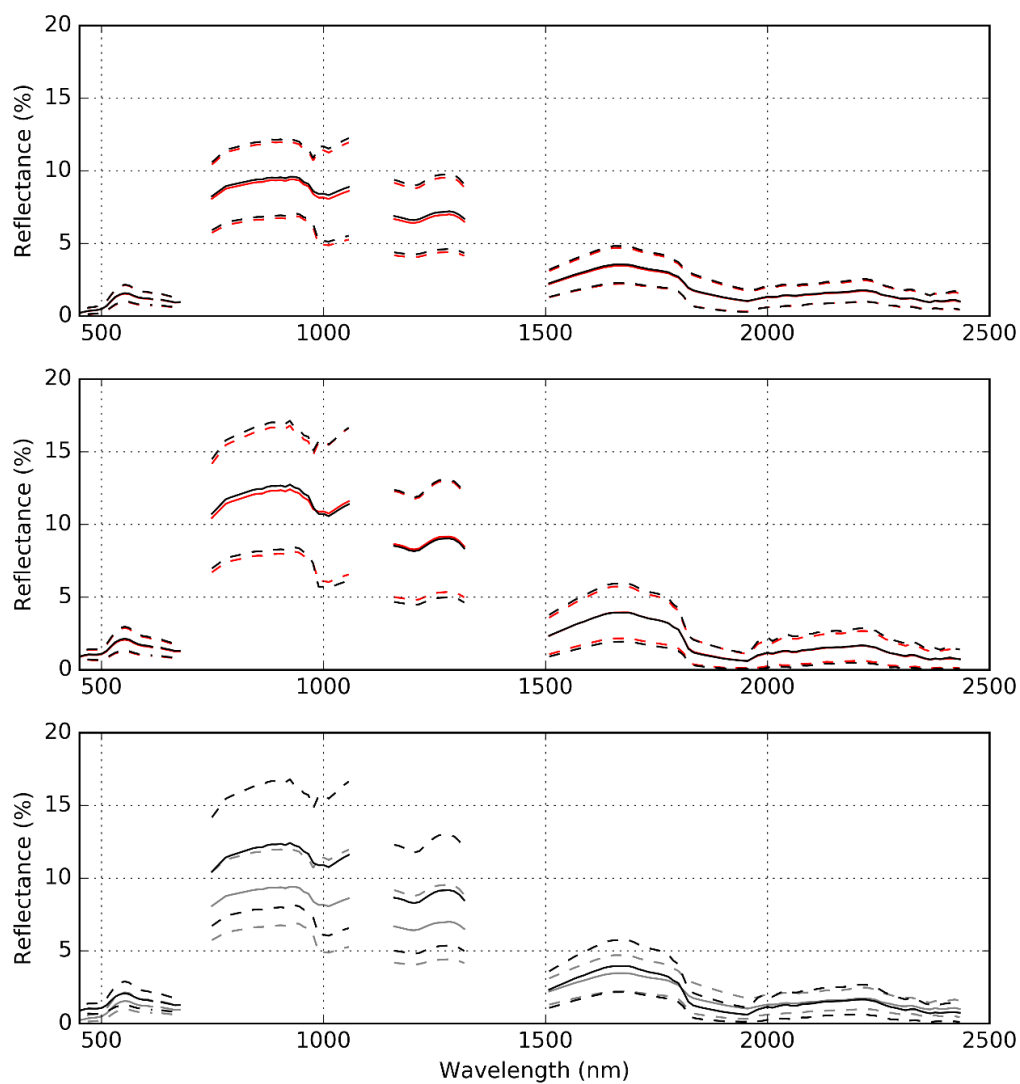
Figure 7.11: Mean reflectance spectra for plots C (top) and D (middle) extracted from all canopy pixels (red) and only central pixels (black). The bottom graph shows a comparison between mean reflectance obtained for plots C (grey) and D (black). Dashed lines represent 1σ standard deviation.

The only derivative metrics which could be investigated, because of the discontinuity of the data, were dG and dGE. dG is the minimum first derivative value within the 550-600 nm range, corresponding to the slope of the green reflectance peak, whilst dGE is the maximum first derivative value within the 500-550 nm range, which can be attributed to a decrease in the spectral reflectance between the green and red wavelengths. dG and dGE were shown to discriminate between the plots very poorly due to a significant overlap in the values (Figure 7.12). Even though the metrics proved to be statistically separable (passed Mann-Whitney U test at 0.05 confidence level), the dG and dGE achieved only 51.5% and 58.8% accuracy levels (assessed through LOOCV) in the discriminant function analysis.
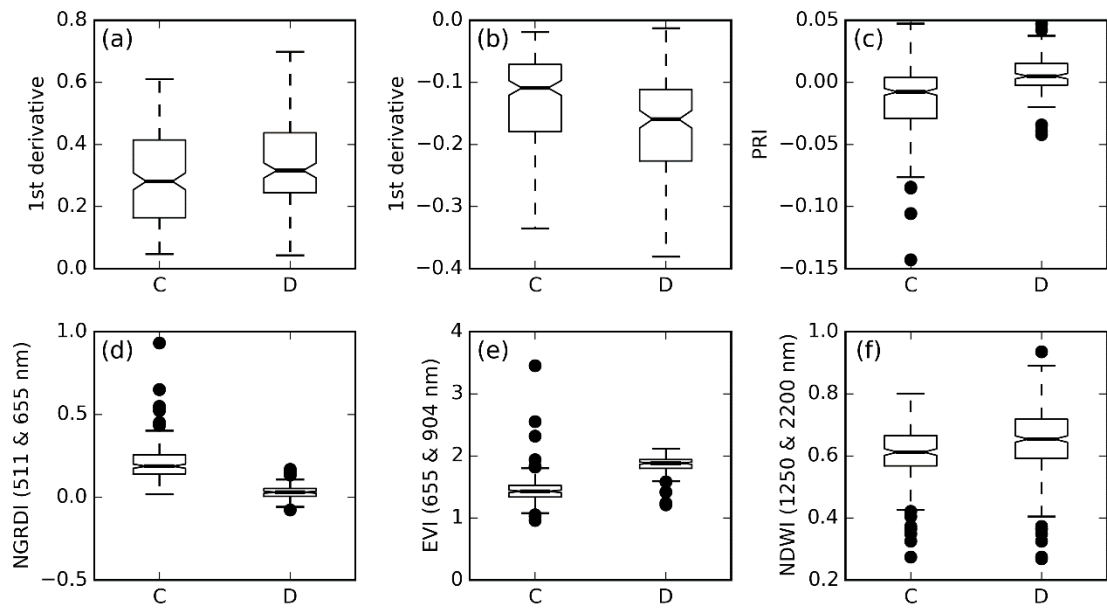
Figure 7.12: Box-and-whisker plots of the extracted dG (a) and dGE (b) derivative metrics and vegetation indices (c-f) for plots C and D. The spectra were retrieved from pixels falling in canopy centres. Outliers are shown as dots, lines represent the 25th percentile, median and 75th percentile, whilst whiskers extend to a maximum of 1.5 times the interquartile range. Notches represent 95% confidence intervals about the median.

Considerably better performance was observed when vegetation indices were used (Table 7.4). PRI, which is associated with changes in the state of the xanthophyll cycle (Gamon *et al.*, 1997), achieved high accuracy (81.1%), minimally surpassing its performance in the leaf spectroscopy experiment (77.5%). Broad-band indices exhibited a decent, but varied performance, with NGRDI achieving accuracies above 90% when utilising a narrow green reflectance strip (500 – 515 nm, Figure 7.13). EVI exhibited equally high and more consistent performance, when combining red wavelengths with NIR bands up

to around 970 nm (Figure 7.13). Past that region, a sudden drop of 9-16% was present, caused most probably by miscalibration of the VNIR and SWIR detectors within the AisaFENIX instrument. Prior to data collection, the SWIR detector was not given enough time to cool down resulting in an unstable response over time, and abnormally high noise signal. It was therefore concluded that for this dataset bands from the two separate detectors should not be combined within a single vegetation index, such as is the case in DSWI, NDSWIR and WI.
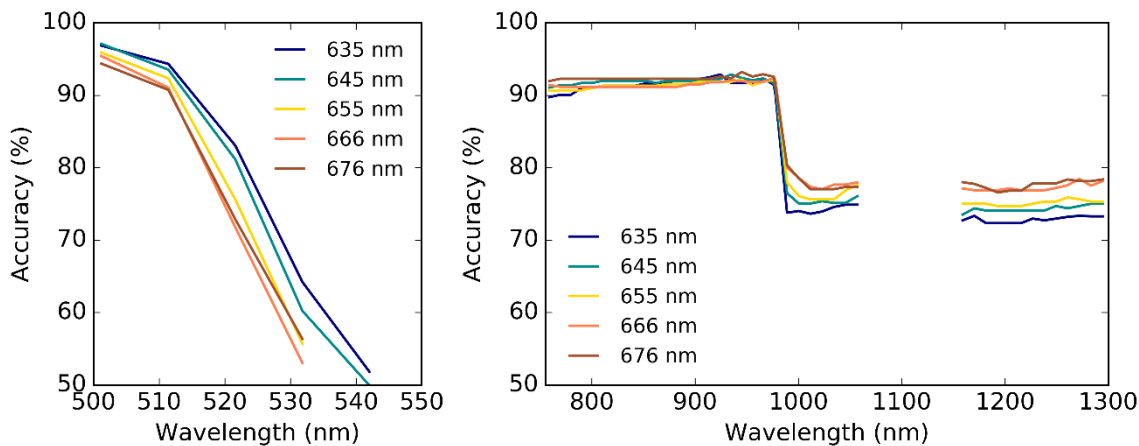
Figure 7.13: Accuracy levels achieved by the discriminant function analysis performed on NGRDI (left) and EVI (right) computed from the spectra of plots C and D. The accuracy levels were retrieved through LOOCV method. A sudden drop in accuracy can be observed when bands from two spearate detectors within the AisaFENIX instrument are used (i.e. for EVI computed using NIR bands beyond 970 nm) – a result of the supposed miscalibration.

A sudden drop in performance was also observed for the NDWI when readings from both detectors were used (Figure 7.14); significantly lower accuracies were achieved when NIR bands up to around 970 nm were used for NDWI calculation. Restricting the analysis to longer NIR wavelengths, the achieved accuracies ranged from 65.2 to 78.3%. Similar SWIR regions, to those identified in the leaf spectroscopy were shown to be least (1800-2050 nm) and most (1600-1800 and 2100-2300 nm) effective. However, a large overlap in the index value between the two plots was present (Figure 7.12). Despite several outliers, a very good separation was present for NGRDI, EVI and PRI. The values of those indices had a wider distribution in plot C, which could potentially be caused by a broader range of infection levels across the canopies. The potential influence of different

canopy architectural effects between the plots was ruled out on the basis of LiDAR metrics, which showed the trees in both plots had nearly identical extents of canopies.
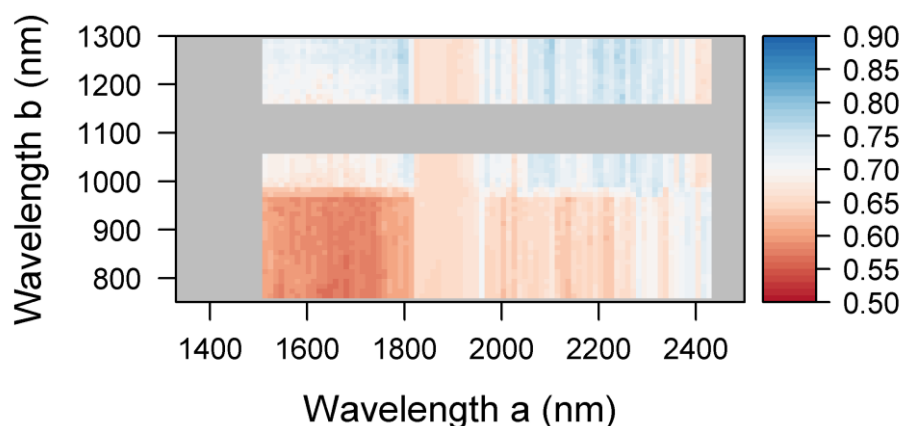
Figure 7.14: Accuracy levels achieved by the discriminant function analysis performed on NDWI computed from the spectra of plots C and D. NDWI values were computed as $(\lambda b - \lambda a) / (\lambda b + \lambda a)$. The accuracy levels were retrieved through LOOCV method. A sudden drop in accuracy can be observed when bands from two spearate detectors within the AisaFENIX instrument are used (i.e. for NDWI computed using NIR bands up to 970 nm) – a result of the supposed miscalibration.

7.5.4 Sensitivity to tree disease level

In plot C (offering a significantly wider range of infection levels than plot D), the relationship between disease levels visually estimated in the field and the identified LiDAR metrics and average indices values were investigated. However, no statistically significant correlations were found (Table 7.3).

Table 7.3: Achieved correlation coefficients (with the associated p values) of the investigated metrics compared against the estimated tree disease levels.

Metric	Correlation	P value
EVI (655 + 904nm)	-0.147	0.391
NGRDI (511 + 655nm)	0.158	0.373
PRI	-0.333	0.054
p50	0.091	0.563
Ground returns (%)	-0.130	0.407

Table 7.4: Accuracy levels achieved (using leave-one-out cross-validation method) by the discriminant function analysis performed on vegetation indices retrieved from all canopy pixels and only central pixels. The separation between plots C and D was tested using Mann-Whitney U test.

Vegetation index	Spectral regions	All canopy pixels		Canopy centre pixels	
		Mann-Whitney U test ($p < 0.05$)	LOOCV accuracy (%)	Mann-Whitney U test ($p < 0.05$)	LOOCV accuracy (%)
DSWI	R, NIR, SWIR	Passed	58.2	Passed	59.6
EVI	B, R, NIR	Passed at all bands	73.3 – 93.1	Passed at all bands	72.3 – 93.2
NDSWIR	NIR, SWIR	Passed	57.8	Passed	58.6
NDWI	NIR, SWIR	Passed at all bands	56.6 – 78.2	Passed at all bands	56.6 – 78.3
NGRDI	G, R	Passed at 58% of bands	49.0 – 96.6	Passed at 55% of bands	49.9 – 97.1
MTVI1	G, R, NIR	Passed	67.0	Passed	63.8
MTVI2	G, R, NIR	Passed	50.9	Passed	51.2
PRI	G	Passed	81.7	Passed	81.1
SR	R, NIR	Passed	52.1	Failed	-
mSR	R, NIR	Passed	51.5	Failed	-
WI	NIR	Passed	58.3	Passed	58.0

7.6 Discussion

This chapter investigated spectrum analysis approaches, applied to airborne hyperspectral data, and LiDAR-derived structural metrics for detection of changes in the canopy induced by red band needle blight. The experiment was based in plots C and D, planted with Lodgepole pines. Plot C was characterised by a considerably higher disease level, and lower uncompacted live crown ratio.

The LiDAR analysis focused on vertical distribution of points within the canopy to provide an indication on the spread of the foliage. Trees in both of the plots were characterised by higher density of points in the upper canopy, but the proportions were more shifted in the case of plot C. Investigation of height-normalised canopy percentiles confirmed the different inter-canopy distribution of returns. The trees in plot C had significantly fewer echoes coming from the lower canopy, suggesting lower foliage density in those parts, which is expected to have been caused by red band needle blight defoliation. Red band needle blight infection usually starts in the lower parts of the tree on older foliage and spreads upward, systematically defoliating the affected tree in a bottom-up manner. Plot C was characterised by higher disease level and lower (by almost 20%) uncompacted live crown ratio. The clearest difference was found in the percentage of ground returns within the canopy extents, with plot C characterised by more laser pulses reaching the ground (31% as opposed to 18% in plot D), and consequently fewer pulses hitting the vegetation layer. As a tree loses its foliage, it is more probable for a pulse to penetrate the canopy layer; a similar pattern was identified in pine stands damaged by moose browsing (Melin *et al.*, 2016).

Stepwise discriminant analysis performed on all LiDAR metrics identified the percentage of ground returns and the 50th percentile as the most useful features for separation of trees between plots. Analysis based on those metrics yielded an accuracy of 79.4%, indicating a potential for analysis of defoliation at a tree level. To develop a more comprehensive understanding of changes in the canopy following the infection, a multi-temporal approach could be employed. Investigation of the LiDAR metrics retrieved from a multi-temporal dataset could provide an indication of the year-to-year defoliation caused by the disease. For instance, Solberg *et al.* (2006) mapped the defoliation caused by pine sawfly, in terms of changing LAI, using a multi-temporal dataset. So far, studies have mainly inspected forest defoliation at a stand level (Solberg *et al.*, 2006; Coops *et al.*, 2009; Melin *et al.*, 2016). At an individual tree-level the focus was primarily put on snag detection (Yao *et al.*, 2012; Wing *et al.*, 2015). Recently Shendryk *et al.* (2016) performed a tree

level health classification in terms of crown dieback in eucalyptus trees using full-waveform LiDAR data. The most successful metrics were based on pulse width and intensity, such as the average returned pulse width below median height and average range-corrected intensity above median height. However, the ratio of laser returns from leaves at the tree trunk and returns at the tree periphery, and the ratio of the number of laser returns from woody components to number of laser returns from leaves showed high importance as well. The metrics identified by Shendryk *et al.* (2016) could also be transferable to analysis of red band needle blight defoliation, as they were found to be sensitive to crown dieback and transparency. However, they would require full-waveform datasets with high point density (in the study data with 36 points/m^2 were used), which were unavailable for these sites.

No differences in the canopy volume were observed; however, this could have been caused by the flawed nature of the applied convex hulls approach, which does not account for the inter-crown variability (such as foliage distribution, including gaps between branches). The convex hull method only chooses points on the outermost boundary of the point cloud, and therefore was found to overestimate the shape of tree crowns, and consequently overestimate the canopy volume (Kato *et al.*, 2009; Tao *et al.*, 2014). The alpha shapes method is a common alternative to convex hulls. A predefined alpha parameter allows restriction of the number of facets belonging to the minimum convex polygon, defining the level of detail in the obtained shape (Koch *et al.*, 2014). A promising approach yielding $R^2>0.8$ for crown volume estimation in both deciduous and coniferous tree species was suggested by Kato *et al.* (2009); this derives two-dimensional horizontal convex hulls at different heights to select outline points, and then performs wrapped surface reconstruction (by employing radial basis functions and an isosurface). Voxel-based methods have also been used for reconstruction of the tree shape and the calculation of total crown volume (Popescu and Zhao, 2008; Wang *et al.*, 2008); however, the results depend on the spatial allocation and voxel resolution (Phattaralerphong and Sinoquet, 2005). The voxel-based approach was shown to work better for full-waveform datasets as these capture the lower strata of the canopy (Reitberger *et al.*, 2009).

Detection of diseased trees in forests, as opposed to crops, using spectroscopy is complicated by spatially complex forest structure, which may differ between sites (Zhang *et al.*, 2008). Based on the derived LiDAR metrics, the potential influence of different canopy architectural effects between the plots was ruled out as trees in both plots had nearly identical extents of canopies. The two derivative metrics (dG and dGE), which

were investigated proved to discriminate poorly between the plots. No analysis could be performed on the red-edge region (690 – 740 nm), which was found to provide early indications of plant stress or disease onset (Penuelas and Filella, 1998; Wilson *et al.*, 1998; Carter and Knapp, 2001; Stone *et al.*, 2001), due to data gaps (i.e. between 685 and 740 nm). The narrow-band indices, apart from PRI, performed poorly, giving way to broad-band indices. The Photochemical Reflectance Index is sensitive to the epoxidation state of the xanthophyll cycle pigments and to photosynthetic processes (Gamon *et al.*, 1992). PRI has been related to light use efficiency both at leaf and canopy scale, chlorophyll fluorescence and non-photochemical quenching, and served a pre-visual indicator of stress (Nichol *et al.*, 2006; Peguero-Pina *et al.*, 2008; Zarco-Tejada *et al.*, 2009). However, at canopy scale, PRI was shown to be strongly affected by different factors, such as viewing and illumination geometry, crown architecture and shadowing (Nichol *et al.*, 2000; Barton and North, 2001; Hernandez-Clemente *et al.*, 2011). As such, it might prove infeasible for use at a larger scale. Among broadband indices, both NGRDI and EVI achieved high accuracies, with EVI exhibiting a more consistent performance, independently of the band placement. NDWI showed a poorer, yet still decent performance (accuracy of up to 78.3%). The results for NDWI have to be taken with caution as the SWIR region had abnormally high noise signal due to the detector not being given enough time to cool down (and hence providing unstable response). Nevertheless, it has been shown that relatively accessible spectral indices, potentially obtainable with broad-band sensors, could be used to investigate stands affected by red band needle blight.

No correlations between the LiDAR metrics or spectral indices and the visually estimated disease levels were found at an individual tree level. The utilised framework for disease level assessment might be insufficiently sensitive to quantify the complexity of disease symptoms. For instance, in the investigated plots there was no correlation between the leaf water content obtained from needles collected from lower branches and the disease level, whilst a significant correlation was found for plot A, in which defoliation was minimal (Chapter 3). Following the guidelines from Bulman et al. (2004), the infection levels were expressed as percentage of total unsuppressed crown volume. As bare branches caused by needle loss are normally excluded from the estimation, the measure does not take into account defoliation. The foliage loss within the canopy extent is not considered either. Another constraining factor is the subjectivity of this measure, and the human error attributed with it. Other measures that could be used are the amount of defoliation given as a visual estimate of crown transparency (Shendryk *et al.*, 2016), dieback, which can be defined as the proportion of dead branches to the total number of

branches (Shendryk *et al.*, 2016), or the combination of both (Coops *et al.*, 2003). Kantola (2013) assessed the defoliation levels by comparing the amount of needles on an investigated tree to an imaginary reference tree with full, healthy foliage. More objective measures defined at a plot level could include LAI or gap fraction (Solberg, 2010). Another limiting factor was the spatial resolution of the hyperspectral imagery (2m), meaning the used pixels extended outside of the investigated tree crowns. With higher spatial resolution imagery, a 'halo' sampling method could be used, which was implemented by Coops *et al.* (2003). The approach ignores the central brightest pixel in the tree crown, and extracts a signature from the surrounding pixels. As red band needle blight normally develops in the lower crown, and then spreads upwards, the 'halo' method may provide a better indication of crown condition.

7.7 Conclusions

The results of leaf spectroscopic measurements presented in Chapter 6 informed the airborne hyperspectral analysis performed on Lodgepole pine plantation sites. A k means clustering algorithm was used to segment individual trees from the LiDAR point cloud, and create canopy cover masks to extract spectral signatures from the plots. Furthermore, a number of metrics describing canopy structure were extracted from the segmented point clusters. A good separation was found between the more diseased and consequently more defoliated plot, and the healthier pine stand using a number of spectral indices: the Enhanced Vegetation Index (72.3–93.2%), Normalised Difference Water Index (56.6–78.3%), Normalised Green-Red Difference Index (49.9–97.1%) and Photochemical Reflectance Index (81.1%). Similarly a distinction was found when intra-canopy distribution of LiDAR returns were analysed. The clearest difference (of 13%) was found in the percentage of ground returns within the canopy extents. Nevertheless, no correlations between the LiDAR metrics or spectral indices and the visually estimated disease levels were found at an individual tree level, which could be due to limited spatial resolution of the imagery and the disease metric being insufficiently sensitive by not taking into account the level of defoliation.

Chapter 8. Discussion and conclusions

8.1 Thesis motivation

Forests provide multiple benefits to the environment, people and wildlife, but they are currently threatened by a number of factors. Monoculture plantation woodlands, such as those commonly grown in the UK, are particularly vulnerable to disturbance events due to the relative species uniformity. Pests and diseases are among the most significant stressors, having a potential to cause significant and widespread damage; for instance, the Dutch elm disease lead to death of over 30 million English elms in the 1960s/70s. Both pathogens and insect populations will generally benefit from climate change in UK, increasing their potential to cause damage. Furthermore, the predicted extended periods of droughts and waterlogging are likely to make trees more vulnerable to attack (Ray *et al.*, 2010). It is believed the future of planted forests will depend on the ability to detect and respond to the threat of biological invasions, especially from non-native pests and diseases (Wingfield et al., 2015).

Red band needle blight, caused by fungus *Dothistroma septosporum*, is one of the non-native diseases currently threatening British forests. It was first recorded in 1997, and since then has caused significant damages to many pine stands across the UK. The disease has a particularly significant economic impact on plantation forests, having a dramatic effect on diameter and height growth of trees in heavily infected stands. Monitoring the spread and intensity of red band needle blight is complicated by the fact that the diseased trees are often only visible from aircraft in the advanced stages of the epidemic. Remote sensing could potentially aid in the early detection of affected stands and in monitoring disease development and spread. Such information on the spatial distribution and intensity of infection would allow for effective planning and implementation of appropriate countermeasures by forest managers. In the case of red band needle blight, those could include stand manipulations or application of copper-based fungicides.

8.2 Revisiting the aim and objectives

The aim of this research was to examine the ability to detect the severity of red band needle blight with different remote sensing technologies, and assess the potential for use of low cost platforms and sensor fusion approaches for infection detection. For this purpose, a range of remote sensing instrumentation and associated analysis techniques

were used, i.e. UAV-borne thermal imagery, as well as airborne hyperspectral and LiDAR data, to address the five objectives of the research, which were:

Objective one: To successfully calibrate a low-cost thermal infrared camera for use in a UAV-borne survey, and test its performance in laboratory and outdoor conditions.

This objective was addressed in Chapter 4. During camera calibration against a flat plate blackbody source, a significant non-uniformity was found across the camera's field of view with differences exceeding 2°C in some cases. In thermography of plants, where differences in temperature are usually small (in this thesis maximum recorded difference between trees was 3.5°C), such non-uniformity, if left unaccounted for, might significantly affect the results when measurements originating from different pixels are compared. Following the correction utilising the two-point calibration technique, the non-uniformity across the image was minimised; 95.4% (2σ) of the pixels fell within ± 0.14 K of the reference temperature. Field-based tests of the camera, placed 25 and 7 metres away from the calibration target, showed that it is capable of obtaining absolute temperatures of non-blackbody objects under typical UAV operation wind speed range (up to 10 mph, with gusts up to 15 mph), providing the emissivity of surfaces is accurately known; 98% of target's temperature readings remained within the accuracy threshold of reference thermocouple measurements. Nevertheless, laboratory tests suggested that a rapid change in camera temperature (i.e. 0.12-0.28°C per minute) is reflected in subsequently acquired images. However, no such effect was observed with gradual changing temperatures (i.e. 0.02°C per minute).

Results of Chapter 4 indicate that low-cost thermal sensors, deployable on UAVs have the capability to provide radiometrically accurate temperature measurements of surfaces with known emissivity. However, in order to ensure consistent temperature readings with a microbolometer camera, thermal surveys should not be conducted within several minutes of rapid camera temperature change. Furthermore, the investigated camera required stabilisation prior to undertaking any imaging; the stabilisation period was shown to last 30 minutes following the turning on of the camera. The expected ambient temperature change rate experienced during a UAV launch should have no significant effect on the quality of thermal imagery. Based on the international standard atmosphere model, for UAV operation at altitudes of 200 and 400 feet, the expected ambient temperature decrease would have been 0.396 and 0.792°C (which is of similar magnitude as in the laboratory datasets acquired under stable conditions).

Objective two: To assess the potential for using the calibrated low-cost thermal infrared sensor to investigate tree stress in coniferous species and examine the influence of data acquisition timing on the signal.

In Chapter 5 the thermal camera was used to investigate stress-induced temperature increase in young drought-stressed larch trees and in a young pine plantation infected with red band needle blight. The greenhouse experiments on larch trees showed that the thermal camera, following a basic normalisation for background radiation, is capable of monitoring both the spatial and temporal variation of canopy temperature. The differences between image values and thermocouples positioned at different canopy parts were relatively stable throughout the experiments (exhibiting standard deviation of temperature offsets of 0.20°C in the first experiment and 0.32°C in the second experiment). Very mild stress (33% soil moisture level) did not exhibit itself, as the temperature readings for both stressed and healthy plants were similar. However, under higher stress (7% soil moisture level), there was a clear distinction (temperature difference of 1.5°C) between the plants, showing potential for using low-cost thermography to investigate stress in conifers.

In the UAV-borne survey, a statistically significant correlation between canopy temperatures and infection levels was found (correlation coefficient of 0.64 at $p < 0.001$). Furthermore, the standard deviation of the crown temperature exhibited weak, but significant correlation (correlation coefficient of 0.36 at $p < 0.001$). The combination of canopy temperatures and standard deviations in a partial least squares regression improved the observed relationship with the estimated disease level. However, as only 44% of the observed variation could be explained by the model, the thermal images could not be used on their own to assess the disease level. Only a slight improvement was observed when LiDAR structural metrics were incorporated in the analysis (47% of explained variation); as the defoliation within the plot was minimal, it could therefore remain undetected by LiDAR.

A change in environmental conditions altered the magnitude of differences between canopy temperatures. In the greenhouse experiment, rising radiation level and ambient temperature led to an increase in the difference between the average canopy temperatures. In the UAV-borne survey, no significant relationship was found between the canopy temperature and the field-assessed disease level in the morning flight (10:15), whilst for all later flights (11:10, 12:10, 13:15, 15:10 and 16:50) a significant correlation ranging from 52 to 64% was found, with the strongest relationship obtained at the time of highest solar radiation. The performance of thermography when applied to conifer stress

investigation may therefore depend on environmental conditions under which the data are acquired. In theory, the weather conditions favouring increased transpiration rates (such as high incoming radiation and low relative humidity) should accentuate the differences between the trees, as stomata of the stressed plants would be closed to prevent the loss of water, which in turn should lead to an increase in leaf and canopy temperature. This is partially reflected by this study as the highest correlations with disease levels were achieved for times when the intermittent sunshine was present. Research in a fully controlled environment could quantify the influence of different environmental factors, and define conditions under which thermal imagery can be used most effectively in different climates. Such guidance might help with planning UAV-borne campaigns utilising low-cost sensors by identification of best acquisition times, when temperature differences between plants are expected to be greatest.

Objective three: To investigate the spectral properties of diseased needles, derive the most distinctive disease indicators, and test their transferability to airborne imagery.

Chapter 6 presented the analysis of leaf spectroscopic measurements performed on green and partially chlorotic needles affected by red band needle blight. The reflectance changes (decrease in the NIR and increase in the red and SWIR regions, and broadening of the peak located near 550 nm) were in accordance with typical symptoms caused by an onset of stress, expected to be exhibited by needles affected by red band needle blight as well (that is chlorosis and decreasing water content). Three approaches for spectra analysis were investigated: spectral indices, derivative-based indices and continuum removal analysis, all of which highlighted the green, red and NIR parts of the electromagnetic spectrum as the most promising.

Among the derivative metrics tested for separating the spectral response of the two sample groups, the best were based on first order derivative values retrieved in the green to red-edge region (leave-one-out cross validation accuracy of 87.5–90%). Similar parts of the electromagnetic spectrum were found to yield the best performance during the continuum removal analysis, i.e. the two chlorophyll absorption features in the green and red regions, followed by the water feature located on the NIR plateau. However, the retrieved shape metrics on average performed poorer, suggesting the use of derivatives would be more appropriate for detecting the infection. The broadband vegetation indices showed the most varied performance, dependent on the band placement (for instance the performance of RDVI ranged between 55 and 82.5%). The best index was found to be NGRDI (up to 90.0%), combining green and NIR regions, followed by EVI (77.5 –

87.5%). NDWI, which is sensitive to water content within the leaf also showed promising results (70.0 – 85.0%). The investigated narrow-band indices showed a more consistent performance, with all of them exceeding 75% success rate, and the highest score of 87.5% achieved by MTVI1. A comparison was made between metrics retrieved for the upper canopy spectra (green foliage) and the estimated tree disease levels, but no significant correlations were found. Stone *et al.* (2003) in their study of red band needle blight found highly significant correlations between needle damage categories and vegetation indices, with the healthy green needle category exhibiting very little variation. The ability to detect red band needle blight in foliage, therefore appears to be dependent on the development of visual symptoms, meaning presymptomatic detection of the disease might not be possible.

The results presented in Chapter 6 informed the airborne hyperspectral analysis performed on Lodgepole pine plantation sites (Chapter 7). A good separation was found between the more diseased and consequently more defoliated plot, and the healthier pine stand using a number of spectral indices: EVI (72.3–93.2%), NDWI (56.6–78.3%), NGRDI (49.9–97.1%) and PRI (81.1%). Although, PRI might prove infeasible for use over a larger area as it was shown to be strongly affected by different factors, such as viewing and illumination geometry, crown architecture and shadowing (Nichol *et al.*, 2000; Barton and North, 2001; Hernandez-Clemente *et al.*, 2011). No correlations between the spectral indices and the visually estimated disease levels were found at an individual tree level, which could be due the disease metric being insufficiently sensitive and the limited spatial resolution of the imagery (2m), meaning the used pixels extended outside of the investigated tree crowns. Nevertheless, it has been shown that broad-band spectral indices, potentially obtainable with multispectral sensors, could be used to investigate stands affected by red band needle blight.

Objective four: To examine canopy structural changes caused by the disease-induced defoliation.

Objective four was tackled in Chapter 7. A k-means clustering algorithm was used to segment individual trees from the LiDAR point cloud, and extract a number of metrics describing canopy structure. A distinction was found when intra-canopy distribution of LiDAR returns were analysed. Both plots were characterised by higher density of points in the upper canopy, but the proportions were more shifted in the more diseased plot, with significantly fewer echoes coming from the lower canopy. This suggests lower foliage density in those parts, which is expected to be a result of red band needle blight

defoliation. Red band needle blight infection usually starts in the lower parts of the tree on older foliage and spreads upward, systematically defoliating the affected tree in a bottom-up manner. The clearest difference (13%) was found in the percentage of ground returns within the canopy extents, with greater number of laser pulses reaching the ground in the more diseased plot. As a laser pulse is more likely to penetrate the canopy layer and reach the ground when trees' lose foliage, this indicator can also be linked to defoliation. Stepwise discriminant analysis identified the percentage of ground returns and the 50th percentile as the most useful features for separation of trees between plots, yielding an accuracy of 79.4%. This indicates a potential for using LiDAR metrics to detect disease-induced defoliation, possibly at a tree level if spatial resolution allows. For instance, Shendryk *et al.* (2016) classified individual tree health status in terms of crown dieback in an eucalypt forest using full-waveform LiDAR with a point density of 36 points per m^2.

No differences in canopy volume were observed; however, this could have been caused by the flawed nature of the applied convex hull approach, which does not account for inter-crown variability (such as foliage distribution, including gaps between branches). Similarly, no correlations between the LiDAR metrics and the visually estimated disease levels were found at an individual tree level, which could be due to the disease metric being insufficiently sensitive. As bare branches caused by needle loss are normally excluded from the estimation, the measure does not take into account defoliation. The foliage loss within the canopy extent is not considered either. To fully evaluate the applicability of LiDAR metrics for a tree level assessment, other tree condition measures should be investigated, such as crown transparency (Shendryk *et al.*, 2016), dieback (Shendryk *et al.*, 2016), LAI or gap fraction (Solberg, 2010).

Objective five: To discuss the potential of integration of different remotely sensed data for improved detection of the disease, and the potential of low-cost platforms for assessment of tree health.

Whilst the previous four objectives were addressed separately in previous chapters, the final objective requires drawing from all results of this thesis and broader literature. It will therefore be tackled in the following sections. The potential of integration of the three different remotely sensed data used in this work (thermal, hyperspectral and LiDAR) for improved detection of the disease is discussed in Chapter 8 Section 2.1. The prospects of using low-cost platforms (UAVs) in the forest sector, in particular for assessing tree health, are explored in Chapter 8 Section 2.2.

8.2.1 Potential integration of sensors for improved disease detection

This thesis examined the ability to detect the severity of red band needle blight with different remote sensing technologies. In the UAV-borne thermal study (Chapter 5), an increase in tree crown temperature was observed in the investigated pines with increasing disease severity. This temperature increase can be related to the needle damage symptoms caused by the disease, i.e. loss of cellular integrity, necrosis, and eventual desiccation (Stone *et al.*, 2003). In Chapter 7, a good separation was found between the more diseased plot, and the healthier pine stand using a number of spectral indices sensitive to discolouration of the foliage (a characteristic symptom of red band needle blight). Similarly, a distinction was found when intra-canopy distribution of LiDAR returns was analysed, which can be linked to disease-induced defoliation (Chapter 7).

Integration of different remote sensing datasets for detection of disease severity could not be meaningfully investigated within this research due to availability and limitations of the acquired data. The thermal study was based in Plot A, for which LiDAR data was also available. Inclusion of LiDAR metrics was attempted, but provided only a slight improvement to the relationship (a likely effect of minimal level of defoliation present within the plot). For plots C and D, representing heavily and mildly diseased stands, LiDAR and hyperspectral data (of much lower spatial resolution than anticipated) were available. There was a clear distinction between the plots, but no relationships could be established at a tree level with the disease severity. This could be attributed to limited spatial resolution of the imagery (2m) and the disease metric being insufficiently sensitive by not taking into account the level of defoliation. Nevertheless, it was shown that each of the investigated datasets is sensitive to the disease onset.

Among the main symptoms of a disease onset are the breakdown of the photosynthetic pigments, water shortage, loss of foliage and alterations in transpiration. Each of those physiological responses can potentially be detected with different remote sensing technologies, as shown in Figure 8.1. Spectroscopy is capable of detecting changes to water content and photosynthetic pigments concentration, as well as defoliation, thermography is sensitive to alterations in transpiration and leaf water content, whilst LiDAR can provide information on structural changes. Current trends in research for detection of infections, almost exclusively involves the use of a single imaging sensor, i.e. multispectral or hyperspectral imagery. However, using individual imaging technology could lead to confusion between stressed and diseased forest stands. Leckie *et al.* (2004), whilst attempting to identify laminated root rot in a Douglas fir forest with

multispectral imagery, found that some of the detected damage zones corresponded to trees, which were not infected, but exhibited poor health. Other false alarms included isolated trees with similar characteristics as the infected trees in locations unrelated to root disease activity. This is due to the fact that there are many abiotic (temperature, water, gases, minerals) and biotic (induced by micro-organisms, animals, plants, anthropogenic factors) stresses that affect plant functioning (Chaerle *et al.*, 2009). Any individual stress can disturb a wide range of different processes, which have the potential of being separately identified with remote sensing technology. For instance, drought leads to stomatal closure, decrease of photosynthesis rate, reduced growth and leaf wilting, and can result in the loss of photosynthetic pigments (Jones and Schofield, 2008). Any given symptom can also arise from a wide range of alternative stresses. For example, leaf temperature rise can be triggered by very different stressors, such as drought, viral infection, salinity or herbicides (Chaerle *et al.*, 2009). As many different stress factors have common intermediate responses that can potentially be detected, identification of the primary stressor when using individual imaging technology is difficult. Further information would be required to distinguish between the possible causes.
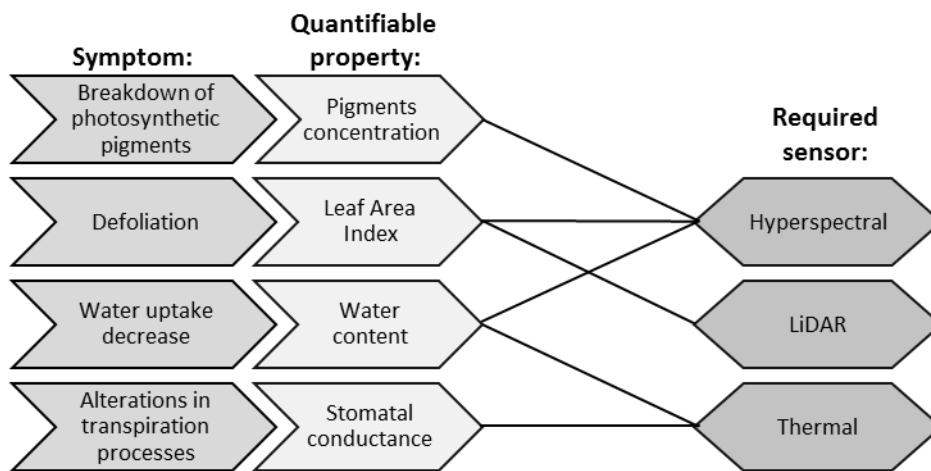
Figure 8.1: Relationships between disease symptoms and quantifiable properties measuring them, together with required remote sensing technologies.

Combining information from a range of sensors, detecting different physiological responses, could enhance the ability to diagnose and quantify the infection. Remote sensing fusion for detection of disease severity in woody plants has only recently started being considered in agriculture. Calderon *et al.* (2015) used hyperspectral and thermal imagery to classify five stages of Verticillium Wilt in olive trees achieving overall accuracy of 59.0% and 79.2% (depending on a method), and identified canopy

temperature depression and chlorophyll fluorescence as early remote sensing indicators of the disease. Lopez-Lopez *et al.* (2016) using the same set-up detected almond red leaf blotch at three severity classes (average overall accuracy of 88.5%). Sankaran *et al.* (2013) utilised visible-NIR part of the spectrum (440–900 nm) and thermal imagery for detecting citrus greening disease (Huanglongbing), and distinguished diseased from healthy trees, reporting overall classification accuracy of 87%.

However, to date no studies exploring a multi-sensor approach to detect diseases in forests have been conducted, leaving a major research gap. Further research would be required to assess whether the integration of different remote sensing data can improve the ability to detect and assess the level of red band needle blight infection. To develop a more comprehensive understanding of changes in the canopy following the infection, a multi-temporal approach could also be employed. Multi-temporal remote sensing has long been used to detect insect-induced defoliation in both coniferous and broadleaved forests (Muchoney and Haack, 1994; Radeloff *et al.*, 1999; Hall *et al.*, 2003; Kharuk *et al.*, 2004; Fraser and Latifovic, 2005; Solberg *et al.*, 2006; Franklin *et al.*, 2008; Eklundh *et al.*, 2009; Babst *et al.*, 2010; Somers *et al.*, 2010). The analysis of imagery from a number of years may improve the detection accuracy, as an increased number of repeat observations would allow characterisation and interpretation of the reflectance patterns before and at different stages of the disease. For instance, the analysis of forest stands prior to disturbance, after gypsy moth defoliation and during refoliation, resulted in an improved detection accuracy of areas infested by gypsy moth (Hurley *et al.*, 2004).

8.2.2 Potential for use of UAVs in the forestry

The use of conventional remote sensing data obtained from airborne and satellite platforms requires making trade-offs between costs, operational flexibility, as well as spatial and temporal resolution. In forestry studies, the main challenge arises from the need for high spatial resolution data to identify individual diseased trees or monitor areas of fragmented forest cover, typical for the UK. Such data are usually obtained with low temporal frequency, due to limitations of satellite revisit times and high costs of aerial imagery or acquisition from commercial satellites. In addition, cloud cover significantly restricts the availability of suitable data in the UK. UAVs could supplement conventional remote sensing data acquisition, and allow for image collection, even under cloud cover conditions. UAV technology is now mainstream and affordable, although the limited payload restricting the size of sensors still remains an issue. UAVs have already been used in a wide range of environmental monitoring applications, such as mapping

geothermal environments (Nishar *et al.*, 2016), quantifying retreat of an arctic glacier (Whitehead *et al.*, 2013), counting elephants (Vermeulen *et al.*, 2013), or even for surveys of humpback whales (Hodgson *et al.*, 2017).

The main advantage of UAV-borne data is the very high level of detail, giving the ability to perform analysis at an individual tree level. The use of a UAV platform in Chapter 5 not only enabled retrieval of canopy temperature at an individual tree-level, but also allowed for extraction of canopy temperature variation (i.e. standard deviation), which improved the observed relationship with disease severity. In Chapter 7 the tree-level investigation of spectral response was inhibited by the limited spatial resolution (2 m) of airborne data, with pixels extending outside of the investigated tree crowns. Higher resolution imagery could be particularly advantageous for assessing the severity of red band needle blight, allowing application of a similar approach to Coops *et al.* (2003), who using of a "halo" sampling approach could detect three severity levels of infection with an accuracy of over 70%. The 'halo' sampling method ignores the central brightest pixel in the tree crown, and extracts a signature from the surrounding pixels. As red band needle blight normally develops in the lower crown, and then spreads upwards, such approach may provide a better indication of crown condition.

UAVs are also praised for being a low-cost and flexible solution. The user can optimise the desired timing of data collection, for example to effectively monitor phenological stages (Berra *et al.*, 2016), to avoid cloud cover or for rapid data collection following a wildfire (Merino *et al.*, 2012) or pest outbreak (Lehmann *et al.*, 2015). Such capability can be particularly useful for regions characterised by a persistent cloud cover and consequently offering narrow acquisition windows, limiting the applicability of performing airborne surveys (such as was the case in this project).

Over the past decade, UAVs have been used to collect data for various forestry purposes. Potential of UAV-borne imagery for performing forest inventories was shown by Puliti *et al.* (2015) and Lisein *et al.* (2013). Puliti *et al.* (2015) retrieved mean height, dominant height, stem number, basal area, and stem volume with an accuracy comparable to that obtained using other popular remotely sensed data, such as airborne LiDAR. Similarly, Lisein *et al.* (2013) showed that the photogrammetric canopy height model was of good quality for deciduous stands to predict dominant height and individual tree height. Furthermore, UAV-borne LiDAR systems, achieving very high point densities, were shown to further improve the accuracy of individual tree crown forest inventories, yielding accurate results when predicting single-tree biophysical properties such as

location, stem number, height, DBH, crown width, crown base height, biomass change, and rate of pruning (Jaakkola *et al.*, 2010; Wallace *et al.*, 2012; Wallace, 2013; Wallace *et al.*, 2014). Nevertheless, the use of UAV-borne LiDAR is currently limited exclusively to research activities due to its limitations, including the small coverage area, high cost of the equipment, and the need for specific technical expertise to process the data (Salami *et al.*, 2014).

UAV-borne imagery has also been used to estimate soil displacement in steep terrain caused by timber harvest (Pierzchala *et al.*, 2014), and to analyse gap patterns in forests with different land use intensities (Getzin *et al.*, 2014). The use of UAVs for forest fires has been explored as well. Merino *et al.* (2012) used a heterogeneous fleet of three UAVs with cameras and thermal sensors for detection and monitoring of a controlled forest fire, including real-time computation of the evolution of the fire front shape. On a larger scale, Ambrosia *et al.* (2011) used a big unmanned aircraft called Ikhana (a modified civilian-version of MQ-9 Reaper), which is 36 feet long with a 66-foot wingspan, to obtain high-altitude imagery for collection of accurate real-time fire information.

In recent years, UAV-borne multispectral and hyperspectral approaches have started being used for forest studies. Nasi *et al.* (2015) mapped bark beetle (*Ips typographus L.*) damage at a tree level in an urban forest with a miniaturised hyperspectral sensor. Overall accuracies of 90% for two classes (healthy and dead) and 76% for three classes (healthy, infested, and dead) were achieved. Miniaturised lightweight hyperspectral sensors, such as the one used in that study, have only started emerging recently. However, like LiDAR systems, they are expensive, and as such they are currently being used only sporadically. Nevertheless, the significant potential of low-cost multispectral sensors has been shown by other studies. Berra *et al.* (2016) monitored spring phenology at individual tree level with Red-Green-Blue (RGB) colour channels. Michez *et al.* (2016a) acquired imagery with two off-the-shelf cameras, one of which was adapted for near-infrared acquisition, to map invasive species in a riparian forest. In a different study, Michez *et al.* (2016b) classified four deciduous riparian forest species using multi-temporal images acquired during a vegetative period, achieving accuracies of 79.5% and 84.1%. Furthermore, the health status of black alder trees (*Alnus glutinosa*) infected with *Phytophthora alni* was mapped, focusing on the distinction between symptomatic and asymptomatic foliage; accuracies of over 90% were achieved, with most variables derived from the NIR imagery. With a similar camera set-up, Lehmann *et al.* (2015) produced maps of

infestation by the oak splendour beetle (*Agrilus biguttatus*). Healthy, infested and dead branches were classified with producer's accuracy of 86-89%, 69-83% and 71-79%.

The small number of studies utilising low-cost UAVs, as well this thesis, show a great potential for this technology to be used as a tool for forest health monitoring at a local scale. The main constraint of UAVs is that they are unable to cover large spatial extents due to the limited flight endurance, making them an effective solution only for small-area inspections. Regulatory frameworks further restrict the use of UAVs, which has an impact on the types of data that can be acquired. In the United Kingdom, UAVs have to be operated at a flying height below 400 feet (122 m) and within a visual range at all times, which will depend on the size, shape and colour of the aircraft, as well as the atmospheric conditions. The size of the survey area is therefore limited meaning multiple flights might be needed to cover larger sites. Another limitation is the limited payload UAVs offer, which limits the number and types of sensors that can be mounted. Nevertheless, integrating UAVs with satellite instruments could result in a comprehensive forest health monitoring programme. Satellite imagery could be analysed to highlight diseased and stressed areas at a regional level, whilst more detailed assessments at an individual tree level in these areas could then be performed utilising UAVs. Repeated UAV surveys could be performed at low-cost, giving an insight into the disease progression and spread in the infected areas. Such information on spatial distribution and intensity of infection would allow for effective planning and implementation of appropriate countermeasures by forest managers.

8.3 Suggestions for future research directions

While this thesis has addressed the use of thermal, hyperspectral and LiDAR sensors for detecting the severity of red band needle blight, there remain a number of significant challenges to be addressed before a true multi-sensor and/or UAV-based approach to disease monitoring can be operationally employed. The most significant of these and key areas for future research building upon this thesis are:

Multi-temporal analysis of LiDAR metrics to develop a more comprehensive understanding of changes in the canopy following the infection.

The effects of disturbance events, such as insect or disease outbreaks, are most commonly characterised through the examination of a temporal sequence of images, allowing quantification of changes. Multi-temporal satellite imagery has long been used to detect insect-induced defoliation in both coniferous and broadleaved forests, including such

insects as moths (Muchoney and Haack, 1994; Kharuk *et al.*, 2004; Babst *et al.*, 2010), budworms (Radeloff *et al.*, 1999; Franklin *et al.*, 2008), pine sawfly (Eklundh *et al.*, 2009), and others (Hall *et al.*, 2003; Fraser and Latifovic, 2005; Somers *et al.*, 2010). The main advantage of such approach is that a record of spectral reflectance change can be extracted to characterise both the magnitude and direction of physiological processes or disturbance events (Hostert *et al.*, 2003). For example, the analysis of three Landsat images of forest stands prior to disturbance, after gypsy moth defoliation and during refoliation, resulted in a stronger and less ambiguous signal of gypsy moth damage, and consequently an improved detection accuracy of infested areas (Hurley *et al.*, 2004).

A multi-temporal LiDAR dataset could not only help develop a more comprehensive understanding of changes in the canopy following the infection, but also provide an indication of the year-to-year defoliation caused by the disease. Within this thesis the metrics, which were identified as the most useful features for separation of trees between the plots were the percentage of ground returns and the 50th percentile. Other metrics which could prove to be useful, and therefore worth investigation in the future, are those implemented by Shendryk *et al.* (2016). These include the average returned pulse width below median height, average range-corrected intensity above median height, the ratio of laser returns from leaves at the tree trunk and returns at the tree periphery, and the ratio of the number of laser returns from woody components to number of laser returns from leaves. These were found to be sensitive to crown dieback and transparency, and thus could be transferable to analysis of red band needle blight defoliation. However, they would require full-waveform datasets with high point density.

No differences in the canopy volume between plots at different disease stages were observed; however, this could have been a result of the convex hull approach employed. In the future other approaches for retrieving canopy volume could be investigated, such as the alpha shapes, which are a common alternative. A predefined alpha parameter allows restriction of the number of facets belonging to the minimum convex polygon, defining the level of detail in the obtained shape (Koch *et al.*, 2014). The most promising approach currently seems to be the one suggested by Kato *et al.* (2009), which derives two-dimensional horizontal convex hulls at different heights to select outline points, and then performs wrapped surface reconstruction (by employing radial basis functions and an isosurface). Voxel-based methods have also been used for reconstruction of the tree shape and the calculation of total crown volume (Popescu and Zhao, 2008; Wang *et al.*, 2008);

however, the results depend on the spatial allocation and voxel resolution (Phattaralerphong and Sinoquet, 2005).

One of the issues encountered in this research was the fact that the utilised framework for disease level assessment might be insufficiently sensitive to quantify the complexity of disease symptoms. Following the guidelines from Bulman et al. (2004), the infection levels were expressed as percentage of total unsuppressed crown volume. As bare branches caused by needle loss are normally excluded from the estimation, the measure does not take into account defoliation. The foliage loss within the canopy extent is not considered either. In plots C and D there was no correlation between the leaf water content obtained from needles collected from lower branches and the disease level, whilst a significant correlation was found for plot A, in which defoliation was minimal (Chapter 3). Another constraining factor is the subjectivity of this measure, and the human error attributed with it. In future other measures of tree health status should be investigated as well. These could include the amount of defoliation given as a visual estimate of crown transparency (Shendryk *et al.*, 2016), dieback, which can be defined as the proportion of dead branches to the total number of branches (Shendryk *et al.*, 2016), or the combination of both (Coops *et al.*, 2003). Other than that, Kantola (2013) assessed the defoliation levels by comparing the amount of needles on an investigated tree to an imaginary reference tree with full, healthy foliage. More objective measures defined at a plot level could also include LAI or gap fraction (Solberg, 2010). For instance, Solberg *et al.* (2006) detected pine sawfly defoliation in terms of estimated LAI changes using multi-temporal laser scanning acquisitions.

Testing the identified spectral analysis approaches on high spatial resolution multispectral and/or hyperspectral imagery, facilitating a tree level analysis.

Leaf-level spectroscopy of diseased needles informed airborne hyperspectral analysis, which showed a good separation between the more diseased and consequently more defoliated plot, and the healthier pine stand using a number of spectral indices: EVI, NDWI, NGRDI and PRI. During leaf-level reflectance analysis, derivative metrics were also shown to be a promising approach, with best performing metrics being based on first derivative values in the green and red regions, as well as the NIR plateau. However, due to gaps within the airborne spectra, derivative analysis at a plot level had to be restricted only to two metrics in the green region, which performed poorly. Furthermore, during the analysis it was discovered that a miscalibration of the VNIR and SWIR detectors within the AisaFENIX instrument occurred. Prior to data collection, the SWIR detector was not

given enough time to cool down resulting in an unstable response over time, and abnormally high noise signal. It was therefore concluded that for this dataset, bands from the two separate detectors should not be combined within a single vegetation index. As a result a number of indices (such as DSWI, NDSWIR and WI) were not investigated at a plot level. The limited spatial resolution of the imagery also prevented a meaningful analysis at an individual tree level (as the used pixels extended outside of the investigated tree crowns). Given the quality of airborne data was far from ideal, retesting the investigated approaches, together with indices and derivative metrics which could not be calculated at a plot level, would be beneficial for identification of best methods for detecting the infection.

Using higher spatial resolution airborne or UAV-borne imagery would facilitate a tree-level analysis. For this purpose low-cost UAV-borne multispectral sensors, such as the ones used by Lehmann *et al.* (2015), Berra *et al.* (2016) or Michez *et al.* (2016a), or miniaturised hyperspectral sensors, such as the one used by Nasi *et al.* (2015), could be employed. With high resolution imagery a 'halo' sampling method implemented by Coops *et al.* (2003) could be applied. The approach ignores the central brightest pixel in the tree crown, and extracts a signature from the surrounding pixels. As red band needle blight normally develops in the lower crown, and then spreads upwards, the 'halo' method may provide a better indication of crown condition. Furthermore, the variability of reflectance within the crown could be investigated, potentially providing an indication of the disease level; in Chapter 6 leaf samples from the top and bottom canopy were shown to have a significantly different response.

Retrieval of thermal metrics allowing for multi-spatial and/or multi-temporal investigation of thermal response of trees in forest conditions.

This thesis found statistically significant correlations between canopy temperatures and red band needle blight infection levels. Even though it appears the thermal images cannot be used on their own to assess the disease level (as only 44% of the observed variation could be explained by the model), they could potentially enhance the ability to diagnose and quantify the infection in a multi-sensor approach.

The method used in this study of direct investigation of canopy temperature can only be applied in a relative mode, comparing plants imaged under exactly the same conditions (in practice that means plants located within the same image). This is due to leaf and canopy temperature being dependent on air temperature, humidity, wind speed and

absorbed net radiation (Jones and Schofield, 2008). The use of thermal indices (described in Section 5.2), normalising the results for environmental variation, could overcome this problem and allow for multi-spatial and/or multi-temporal comparison, required for operational use of the sensor. The most commonly used stress indices, which could be investigated for this purpose include the CTD, CWSI and Ig. The thermal stress indices have already been widely and successfully applied to agricultural crops (Alderfasi and Nielsen, 2001; Erdem *et al.*, 2010; Taghvaeian *et al.*, 2014). Yet, the use of thermography for investigation of stress in trees has been predominantly limited to orchards (Berni *et al.*, 2009a; Gonzalez-Dugo *et al.*, 2012; Ballester *et al.*, 2013), and no attention has been given to forest environments.

Calculation of thermal stress indices would require accurate retrieval of tree temperature, which can be achieved by employing an empirical line correction. Using at least three contrasting ground targets of known emissivity, whose temperatures are continuously being monitored, radiometric calibration coefficients can be calculated, allowing brightness temperature (as measured by the camera) to be related to the actual surface temperature. The third target provides redundancy and allows assessment of the quality of fit between recorded and actual temperatures. Further validation can be provided by measuring canopy temperature using thermo-radiometers. Calibration targets would normally be imaged at the beginning and the end of the survey (Santesteban *et al.*, 2017), although additional mid-flight calibrations (Gomez-Candon *et al.*, 2016) may be preferred on longer flights or if weather conditions are rapidly changing.

In the UAV-borne survey presented in this thesis, the differences between differently diseased trees were most accentuated at the time of solar noon, when the radiation levels were highest. It was therefore concluded UAV-borne thermal surveys investigating tree stress should be performed at the time of maximum evaporative demand. Maximum evaporative demand is normally expected to occur in the early afternoon (Phillips *et al.*, 1997), when air temperatures are driven by peak radiation. However, other environmental factors, such as humidity or wind speed, have also been shown to affect the evaporative demand, and consequently temperature at a canopy level (Leinonen *et al.*, 2006). Maes and Steppe (2012), based on modelled discriminative power, suggested the optimal conditions for application of CSWI and Ig stress indices include high air temperature, incoming shortwave radiation and vapour pressure deficit and low wind speed. Furthermore, they showed the CTD is adversely affected by weather conditions. The question remains how the different environmental conditions may influence the ability to

distinguish stressed plants, in particular in countries with moderate air temperatures year-round, such as Scotland. A test study on a subset of plants under controlled conditions (for instance in an environmental chamber) could help identify best acquisition times, when temperature differences between stressed and healthy plants are expected to be greatest. Such guidance might help with planning UAV-borne campaigns utilising low-cost sensor.

Multi-sensor analysis of forest stands affected by red band needle blight.

Current trends in research for detection of infections, almost exclusively involves the use of a single imaging sensor, i.e. multispectral or hyperspectral imagery. However, as many different stress factors have common intermediate responses, identification of the primary stressor is hindered when individual imaging technology is used. The combination of metrics/indices derived from a range of sensors may provide increased interpretation capabilities and more reliable results since data with different characteristics are combined. Remote sensing data fusion is a research area with growing importance, aiming to optimise information extraction (Gomez-Chova et al., 2015). The fusion can occur at different processing stages, depending on the application. The main commonly recognised levels are: pixel level fusion, feature level fusion and decision level fusion (Pohl and van Genderen, 2016). As an extension of this research and of previous suggestions for future work a decision level fusion would be the preferred choice; it involves processing data separately to obtain information, and exploring it to obtain a final fused result (Pohl and van Genderen, 2016). Decision level fusion would allow simultaneous investigation of different metrics and/or indices extracted from a range of sensors (i.e. hyperspectral, thermal and LiDAR) in the search of most promising combinations for disease level assessment.

Derivation of meaningful and reliable results from a vast array of datasets requires advanced analytical and numerical fusion techniques. Data mining is a computational process of searching and discovering valuable information in large volumes of data, and is currently an emerging research field. There are many different data mining techniques, among which, Artificial Neural Network (ANN) is one of the most widely used due to its ability to learn complex patterns quickly through iterative learning cycles of representative data. ANNs were inspired on biological neural networks with processing elements having similar behaviours as a biological neuron (Mitchell, 1997). The Support Vector Machine (SVM) is another learning technique, which transforms data into a high-dimensional space and constructs a hyperplane, aiming to maximise the distance

between it and the nearest data point of any of the input classes (Cortes and Vapnik, 1995; Vapnik, 1999). Other than that, decision tree algorithms are commonly implemented. Although these are more directly suited to classification as data are sorted through the decision tree structure to fall into a predefined category (Quinlan, 1986; Breiman, 2001). Data mining techniques have started being widely used in remote sensing field for such applications as tree species classification (Immitzer et al., 2012; Matsuki et al., 2015), land cover mapping (Parsons and Carpenter, 2003; Pal and Mather, 2005; Rodriguez-Galiano et al., 2012) or examination of large multi-temporal datasets (Mitsa, 2010). A multi-sensor analysis of red band needle blight infection would require investigation of different data mining techniques, such as ANNs and SVMs, and evaluation of their performance in terms of disease level assessment.

8.4 Conclusions

The research presented in this thesis has demonstrated the potential for the use of thermographic, hyperspectral and LiDAR sensors for detection of red band needle blight-induced changes in pine trees. The three datasets are sensitive to different disease symptoms, i.e. thermography to alterations in transpiration, LiDAR to defoliation, and hyperspectral imagery to changes in leaf biochemical properties. The combination of the sensors could potentially enhance the ability to diagnose infection. During the hyperspectral analysis, common broad-band indices were generally shown to be more reliable, and consequently superior to narrow-band indices, demonstrating scope for use of multispectral imagery, providing bands are carefully chosen. There is therefore vast potential for the use of UAVs with low-cost sensors, currently capable of providing multispectral imagery. The very fine spatial resolution provided by such platforms would facilitate tree-level analysis of diseased trees.

References

Adelabu, S., Mutanga, O. and Adam, E. (2014) 'Evaluating the impact of red-edge band from Rapideye image for classifying insect defoliation levels', *ISPRS Journal of Photogrammetry and Remote Sensing*, 95, pp. 34-41.

Alderfasi, A.A. and Nielsen, D.C. (2001) 'Use of crop water stress index for monitoring water status and scheduling irrigation in wheat', *Agricultural Water Management*, 47(1), pp. 69-75.

Alila, Y., Kuras, P.K., Schnorbus, M. and Hudson, R. (2009) 'Forests and floods: A new paradigm sheds light on age-old controversies', *Water Resources Research*, 45(8).

Alonso, L., Gómez-Chova, L., Vila-Frances, J., Amoros-Lopez, J., Guanter, L., Calpe, J. and Moreno, J. (2007) Sensitivity analysis of the fraunhofer line discrimination method for the measurement of chlorophyll fluorescence using a field spectroradiometer. *Geoscience and Remote Sensing Symposium, 2007. IGARSS 2007. IEEE International*. 23-28 July 2007.

Alonso, L., Gómez-Chova, L., Vila-Frances, J., Amoros-Lopez, J., Guanter, L., Calpe, J. and Moreno, J. (2008) 'Improved Fraunhofer Line Discrimination Method for Vegetation Fluorescence Quantification', *Geoscience and Remote Sensing Letters, IEEE*, 5(4), pp. 620-624.

Ambrosia, V.G., Wegener, S., Zajkowski, T., Sullivan, D.V., Buechel, S., Enomoto, F., Lobitz, B., Johan, S., Brass, J. and Hinkley, E. (2011) 'The Ikhana unmanned airborne system (UAS) western states fire imaging missions: from concept to reality (2006-2010)', *Geocarto International*, 26(2), pp. 85-101.

Apan, A., Held, A., Phinn, S. and Markley, J. (2004) 'Detecting sugarcane 'orange rust' disease using EO-1 Hyperion hyperspectral imagery', *International Journal of Remote Sensing*, 25(2), pp. 489-498.

Babst, F., Esper, J. and Parlow, E. (2010) 'Landsat TM/ETM+ and tree-ring based assessment of spatiotemporal patterns of the autumnal moth (Epirrita autumnata) in northernmost Fennoscandia', *Remote Sensing of Environment*, 114(3), pp. 637-646.

Bakoariniaina, L.N., Kusky, T. and Raharimahefa, T. (2006) 'Disappearing Lake Alaotra: Monitoring catastrophic erosion, waterway silting, and land degradation hazards in Madagascar using Landsat imagery', *Journal of African Earth Sciences*, 44(2), pp. 241-252.

Baldridge, A.M., Hook, S.J., Grove, C.I. and Rivera, G. (2009) 'The ASTER spectral library version 2.0', *Remote Sensing of Environment*, 113(4), pp. 711-715.

Ballester, C., Jiménez-Bello, M.A., Castel, J.R. and Intrigliolo, D.S. (2013) 'Usefulness of thermography for plant water stress detection in citrus and persimmon trees', *Agricultural and Forest Meteorology*, 168, pp. 120-129.

Balzter, H. (2001) 'Forest mapping and monitoring with interferometric synthetic aperture radar (InSAR)', *Progress in Physical Geography*, 25(2), pp. 159-177.

Baret, F. and Buis, S. (2008) 'Estimating Canopy Characteristics from Remote Sensing Observations: Review of Methods and Associated Problems', in Liang, S. (ed.) *Advances in Land Remote Sensing*. Springer Netherlands, pp. 173-201.

Baret, F., Hagolle, O., Geiger, B., Bicheron, P., Miras, B., Huc, M., Berthelot, B., Niño, F., Weiss, M., Samain, O., Roujean, J.L. and Leroy, M. (2007) 'LAI, fAPAR and fCover CYCLOPES global products derived from VEGETATION: Part 1: Principles of the algorithm', *Remote Sensing of Environment*, 110(3), pp. 275-286.

Baret, F., Jacquemoud, S., Guyot, G. and Leprieur, C. (1992) 'Modeled analysis of the biophysical nature of spectral shifts and comparison with information content of broad bands', *Remote Sensing of Environment*, 41(2), pp. 133-142.

Barton, C.V.M. and North, P.R.J. (2001) 'Remote sensing of canopy light use efficiency using the photochemical reflectance index - Model and sensitivity analysis', *Remote Sensing of Environment*, 78(3), pp. 264-273.

Beets, P.N., Reutebuch, S., Kimberley, M.O., Oliver, G.R., Pearce, S.H. and McGaughey, R.J. (2011) 'Leaf Area Index, Biomass Carbon and Growth Rate of Radiata Pine Genetic Types and Relationships with LiDAR', *Forests*, 2(3), pp. 637-659.

Behmann, J., Steinrucken, J. and Plumer, L. (2014) 'Detection of early plant stress responses in hyperspectral images', *ISPRS Journal of Photogrammetry and Remote Sensing*, 93, pp. 98-111.

Berdugo, C.A., Zito, R., Paulus, S. and Mahlein, A.K. (2014) 'Fusion of sensor data for the detection and differentiation of plant diseases in cucumber', *Plant Pathology*, 63(6), pp. 1344-1356.

Berk, A., Anderson, G.P., Bernstein, L.S., Acharya, P.K., Dothe, H., Matthew, M.W., Adler-Golden, S.M., Chetwynd, J.H., Richtsmeier, S.C., Pukall, B., Allred, C.L., Jeong, L.S. and Hoke, M.L. (1999) 'MODTRAN4 radiative transfer modeling for atmospheric correction', *Optical Spectroscopic Techniques and Instrumentation for Atmospheric and Space Research Iii*, 3756, pp. 348-353.

Berni, J.A.J., Zarco-Tejada, P.J., Sepulcre-Cantó, G., Fereres, E. and Villalobos, F. (2009a) 'Mapping canopy conductance and CWSI in olive orchards using high resolution thermal remote sensing imagery', *Remote Sensing of Environment*, 113(11), pp. 2380-2388.

Berni, J.A.J., Zarco-Tejada, P.J., Suarez, L. and Fereres, E. (2009b) 'Thermal and Narrowband Multispectral Remote Sensing for Vegetation Monitoring From an Unmanned Aerial Vehicle', *IEEE Transactions on Geoscience and Remote Sensing*, 47(3), pp. 722-738.

Berra, E.F., Gaulton, R. and Barr, S. (2016) 'Use of a Digital Camera Onboard a Uav to Monitor Spring Phenology at Individual Tree Level', *2016 IEEE International Geoscience and Remote Sensing Symposium (IGARSS)*, pp. 3496-3499.

Blackburn, G.A. (1998a) 'Quantifying Chlorophylls and Caroteniods at Leaf and Canopy Scales: An Evaluation of Some Hyperspectral Approaches', *Remote Sensing of Environment*, 66(3), pp. 273-285.

Blackburn, G.A. (1998b) 'Spectral indices for estimating photosynthetic pigment concentrations: A test using senescent tree leaves', *International Journal of Remote Sensing*, 19(4), pp. 657-675.

Blackburn, G.A. (2002) 'Remote sensing of forest pigments using airborne imaging spectrometer and LIDAR imagery', *Remote Sensing of Environment*, 82(2–3), pp. 311-321.

Blenkinsop, S. and Fowler, H.J. (2007) 'Changes in European drought characteristics projected by the PRUDENCE regional climate models', *International Journal of Climatology*, 27(12), pp. 1595-1610.

Bloomberg, W.J.M., D.J. (1989) 'Relationship of growth reduction in Douglas-fir to infection by Armillaria root disease in southeastern British Columbia', *Phytopathology*, 79(4), pp. 482-487.

Brasier, C. (1999) *Phytophthora Pathogens of Trees: Their Rising Profile in Europe*. Forest Research.

Breiman, L. (2001) 'Random forests', *Machine Learning*, 45(1), pp. 5-32.

Broadmeadow, M. and Ray, D. (2005) *Climate Change and British Woodland*. Forest Research.

Broge, N.H. and Leblanc, E. (2001) 'Comparing prediction power and stability of broadband and hyperspectral vegetation indices for estimation of green leaf area index and canopy chlorophyll density', *Remote Sensing of Environment*, 76(2), pp. 156-172.

Brown, A. (2010) *Red band needle blight*. Forest Research.

Brown, A. and Webber, J. (2008) *Red band needle blight of conifers in Britain*. Forest Research.

Brown, L., Chen, J.M., Leblanc, S.G. and Cihlar, J. (2000) 'A Shortwave Infrared Modification to the Simple Ratio for LAI Retrieval in Boreal Forests: An Image and Model Analysis', *Remote Sensing of Environment*, 71(1), pp. 16-25.

Buchhorn, M., Walker, D.A., Heim, B., Raynolds, M.K., Epstein, H.E. and Schwieder, M. (2013) 'Ground-Based Hyperspectral Characterization of Alaska Tundra Vegetation along Environmental Gradients', *Remote Sensing*, 5(8), pp. 3971-4005.

Bulman, L., Ganley, R. and Dick, M. (2008) *Needle diseases of radiata pine in New Zealand*. Scion.

Bulman, L.S., Gadgil, P.D., Kershaw, D.J. and Ray, J.W. (2004) *Assessment and Control of Dothistroma Needle Blight*. Forest Research, Rotorua, New Zealand.

Burdon, J.J. (1987) 'The effects of pathogens on individual plants', in *Diseases and Plant Population Biology*. Cambridge: Cambridge University Press, pp. 8-27.

Butin, H. (1995) *Tree Diseases and Disorders: Causes, Biology, and Control in Forest and Amenity Trees*. New York, USA: Oxford University Press.

Calderón, R., Navas-Cortés, J.A., Lucena, C. and Zarco-Tejada, P.J. (2013) 'High-resolution airborne hyperspectral and thermal imagery for early detection of Verticillium wilt of olive using fluorescence, temperature and narrow-band spectral indices', *Remote Sensing of Environment*, 139, pp. 231-245.

Calderon, R., Navas-Cortes, J.A. and Zarco-Tejada, P.J. (2015) 'Early Detection and Quantification of Verticillium Wilt in Olive Using Hyperspectral and Thermal Imagery over Large Areas', *Remote Sensing*, 7(5), pp. 5584-5610.

Carter, G.A. (1991) 'Primary and Secondary Effects of Water-Content on the Spectral Reflectance of Leaves', *American Journal of Botany*, 78(7), pp. 916-924.

Carter, G.A. and Knapp, A.K. (2001) 'Leaf optical properties in higher plants: Linking spectral characteristics to stress and chlorophyll concentration', *American Journal of Botany*, 88(4), pp. 677-684.

Cassel, C., Hackl, P. and Westlund, A.H. (1999) 'Robustness of partial least-squares method for estimating latent variable quality structures', *Journal of Applied Statistics*, 26(4), pp. 435-446.

Ceccato, P., Flasse, S. and Grégoire, J.-M. (2002) 'Designing a spectral index to estimate vegetation water content from remote sensing data: Part 2. Validation and applications', *Remote Sensing of Environment*, 82(2–3), pp. 198-207.

Ceccato, P., Flasse, S., Tarantola, S., Jacquemoud, S. and Grégoire, J.-M. (2001) 'Detecting vegetation leaf water content using reflectance in the optical domain', *Remote Sensing of Environment*, 77(1), pp. 22-33.

Chaerle, L., Caeneghem, W.V., Messens, E., Lambers, H., Van Montagu, M. and Van Der Straeten, D. (1999a) 'Presymptomatic visualization of plant-virus interactions by thermography', *Nature Biotechnology*, 17(8), pp. 813-816.

Chaerle, L., Hagenbeek, D., De Bruyne, E., Valcke, R. and Van Der Straeten, D. (2004) 'Thermal and chlorophyll-fluorescence imaging distinguish plant-pathogen interactions at an early stage', *Plant and Cell Physiology*, 45(7), pp. 887-896.

Chaerle, L., Lenk, S., Leinonen, I., Jones, H.G., Van Der Straeten, D. and Buschmann, C. (2009) 'Multi-sensor plant imaging: Towards the development of a stress-catalogue', *Biotechnology Journal*, 4(8), pp. 1152-1167.

Chaerle, L., Van Caeneghem, W., Messens, E., Lambers, H., Van Montagu, M. and Van Der Straeten, D. (1999b) 'Presymptomatic visualization of plant-virus interactions by thermography', *Nature Biotechnology*, 17(8), pp. 813-816.

Chaerle, L. and Van Der Straeten, D. (2000) 'Imaging techniques and the early detection of plant stress', *Trends in Plant Science*, 5(11), pp. 495-501.

Chen, J.M. (1996) 'Evaluation of Vegetation Indices and a Modified Simple Ratio for Boreal Applications', *Canadian Journal of Remote Sensing*, 22(3), pp. 229-242.

Chen, J.M., Pavlic, G., Brown, L., Cihlar, J., Leblanc, S.G., White, H.P., Hall, R.J., Peddle, D.R., King, D.J., Trofymow, J.A., Swift, E., Van der Sanden, J. and Pellikka, P.K.E. (2002) 'Derivation and validation of Canada-wide coarse-resolution leaf area index maps using high-resolution satellite imagery and ground measurements', *Remote Sensing of Environment*, 80(1), pp. 165-184.

Cheng, Y.-B., Ustin, S.L., Riaño, D. and Vanderbilt, V.C. (2008) 'Water content estimation from hyperspectral images and MODIS indexes in Southeastern Arizona', *Remote Sensing of Environment*, 112(2), pp. 363-374.

Christensen, J.H. and Christensen, O.B. (2007) 'A summary of the PRUDENCE model projections of changes in European climate by the end of this century', *Climatic Change*, 81(1), pp. 7-30.

Christensen, O.B., Goodess, C.M., Harris, I. and Watkiss, P. (2011) 'European and Global Climate Change Projections: Discussion of Climate Change Model Outputs, Scenarios and Uncertainty in the EC RTD ClimateCost Project', in Watkiss, P. (ed.) *The ClimateCost Project. Final Report. Volume 1: Europe*. Stockholm Environment Institute, Sweden.

Ciesla, W.M. (2000) *Remote Sensing in Forest Health Protection*. U.S. Dept. of Agriculture, Forest Service, Forest Health Technology Enterprise Team.

Clancy, K.M., Wagner, M.R. and Reich, P.B. (1995) 'Ecophysiology and Insect Herbivory', in Smith, W.K., Roy, J. and Hinckley, T.M. (eds.) *Ecophysiology of Coniferous Forests*. San Diego: Academic Press, pp. 125-180.

Clark, R.N. and Roush, T.L. (1984) 'Reflectance spectroscopy: Quantitative analysis techniques for remote sensing applications', *Journal of Geophysical Research: Solid Earth*, 89(B7), pp. 6329-6340.

Cloutis, E.A. (1996) 'Hyperspectral geological remote sensing: Evaluation of analytical techniques', *International Journal of Remote Sensing*, 17(12), pp. 2215-2242.

Cohen, W.B. (1991) 'Temporal versus spatial variation in leaf reflectance under changing water stress conditions', *International Journal of Remote Sensing*, 12(9), pp. 1865-1876.

Cohen, W.B., Maiersperger, T.K., Gower, S.T. and Turner, D.P. (2003) 'An improved strategy for regression of biophysical variables and Landsat ETM+ data', *Remote Sensing of Environment*, 84(4), pp. 561-571.

Colombo, R., Meroni, M., Marchesi, A., Busetto, L., Rossini, M., Giardino, C. and Panigada, C. (2008) 'Estimation of leaf and canopy water content in poplar plantations by means of hyperspectral indices and inverse modeling', *Remote Sensing of Environment*, 112(4), pp. 1820-1834.

Coops, N., Stanford, M., Old, K., Dudzinski, M., Culvenor, D. and Stone, C. (2003) 'Assessment of Dothistroma Needle Blight of Pinus radiata Using Airborne Hyperspectral Imagery', *Phytopathology*, 93(12), pp. 1524-1532.

Coops, N.C., Varhola, A., Bater, C.W., Teti, P., Boon, S., Goodwin, N. and Weiler, M. (2009) 'Assessing differences in tree and stand structure following beetle infestation using lidar data', *Canadian Journal of Remote Sensing*, 35(6), pp. 497-508.

Cortes, C. and Vapnik, V. (1995) 'Support-Vector Networks', *Machine Learning*, 20(3), pp. 273-297.

Cryer, J.D. and Chan, K.-S. (2008) 'Time Series Regression Models', in *Time Series Analysis: With Applications in R*. New York, NY: Springer New York, pp. 249-276.

CSL (2004) *Asian longhorn beetles*. Department for Environment, Food & Rural Affairs and Central Science Laboratory.

Curran, P.J., Dungan, J.L. and Gholz, H.L. (1990) 'Exploring the relationship between reflectance red edge and chlorophyll content in slash pine', *Tree Physiology*, 7, pp. 33-48.

Curran, P.J., Dungan, J.L. and Peterson, D.L. (2001) 'Estimating the foliar biochemical concentration of leaves with reflectance spectrometry: Testing the Kokaly and Clark methodologies', *Remote Sensing of Environment*, 76(3), pp. 349-359.

Damm, A., Erler, A., Hillen, W., Meroni, M., Schaepman, M.E., Verhoef, W. and Rascher, U. (2011) 'Modeling the impact of spectral sensor configurations on the FLD retrieval accuracy of sun-induced chlorophyll fluorescence', *Remote Sensing of Environment*, 115(8), pp. 1882-1892.

Danson, F.M. and Bowyer, P. (2004) 'Estimating live fuel moisture content from remotely sensed reflectance', *Remote Sensing of Environment*, 92(3), pp. 309-321.

Danson, F.M. and Plummer, S.E. (1995) 'Red-edge response to forest leaf area index', *International Journal of Remote Sensing*, 16(1), pp. 183-188.

Danson, F.M., Steven, M.D., Malthus, T.J. and Clark, J.A. (1992) 'High-spectral resolution data for determining leaf water content', *International Journal of Remote Sensing*, 13(3), pp. 461-470.

Datskos, P.C. and Lavrik, N.V. (2004) 'Detectors - Figures of Merit', in Driggers, R.G. (ed.) *Encyclopedia of optical engineering*. New York, USA: Marcel Dekker, Inc., pp. 349-357.

Datt, B. (1998) 'Remote Sensing of Chlorophyll a, Chlorophyll b, Chlorophyll a+b, and Total Carotenoid Content in Eucalyptus Leaves', *Remote Sensing of Environment*, 66(2), pp. 111-121.

Dawson, T.P., North, P.R.J., Plummer, S.E. and Curran, P.J. (2003) 'Forest ecosystem chlorophyll content: Implications for remotely sensed estimates of net primary productivity', *International Journal of Remote Sensing*, 24(3), pp. 611-617.

de Jong, S.M., Addink, E.A., Hoogenboom, P. and Nijland, W. (2012) 'The spectral response of Buxus sempervirens to different types of environmental stress – A laboratory experiment', *ISPRS Journal of Photogrammetry and Remote Sensing*, 74, pp. 56-65.

DEFRA (2008) *Phytophthora ramorum. A Practical Guide for Established Parks & Gardens, Amenity Landscape and Woodland Areas*.

DEFRA and Forestry Commission (2014) *Tree Health Management Plan*.

Delegido, J., Verrelst, J., Meza, C.M., Rivera, J.P., Alonso, L. and Moreno, J. (2013) 'A red-edge spectral index for remote sensing estimation of green LAI over agroecosystems', *European Journal of Agronomy*, 46, pp. 42-52.

Demetriades-Shah, T.H., Steven, M.D. and Clark, J.A. (1990) 'High resolution derivative spectra in remote sensing', *Remote Sensing of Environment*, 33(1), pp. 55-64.

Déqué, M., Rowell, D.P., Lüthi, D., Giorgi, F., Christensen, J.H., Rockel, B., Jacob, D., Kjellström, E., de Castro, M. and van den Hurk, B. (2007) 'An intercomparison of regional climate simulations for Europe: assessing uncertainties in model projections', *Climatic Change*, 81(1), pp. 53-70.

Dobrowski, S.Z., Pushnik, J.C., Zarco-Tejada, P.J. and Ustin, S.L. (2005) 'Simple reflectance indices track heat and water stress-induced changes in steady-state chlorophyll fluorescence at the canopy scale', *Remote Sensing of Environment*, 97(3), pp. 403-414.

Donoghue, D.N.M., Watt, P.J., Cox, N.J. and Wilson, J. (2007) 'Remote sensing of species mixtures in conifer plantations using LiDAR height and intensity data', *Remote Sensing of Environment*, 110(4), pp. 509-522.

Dorren, L.K.A., Berger, F., Imeson, A.C., Maier, B. and Rey, F. (2004) 'Integrity, stability and management of protection forests in the European Alps', *Forest Ecology and Management*, 195(1-2), pp. 165-176.

Downing, E. (2012) *Ash dieback disease: Chalara fraxinea*. Commons Library Standard Note.

Du, Q., Chang, N.-B., Yang, C. and Srilakshmi, K.R. (2008) 'Combination of multispectral remote sensing, variable rate technology and environmental modeling for citrus pest management', *Journal of Environmental Management*, 86(1), pp. 14-26.

Dutta, S., Bhattacharya, B.K., Rajak, D.R., Chattopadhayay, C., Patel, N.K. and Parihar, J.S. (2006) 'Disease detection in mustard crop using eo-1 hyperion satellite data', *Journal of the Indian Society of Remote Sensing*, 34(3), pp. 325-330.

Edson, C. and Wing, M.G. (2011) 'Airborne Light Detection and Ranging (LiDAR) for Individual Tree Stem Location, Height, and Biomass Measurements', *Remote Sensing*, 3(11), pp. 2494-2528.

Eismann, M.T. (2012) 'Spectral Properties of Materials', in *Hyperspectral Remote Sensing*. Bellingham: SPIE.

Eitel, J.U.H., Gessler, P.E., Smith, A.M.S. and Robberecht, R. (2006) 'Suitability of existing and novel spectral indices to remotely detect water stress in Populus spp.', *Forest Ecology and Management*, 229(1-3), pp. 170-182.

Eklundh, L., Harrie, L. and Kuusk, A. (2001) 'Investigating relationships between Landsat ETM+ sensor data and leaf area index in a boreal conifer forest', *Remote Sensing of Environment*, 78(3), pp. 239-251.

Eklundh, L., Johansson, T. and Solberg, S. (2009) 'Mapping insect defoliation in Scots pine with MODIS time-series data', *Remote Sensing of Environment*, 113(7), pp. 1566-1573.

Elmendorf, B., Moorman, G. and Gerhold, H. (2000) *Seven Common Diseases of Landscape Trees*. The Pennsylvania State University.

Erdem, Y., Arin, L., Erdem, T., Polat, S., Deveci, M., Okursoy, H. and Gültaş, H.T. (2010) 'Crop water stress index for assessing irrigation scheduling of drip irrigated broccoli (Brassica oleracea L. var. italica)', *Agricultural Water Management*, 98(1), pp. 148-156.

Evans, H. and Oszako, T. (2007) *Alien Invasive Species and International Trade*. Warsaw: Forest Research Institute.

Fassnacht, F.E., Latifi, H., Ghosh, A., Joshi, P.K. and Koch, B. (2014) 'Assessing the potential of hyperspectral imagery to map bark beetle-induced tree mortality', *Remote Sensing of Environment*, 140, pp. 533-548.

Fensholt, R. and Sandholt, I. (2003) 'Derivation of a shortwave infrared water stress index from MODIS near- and shortwave infrared data in a semiarid environment', *Remote Sensing of Environment*, 87(1), pp. 111-121.

Fereres, E., Goldhamer, D.A. and Parsons, L.R. (2003) 'Irrigation water management of horticultural crops', *Hortscience*, 38(5), pp. 1036-1042.

Filella, I. and Penuelas, J. (1994) 'The Red Edge Position and Shape as Indicators of Plant Chlorophyll Content, Biomass and Hydric Status', *International Journal of Remote Sensing*, 15(7), pp. 1459-1470.

Fitter, A.H. and Hay, R.K.M. (2001) *Environmental Physiology of Plants*. Elsevier Science.

Flannigan, M.D., Krawchuk, M.A., de Groot, W.J., Wotton, B.M. and Gowman, L.M. (2009) 'Implications of changing climate for global wildland fire', *International Journal of Wildland Fire*, 18(5), pp. 483-507.

Forest Research (2017a) *Location of intensive long term monitoring of forest ecosystems plots in Britain and their summary data*. Available at: https://www.forestry.gov.uk/fr/INFD-67NBAT (Accessed: 3.08.2017).

Forest Research (2017b) *Oak Processionary Moth Programme: Operational Report 2016*.

Forestry Commission (2009) *Report on survey and control of Oak Processionary Moth Thaumetopoea processionea (Linnaeus) (Lepidoptera: Thaumetopoeidae) (OPM) in London in 2008*.

Forestry Commission (2012) *Dothistroma needle blight: GB Strategy*.

Forestry Commission (2013) *Asian longhorn beetle*.

Forestry Commission (2016) *Forestry Statistics 2016*.

Forestry Commission (2017) *Top tree pests and diseases in the UK*. Available at: https://www.forestry.gov.uk/pestsanddiseases (Accessed: 3.08.2017).

Forestry Commission Scotland (2013a) *Action Plan for Ramorum on Larch in Scotland (2013/14)*.

Forestry Commission Scotland (2013b) *Chalara Action Plan – Scotland (2013/14)*.

Fourty, T. and Baret, F. (1998) 'On spectral estimates of fresh leaf biochemistry', *International Journal of Remote Sensing*, 19(7), pp. 1283-1297.

Franklin, S.E., Fan, H. and Guo, X. (2008) 'Relationship between Landsat TM and SPOT vegetation indices and cumulative spruce budworm defoliation', *International Journal of Remote Sensing*, 29(4), pp. 1215-1220.

Fraser, R.H. and Latifovic, R. (2005) 'Mapping insect-induced tree defoliation and mortality using coarse spatial resolution satellite imagery', *International Journal of Remote Sensing*, 26(1), pp. 193-200.

Frazer, G.W., Wulder, M.A. and Niemann, K.O. (2005) 'Simulation and quantification of the fine-scale spatial pattern and heterogeneity of forest canopy structure: A lacunarity-based method designed for analysis of continuous canopy heights', *Forest Ecology and Management*, 214(1-3), pp. 65-90.

Fuchs, M. (1990) 'Infrared Measurement of Canopy Temperature and Detection of Plant Water-Stress', *Theoretical and Applied Climatology*, 42(4), pp. 253-261.

Gamon, J.A., Penuelas, J. and Field, C.B. (1992) 'A Narrow-Waveband Spectral Index That Tracks Diurnal Changes in Photosynthetic Efficiency', *Remote Sensing of Environment*, 41(1), pp. 35-44.

Gamon, J.A., Serrano, L. and Surfus, J.S. (1997) 'The photochemical reflectance index: an optical indicator of photosynthetic radiation use efficiency across species, functional types, and nutrient levels', *Oecologia*, 112(4), pp. 492-501.

Ganguly, S., Nemani, R.R., Zhang, G., Hashimoto, H., Milesi, C., Michaelis, A., Wang, W., Votava, P., Samanta, A., Melton, F., Dungan, J.L., Vermote, E., Gao, F., Knyazikhin, Y. and Myneni, R.B. (2012) 'Generating global Leaf Area Index from Landsat: Algorithm formulation and demonstration', *Remote Sensing of Environment*, 122, pp. 185-202.

Gao, B.-C. (1996) 'NDWI—A normalized difference water index for remote sensing of vegetation liquid water from space', *Remote Sensing of Environment*, 58(3), pp. 257-266.

Gao, B.-C. and Goetzt, A.F.H. (1995) 'Retrieval of equivalent water thickness and information related to biochemical components of vegetation canopies from AVIRIS data', *Remote Sensing of Environment*, 52(3), pp. 155-162.

Gastellu-Etchegorry, J.P., Demarez, V., Pinel, V. and Zagolski, F. (1996) 'Modeling radiative transfer in heterogeneous 3-D vegetation canopies', *Remote Sensing of Environment*, 58(2), pp. 131-156.

Gauthier, S., Bernier, P., Kuuluvainen, T., Shvidenko, A.Z. and Schepaschenko, D.G. (2015) 'Boreal forest health and global change', *Science*, 349(6250), pp. 819-822.

Gerard, F., Plummer, S., Wadsworth, R., Sanfeliu, A.F., Iliffe, L., Balzter, H. and Wyatt, B. (2003) 'Forest fire scar detection in the boreal forest with multitemporal SPOT-VEGETATION data', *Ieee Transactions on Geoscience and Remote Sensing*, 41(11), pp. 2575-2585.

Getzin, S., Nuske, R.S. and Wiegand, K. (2014) 'Using Unmanned Aerial Vehicles (UAV) to Quantify Spatial Gap Patterns in Forests', *Remote Sensing*, 6(8), pp. 6988-7004.

Gilbert, G.S. (2002) 'Evolutionary Ecology of Plant Diseases in Natural Ecosystems', *Annual Review of Phytopathology*, 40(1), pp. 13-43.

Gitelson, A.A., Kaufman, Y.J. and Merzlyak, M.N. (1996a) 'Use of a green channel in remote sensing of global vegetation from EOS-MODIS', *Remote Sensing of Environment*, 58(3), pp. 289-298.

Gitelson, A.A., Merzlyak, M.N. and Lichtenthaler, H.K. (1996b) 'Detection of Red Edge Position and Chlorophyll Content by Reflectance Measurements Near 700 nm', *Journal of Plant Physiology*, 148(3), pp. 501-508.

Gitelson, A.A., Vina, A., Ciganda, V., Rundquist, D.C. and Arkebauer, T.J. (2005) 'Remote estimation of canopy chlorophyll content in crops', *Geophysical Research Letters*, 32(8).

Goel, N.S. and Thompson, R.L. (2000) 'A snapshot of canopy reflectance models and a universal model for the radiation regime', *Remote Sensing Reviews*, 18(2-4), pp. 197-225.

Goetz, A.F.H. and Boardman, J.W. (1995) Spectroscopic measurement of leaf water status. *Geoscience and Remote Sensing Symposium, 1995. IGARSS '95. 'Quantitative Remote Sensing for Science and Applications', International*. 10-14 Jul1995.

Gomez-Candon, D., Virlet, N., Labbe, S., Jolivot, A. and Regnard, J.L. (2016) 'Field phenotyping of water stress at tree scale by UAV-sensed imagery: new insights for thermal acquisition and calibration', *Precision Agriculture*, 17(6), pp. 786-800.

Gómez-Chova, L., Alonso-Chorda, L., Amorós-Lopez, J., Vila Frances, J., del ValleTascon, S., Calpe, J. and Moreno, J. (2006) 'Solar induced fluorescence measurements using a field spectroradiometer', *AIP Conference Proceedings*, 852, pp. 274-281.

Gomez-Chova, L., Tuia, D., Moser, G. and Camps-Valls, G. (2015) 'Multimodal Classification of Remote Sensing Images: A Review and Future Directions', *Proceedings of the Ieee*, 103(9), pp. 1560-1584.

González-Dugo, M.P., Moran, M.S., Mateos, L. and Bryant, R. (2006) 'Canopy temperature variability as an indicator of crop water stress severity', *Irrigation Science*, 24(4), pp. 233-240.

Gonzalez-Dugo, V., Zarco-Tejada, P., Berni, J.A.J., Suárez, L., Goldhamer, D. and Fereres, E. (2012) 'Almond tree canopy temperature reveals intra-crown variability that is water stress-dependent', *Agricultural and Forest Meteorology*, 154–155, pp. 156-165.

Gonzalez-Dugo, V., Zarco-Tejada, P.J. and Fereres, E. (2014) 'Applicability and limitations of using the crop water stress index as an indicator of water deficits in citrus orchards', *Agricultural and Forest Meteorology*, 198–199, pp. 94-104.

Gotze, C., Glasser, C. and Jung, A. (2016) 'Detecting heavy metal pollution of floodplain vegetation in a pot experiment using reflectance spectroscopy', *International Journal of River Basin Management*, 14(4), pp. 499-507.

Govender, M., Dye, P.J., Weiersbye, I.M., Witkowski, E.T.F. and Ahmed, F.B. (2009) 'Review of commonly used remote sensing and ground-based technologies to measure plant water stress', *Water SA*, 35(5), pp. 741-752.

Grant, O.M., Tronina, L., Jones, H.G. and Chaves, M.M. (2007) 'Exploring thermal imaging variables for the detection of stress responses in grapevine under different irrigation regimes', *Journal of Experimental Botany*, 58(4), pp. 815-825.

Grant, O.M., Tronina, L., Ramalho, J.C., Besson, C.K., Lobo-Do-Vale, R., Pereira, J.S., Jones, H.G. and Chaves, M.M. (2010) 'The impact of drought on leaf physiology of Quercus suber L. trees: comparison of an extreme drought event with chronic rainfall reduction', *Journal of Experimental Botany*, 61(15), pp. 4361-4371.

Green, S. and Duncan, R. (2009) *Potential impacts of drought and disease on forestry in Scotland*. Forest Research.

Green, S., Laue, B., Steele, H. and Nowell, R. (2014) *Horse chestnut bleeding canker*.

Grgic, G. and Pusnik, I. (2011) 'Analysis of Thermal Imagers', *International Journal of Thermophysics*, 32(1-2), pp. 237-247.

Griffin, A.M., Popescu, S. and Zhao, K. (2008) Using LIDAR and normalized difference vegetation index to remotely determine LAI and percent canopy cover. *Proceedings of SilviLaser (8th)*.

Gupta, S., Weinacker, H. and Koch, B. (2010) 'Comparative Analysis of Clustering-Based Approaches for 3-D Single Tree Detection Using Airborne Fullwave Lidar Data', *Remote Sensing*, 2(4), pp. 968-989.

Haboudane, D., Miller, J.R., Pattey, E., Zarco-Tejada, P.J. and Strachan, I.B. (2004) 'Hyperspectral vegetation indices and novel algorithms for predicting green LAI of crop canopies: Modeling and validation in the context of precision agriculture', *Remote Sensing of Environment*, 90(3), pp. 337-352.

Haboudane, D., Miller, J.R., Tremblay, N., Zarco-Tejada, P.J. and Dextraze, L. (2002) 'Integrated narrow-band vegetation indices for prediction of crop chlorophyll content for application to precision agriculture', *Remote Sensing of Environment*, 81(2–3), pp. 416-426.

Hais, M. and Kučera, T. (2008) 'Surface temperature change of spruce forest as a result of bark beetle attack: remote sensing and GIS approach', *European Journal of Forest Research*, 127(4), pp. 327-336.

Hall, R.J., Fernandes, R.A., Hogg, E.H., Brandt, J.P., Butson, C., Case, B.S. and Leblanc, S.G. (2003) 'Relating aspen defoliation to changes in leaf area derived from field and satellite remote sensing data', *Canadian Journal of Remote Sensing*, 29(3), pp. 299-313.

Hansen, E.M., Goheen, D.J., Jules, E.S. and Ullian, B. (2000) 'Managing Port-Orford-Cedar and the Introduced Pathogen Phytophthora lateralis', *Plant Disease*, 84(1), pp. 4-14.

HDC (2011) *Red band needle blight - a review of the potential for disease management in forest nurseries using fungicides*.

Hecker, C.A., Smith, T.E.L., Luz, B.R. and Wooster, M.J. (2013) 'Thermal Infrared Spectroscopy in the Laboratory and Field in Support of Land Surface Remote Sensing', in Kuenzer, C. and Dech, S. (eds.) *Thermal Infrared Remote Sensing: Sensors, Methods, Applications*. Dordrecht: Springer Netherlands, pp. 43-67.

Hendry, S. (2004) *Monitoring of forest health in Britain: The Forest Condition Survey and Level I networks*. Forest Research.

Hendry, S. (2013) *Pest and disease update*. Forest Research.

Hernandez-Clemente, R., Navarro-Cerrillo, R.M., Suarez, L., Morales, F. and Zarco-Tejada, P.J. (2011) 'Assessing structural effects on PRI for stress detection in conifer forests', *Remote Sensing of Environment*, 115(9), pp. 2360-2375.

Hinckley, T.M., Brooks, J.R., Čermák, J., Ceulemans, R., Kučera, J., Meinzer, F.C. and Roberts, D.A. (1994) 'Water flux in a hybrid poplar stand', *Tree Physiology*, 14(7-8-9), pp. 1005-1018.

Hodgson, A., Peel, D. and Kelly, N. (2017) 'Unmanned aerial vehicles for surveying marine fauna: assessing detection probability', *Ecological Applications*, 27(4), pp. 1253-1267.

Hoelter, T. and Meyer, B. (1998) 'The Challenges of Using an Uncooled Microbolometer Array in a Thermographic Application'. Available at: http://www.dtic.mil/docs/citations/ADA399432.

Holmgren, J., Nilsson, M. and Olsson, H. (2003) 'Estimation of tree height and stem volume on plots-using airborne laser scanning', *Forest Science*, 49(3), pp. 419-428.

Holst, G.C. (1998) *CCD arrays, cameras, and displays*. Bellingham, WA, USA: SPIE Optical Engineering Press.

Holsten, E.H., Hennon, P., Trummer, L., Kruse, J., Schultz, M. and Lundquist, J. (2008) *Insects and Diseases of Alaskan Forests*. USDA Forest Service, Alaska Region.

Hopkins, W.G. and Hüner, N.P.A. (2008) *Introduction to plant physiology*. 4th edn. USA: John Wiley & Sons, Inc.

Hoque, E. and Hutzler, P.J.S. (1992) 'Spectral blue-shift of red edge minitors damage class of beech trees', *Remote Sensing of Environment*, 39(1), pp. 81-84.

Hostert, P., Roder, A. and Hill, J. (2003) 'Coupling spectral unmixing and trend analysis for monitoring of long-term vegetation dynamics in Mediterranean rangelands', *Remote Sensing of Environment*, 87(2-3), pp. 183-197.

Houborg, R., McCabe, M., Cescatti, A., Gao, F., Schull, M. and Gitelson, A. (2015) 'Joint leaf chlorophyll content and leaf area index retrieval from Landsat data using a regularized model inversion system (REGFLEC)', *Remote Sensing of Environment*, 159, pp. 203-221.

Huete, A., Didan, K., Miura, T., Rodriguez, E.P., Gao, X. and Ferreira, L.G. (2002) 'Overview of the radiometric and biophysical performance of the MODIS vegetation indices', *Remote Sensing of Environment*, 83(1–2), pp. 195-213.

Huete, A.R. (2012) 'Vegetation Indices, Remote Sensing and Forest Monitoring', *Geography Compass*, 6(9), pp. 513-532.

Huete, A.R., Jackson, R.D. and Post, D.F. (1985) 'Spectral response of a plant canopy with different soil backgrounds', *Remote Sensing of Environment*, 17(1), pp. 37-53.

Hugenin, R.L. and Jones, J.L. (1986) 'Intelligent Information Extraction from Reflectance Spectra - Absorption-Band Positions', *Journal of Geophysical Research-Solid Earth and Planets*, 91(B9), pp. 9585-9598.

Hurley, A., Watts, D., Burke, B. and Richards, C. (2004) 'Identifying Gypsy Moth Defoliation in Ohio Using Landsat Data', *Environmental & Engineering Geoscience*, 10(4), pp. 321-328.

Hyndman, R.J. and Khandakar, Y. (2008) 'Automatic Time Series Forecasting: The forecast Package for R', *Journal of Statistical Software*, 27(1), pp. 1-22.

Idso, S.B., Jackson, R.D., Pinter Jr, P.J., Reginato, R.J. and Hatfield, J.L. (1981) 'Normalizing the stress-degree-day parameter for environmental variability', *Agricultural Meteorology*, 24, pp. 45-55.

Immitzer, M., Atzberger, C. and Koukal, T. (2012) 'Tree Species Classification with Random Forest Using Very High Spatial Resolution 8-Band WorldView-2 Satellite Data', *Remote Sensing*, 4(9), pp. 2661-2693.

IPCC (2013) 'Summary for Policymakers', in Stocker, T.F., Qin, D., Plattner, G.-K., Tignor, M., Allen, S.K., Boschung, J., Nauels, A., Xia, Y., Bex, V. and Midgley, P.M. (eds.) *Climate Change 2013: The Physical Science Basis. Contribution of Working Group I to the Fifth Assessment*

Report of the Intergovernmental Panel on Climate Change. Cambridge University Press, Cambridge, United Kingdom and New York, NY, USA.

Jaakkola, A., Hyyppa, J., Kukko, A., Yu, X.W., Kaartinen, H., Lehtomaki, M. and Lin, Y. (2010) 'A low-cost multi-sensoral mobile mapping system and its feasibility for tree measurements', *Isprs Journal of Photogrammetry and Remote Sensing*, 65(6), pp. 514-522.

Jackson, R.D., Idso, S.B., Reginato, R.J. and Pinter, P.J. (1981) 'Canopy temperature as a crop water stress indicator', *Water Resources Research*, 17(4), pp. 1133-1138.

Jackson, R.G., Foody, G.M. and Quine, C.P. (2000) 'Characterising windthrown gaps from fine spatial resolution remotely sensed data', *Forest Ecology and Management*, 135(1–3), pp. 253-260.

Jacquemoud, S. and Baret, F. (1990) 'PROSPECT: A model of leaf optical properties spectra', *Remote Sensing of Environment*, 34(2), pp. 75-91.

Jacquemoud, S., Baret, F., Andrieu, B., Danson, F.M. and Jaggard, K. (1995) 'Extraction of vegetation biophysical parameters by inversion of the PROSPECT + SAIL models on sugar beet canopy reflectance data. Application to TM and AVIRIS sensors', *Remote Sensing of Environment*, 52(3), pp. 163-172.

James, M.R. and Robson, S. (2014) 'Mitigating systematic error in topographic models derived from UAV and ground-based image networks', *Earth Surface Processes and Landforms*, 39(10), pp. 1413-1420.

Jeganathan, C., Dash, J. and Atkinson, P.M. (2014) 'Remotely sensed trends in the phenology of northern high latitude terrestrial vegetation, controlling for land cover change and vegetation type', *Remote Sensing of Environment*, 143, pp. 154-170.

Jensen, J.L.R., Humes, K.S., Vierling, L.A. and Hudak, A.T. (2008) 'Discrete return lidar-based prediction of leaf area index in two conifer forests', *Remote Sensing of Environment*, 112(10), pp. 3947-3957.

Jiang, Z.Y., Huete, A.R., Didan, K. and Miura, T. (2008) 'Development of a two-band enhanced vegetation index without a blue band', *Remote Sensing of Environment*, 112(10), pp. 3833-3845.

Jin, S. and Sader, S.A. (2005) 'Comparison of time series tasseled cap wetness and the normalized difference moisture index in detecting forest disturbances', *Remote Sensing of Environment*, 94(3), pp. 364-372.

Joint Liaison Group (2008) *Forests. Climate Change, Biodiversity and Land Degradation*.

Jones, H.G. (1992) *Plants and Microclimate: A Quantitative Approach to Environmental Plant Physiology*. 2nd edn. Cambridge University Press.

Jones, H.G. (1999) 'Use of infrared thermometry for estimation of stomatal conductance as a possible aid to irrigation scheduling', *Agricultural and Forest Meteorology*, 95(3), pp. 139-149.

Jones, H.G. (2004) 'Application of thermal imaging and infrared sensing in plant physiology and ecophysiology', *Advances in Botanical Research Incorporating Advances in Plant Pathology*, 41, pp. 107-163.

Jones, H.G. and Schofield, P. (2008) 'Thermal and other remote sensing of plant stress', *General and Applied Plant Physiology*, 34(1-2), pp. 19-34.

Jones, H.G., Stoll, M., Santos, T., Sousa, C.d., Chaves, M.M. and Grant, O.M. (2002) 'Use of infrared thermography for monitoring stomatal closure in the field: application to grapevine', *Journal of Experimental Botany*, 53(378), pp. 2249-2260.

Jordan, C.F. (1969) 'Derivation of Leaf-Area Index from Quality of Light on the Forest Floor', *Ecology*, 50(4), pp. 663-666.

Jyrki, T., Tarmo, L., Viljo, K. and Reija, H. (2009) *Remote Sensing of Forest Health*.

Kaartinen, H., Hyyppa, J., Yu, X.W., Vastaranta, M., Hyyppa, H., Kukko, A., Holopainen, M., Heipke, C., Hirschmugl, M., Morsdorf, F., Naesset, E., Pitkanen, J., Popescu, S., Solberg, S., Wolf, B.M. and Wu, J.C. (2012) 'An International Comparison of Individual Tree Detection and Extraction Using Airborne Laser Scanning', *Remote Sensing*, 4(4), pp. 950-974.

Kaiser, J.F. (1966) 'Digital Filters', in Kuo, F.F. and Kaiser, J.F. (eds.) *System analysis by digital computer*. New York: John Wiley and Sons, pp. 218-285.

Kantola, T., Vastaranta, M., Lyytikainen-Saarenmaa, P., Holopainen, M., Kankare, V., Talvitie, M. and Hyyppa, J. (2013) 'Classification of Needle Loss of Individual Scots Pine Trees by Means of Airborne Laser Scanning', *Forests*, 4(2), pp. 386-403.

Kato, A., Moskal, L.M., Schiess, P., Swanson, M.E., Calhoun, D. and Stuetzle, W. (2009) 'Capturing tree crown formation through implicit surface reconstruction using airborne lidar data', *Remote Sensing of Environment*, 113(6), pp. 1148-1162.

Keener, M.E. and Kircher, P.L. (1983) 'The Use of Canopy Temperature as an Indicator of Drought Stress in Humid Regions', *Agricultural Meteorology*, 28(4), pp. 339-349.

Kelly, M. and Liu, D. (2004) 'Mapping Diseased Oak Trees Using ADAR Imagery', *Geocarto International*, 19(1), pp. 57-64.

Kerekes, J.P., Strackerjan, K.E. and Salvaggio, C. (2008) 'Spectral reflectance and emissivity of man-made surfaces contaminated with environmental effects', *Optical Engineering*, 47(10).

Kharuk, V.I., Ranson, K.J., Kozuhovskaya, A.G., Kondakov, Y.P. and Pestunov, I.A. (2004) 'NOAA/AVHRR satellite detection of Siberian silkmoth outbreaks in eastern Siberia', *International Journal of Remote Sensing*, 25(24), pp. 5543-5556.

Kim, Y., Still, C.J., Hanson, C.V., Kwon, H., Greer, B.T. and Law, B.E. (2016) 'Canopy skin temperature variations in relation to climate, soil temperature, and carbon flux at a ponderosa pine forest in central Oregon', *Agricultural and Forest Meteorology*, 226, pp. 161-173.

Kliejunas, J.T. (2010) *Sudden Oak Death and Phytophthora ramorum: A Summary of the Literature*. Albany, CA, USA: Department of Agriculture and Forest Service Pacific Southwest Research Station.

Kobayashi, H. and Iwabuchi, H. (2008) 'A coupled 1-D atmosphere and 3-D canopy radiative transfer model for canopy reflectance, light environment, and photosynthesis simulation in a heterogeneous landscape', *Remote Sensing of Environment*, 112(1), pp. 173-185.

Koch, B. (2010) 'Status and future of laser scanning, synthetic aperture radar and hyperspectral remote sensing data for forest biomass assessment', *ISPRS Journal of Photogrammetry and Remote Sensing*, 65(6), pp. 581-590.

Koch, B., Kattenborn, T., Straub, C. and Vauhkonen, J. (2014) 'Segmentation of Forest to Tree Objects', in Maltamo, M., Næsset, E. and Vauhkonen, J. (eds.) *Forestry Applications of Airborne Laser Scanning: Concepts and Case Studies*. Dordrecht: Springer Netherlands, pp. 89-112.

Köhl, M., Magnussen, S. and Marchetti, M. (2006) 'Remote Sensing', in *Sampling Methods, Remote Sensing and GIS Multiresource Forest Inventory*. Springer Berlin Heidelberg, pp. 197-238.

Kokaly, R.F. and Clark, R.N. (1999) 'Spectroscopic Determination of Leaf Biochemistry Using Band-Depth Analysis of Absorption Features and Stepwise Multiple Linear Regression', *Remote Sensing of Environment*, 67(3), pp. 267-287.

Kokaly, R.F., Clark, R.N., Swayze, G.A., Livo, K.E., Hoefen, T.M., Pearson, N.C., Wise, R.A., Benzel, W.M., Lowers, H.A., Driscoll, R.L. and Klein, A.J. (2017) *USGS Spectral Library Version 7* (1035). Reston, VA: Survey, U.S.G. [Online]. Available at: http://pubs.er.usgs.gov/publication/ds1035.

Kokaly, R.F., Despain, D.G., Clark, R.N. and Livo, K.E. (2003) 'Mapping vegetation in Yellowstone National Park using spectral feature analysis of AVIRIS data', *Remote Sensing of Environment*, 84(3), pp. 437-456.

Kolb, T.E., Wagner, M.R. and Covington, W.W. (1994) 'Concepts of Forest Health - Utilitarian and Ecosystem Perspectives', *Journal of Forestry*, 92(7), pp. 10-15.

Kotthaus, S., Smith, T.E.L., Wooster, M.J. and Grimmond, C.S.B. (2014) 'Derivation of an urban materials spectral library through emittance and reflectance spectroscopy', *Isprs Journal of Photogrammetry and Remote Sensing*, 94, pp. 194-212.

Kötz, B., Schaepman, M., Morsdorf, F., Bowyer, P., Itten, K. and Allgöwer, B. (2004) 'Radiative transfer modeling within a heterogeneous canopy for estimation of forest fire fuel properties', *Remote Sensing of Environment*, 92(3), pp. 332-344.

Kuenzer, C. and Dech, S. (2013) 'Theoretical Background of Thermal Infrared Remote Sensing', in Kuenzer, C. and Dech, S. (eds.) *Thermal Infrared Remote Sensing: Sensors, Methods, Applications*. Dordrecht: Springer Netherlands, pp. 1-26.

Kuusk, A. and Nilson, T. (2000) 'A Directional Multispectral Forest Reflectance Model', *Remote Sensing of Environment*, 72(2), pp. 244-252.

Lausch, A., Heurich, M., Gordalla, D., Dobner, H.J., Gwillym-Margianto, S. and Salbach, C. (2013) 'Forecasting potential bark beetle outbreaks based on spruce forest vitality using hyperspectral remote-sensing techniques at different scales', *Forest Ecology and Management*, 308, pp. 76-89.

Law, B.E. and Waring, R.H. (1994) 'Remote Sensing of Leaf Area Index and Radiation Intercepted by Understory Vegetation', *Ecological Applications*, 4(2), pp. 272-279.

le Maire, G., François, C. and Dufrêne, E. (2004) 'Towards universal broad leaf chlorophyll indices using PROSPECT simulated database and hyperspectral reflectance measurements', *Remote Sensing of Environment*, 89(1), pp. 1-28.

Leckie, D.G., Jay, C., Gougeon, F.A., Sturrock, R.N. and Paradine, D. (2004) 'Detection and assessment of trees with Phellinus weirii (laminated root rot) using high resolution multi-spectral imagery', *International Journal of Remote Sensing*, 25(4), pp. 793-818.

Lee, K.-S., Cohen, W.B., Kennedy, R.E., Maiersperger, T.K. and Gower, S.T. (2004) 'Hyperspectral versus multispectral data for estimating leaf area index in four different biomes', *Remote Sensing of Environment*, 91(3–4), pp. 508-520.

Lee, S.H. and Cho, H.K. (2006) 'Detection of the pine trees damaged by pine wilt disease using high spatial remote sensing data', *Proceedings of the ISPRS Commission VII Symposium 'Remote Sensing: From Pixels to Processes'*. Enschede, The Netherlands.

Lee, W.S., Alchanatis, V., Yang, C., Hirafuji, M., Moshou, D. and Li, C. (2010) 'Sensing technologies for precision specialty crop production', *Computers and Electronics in Agriculture*, 74(1), pp. 2-33.

Lehmann, J.R.K., Nieberding, F., Prinz, T. and Knoth, C. (2015) 'Analysis of Unmanned Aerial System-Based CIR Images in Forestry-A New Perspective to Monitor Pest Infestation Levels', *Forests*, 6(3), pp. 594-612.

Lehnert, L.W., Meyer, H. and Bendix, J. (2016) *hsdar: Manage, analyse and simulate hyperspectral data in R.*

Lein, J.K. (2012a) 'Hyperspectral Sensing', in Lein, J.K. (ed.) *Environmental Sensing: Analytical Techniques for Earth Observation*. New York, NY, USA: Springer, pp. 213-238.

Lein, J.K. (2012b) 'Thermal Sensing and Anomaly Detection', in Lein, J.K. (ed.) *Environmental Sensing: Analytical Techniques for Earth Observation*. New York, NY, USA: Springer, pp. 193-212.

Leinonen, I., Grant, O.M., Tagliavia, C.P.P., Chaves, M.M. and Jones, H.G. (2006) 'Estimating stomatal conductance with thermal imagery', *Plant, Cell & Environment*, 29(8), pp. 1508-1518.

Leinonen, I. and Jones, H.G. (2004) 'Combining thermal and visible imagery for estimating canopy temperature and identifying plant stress', *Journal of Experimental Botany*, 55(401), pp. 1423-1431.

Lelong, C.C.D., Burger, P., Jubelin, G., Roux, B., Labbe, S. and Baret, F. (2008) 'Assessment of unmanned aerial vehicles imagery for quantitative monitoring of wheat crop in small plots', *Sensors*, 8(5), pp. 3557-3585.

Lewis, S.L., Edwards, D.P. and Galbraith, D. (2015) 'Increasing human dominance of tropical forests', *Science*, 349(6250), pp. 827-832.

Lillesand, T.M., Kiefer, R.W. and Chipman, J. (2008) *Remote sensing and image interpretation*. 6th Edition edn. USA: John Wiley & Sons, Inc.

Lim, K., Treitz, P., Wulder, M., St-Onge, B. and Flood, M. (2003) 'LiDAR remote sensing of forest structure', *Progress in Physical Geography*, 27(1), pp. 88-106.

Lindenthal, M., Steiner, U., Dehne, H.W. and Oerke, E.C. (2005) 'Effect of Downy Mildew Development on Transpiration of Cucumber Leaves Visualized by Digital Infrared Thermography', *Phytopathology*, 95(3), pp. 233-240.

Lisein, J., Pierrot-Deseilligny, M., Bonnet, S. and Lejeune, P. (2013) 'A Photogrammetric Workflow for the Creation of a Forest Canopy Height Model from Small Unmanned Aerial System Imagery', *Forests*, 4(4), pp. 922-944.

Liu, F., Liu, X.N., Ding, C. and Wu, L. (2015) 'The dynamic simulation of rice growth parameters under cadmium stress with the assimilation of multi-period spectral indices and crop model', *Field Crops Research*, 183, pp. 225-234.

Liu, J., Miller, J.R., Haboudane, D. and Pattey, E. (2004) Exploring the relationship between red edge parameters and crop variables for precision agriculture. *Geoscience and Remote Sensing Symposium, 2004. IGARSS '04. Proceedings. 2004 IEEE International*. 20-24 Sept. 2004.

Liu, M., Liu, X., Ding, W. and Wu, L. (2011) 'Monitoring stress levels on rice with heavy metal pollution from hyperspectral reflectance data using wavelet-fractal analysis', *International Journal of Applied Earth Observation and Geoinformation*, 13(2), pp. 246-255.

Lopez-Lopez, M., Calderon, R., Gonzalez-Dugo, V., Zarco-Tejada, P.J. and Fereres, E. (2016) 'Early Detection and Quantification of Almond Red Leaf Blotch Using High-Resolution Hyperspectral and Thermal Imagery', *Remote Sensing*, 8(4).

Lovisolo, C., Perrone, I., Carra, A., Ferrandino, A., Flexas, J., Medrano, H. and Schubert, A. (2010) 'Drought-induced changes in development and function of grapevine (Vitis spp.) organs and in their hydraulic and non-hydraulic interactions at the whole-plant level: a physiological and molecular update', *Functional Plant Biology*, 37(2), pp. 98-116.

Lugassi, R., Goldshleger, N. and Chudnovsky, A. (2017) 'Studying Vegetation Salinity: From the Field View to a Satellite-Based Perspective', *Remote Sensing*, 9(2).

Luhmann, T., Piechel, J. and Roelfs, T. (2013) 'Geometric Calibration of Thermographic Cameras', in Kuenzer, C. and Dech, S. (eds.) *Thermal Infrared Remote Sensing: Sensors, Methods, Applications*. Dordrecht: Springer Netherlands, pp. 27-42.

Macdonald, E. (2011) *Sustainable Management of Scots Pine in the Northern Periphery: Silvicultural Guidance Note 6 - Diseases and Pests of Scots Pine*.

Mack, R.N., Simberloff, D., Lonsdale, W.M., Evans, H., Clout, M. and Bazzaz, F.A. (2000) 'Biotic invasions: Causes, epidemiology, global consequences, and control', *Ecological Applications*, 10(3), pp. 689-710.

Maes, W.H., Achten, W.M.J., Reubens, B. and Muys, B. (2011) 'Monitoring stomatal conductance of Jatropha curcas seedlings under different levels of water shortage with infrared thermography', *Agricultural and Forest Meteorology*, 151(5), pp. 554-564.

Maes, W.H. and Steppe, K. (2012) 'Estimating evapotranspiration and drought stress with ground-based thermal remote sensing in agriculture: a review', *Journal of Experimental Botany*, 63(13), pp. 4671-4712.

Mahan, J.R. and Upchurch, D.R. (1988) 'Maintenance of constant leaf temperature by plants - I. Hypothesis - limited homeothermy', *Environmental and Experimental Botany*, 28(4), pp. 351–357.

Mahlein, A.K., Rumpf, T., Welke, P., Dehne, H.W., Plümer, L., Steiner, U. and Oerke, E.C. (2013) 'Development of spectral indices for detecting and identifying plant diseases', *Remote Sensing of Environment*, 128, pp. 21-30.

Maier, S.W. (2001) 'Method of deriving sunlight induced fluorescence from radiance measurements and devices for executing the method'. United States Patent US 6329660 B1.

Maier, S.W., Günther, K.P. and Stellmes, M. (2003) 'Sun-Induced Fluorescence: A New Tool for Precision Farming', in Schepers, J. and VanToai, T. (eds.) *Digital Imaging and Spectral Techniques: Applications to Precision Agriculture and Crop Physiology*. American Society of Agronomy, Crop Science Society of America, and Soil Science Society of America, pp. 209-222.

Malenovsky, Z., Homolova, L., Zurita-Milla, R., Lukes, P., Kaplan, V., Hanus, J., Gastellu-Etchegorry, J.P. and Schaepman, M.E. (2013) 'Retrieval of spruce leaf chlorophyll content from airborne image data using continuum removal and radiative transfer', *Remote Sensing of Environment*, 131, pp. 85-102.

Malenovsky, Z., Ufer, C., Lhotakova, Z., Clevers, J.G.P.W., Schaepman, M.E., Albrechtova, J. and Cudlin, P. (2006) 'A new hyperspectral index for chlorophyll estimation of a forest canopy: Area under curve normalised to maximal band depth between 650-725 nm', *EARSeL eProceedings*, 5(2), pp. 161-172.

Malthus, T.J., Suarez-Minguez, J.C., Woodhouse, I.H. and Shaw, D.T. (2002) *Review of remote sensing in commercial forestry*. Forest Research.

Mann, P.S. and Lacke, C.J. (2010) *Introductory Statistics*. John Wiley & Sons Canada, Limited.

Matsuki, T., Yokoya, N. and Iwasaki, A. (2015) 'Hyperspectral Tree Species Classification of Japanese Complex Mixed Forest With the Aid of Lidar Data', *Ieee Journal of Selected Topics in Applied Earth Observations and Remote Sensing*, 8(5), pp. 2177-2187.

Maxwell, K. and Johnson, G.N. (2000) 'Chlorophyll fluorescence - a practical guide', *Journal of Experimental Botany*, 51(345), pp. 659-668.

Maynard, R. and Allen, S. (2012) *The threat to England's trees from Invasive Non-Native Species of Pest and Disease: A briefing from Zac Goldsmith MP in collaboration with the Countryside Restoration Trust*.

Mazzoni, M., Agati, G., Del Bianco, S., Cecchi, G., & Mazzinghi, P. (2007) High resolution measurements of solar induced chlorophyll fluorescence in the Fraunhofer Hα and in the atmospheric oxygen lines. *Proceedings of the 3rd International Workshop on Remote Sensing of Vegetation Fluorescence*. Florence, Italy, 7–9 February 2007.

McGaughey, R.J. (2016) *FUSION/LDV: Software for LIDAR Data Analysis and Visualization*. USDA Forest Service Pacific Northwest Research Station.

Mclaughlin, S.B. (1985) 'Effects of Air-Pollution on Forests - a Critical-Review', *Journal of the Air Pollution Control Association*, 35(5), pp. 512-534.

Melin, M., Matala, J., Mehtatalo, L., Suvanto, A. and Packalen, P. (2016) 'Detecting moose (Alces alces) browsing damage in young boreal forests from airborne laser scanning data', *Canadian Journal of Forest Research*, 46(1), pp. 10-19.

Merino, L., Caballero, F., Martinez-de-Dios, J.R., Maza, I. and Ollero, A. (2012) 'An Unmanned Aircraft System for Automatic Forest Fire Monitoring and Measurement', *Journal of Intelligent & Robotic Systems*, 65(1-4), pp. 533-548.

Meroni, M., Busetto, L., Colombo, R., Guanter, L., Moreno, J. and Verhoef, W. (2010) 'Performance of Spectral Fitting Methods for vegetation fluorescence quantification', *Remote Sensing of Environment*, 114(2), pp. 363-374.

Meroni, M. and Colombo, R. (2006) 'Leaf level detection of solar induced chlorophyll fluorescence by means of a subnanometer resolution spectroradiometer', *Remote Sensing of Environment*, 103(4), pp. 438-448.

Meroni, M., Rossini, M., Guanter, L., Alonso, L., Rascher, U., Colombo, R. and Moreno, J. (2009) 'Remote sensing of solar-induced chlorophyll fluorescence: Review of methods and applications', *Remote Sensing of Environment*, 113(10), pp. 2037-2051.

Merton, R.N. (1999) Monitoring community hysteresis using spectral shift analysis and the red-edge vegetation stress index. *Proceedings of the Seventh Annual JPL Airborne Earth Science Workshop*. NASA, Jet Propulsion Laboratoty, Pasadena, California, USA.

Merzlyak, M.N., Gitelson, A.A., Chivkunova, O.B. and Rakitin, V.Y.U. (1999) 'Non-destructive optical detection of pigment changes during leaf senescence and fruit ripening', *Physiologia Plantarum*, 106(1), pp. 135-141.

Mevik, B.H. and Wehrens, R. (2007) 'The pls package: Principal component and partial least squares regression in R', *Journal of Statistical Software*, 18(2), pp. 1-23.

Michez, A., Piegay, H., Jonathan, L., Claessens, H. and Lejeune, P. (2016a) 'Mapping of riparian invasive species with supervised classification of Unmanned Aerial System (UAS) imagery', *International Journal of Applied Earth Observation and Geoinformation*, 44, pp. 88-94.

Michez, A., Piegay, H., Lisein, J., Claessens, H. and Lejeune, P. (2016b) 'Classification of riparian forest species and health condition using multi-temporal and hyperspatial imagery from unmanned aerial system', *Environmental Monitoring and Assessment*, 188(3).

Mildrexler, D., Yang, Z.Q., Cohen, W.B. and Bell, D.M. (2016) 'A forest vulnerability index based on drought and high temperatures', *Remote Sensing of Environment*, 173, pp. 314-325.

Millar, C.I. and Stephenson, N.L. (2015) 'Temperate forest health in an era of emerging megadisturbance', *Science*, 349(6250), pp. 823-826.

Minten, B. and Randrianarisoa, C. (2012) *Forest Preservation, Flooding and Soil Fertility: Evidence from Madagascar*.

Mirik, M., Jones, D.C., Price, J.A., Workneh, F., Ansley, R.J. and Rush, C.M. (2011) 'Satellite Remote Sensing of Wheat Infected by Wheat streak mosaic virus', *Plant Disease*, 95(1), pp. 4-12.

Mitchell, T.M. (1997) *Machine learning*. New York: New York : McGraw-Hill.

Mitsa, T. (2010) *Temporal Data Mining*. CRC Press.

Moeser, D., Roubinek, J., Schleppi, P., Morsdorf, F. and Jonas, T. (2014) 'Canopy closure, LAI and radiation transfer from airborne LiDAR synthetic images', *Agricultural and Forest Meteorology*, 197, pp. 158-168.

Moller, M., Alchanatis, V., Cohen, Y., Meron, M., Tsipris, J., Naor, A., Ostrovsky, V., Sprintsin, M. and Cohen, S. (2007) 'Use of thermal and visible imagery for estimating crop water status of irrigated grapevine', *Journal of Experimental Botany*, 58(4), pp. 827-838.

Monsi, M. and Saeki, T. (1953) 'Uber den Lichtfaktor in den Pflanzengesellschaften und seine Bedeutung fur die Stoffproduktion', *Jpn. J. Bot.*, (14), pp. 22-52.

Monsi, M. and Saeki, T. (2005) 'On the factor light in plant communities and its importance for matter production', *Annals of Botany*, 95(3), pp. 549-567.

Montillet, J.-L. and Hirt, H. (2013) 'New checkpoints in stomatal defense', *Trends in Plant Science*, 18(6), pp. 295-297.

Moran, M.S., Clarke, T.R., Inoue, Y. and Vidal, A. (1994) 'Estimating crop water deficit using the relation between surface-air temperature and spectral vegetation index', *Remote Sensing of Environment*, 49(3), pp. 246-263.

Morsdorf, F., Kotz, B., Meier, E., Itten, K.I. and Allgower, B. (2006) 'Estimation of LAI and fractional cover from small footprint airborne laser scanning data based on gap fraction', *Remote Sensing of Environment*, 104(1), pp. 50-61.

Moshou, D., Gravalos, I., Bravo, D., Oberti, R., West, J. and Ramon, H. (2012) 'Multisensor Fusion of Remote Sensing Data for Crop Disease Detection', in Thakur, J., Singh, S., Ramanathan, A.L., Prasad, M.B. and Gossel, W. (eds.) *Geospatial Techniques for Managing Environmental Resources*. Springer Netherlands, pp. 201-219.

Moya, I., Daumard, F., Moise, N., Ounis, A. and Goulas, Y. (2007) 'First airborne multiwavelenght passive chlorophyll fluorescence measurements over La Mancha (Spain) Fields',

in Sobrino, J.A. (ed.) *Second Recent Advances in Quantitative Remote Sensing*. València, Spain: Publicacions de la Universitat de València, pp. 820-825.

Muchoney, D.M. and Haack, B.N. (1994) 'Change Detection for Monitoring Forest Defoliation', *Photogrammetric Engineering and Remote Sensing*, 60(10), pp. 1243-1251.

Murphy, J.M., Sexton, D.M.H., Jenkins, G.J., Boorman, P.M., Booth, B.B.B., Brown, C.C., Clark, R.T., Collins, M., Harris, G.R., Kendon, E.J., Betts, R.A., Brown, S.J., Howard, T.P., Humphrey, K.A., McCarthy, M.P., McDonald, R.E., Stephens, A., Wallace, C., Warren, R., Wilby, R. and Wood, R.A. (2009) *UK Climate Projections Science Report: Climate change projections*. Met Office Hadley Centre, Exeter.

Mutanga, O. and Skidmore, A.K. (2007) 'Red edge shift and biochemical content in grass canopies', *Isprs Journal of Photogrammetry and Remote Sensing*, 62(1), pp. 34-42.

Naesset, E., Gobakken, T., Holmgren, J., Hyyppa, H., Hyyppa, J., Maltamo, M., Nilsson, M., Olsson, H., Persson, A. and Soderman, U. (2004) 'Laser scanning of forest resources: The Nordic experience', *Scandinavian Journal of Forest Research*, 19(6), pp. 482-499.

Nasi, R., Honkavaara, E., Lyytikainen-Saarenmaa, P., Blomqvist, M., Litkey, P., Hakala, T., Viljanen, N., Kantola, T., Tanhuanpaa, T. and Holopainen, M. (2015) 'Using UAV-Based Photogrammetry and Hyperspectral Imaging for Mapping Bark Beetle Damage at Tree-Level', *Remote Sensing*, 7(11), pp. 15467-15493.

Nguy-Robertson, A.L., Peng, Y., Gitelson, A.A., Arkebauer, T.J., Pimstein, A., Herrmann, I., Karnieli, A., Rundquist, D.C. and Bonfil, D.J. (2014) 'Estimating green LAI in four crops: Potential of determining optimal spectral bands for a universal algorithm', *Agricultural and Forest Meteorology*, 192–193, pp. 140-148.

Nichol, C.J., Huemmrich, K.F., Black, T.A., Jarvis, P.G., Walthall, C.L., Grace, J. and Hall, F.G. (2000) 'Remote sensing of photosynthetic-light-use efficiency of boreal forest', *Agricultural and Forest Meteorology*, 101(2-3), pp. 131-142.

Nichol, C.J., Rascher, U., Matsubara, S. and Osmond, B. (2006) 'Assessing photosynthetic efficiency in an experimental mangrove canopy using remote sensing and chlorophyll fluorescence', *Trees-Structure and Function*, 20(1), pp. 9-15.

Niemann, K.O., Quinn, G., Stephen, R., Visintini, F. and Parton, D. (2015) 'Hyperspectral Remote Sensing of Mountain Pine Beetke with an Emphasis on Pre-visual Assessment', *Canadian Journal of Remote Sensing*, 41(3), pp. 191-202.

Nishar, A., Richards, S., Breen, D., Robertson, J. and Breen, B. (2016) 'Thermal infrared imaging of geothermal environments and by an unmanned aerial vehicle (UAV): A case study of the Wairakei – Tauhara geothermal field, Taupo, New Zealand', *Renewable Energy*, 86, pp. 1256-1264.

Nugent, P.W., Shaw, J.A. and Pust, N.J. (2013) 'Correcting for focal-plane-array temperature dependence in microbolometer infrared cameras lacking thermal stabilization', *Optical Engineering*, 52(6).

Olsson, P.O., Lindstrom, J. and Eldundh, L. (2016) 'Near real-time monitoring of insect induced defoliation in subalpine birch forests with MODIS derived NDVI', *Remote Sensing of Environment*, 181, pp. 42-53.

Omasa, K. and Croxdale, J.G. (1992) 'Image analysis of stomatal movements and gas exchange', in Häder, D.P. (ed.) *Image Analysis in Biology*. Boca Raton: CRC Press, pp. 171–193.

Omasa, K. and Takayama, K. (2003) 'Simultaneous Measurement of Stomatal Conductance, Non-photochemical Quenching, and Photochemical Yield of Photosystem II in Intact Leaves by Thermal and Chlorophyll Fluorescence Imaging', *Plant and Cell Physiology*, 44(12), pp. 1290-1300.

Ostrower, D. (2006) 'Optical Thermal Imaging – replacing microbolometer technology and achieving universal deployment', *III-Vs Review*, 19(6), pp. 24-27.

Pal, M. and Mather, P.M. (2005) 'Support vector machines for classification in remote sensing', *International Journal of Remote Sensing*, 26(5), pp. 1007-1011.

Parsons, O. and Carpenter, G.A. (2003) 'ARTMAP neural networks for information fusion and data mining: map production and target recognition methodologies', *Neural Networks*, 16(7), pp. 1075-1089.

Pearse, G.D., Morgenroth, J., Watt, M.S. and Dash, J.P. (2017) 'Optimising prediction of forest leaf area index from discrete airborne lidar', *Remote Sensing of Environment*, 200, pp. 220-239.

Pedrós, R., Moya, I., Goulas, Y. and Jacquemoud, S. (2008) 'Chlorophyll fluorescence emission spectrum inside a leaf', *Photochemical & Photobiological Sciences*, 7(4), pp. 498-502.

Peduzzi, A., Wynne, R.H., Fox, T.R., Nelson, R.F. and Thomas, V.A. (2012) 'Estimating leaf area index in intensively managed pine plantations using airborne laser scanner data', *Forest Ecology and Management*, 270, pp. 54-65.

Peguero-Pina, J.J., Morales, F., Flexas, J., Gil-Pelegrin, E. and Moya, I. (2008) 'Photochemistry, remotely sensed physiological reflectance index and de-epoxidation state of the xanthophyll cycle in Quercus coccifera under intense drought', *Oecologia*, 156(1), pp. 1-11.

Pena, M.A. and Altmann, S.H. (2009) 'Use of satellite-derived hyperspectral indices to identify stress symptoms in an Austrocedrus chilensis forest infested by the aphid Cinara cupressi', *International Journal of Pest Management*, 55(3), pp. 197-206.

Peñuelas, J., Baret, F. and Filella, I. (1995) 'Semi-empirical indices to assess carotenoids/chlorophyll a ratio from leaf spectral reflectance', *Photosynthetica*, 31(2), pp. 221-230.

Penuelas, J. and Filella, I. (1998) 'Visible and near-infrared reflectance techniques for diagnosing plant physiological status', *Trends in Plant Science*, 3(4), pp. 151-156.

Peñuelas, J., Filella, I., Biel, C., Serrano, L. and Savé, R. (1993) 'The reflectance at the 950–970 nm region as an indicator of plant water status', *International Journal of Remote Sensing*, 14(10), pp. 1887-1905.

Penuelas, J., Filella, I., Serrano, L. and Save, R. (1996) 'Cell wall elasticity and water index (R970 nm R900 nm) in wheat under different nitrogen availabilities', *International Journal of Remote Sensing*, 17(2), pp. 373-382.

Penuelas, J., Gamon, J.A., Fredeen, A.L., Merino, J. and Field, C.B. (1994) 'Reflectance Indexes Associated with Physiological-Changes in Nitrogen-Limited and Water-Limited Sunflower Leaves', *Remote Sensing of Environment*, 48(2), pp. 135-146.

Penuelas, J., Pinol, J., Ogaya, R. and Filella, I. (1997) 'Estimation of plant water concentration by the reflectance water index WI (R900/R970)', *International Journal of Remote Sensing*, 18(13), pp. 2869-2875.

Pérez-Priego, O., Zarco-Tejada, P.J., Miller, J.R., Sepulcre-Cantó, G. and Fereres Castiel, E. (2005) 'Detection of Water Stress in Orchard Trees with a High-Resolution Spectrometer through

Chlorophyll Fluorescence in-filling of the O2-A band', *IEEE Transactions on Geoscience and Remote Sensing*, 43(12), pp. 2759-2769.

Perez-Sierra, A. (2016) *TreeAlert*.

Phattaralerphong, J. and Sinoquet, H. (2005) 'A method for 3D reconstruction of tree crown volume from photographs: assessment with 3D-digitized plants', *Tree Physiology*, 25(10), pp. 1229-1242.

Phillips, N., Nagchaudhuri, A., Oren, R. and Katul, G. (1997) 'Time constant for water transport in loblolly pine trees estimated from time series of evaporative demand and stem sapflow', *Trees-Structure and Function*, 11(7), pp. 412-419.

Piao, S.L., Mohammat, A., Fang, J.Y., Cai, Q. and Feng, J.M. (2006) 'NDVI-based increase in growth of temperate grasslands and its responses to climate changes in China', *Global Environmental Change*, 16(4), pp. 340-348.

Pierzchala, M., Talbot, B. and Astrup, R. (2014) 'Estimating Soil Displacement from Timber Extraction Trails in Steep Terrain: Application of an Unmanned Aircraft for 3D Modelling', *Forests*, 5(6), pp. 1212-1223.

Pinter Jr., P.J., Hatfield, J.L., Schepers, J.S., Barnes, E.M., Moran, M.S., Daughtry, C.S.T. and Upchurch, D.R. (2003) 'Remote Sensing for Crop Management', *Photogrammetric Engineering & Remote Sensing*, 69(6), pp. 647-664.

Pohl, C. and van Genderen, J. (2016) *Remote Sensing Image Fusion: A Practical Guide*. CRC Press.

Pontius, J., Martin, M., Plourde, L. and Hallett, R. (2008) 'Ash decline assessment in emerald ash borer-infested regions: A test of tree-level, hyperspectral technologies', *Remote Sensing of Environment*, 112(5), pp. 2665-2676.

Pope, G. and Treitz, P. (2013) 'Leaf Area Index (LAI) Estimation in Boreal Mixedwood Forest of Ontario, Canada Using Light Detection and Ranging (LiDAR) and WorldView-2 Imagery', *Remote Sensing*, 5(10), pp. 5040-5063.

Popescu, S.C. and Zhao, K. (2008) 'A voxel-based lidar method for estimating crown base height for deciduous and pine trees', *Remote Sensing of Environment*, 112(3), pp. 767-781.

Prabhakar, M., Prasad, Y.G. and Rao, M. (2012) 'Remote Sensing of Biotic Stress in Crop Plants and Its Applications for Pest Management', in Venkateswarlu, B., Shanker, A.K., Shanker, C. and Maheswari, M. (eds.) *Crop Stress and its Management: Perspectives and Strategies*. Springer Netherlands, pp. 517-545.

Prashar, A. and Jones, H.G. (2014) 'Infra-Red Thermography as a High-Throughput Tool for Field Phenotyping', *Agronomy*, 4(3), pp. 397-417.

Pu, R., Foschi, L. and Gong, P. (2004) 'Spectral feature analysis for assessment of water status and health level in coast live oak (Quercus agrifolia) leaves', *International Journal of Remote Sensing*, 25(20), pp. 4267-4286.

Pu, R. and Gong, P. (2004) 'Wavelet transform applied to EO-1 hyperspectral data for forest LAI and crown closure mapping', *Remote Sensing of Environment*, 91(2), pp. 212-224.

Pu, R., Kelly, M., Anderson, G.L. and Gong, P. (2008) 'Using CASI hyperspectral imagery to detect mortality and vegetation stress associated with a new hardwood forest disease', *Photogrammetric Engineering & Remote Sensing*, 74(1), pp. 65-75.

Puliti, S., Orka, H.O., Gobakken, T. and Naesset, E. (2015) 'Inventory of Small Forest Areas Using an Unmanned Aerial System', *Remote Sensing*, 7(8), pp. 9632-9654.

Qi, Y., Li, F., Liu, Z. and Jin, G. (2014) 'Impact of understorey on overstorey leaf area index estimation from optical remote sensing in five forest types in northeastern China', *Agricultural and Forest Meteorology*, 198–199, pp. 72-80.

Qin, Z. and Zhang, M. (2005) 'Detection of rice sheath blight for in-season disease management using multispectral remote sensing', *International Journal of Applied Earth Observation and Geoinformation*, 7(2), pp. 115-128.

Quinlan, J.R. (1986) 'Induction of Decision Trees', *Machine Learning*, 1(1), pp. 81-106.

Quintano, C., Fernández-Manso, A., Stein, A. and Bijker, W. (2011) 'Estimation of area burned by forest fires in Mediterranean countries: A remote sensing data mining perspective', *Forest Ecology and Management*, 262(8), pp. 1597-1607.

Radeloff, V.C., Mladenoff, D.J. and Boyce, M.S. (1999) 'Detecting Jack Pine Budworm Defoliation Using Spectral Mixture Analysis: Separating Effects from Determinants', *Remote Sensing of Environment*, 69(2), pp. 156-169.

Raffa, K.F., Aukema, B., Bentz, B.J., Carroll, A., Erbilgin, N., Herms, D.A., Hicke, J.A., Hofstetter, R.W., Katovich, S., Lindgren, B.S., Logan, J., Mattson, W., Munson, A.S., Robison, D.J., Six, D.L., Tobin, P.C., Townsend, P.A. and Wallin, K.F. (2009) 'A Literal Use of "Forest Health" Safeguards against Misuse and Misapplication', *Journal of Forestry*, 107(5), pp. 276-277.

Rautiainen, M. (2005) 'Retrieval of leaf area index for a coniferous forest by inverting a forest reflectance model', *Remote Sensing of Environment*, 99(3), pp. 295-303.

Ray, D., Morison, J. and Broadmeadow, M. (2010) *Climate change: impacts and adaptation in England's woodlands*. Forest Research.

Ray, D., Wainhouse, D., Webber, J. and Gardiner, B. (2008) *Impacts of climate change on forests and forestry in Scotland*. Forest Research.

Read, D.J., Freer-Smith, P.H., Morison, J.I.L., Hanley, N., West, C.C. and Snowdon, P. (2009) *Combating climate change – a role for UK forests. An assessment of the potential of the UK's trees and woodlands to mitigate and adapt to climate change.* The Stationery Office, Edinburgh.

Reed, B.C., Brown, J.F., Vanderzee, D., Loveland, T.R., Merchant, J.W. and Ohlen, D.O. (1994) 'Measuring Phenological Variability from Satellite Imagery', *Journal of Vegetation Science*, 5(5), pp. 703-714.

Reinert, S., Bögelein, R. and Thomas, F.M. (2012) 'Use of thermal imaging to determine leaf conductance along a canopy gradient in European beech (Fagus sylvatica)', *Tree Physiology*, 32(3), pp. 294-302.

Reitberger, J., Schnorr, C., Krzystek, P. and Stilla, U. (2009) '3D segmentation of single trees exploiting full waveform LIDAR data', *Isprs Journal of Photogrammetry and Remote Sensing*, 64(6), pp. 561-574.

Riano, D., Valladares, F., Condes, S. and Chuvieco, E. (2004) 'Estimation of leaf area index and covered ground from airborne laser scanner (Lidar) in two contrasting forests', *Agricultural and Forest Meteorology*, 124(3-4), pp. 269-275.

Roberts, J.W., Tesfamichael, S., Gebreslasie, M., van Aardt, J. and Ahmed, F.B. (2007) 'Forest structural assessment using remote sensing technologies: an overview of the current state of the art', *Southern Hemisphere Forestry Journal*, 69(3), pp. 183-203.

Rodriguez-Galiano, V.F., Ghimire, B., Rogan, J., Chica-Olmo, M. and Rigol-Sanchez, J.P. (2012) 'An assessment of the effectiveness of a random forest classifier for land-cover classification', *Isprs Journal of Photogrammetry and Remote Sensing*, 67, pp. 93-104.

Roujean, J.L. and Breon, F.M. (1995) 'Estimating Par Absorbed by Vegetation from Bidirectional Reflectance Measurements', *Remote Sensing of Environment*, 51(3), pp. 375-384.

Royle, D.D. and Lathrop, R.G. (1997) 'Monitoring hemlock forest health in New Jersey using Landsat TM data and change detection techniques', *Forest Science*, 43(3), pp. 327-335.

Ruiliang, P., Peng, G., Biging, G.S. and Larrieu, M.R. (2003) 'Extraction of red edge optical parameters from Hyperion data for estimation of forest leaf area index', *IEEE Transactions on Geoscience and Remote Sensing*, 41(4), pp. 916-921.

Salami, E., Barrado, C. and Pastor, E. (2014) 'UAV Flight Experiments Applied to the Remote Sensing of Vegetated Areas', *Remote Sensing*, 6(11), pp. 11051-11081.

Sanches, I.D., Souza, C.R. and Kokaly, R.F. (2014) 'Spectroscopic remote sensing of plant stress at leaf and canopy levels using the chlorophyll 680 nm absorption feature with continuum removal', *ISPRS Journal of Photogrammetry and Remote Sensing*, 97, pp. 111-122.

Sankaran, S., Maja, J.M., Buchanon, S. and Ehsani, R. (2013) 'Huanglongbing (Citrus Greening) Detection Using Visible, Near Infrared and Thermal Imaging Techniques', *Sensors*, 13(2), pp. 2117-2130.

Santesteban, L.G., Di Gennaro, S.F., Herrero-Langreo, A., Miranda, C., Royo, J.B. and Matese, A. (2017) 'High-resolution UAV-based thermal imaging to estimate the instantaneous and seasonal variability of plant water status within a vineyard', *Agricultural Water Management*, 183, pp. 49–59.

Santoso, H., Gunawan, T., Jatmiko, R., Darmosarkoro, W. and Minasny, B. (2011) 'Mapping and identifying basal stem rot disease in oil palms in North Sumatra with QuickBird imagery', *Precision Agriculture*, 12(2), pp. 233-248.

Sasaki, T., Imanishi, J., Ioki, K., Song, Y. and Morimoto, Y. (2013) 'Estimation of leaf area index and gap fraction in two broad-leaved forests by using small-footprint airborne LiDAR', *Landscape and Ecological Engineering*, pp. 1-11.

Savitzky, A. and Golay, M.J.E. (1964) 'Smoothing and Differentiation of Data by Simplified Least Squares Procedures', *Analytical Chemistry*, 36(8), pp. 1627-1639.

Scherrer, D., Bader, M.K.F. and Korner, C. (2011) 'Drought-sensitivity ranking of deciduous tree species based on thermal imaging of forest canopies', *Agricultural and Forest Meteorology*, 151(12), pp. 1632-1640.

Schlerf, M. and Atzberger, C. (2006) 'Inversion of a forest reflectance model to estimate structural canopy variables from hyperspectral remote sensing data', *Remote Sensing of Environment*, 100(3), pp. 281-294.

Schmidt, K.S. and Skidmore, A.K. (2003) 'Spectral discrimination of vegetation types in a coastal wetland', *Remote Sensing of Environment*, 85(1), pp. 92-108.

Schomaker, M.E., Zarnoch, S.J., Bechtold, W.A., Latelle, D.J., Burkman, W.G. and Cox, S.M. (2007) *Crown-condition classification: a guide to data collection and analysis*. U.S. Department of Agriculture, Forest Service, Southern Research Station.

Seidel, H., Schunk, C., Matiu, M. and Menzel, A. (2016) 'Diverging Drought Resistance of Scots Pine Provenances Revealed by Infrared Thermography', *Frontiers in Plant Science*, 7.

Serrano, L., Ustin, S.L., Roberts, D.A., Gamon, J.A. and Peñuelas, J. (2000) 'Deriving Water Content of Chaparral Vegetation from AVIRIS Data', *Remote Sensing of Environment*, 74(3), pp. 570-581.

Shaw, D.T., Malthus, T.J. and Kupiec, J.A. (1998) 'High-spectral resolution data for monitoring Scots pine (Pinus sylvestris L.) regeneration', *International Journal of Remote Sensing*, 19(13), pp. 2601-2608.

Shen, M.G., Zhang, G.X., Cong, N., Wang, S.P., Kong, W.D. and Piao, S.L. (2014) 'Increasing altitudinal gradient of spring vegetation phenology during the last decade on the Qinghai-Tibetan Plateau', *Agricultural and Forest Meteorology*, 189, pp. 71-80.

Shendryk, I., Broich, M., Tulbure, M.G., McGrath, A., Keith, D. and Alexandrov, S.V. (2016) 'Mapping individual tree health using full-waveform airborne laser scans and imaging spectroscopy: A case study for a floodplain eucalypt forest', *Remote Sensing of Environment*, 187, pp. 202-217.

Shumway, R.H. and Stoffer, D.S. (2011) 'ARIMA Models', in *Time Series Analysis and Its Applications: With R Examples*. New York, NY: Springer New York, pp. 83-171.

Simic, A., Chen, J.M. and Noland, T.L. (2011) 'Retrieval of forest chlorophyll content using canopy structure parameters derived from multi-angle data: the measurement concept of combining nadir hyperspectral and off-nadir multispectral data', *International Journal of Remote Sensing*, 32(20), pp. 5621-5644.

Sims, D.A. and Gamon, J.A. (2002) 'Relationships between leaf pigment content and spectral reflectance across a wide range of species, leaf structures and developmental stages', *Remote Sensing of Environment*, 81(2–3), pp. 337-354.

Skakun, R.S., Wulder, M.A. and Franklin, S.E. (2003) 'Sensitivity of the thematic mapper enhanced wetness difference index to detect mountain pine beetle red-attack damage', *Remote Sensing of Environment*, 86(4), pp. 433-443.

Smith, C.L. (2010) 'Temperature', in *Basic Process Measurements*. John Wiley & Sons, Inc., pp. 88-157.

Socolinsky, D.A., Selinger, A. and Neuheisel, J.D. (2003) 'Face recognition with visible and thermal infrared imagery', *Computer Vision and Image Understanding*, 91(1-2), pp. 72-114.

Solberg, S. (2010) 'Mapping gap fraction, LAI and defoliation using various ALS penetration variables', *International Journal of Remote Sensing*, 31(5), pp. 1227-1244.

Solberg, S., Naesset, E., Hanssen, K.H. and Christiansen, E. (2006) 'Mapping defoliation during a severe insect attack on Scots pine using airborne laser scanning', *Remote Sensing of Environment*, 102(3-4), pp. 364-376.

Solomon, S., Qin, D., Manning, M., Chen, Z., Marquis, M., Averyt, K.B., Tignor, M. and Miller, H.L. (2007) *Climate Change 2007: The Physical Science Basis. Contribution of Working Group I to the Fourth Assessment Report of the Intergovernmental Panel on Climate Change*. Cambridge University Press, Cambridge, United Kingdom and New York, NY, USA.

Somers, B., Verbesselt, J., Ampe, E.M., Sims, N., Verstraeten, W.W. and Coppin, P. (2010) 'Spectral mixture analysis to monitor defoliation in mixed-aged Eucalyptus globulus Labill plantations in southern Australia using Landsat 5-TM and EO-1 Hyperion data', *International Journal of Applied Earth Observation and Geoinformation*, 12(4), pp. 270-277.

Spellman, F.R. (2014) 'All about Water', in *The Science of Water: Concepts and Applications, Third Edition*. CRC Press.

Stagakis, S., González-Dugo, V., Cid, P., Guillén-Climent, M.L. and Zarco-Tejada, P.J. (2012) 'Monitoring water stress and fruit quality in an orange orchard under regulated deficit irrigation using narrow-band structural and physiological remote sensing indices', *ISPRS Journal of Photogrammetry and Remote Sensing*, 71, pp. 47-61.

Stenberg, P., Rautiainen, M., Manninen, T., Voipio, P. and Smolander, H. (2004) 'Reduced simple ratio better than NDVI for estimating LAI in Finnish pine and spruce stands', *Silva Fennica*, 38(1), pp. 3-14.

Stone, C., Chisholm, L. and Coops, N. (2001) 'Spectral reflectance characteristics of eucalypt foliage damaged by insects', *Australian Journal of Botany*, 49(6), pp. 687-698.

Stone, C., Chisholm, L.A. and McDonald, S. (2003) 'Spectral reflectance characteristics of Pinus radiata needles affected by dothistroma needle blight', *Canadian Journal of Botany*, 81(6), pp. 560-569.

Suorsa, P., Huhta, E., Nikula, A., Nikinmaa, M., Jantti, A., Helle, H. and Hakkarainen, H. (2003) 'Forest management is associated with physiological stress in an old-growth forest passerine', *Proceedings of the Royal Society of London. Series B: Biological Sciences*, 270(1518), pp. 963-969.

Taghvaeian, S., Comas, L., DeJonge, K.C. and Trout, T.J. (2014) 'Conventional and simplified canopy temperature indices predict water stress in sunflower', *Agricultural Water Management*, 144, pp. 69-80.

Tan-Soo, J.S., Adnan, N., Ahmad, I., Pattanayak, S.K. and Vincent, J.R. (2016) 'Econometric Evidence on Forest Ecosystem Services: Deforestation and Flooding in Malaysia', *Environmental & Resource Economics*, 63(1), pp. 25-44.

Tang, H., Brolly, M., Zhao, F., Strahler, A.H., Schaaf, C.L., Ganguly, S., Zhang, G. and Dubayah, R. (2014) 'Deriving and validating Leaf Area Index (LAI) at multiple spatial scales through lidar remote sensing: A case study in Sierra National Forest, CA', *Remote Sensing of Environment*, 143, pp. 131-141.

Tao, S., Guo, Q., Li, L., Xue, B., Kelly, M., Li, W., Xu, G. and Su, Y. (2014) 'Airborne Lidar-derived volume metrics for aboveground biomass estimation: A comparative assessment for conifer stands', *Agricultural and Forest Meteorology*, 198, pp. 24-32.

Tardieu, F. and Simonneau, T. (1998) 'Variability among species of stomatal control under fluctuating soil water status and evaporative demand: modelling isohydric and anisohydric behaviours', *Journal of Experimental Botany*, 49, pp. 419-432.

Taub, D. (2010) 'Effects of Rising Atmospheric Concentrations of Carbon Dioxide on Plants', *Nature Education Knowledge*, 3(10), p. 21.

Taubenhaus, J.J., Ezekiel, W.N. and Neblette, C.B. (1929) 'Airplane photography in the study of cotton root rot', *Phytopathology*, 19, pp. 1025–1029.

Theisen, A.F. (2002) 'Detecting Chlorophyll Fluorescence from Orbit: The Fraunhofer Line Depth Model', in Muttiah, R. (ed.) *From Laboratory Spectroscopy to Remotely Sensed Spectra of Terrestrial Ecosystems*. Springer Netherlands, pp. 203-232.

Thomas, J.R., Namken, L.N., Oerther, G.F. and Brown, R.G. (1971) 'Estimating Leaf Water Content by Reflectance Measurements', *Agronomy Journal*, 63(6), pp. 845-847.

Thomas, P.J., Sinclair, P., Savachenko, A., Goldman, P., Elinas, P. and Pope, T. (1999) Signal calibration and stability in an uncooled integrated bolometer array. *Proceedings of the IEEE Aerospace Conference*. Snowmass at Aspen, CO, USA, 7 March 1999.

Thomas, V., Treitz, P., McCaughey, J.H., Noland, T. and Rich, L. (2007) 'Canopy chlorophyll concentration estimation using hyperspectral and lidar data for a boreal mixedwood forest in northern Ontario, Canada', *International Journal of Remote Sensing*, 29(4), pp. 1029-1052.

Thompson, I., Mackey, B., McNulty, S. and Mosseler, A. (2009) *Forest Resilience, Biodiversity, and Climate Change. A synthesis of the biodiversity/resilience/stability relationship in forest ecosystems*. Secretariat of the Convention on Biological Diversity, Montreal.

Toomey, M.P. and Vierling, L.A. (2006) 'Estimating equivalent water thickness in a conifer forest using Landsat TM and ASTER data: a comparison study', *Canadian Journal of Remote Sensing*, 32(4), pp. 288-299.

Tsai, F. and Philpot, W. (1998) 'Derivative analysis of hyperspectral data', *Remote Sensing of Environment*, 66(1), pp. 41-51.

Tucker, C.J. (1979) 'Red and Photographic Infrared Linear Combinations for Monitoring Vegetation', *Remote Sensing of Environment*, 8(2), pp. 127-150.

Tucker, C.J. (1980) 'Remote sensing of leaf water content in the near infrared', *Remote Sensing of Environment*, 10(1), pp. 23-32.

Ustin, S.L., Roberts, D.A., Pinzón, J., Jacquemoud, S., Gardner, M., Scheer, G., Castañeda, C.M. and Palacios-Orueta, A. (1998) 'Estimating Canopy Water Content of Chaparral Shrubs Using Optical Methods', *Remote Sensing of Environment*, 65(3), pp. 280-291.

van Leeuwen, M. and Nieuwenhuis, M. (2010) 'Retrieval of forest structural parameters using LiDAR remote sensing', *European Journal of Forest Research*, 129(4), pp. 749-770.

Vanguelova, E., Barsoum, N., Benham, S., Broadmeadow, M., Moffat, A., Nisber, T. and Pitman, R. (2007) *Ten Years of Intensive Environmental Monitoring in British Forests*.

Vapnik, V.N. (1999) 'An overview of statistical learning theory', *Ieee Transactions on Neural Networks*, 10(5), pp. 988-999.

Varshney, P.K. and Arora, M.K. (2004) *Advanced Image Processing Techniques for Remotely Sensed Hyperspectral Data*. Springer.

Verhoef, W. (1984) 'Light scattering by leaf layers with application to canopy reflectance modeling: The SAIL model', *Remote Sensing of Environment*, 16(2), pp. 125-141.

Vermeulen, C., Lejeune, P., Lisein, J., Sawadogo, P. and Bouche, P. (2013) 'Unmanned Aerial Survey of Elephants', *Plos One*, 8(2).

Vincent, L. and Soille, P. (1991) 'Watersheds in Digital Spaces: an Efficient Algorithm Based on Immersion Simulations', *Ieee Transactions on Pattern Analysis and Machine Intelligence*, 13(6), pp. 583-598.

Vogelmann, J.E., Rock, B.N. and Moss, D.M. (1993) 'Red Edge Spectral Measurements from Sugar Maple Leaves', *International Journal of Remote Sensing*, 14(8), pp. 1563-1575.

Wallace, L. (2013) 'Assessing the Stability of Canopy Maps Produced from Uav-Lidar Data', *2013 IEEE International Geoscience and Remote Sensing Symposium (IGARSS)*, pp. 3879-3882.

Wallace, L., Lucieer, A., Watson, C. and Turner, D. (2012) 'Development of a UAV-LiDAR System with Application to Forest Inventory', *Remote Sensing*, 4(6), pp. 1519-1543.

Wallace, L., Watson, C. and Lucieer, A. (2014) 'Detecting pruning of individual stems using Airborne Laser Scanning data captured from an Unmanned Aerial Vehicle', *International Journal of Applied Earth Observation and Geoinformation*, 30, pp. 76-85.

Wang, Q., Adiku, S., Tenhunen, J. and Granier, A. (2005) 'On the relationship of NDVI with leaf area index in a deciduous forest site', *Remote Sensing of Environment*, 94(2), pp. 244-255.

Wang, Q. and Li, P. (2012) 'Hyperspectral indices for estimating leaf biochemical properties in temperate deciduous forests: Comparison of simulated and measured reflectance data sets', *Ecological Indicators*, 14(1), pp. 56-65.

Wang, Y.S., Weinacker, H. and Koch, B. (2008) 'A Lidar point cloud based procedure for vertical canopy structure analysis and 3D single tree modelling in forest', *Sensors*, 8(6), pp. 3938-3951.

Wannasiri, W., Nagai, M., Honda, K., Santitamnont, P. and Miphokasap, P. (2013) 'Extraction of Mangrove Biophysical Parameters Using Airborne LiDAR', *Remote Sensing*, 5(4), pp. 1787-1808.

Webber, J., Brasier, C., Kirk, S., Denman, S. and Jones, B. (2009) *Growing Threat Posed by Phytophthora kernoviae to Native Heathland Ecosystems in Britain*.

Welch, B.L. (1938) 'The Significance of the Difference Between Two Means when the Population Variances are Unequal', *Biometrika*, 29(3/4), pp. 350-362.

Whitehead, K., Moorman, B.J. and Hugenholtz, C.H. (2013) 'Brief Communication: Low-cost, on-demand aerial photogrammetry for glaciological measurement', *Cryosphere*, 7(6), pp. 1879-1884.

Widlowski, J.-L., Mio, C., Disney, M., Adams, J., Andredakis, I., Atzberger, C., Brennan, J., Busetto, L., Chelle, M., Ceccherini, G., Colombo, R., Côté, J.-F., Eenmäe, A., Essery, R., Gastellu-Etchegorry, J.-P., Gobron, N., Grau, E., Haverd, V., Homolová, L., Huang, H., Hunt, L., Kobayashi, H., Koetz, B., Kuusk, A., Kuusk, J., Lang, M., Lewis, P.E., Lovell, J.L., Malenovský, Z., Meroni, M., Morsdorf, F., Mõttus, M., Ni-Meister, W., Pinty, B., Rautiainen, M., Schlerf, M., Somers, B., Stuckens, J., Verstraete, M.M., Yang, W., Zhao, F. and Zenone, T. (2015) 'The fourth phase of the radiative transfer model intercomparison (RAMI) exercise: Actual canopy scenarios and conformity testing', *Remote Sensing of Environment*, 169, pp. 418-437.

Widlowski, J.L., Pinty, B., Lopatka, M., Atzberger, C., Buzica, D., Chelle, M., Disney, M., Gastellu-Etchegorry, J.P., Gerboles, M., Gobron, N., Grau, E., Huang, H., Kallel, A., Kobayashi, H., Lewis, P.E., Qin, W., Schlerf, M., Stuckens, J. and Xie, D. (2013) 'The fourth radiation transfer model intercomparison (RAMI-IV): Proficiency testing of canopy reflectance models with ISO-13528', *Journal of Geophysical Research: Atmospheres*, 118(13), pp. 6869-6890.

Willers, J.L., Jenkins, J.N., Ladner, W.L., Gerard, P.D., Boykin, D.L., Hood, K.B., McKibben, P.L., Samson, S.A. and Bethel, M.M. (2005) 'Site-specific Approaches to Cotton Insect Control. Sampling and Remote Sensing Analysis Techniques', *Precision Agriculture*, 6(5), pp. 431-452.

Willers, J.L., Seal, M.R. and Luttrell, R.G. (1999) 'Remote Sensing, Line-intercept Sampling for Tarnished Plant Bugs (Heteroptera: Miridae) in Mid-south Cotton', *Journal of Cotton Science*, 3(4), pp. 160-170.

Wilson, C.L., Luther, J.E. and Stuart, T.D.T. (1998) 'Spectral Reflectance Characteristics of Dutch Elm Disease', *Canadian Journal of Remote Sensing*, 24(2), pp. 200-205.

Wilson, E.H. and Sader, S.A. (2002) 'Detection of forest harvest type using multiple dates of Landsat TM imagery', *Remote Sensing of Environment*, 80(3), pp. 385-396.

Wing, B.M., Ritchie, M.W., Boston, K., Cohen, W.B. and Olsen, M.J. (2015) 'Individual snag detection using neighborhood attribute filtered airborne lidar data', *Remote Sensing of Environment*, 163, pp. 165-179.

Wingfield, M.J., Brockerhoff, E.G., Wingfield, B.D. and Slippers, B. (2015) 'Planted forest health: The need for a global strategy', *Science*, 349(6250), pp. 832-836.

Wolf, A., Pezoa, J.E. and Figueroa, M. (2016) 'Modeling and Compensating Temperature-Dependent Non-Uniformity Noise in IR Microbolometer Cameras', *Sensors*, 16(7).

Wolf, B.M. and Heipke, C. (2007) 'Automatic extraction and delineation of single trees from remote sensing data', *Machine Vision and Applications*, 18(5), pp. 317-330.

Wulder, M. and Franklin, S.E. (2003) *Remote Sensing of Forest Environments: Concepts and Case Studies*. Springer US.

Wulder, M.A., Bater, C.W., Coops, N.C., Hilker, T. and White, J.C. (2008) 'The role of LiDAR in sustainable forest management', *Forestry Chronicle*, 84(6), pp. 807-826.

Wulder, M.A., White, J.C., Bentz, B., Alvarez, M.F. and Coops, N.C. (2006) 'Estimating the probability of mountain pine beetle red-attack damage', *Remote Sensing of Environment*, 101(2), pp. 150-166.

Yao, W., Krzystek, P. and Heurich, M. (2012) 'Identifying Standing Dead Trees in Forest Areas Based on 3D Single Tree Detection from Full Waveform LiDAR Data', *ISPRS Annals of the Photogrammetry, Remote Sensing and Spatial Information Sciences*.

Yi, Q., Jiapaer, G., Chen, J., Bao, A. and Wang, F. (2014) 'Different units of measurement of carotenoids estimation in cotton using hyperspectral indices and partial least square regression', *ISPRS Journal of Photogrammetry and Remote Sensing*, 91, pp. 72-84.

Yule, U. (1926) 'Why do we Sometimes get Nonsense-Correlations between Time-Series?--A Study in Sampling and the Nature of Time-Series', *Journal of the Royal Statistical Society*, 89(1), pp. 1-63.

Zarco-Tajeda, P.J., Miller, J.R., Haboudane, D., Tremblay, N. and Apostol, S. (2003) Detection of chlorophyll fluorescence in vegetation from airborne hyperspectral CASI imagery in the red edge spectral region. *Geoscience and Remote Sensing Symposium, 2003. IGARSS '03. Proceedings. 2003 IEEE International*. 21-25 July 2003.

Zarco-Tejada, P.J., Berni, J.A.J., Suarez, L., Sepulcre-Canto, G., Morales, F. and Miller, J.R. (2009) 'Imaging chlorophyll fluorescence with an airborne narrow-band multispectral camera for vegetation stress detection', *Remote Sensing of Environment*, 113(6), pp. 1262-1275.

Zarco-Tejada, P.J., Guillén-Climent, M.L., Hernández-Clemente, R., Catalina, A., González, M.R. and Martín, P. (2013) 'Estimating leaf carotenoid content in vineyards using high resolution hyperspectral imagery acquired from an unmanned aerial vehicle (UAV)', *Agricultural and Forest Meteorology*, 171–172, pp. 281-294.

Zarco-Tejada, P.J., Miller, J.R., Mohammed, G.H., Noland, T.L. and Sampson, P.H. (2000) 'Chlorophyll Fluorescence Effects on Vegetation Apparent Reflectance: II. Laboratory and Airborne Canopy-Level Measurements with Hyperspectral Data', *Remote Sensing of Environment*, 74(3), pp. 596-608.

Zarco-Tejada, P.J., Miller, J.R., Morales, A., Berjón, A. and Agüera, J. (2004) 'Hyperspectral indices and model simulation for chlorophyll estimation in open-canopy tree crops', *Remote Sensing of Environment*, 90(4), pp. 463-476.

Zarco-Tejada, P.J., Miller, J.R., Noland, T.L., Mohammed, G.H. and Sampson, P.H. (2001) 'Scaling-up and model inversion methods with narrowband optical indices for chlorophyll content estimation in closed forest canopies with hyperspectral data', *Geoscience and Remote Sensing, IEEE Transactions on*, 39(7), pp. 1491-1507.

Zarco-Tejada, P.J., Pushnik, J.C., Dobrowski, S. and Ustin, S.L. (2003a) 'Steady-state chlorophyll a fluorescence detection from canopy derivative reflectance and double-peak red-edge effects', *Remote Sensing of Environment*, 84(2), pp. 283-294.

Zarco-Tejada, P.J., Rueda, C.A. and Ustin, S.L. (2003b) 'Water content estimation in vegetation with MODIS reflectance data and model inversion methods', *Remote Sensing of Environment*, 85(1), pp. 109-124.

Zhang, F., Yu, K., Zhang, K., Liu, Y., Xu, K. and Liu, Y. (2015) 'An emissivity measurement apparatus for near infrared spectrum', *Infrared Physics & Technology*, 73, pp. 275-280.

Zhang, M., Liu, X. and O'Neill, M. (2002) 'Spectral discrimination of Phytophthora infestans infection on tomatoes based on principal component and cluster analyses', *International Journal of Remote Sensing*, 23(6), pp. 1095-1107.

Zhang, M., Qin, Z. and Liu, X. (2005) 'Remote Sensed Spectral Imagery to Detect Late Blight in Field Tomatoes', *Precision Agriculture*, 6(6), pp. 489-508.

Zhang, M., Qin, Z., Liu, X. and Ustin, S.L. (2003) 'Detection of stress in tomatoes induced by late blight disease in California, USA, using hyperspectral remote sensing', *International Journal of Applied Earth Observation and Geoinformation*, 4(4), pp. 295-310.

Zhang, Y., Chen, J.M., Miller, J.R. and Noland, T.L. (2008) 'Leaf chlorophyll content retrieval from airborne hyperspectral remote sensing imagery', *Remote Sensing of Environment*, 112(7), pp. 3234-3247.

Zheng, G. and Moskal, L.M. (2009) 'Retrieving Leaf Area Index (LAI) Using Remote Sensing: Theories, Methods and Sensors', *Sensors*, 9(4), pp. 2719-2745.

Zimble, D.A., Evans, D.L., Carlson, G.C., Parker, R.C., Grado, S.C. and Gerard, P.D. (2003) 'Characterizing vertical forest structure using small-footprint airborne LiDAR', *Remote Sensing of Environment*, 87(2-3), pp. 171-182.

Appendix A: Atmospheric correction

During the airborne data acquisition ground spectra were collected using an ASD spectrometer for a number of target surfaces. Only one of the sampled areas (a quarry) was encompassed by the atmospherically corrected data provided for this project. The location of the quarry in respect to the research plots is shown in Figure A.1. The comparison between the atmospherically corrected reflectance acquired from the image and the ground spectra of the quarry showed a close match (Figure A.2).
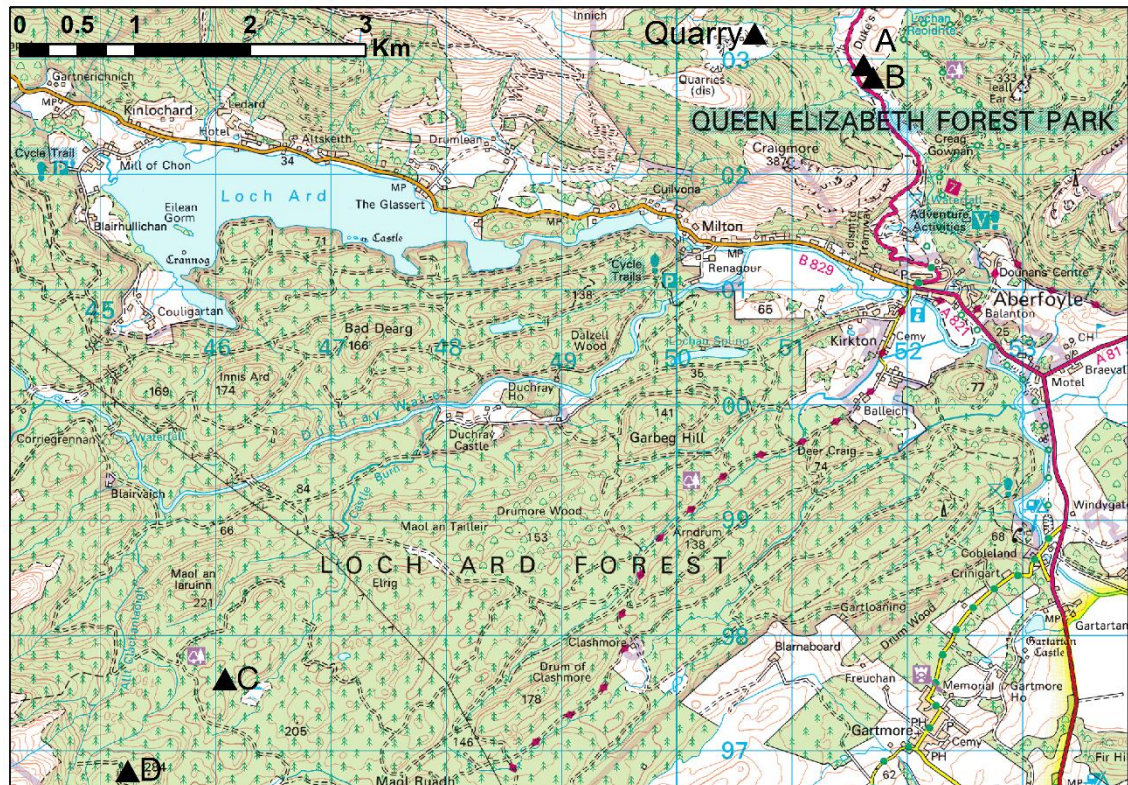
Figure A.1: Location of the quarry in relation to sampling plots A, B, C and D. Contains OS data © Crown copyright and database right 2017.
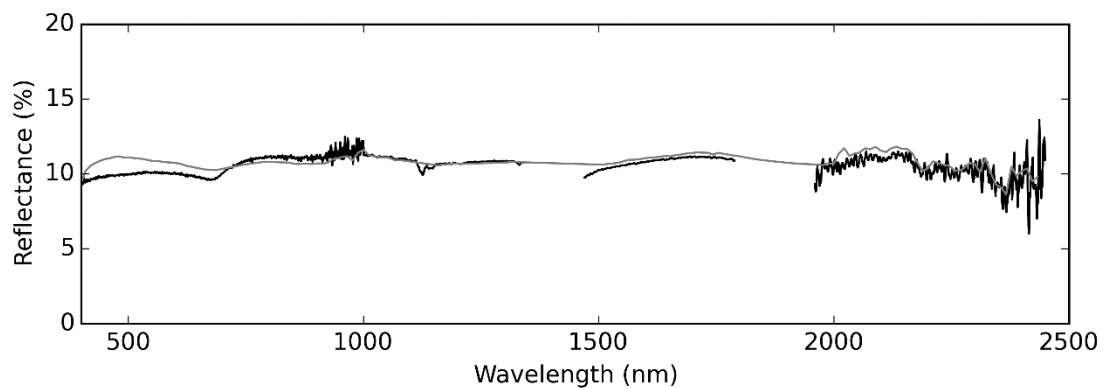
Figure A.1: FENIX sensor's spectrum for the sampled quarry (grey) compared to field measured reflectance (black).

Appendix B: Agisoft PhotoScan processing diagnostics
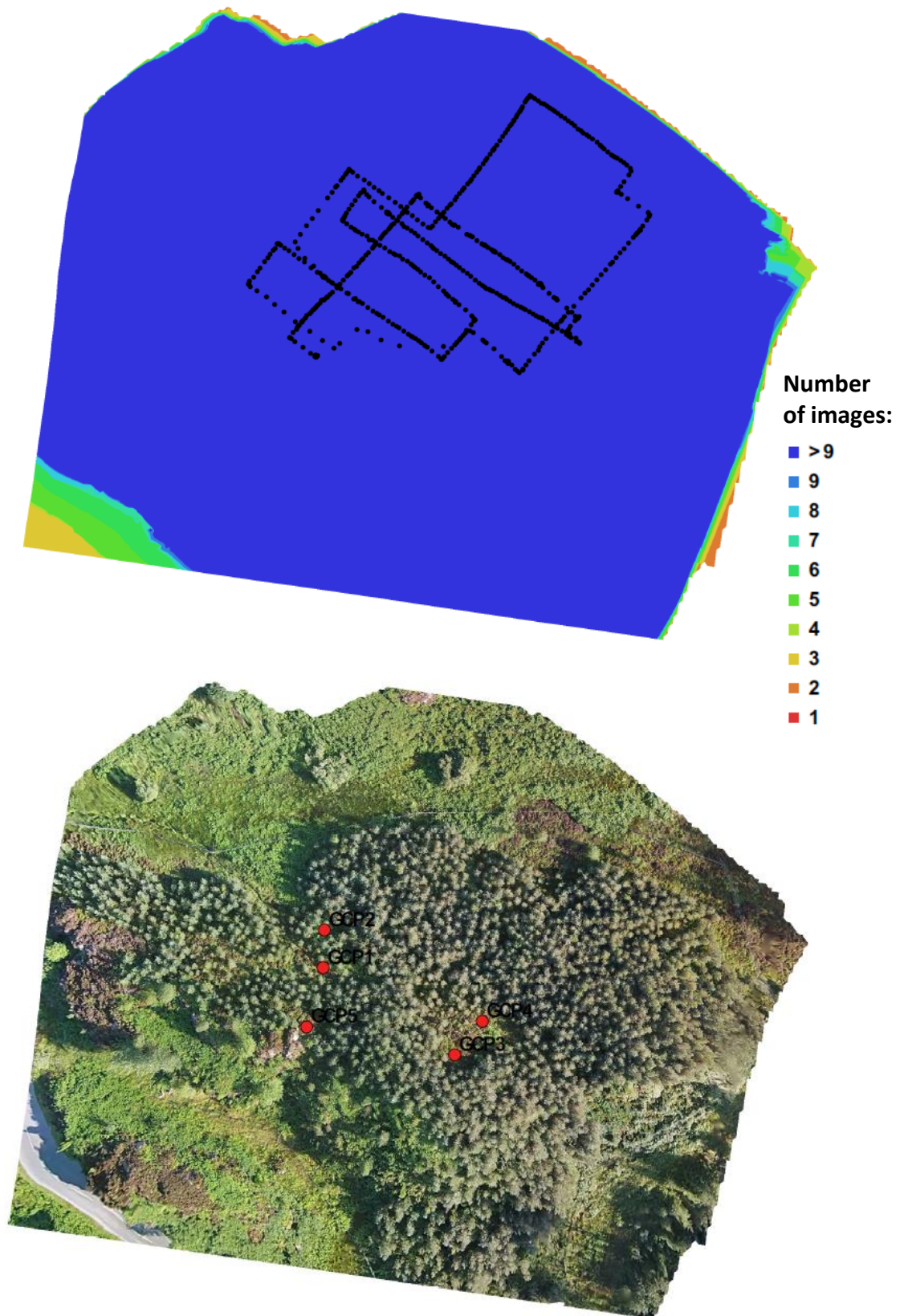
Figure B.1: Camera positions with image overlap (*top*), and locations of GCPs, shown as red points (*bottom*), for plot A.
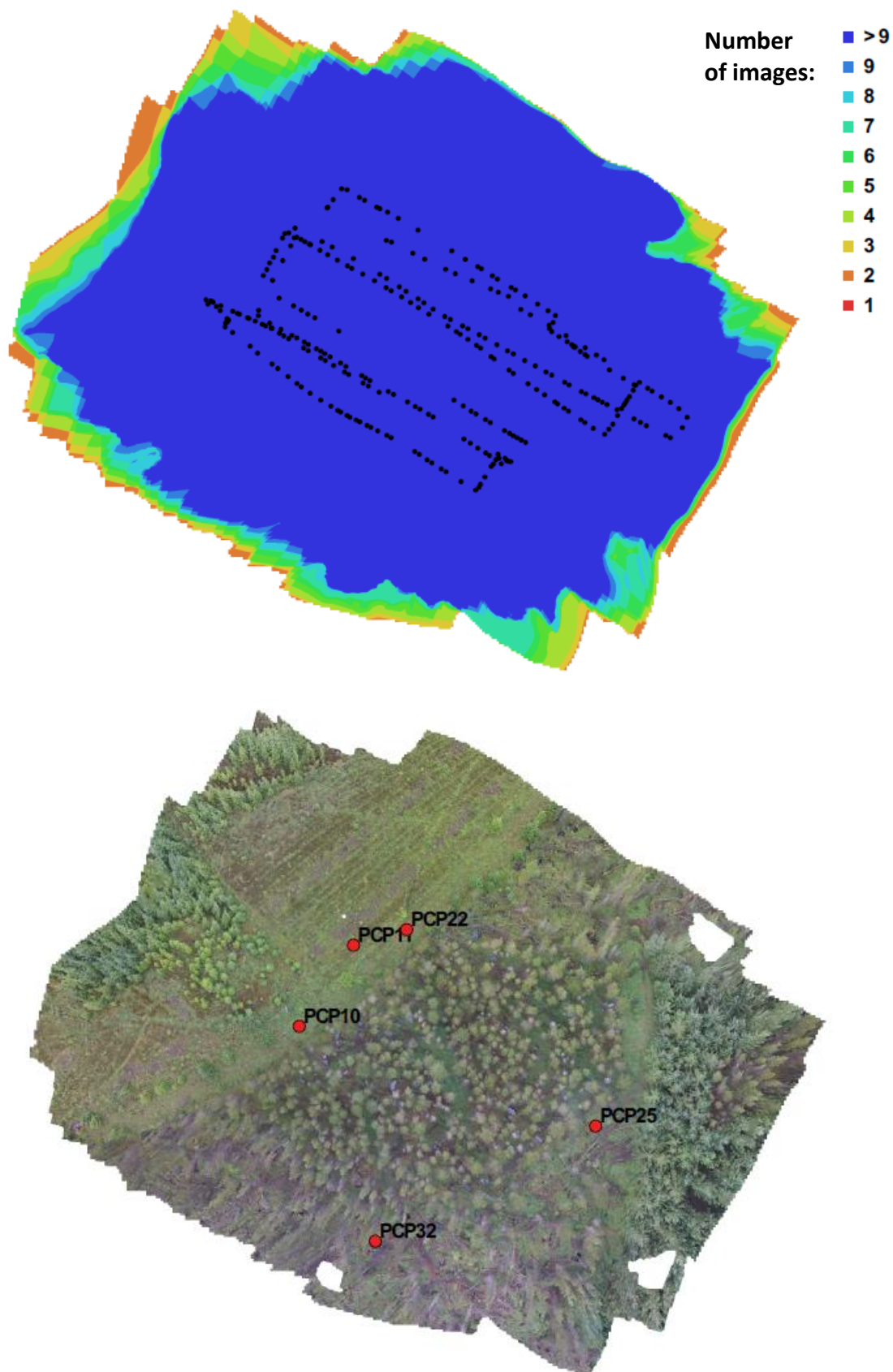
Figure B.2: Camera positions with image overlap (*top*), and locations of GCPs, shown as red points (*bottom*), for plot C.
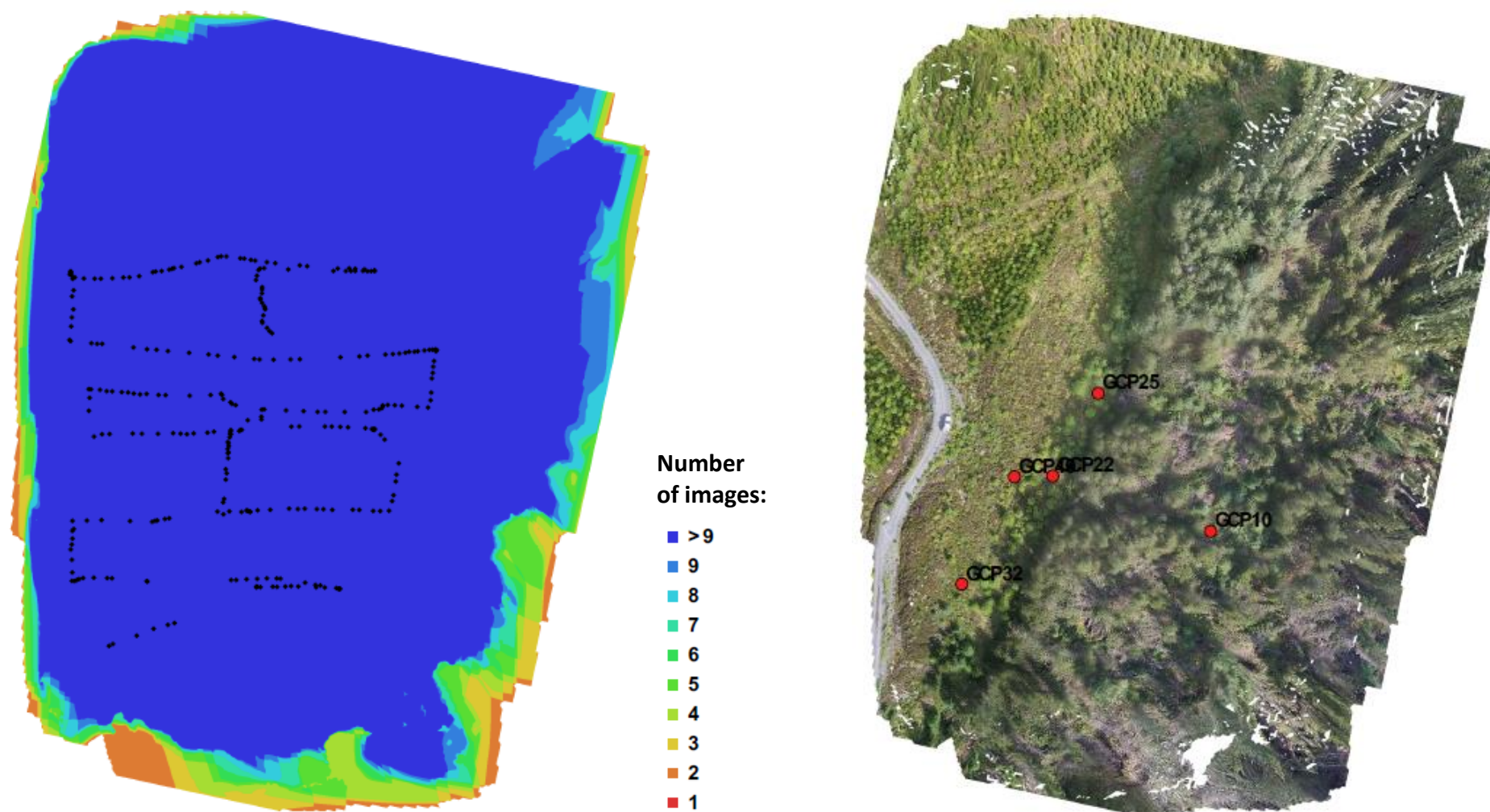
Figure B.3: Camera positions with image overlap (*left*), and locations of GCPs, shown as red points (*right*), for plot D.

Table B.1: Processing details and georeferencing RMSE measures obtained for each plot (based on GCPs used in the processing). The reprojection error provides an indication on quality of alignment of the images.

Projection	Plot A	Plot C	Plot D
No. of images	607	352	291
Camera stations	607	293	291
Flying altitude (m)	69.0	62.2	71.3
No. of tie points	273 819	288 317	376 321
No. of projections	1 470 980	987 759	1 591 894
Ground resolution (cm/pixel)	5.32	4.55	5.52
Coverage area (km^2)	0.0227	0.0298	0.0393
Reprojection error (pixel)	0.776	0.924	1.190
Control points RMSE			
X error (cm)	3.353	16.919	1.069
Y error (cm)	0.670	12.044	14.625
Z error (cm)	4.205	1.042	0.401
XY error (cm)	3.420	20.768	14.664
Total error (cm)	5.420	20.794	14.670
Image error (pixel)	0.395	0.453	0.276

Table B.2: RMSE obtained for each GCP.

	GCP	X error (cm)	Y error (cm)	Z error (cm)	Total (cm)	Image (pixel)
PLOT A	1	-1.723	0.066	6.650	6.870	0.410
	2	0.508	0.464	-3.225	3.230	0.383
	3	-5.343	-0.148	3.109	6.184	0.289
	4	4.530	0.756	-2.935	5.450	0.360
	5	1.983	-1.196	-3.939	4.569	0.457
PLOT C	10	-14.234	-9.856	0.972	17.341	0.459
	11	29.991	21.411	-1.767	36.891	0.556
	22	-17.775	-12.944	1.141	22.018	0.408
	25	-1.336	1.493	0.134	2.008	0.381
	32	3.389	-0.022	0.210	3.395	0.264
PLOT D	10	0.135	4.068	-0.238	4.077	0.174
	22	-1.323	-27.002	0.688	27.043	0.319
	25	0.138	4.857	0.150	4.861	0.313
	32	-0.919	2.027	-0.483	2.278	0.207
	40	1.756	17.208	-0.130	17.298	0.286

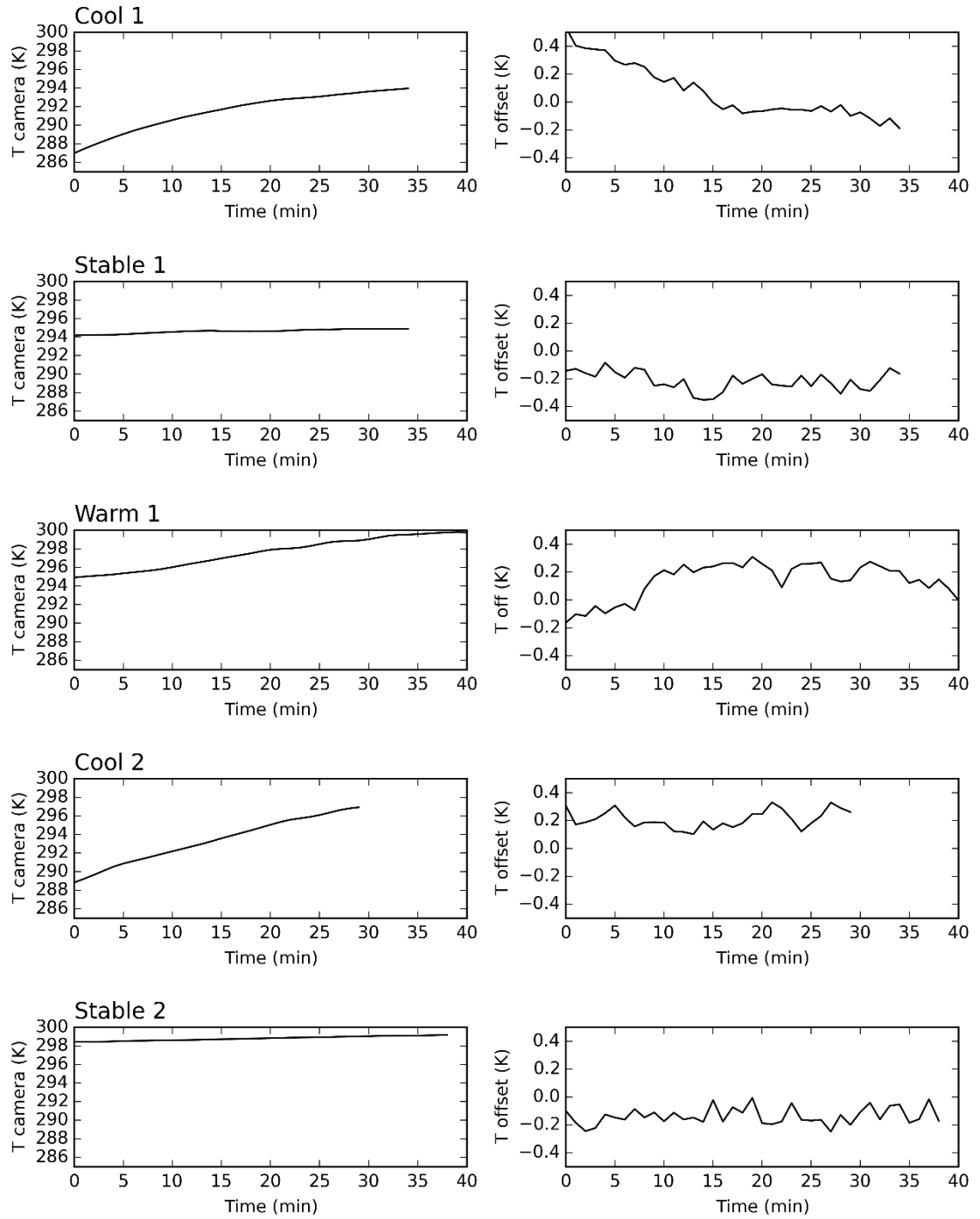# Appendix C: Laboratory time series

Figure C.1: Camera temperatures (*left*) and reading's offsets from the true blackbody temperature (*right*) recorded throughout the laboratory trials.

Appendix D: Prewhitening procedure

Prewhitening is performed by transforming one of the series to white noise using a filter, which is then also applied to the other series:

$$\widetilde{X}_t = \left(1 - \pi_1 B - \pi_2 B^2 - \cdots - \pi_k B^k\right)X_t = \pi(B)X_t \qquad \text{D.1}$$

where X is the original time series, $\widetilde{X}_t$ is a white noise, t is a time point, k is the order of differencing, B is a backshift operator (such that $B^k X_t = X_{t-k}$). Prewhitening was performed using an Autoregressive Integrated Moving Average (ARIMA) model. ARIMA(p,d,q) model combines autoregressive (AR) and moving average (MA) statistical models into a single model with an option to difference the time-series. The model contains three parameters p, d and q, which express the order of the AR, differencing and MA parameters (Shumway and Stoffer, 2011). The AR part of the model expresses the dependence of a time series on its past values and has the following form:

$$Y_t = \varphi_1 Y_{t-1} + \varphi_2 Y_{t-2} + \cdots + \varphi_p Y_{t-p} + e_t \qquad \text{D.2}$$

where t is a time point, ϕ is the autoregressive (AR) coefficient, p is the order of autoregressive (AR) parameter, e is a white noise. The MA part of the model expresses the influence of current and past stochastic processes and is expressed by:

$$Y_t = e_t - \theta_1 e_{t-1} - \theta_2 e_{t-2} - \cdots - \theta_q e_{t-q} \qquad \text{D.3}$$

where t is a time point, e is a white noise, θ is the moving average (MA) coefficient, q is the order of moving average (MA) parameter. The combined general equation for a stationary time series of an ARIMA(p,d,q) model, containing no differencing terms, would therefore be:

$$Y_t = \varphi_1 Y_{t-1} + \cdots + \varphi_p Y_{t-p} + e_t - \theta_1 e_{t-1} - \cdots - \theta_q e_{t-q} \qquad \text{D.4}$$

The order of differencing is expressed by d, i.e. d=1 is given by:

$$\nabla Y_t = Y_t - Y_{t-1} \qquad \text{D.5}$$

Prior to modelling, all non-stationary time series (stationarity was checked with Kwiatkowski–Phillips–Schmidt–Shin test) were stationarised using linear regressions with time as a predictor.

Appendix E: Camera non-uniformity correction script

This python script reads in csv image files, corrects them for non-uniformity across the lens using "gain" and "offset" files and saves the corrected files as tiff and png images. The "thermcorr" module required to execute the script is provided below.

NU_correction.py

```
"""
Author: Magdalena Smigaj
Institution: School of Civil Engineering and Geosciences, Newcastle University, UK
Contact: m.smigaj@ncl.ac.uk or smigajmagdalena@yahoo.com
Created: Oct 2015
"""

import os
import csv
import numpy as np
import thermcorr as tc
from PIL import Image
from matplotlib import pyplot as plt

#Specify locations of the gain and offset calibration files
with open("D:\\Python\\Cal\\gain_new.txt", "rb") as f:
    reader = csv.reader(f, delimiter = ";")
    gain = np.array(list(reader)).astype("float")
with open("D:\\Python\\Cal\\offset_new.txt", "rb") as f:
    reader = csv.reader(f, delimiter = ";")
    offset = np.array(list(reader)).astype("float")

#Specify the working directory
os.chdir("D:\\Image_directory")
listing = os.listdir(os.getcwd())
```

```python
#Non-uniformity correction - outputs saved as text files
os.mkdir('Corrected_Deg')
os.mkdir('Corrected_Kelv')
for a in listing:
    c = tc.OpenCsv(a)
    ck = tc.deg2kelv(c)
    cr = tc.tmp2rad(ck, 10.25)
    cc = tc.GO_corr(cr,gain,offset)
    cck = tc.rad2tmp(cc,10.25)
    cct = tc.kelv2deg(cck)
    np.savetxt("Corrected_Kelv\\" + os.path.splitext(a)[0] + "_cor.txt", cck, fmt='%10.5f',
delimiter=';', newline='\n')
    np.savetxt("Corrected_Deg\\" + os.path.splitext(a)[0] + "_cor_d.txt", cct,
fmt='%10.5f', delimiter=';', newline='\n')


del(a,c,ck,cr,cc,cck,cct)


#Convert text files to image files
os.chdir('\\Corrected_Deg')
listing = os.listdir(os.getcwd())


os.mkdir('Img')
os.mkdir('Tiff')
for a in listing:
    b = tc.OpenCsv(a)
    d = Image.fromarray(b)
    d.save("\\Tiff\\" + os.path.splitext(a)[0] + ".tiff", 'TIFF')
    plt.imsave("\\Img\\" + os.path.splitext(a)[0] + ".png", b, cmap="gray") #***
del(a,b,d)


#*** for other colormap options check https://matplotlib.org/users/colormaps.html
#*** in plt.imsave() "vmin=..., vmax=...." can be added to specify the minimum and
maximum temperature values used for the colour scheme
```

thermcorr.py

```python
import numpy as np
import math
import csv


def OpenCsv(filename):
    data = open(filename, 'rb').read()
    if data.find('\x00') == -1:
        with open(filename, "rb") as f:
            reader = csv.reader(f, delimiter = ";")
            b = np.array(list(reader))
            c = np.array((b[:,:-1])).astype("float")
    else:
        with open(filename,'rb') as f:
            data = csv.reader((line.replace('\0','') for line in f), delimiter=";")
            b=list(data)
            c = np.zeros(shape=(len(b),len(b[0])-1))
            for row in range(len(b)):
                for col in range(len(b[row])-1):
                    c[row,col] = float(b[row][col])
    return c


def deg2kelv(arr_1, **kwargs):
    arr_2 = np.zeros(shape=(len(arr_1),len(arr_1[0])))
    for x in range(len(arr_1)):
        for y in range(len(arr_1[0])):
            arr_2[x,y] = arr_1[x,y] + 273.15
    return arr_2


def kelv2deg(arr_1, **kwargs):
    arr_2 = np.zeros(shape=(len(arr_1),len(arr_1[0])))
    for x in range(len(arr_1)):
        for y in range(len(arr_1[0])):
            arr_2[x,y] = arr_1[x,y] - 273.15
    return arr_2
```

```python
def tmp2rad(arr_1, wvl, **kwargs):
    c1 = 1.191042*(10**8)
    c2 = 1.4387752*(10**4)
    arr_2 = np.zeros(shape=(len(arr_1),len(arr_1[0])))
    for x in range(len(arr_1)):
        for y in range(len(arr_1[0])):
            arr_2[x,y] = c1/((wvl**5)*(math.exp((c2/(wvl*arr_1[x,y])))-1))
    return arr_2


def GO_corr(arr_1, gain, offset, **kwargs):
    arr_2 = np.zeros(shape=(len(arr_1),len(arr_1[0])))
    for x in range(len(arr_1)):
        for y in range(len(arr_1[0])):
            arr_2[x,y] = arr_1[x,y]*gain[x,y]+offset[x,y]
    return arr_2


def GO_calc(BBc_arr, BBc_temp, BBh_arr, BBh_temp, wvl, **kwargs):
    c1 = 1.191042*(10**8)
    c2 = 1.4387752*(10**4)
    gain = np.zeros(shape=(len(BBc_arr),len(BBc_arr[0])))
    offset = np.zeros(shape=(len(BBc_arr),len(BBc_arr[0])))

    BBc_rad = c1/((wvl**5)*(math.exp((c2/(wvl*(BBc_temp+273.15))))-1))
    BBh_rad = c1/((wvl**5)*(math.exp((c2/(wvl*(BBh_temp+273.15))))-1))

    BBc_arr = deg2kelv(BBc_arr)
    BBc_arr = tmp2rad(BBc_arr)
    BBh_arr = deg2kelv(BBh_arr)
    BBh_arr = tmp2rad(BBh_arr)

    for x in range(len(BBc_arr)):
        for y in range(len(BBc_arr[0])):
            gain[x,y] = (BBh_rad - BBc_rad)/(BBh_arr[x,y]-BBc_arr[x,y])
            offset[x,y] = BBc_rad - gain[x,y]*BBc_arr[x,y]
    return gain, offset
```

```python
def GO_calc_n(BBc_arr, BBc_temp, BBh_arr, BBh_temp, wvl, em_bb, **kwargs):
    c1 = 1.191042*(10**8)
    c2 = 1.4387752*(10**4)
    gain = np.zeros(shape=(len(BBc_arr),len(BBc_arr[0])))
    offset = np.zeros(shape=(len(BBc_arr),len(BBc_arr[0])))


    BBc_rad = c1/((wvl**5)*(math.exp((c2/(wvl*(BBc_temp+273.15))))-1))
    BBh_rad = c1/((wvl**5)*(math.exp((c2/(wvl*(BBh_temp+273.15))))-1))


    BBc_rad = em_bb * BBc_rad
    BBh_rad = em_bb * BBh_rad


    BBc_arr = deg2kelv(BBc_arr)
    BBc_arr = tmp2rad(BBc_arr)
    BBh_arr = deg2kelv(BBh_arr)
    BBh_arr = tmp2rad(BBh_arr)


    for x in range(len(BBc_arr)):
        for y in range(len(BBc_arr[0])):
            gain[x,y] = (BBh_rad - BBc_rad)/(BBh_arr[x,y]-BBc_arr[x,y])
            offset[x,y] = BBc_rad - gain[x,y]*BBc_arr[x,y]
    return gain, offset


def rad2tmp(arr_1, wvl, **kwargs):
    c1 = 1.191042*(10**8)
    c2 = 1.4387752*(10**4)
    arr_2 = np.zeros(shape=(len(arr_1),len(arr_1[0])))
    for x in range(len(arr_1)):
        for y in range(len(arr_1[0])):
            arr_2[x,y] = c2/(np.log(c1/((wvl**5)*arr_1[x,y])+1)*wvl)
    return arr_2
```

```python
def rad_em(arr_1, em, **kwargs):
    arr_2 = np.zeros(shape=(len(arr_1),len(arr_1[0])))
    for x in range(len(arr_1)):
        for y in range(len(arr_1[0])):
            arr_2[x,y] = arr_1[x,y]/em
    return arr_2


def GO_calc_n1(BBc_arr, BBc_temp, BBh_arr, BBh_temp, wvl, em_bb, **kwargs):
    c1 = 1.191042*(10**8)
    c2 = 1.4387752*(10**4)
    gain = np.zeros(shape=(len(BBc_arr),len(BBc_arr[0])))
    offset = np.zeros(shape=(len(BBc_arr),len(BBc_arr[0])))

    BBc_rad = c1/((wvl**5)*(math.exp((c2/(wvl*(BBc_temp+273.15))))-1))
    BBh_rad = c1/((wvl**5)*(math.exp((c2/(wvl*(BBh_temp+273.15))))-1))

    BBc_arr = deg2kelv(BBc_arr)
    BBc_arr = tmp2rad(BBc_arr)
    BBh_arr = deg2kelv(BBh_arr)
    BBh_arr = tmp2rad(BBh_arr)

    for x in range(len(BBc_arr)):
        for y in range(len(BBc_arr[0])):
            gain[x,y] = (BBh_rad - BBc_rad)/(BBh_arr[x,y]/em_bb-BBc_arr[x,y]/em_bb)
            offset[x,y] = BBc_rad - gain[x,y]*BBc_arr[x,y]
    return gain, offset
```

Appendix F: Emissivity calculation script (part 1)

This python script takes in up to four FTIR measurements of samples for emissivity calculation. The input files should be given in a csv format, without any header information, and should be formatted as shown in Figure F.1 (wavelength, measurement).
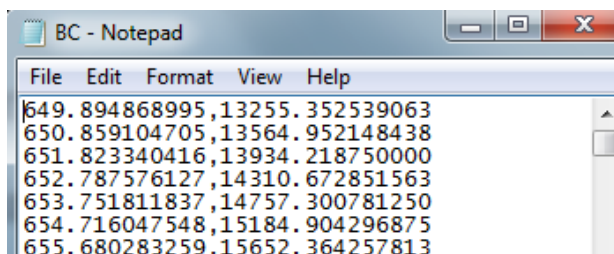

Figure F.1: Example input file with "wavelength, measurement" format.

The user has to provide temperature values in Celsius degrees for the black bodies, the gold panel and the four samples. Abbreviations used in the code are BC ("cold" blackbody), BH ("hot" blackbody), G (gold panel), S1-4 (samples 1 to 4). If any of the samples are missing, '-99' should be input as the temperature reading. There is also an option to adjust the gold panel's and blackbody's emissivity values.

In the next step, paths to and names of each of the input files should be provided. If the files are in the current working directory, only names are required. If any of the samples are missing, input "" as the filename.
A number of functions were created to aid the emissivity retrieval, those are:

- OpenFile - reads in the files
- deg2kelv - converts temperature from Celcius to Kelvins
- PlanckRad - calculates Plancks blackbody radiation
- RadCalc - computes target's radiance
- EmCalc - retrieves apparent and true emissivity values

Those are applied throughout the script to the input files. All calculations are based on the emissivity retrieval principles described in Chapter 4.

The script returns 3 files: (1) Raw_input.csv – containing all input measurements, (2) Intermediate_calc.csv – containing all intermediate calculations, (3) Emissivities.csv – containing calculated apparent and true emissivity values. The files will be saved to the current working directory.

Emissivity_calc_script.py

"""

Author: Magdalena Smigaj

Institution: School of Civil Engineering and Geosciences, Newcastle University, UK

Contact: m.smigaj@ncl.ac.uk or smigajmagdalena@yahoo.com

Created: Aug 2015

"""

############USER INPUT############
INPUT TEMPERATURE VALUES in Celsius degrees. If sample missing, input '-99'

BC_t = 15

BH_t = 59.9

G_t = 27.8

S1_t = 30.4

S2_t = 30.1

S3_t = 30.2

S4_t = 29.9

e_g = 0.06   #gold panel's emissivity
e_bb = 0.96   #blackbody's emissivity

#SPECIFY PATHS, or file names (if located in current working directory). If sample missing, input ""

#BC_path = "D:\\Studia\\PhD\\FTIR\\Test\\BC.csv"   #path + filename
#os.chdir("D:\\Studia\\PhD\\FTIR\\Test\\")   #changing the current working directory

BC_path = "BC.csv"

BH_path = "BH.csv"

G_path = "G.csv"

S1_path = "S1.csv"

S2_path = "S2.csv"

S3_path = "S3.csv"

S4_path = "S4.csv"

```
#############FUNCTIONS############
import csv, math
import numpy as np


def OpenFile(txt):
    if len(txt) == 0:
        res = -99
        return res
    else:
        with open(txt, "rb") as f:
            reader = csv.reader(f, delimiter = ",")
            arr = np.array(list(reader)).astype("float")
        return arr


def deg2kelv(temp):
    res = temp +273.15
    return res


def PlanckRad(arr, temp, ncol,em):
    h = 6.62607E-34              #Planck's constant
    c = 299792500               #speed of light
    k = 1.38066E-23             #Boltzmann's constant
    for a in range(len(arr)):
        arr[a,ncol] = em*((((2*h*c**2)/(arr[a,0]**5))/(math.exp((h*c)/(k*temp*arr[a,0]))-
1))/1000000)
    return arr


def RadCalc(arr, G_col, R_col, out_col, arr_s):
    for a in range(len(arr)):
        arr[a,out_col] = arr[a,G_col] + arr[a,R_col]*arr_s[a,1]
    return arr
```

```python
def EmCalc(arr_i, Lbb_col,Lt_col,DWR_col,arr_o, ae_col, e_col):
    for a in range(len(arr_i)):
        arr_o[a,ae_col] = arr_i[a,Lt_col]/arr_i[a,Lbb_col]
        arr_o[a,e_col] = (arr_i[a,Lt_col]-arr_i[a,DWR_col])/(arr_i[a,Lbb_col]-
arr_i[a,DWR_col])
    return arr_o


#############CALCS############
#open BC, BH, G, S1, S2, S3, S4 files
BC = OpenFile(BC_path)
BH = OpenFile(BH_path)
G = OpenFile(G_path)
S1 = OpenFile(S1_path)
S2 = OpenFile(S2_path)
S3 = OpenFile(S3_path)
S4 = OpenFile(S4_path)


BC_t,BH_t,G_t = deg2kelv(BC_t), deg2kelv(BH_t),deg2kelv(G_t)
Raw, Cal, Em = np.zeros(shape=((len(G)),9)), np.zeros(shape=((len(G)),16)),
                np.zeros(shape=((len(G)),10))


#wavenumber to wavelength conversion
for a in range(len(G)):
    Cal[a,0] = 1/(G[a,0]*100)
    Em[a,0] = Cal[a,0]
    Em[a,1] = 1/G[a,0]*10000


#Planck's BB radiation
Cal = PlanckRad(Cal, BH_t, 1,e_bb)
Cal = PlanckRad(Cal, BC_t, 2,e_bb)
Cal = PlanckRad(Cal, G_t, 5,1)
```

#radiance of inner parts and spectral response of FTIR

```
for a in range(len(Cal)):
    Cal[a,3] = ((Cal[a,1]*BC[a,1])-(Cal[a,2]*BH[a,1]))/(BC[a,1]-BH[a,1])
    Cal[a,4] = (Cal[a,2]-Cal[a,1])/(BC[a,1]-BH[a,1])


#DWR
Cal = RadCalc(Cal,3,4,6,G)
for a in range(len(Cal)):
    Cal[a,7] = (Cal[a,6]-e_g*Cal[a,5])/(1-e_g)


#apparent and true emissivity retrieval for given targets
if type(S1) != int:
    S1_t = deg2kelv(S1_t)
    Cal = PlanckRad(Cal, S1_t, 8,e_bb)
    Cal = RadCalc(Cal,3,4,9,S1)
    Em = EmCalc(Cal,8,9,7,Em,2,3)


if type(S2) != int:
    S2_t = deg2kelv(S2_t)
    Cal = PlanckRad(Cal, S2_t, 10,e_bb)
    Cal = RadCalc(Cal,3,4,11,S2)
    Em = EmCalc(Cal,10,11,7,Em,4,5)
    Raw[:,6] = S2[:,1]


if type(S3) != int:
    S3_t = deg2kelv(S3_t)
    Cal = PlanckRad(Cal, S3_t, 12,e_bb)
    Cal = RadCalc(Cal,3,4,13,S3)
    Em = EmCalc(Cal,12,13,7,Em,6,7)
    Raw[:,7] = S3[:,1]
```

```python
if type(S4) != int:
    S4_t = deg2kelv(S4_t)
    Cal = PlanckRad(Cal, S4_t, 14,e_bb)
    Cal = RadCalc(Cal,3,4,15,S4)
    Em = EmCalc(Cal,14,15,7,Em,8,9)
    Raw[:,8] = S4[:,1]


Raw[:,0],Raw[:,1],Raw[:,2],Raw[:,3],Raw[:,4],Raw[:,5]                          = 
BH[:,0],Em[:,1],BH[:,1],BC[:,1],G[:,1],S1[:,1]


#save matrices to delimited files
with open('Raw_input.csv', 'wb') as f:
  f.write(b'wn (cm-1),wvl (microns),BB hot,BB cold,Gold panel,S1,S2,S3,S4\n')
  np.savetxt(f, Raw, fmt='%10.5f', delimiter=',', newline='\n')


with open('Intermediate_calc.csv', 'wb') as f:
  f.write(b'wvl (m), PRad BB hot, PRad BBcold, G, R, PRad Gold, Rad Gold, DWR, 
Prad S1, Rad S1, Prad S2, Rad S2, Prad S3, Rad S3, Prad S4, Rad S4\n')
  np.savetxt(f, Cal, fmt='%10.5f', delimiter=',', newline='\n')


with open('Emissivities.csv', 'wb') as f:
  f.write(b'wvl (m),wvl (microns),App e S1,E S1,App e S2,E S2,App e S3,E S3,App e 
S4,E S4\n')
  np.savetxt(f, Em, fmt='%10.5f', delimiter=',', newline='\n')


del S1, S2, S3, S4, G, BH, BC, Cal, Em, Raw
del S1_path, S2_path, S3_path, S4_path, G_path, BH_path, BC_path
del S1_t, S2_t, S3_t, S4_t, G_t, BH_t, BC_t, a, e_g
```

Appendix G: Emissivity calculation script (part 2)

Emissivity_plot_quick.py allows to create plots based on the Emissivity_calc_script.py output files (Appendix F). Examples of the plots are shown in Figure G.1, Figure G.2, Figure G.3 and Figure G.4.
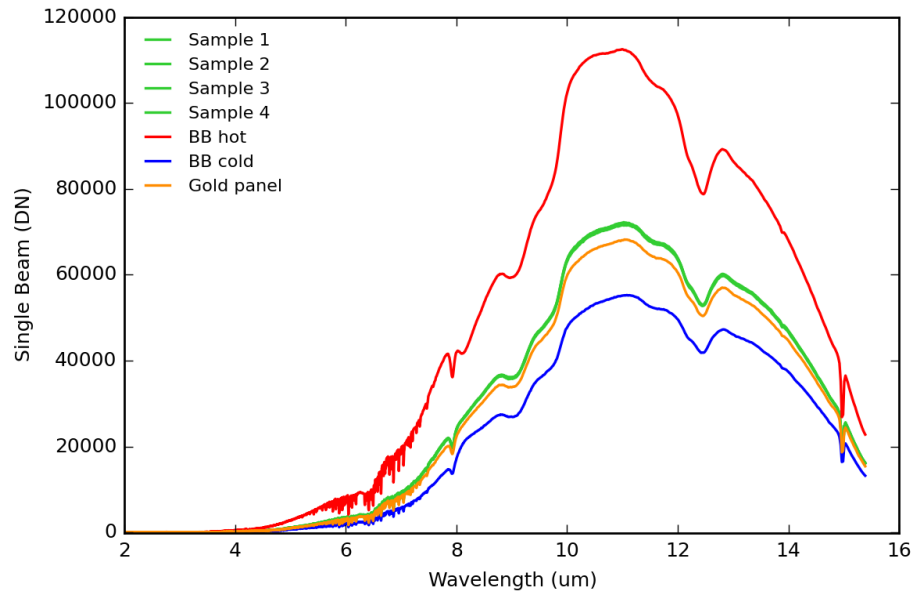

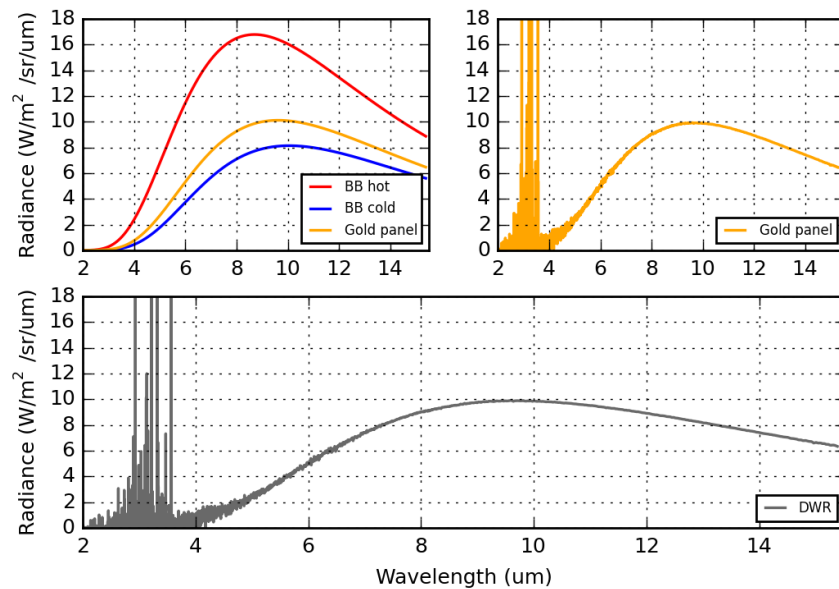Figure G.1: Raw spectra obtained for two blackbodies, the gold panel and four samples.

Figure G.2: Planck blackbody radiances calculated for temperatures of the gold panel, "hot" and "cold" blackbodies (*top left*), radiance of the gold panel (*top right*), reflected downwelling radiance (*bottom*).
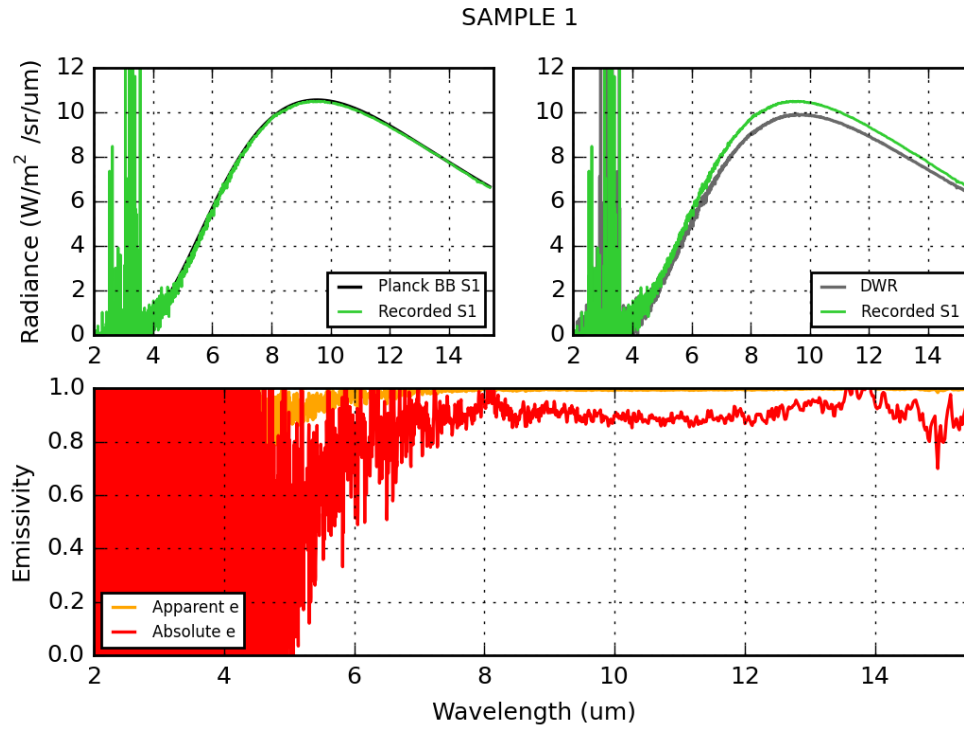
Figure G.3: Measured and Planck blackbody radiance of sample 1 (*top left*), radiance of sample 1 and downwelling radiance (*top right*), apparent and absolute spectral emissivity of sample 1 (*bottom*).
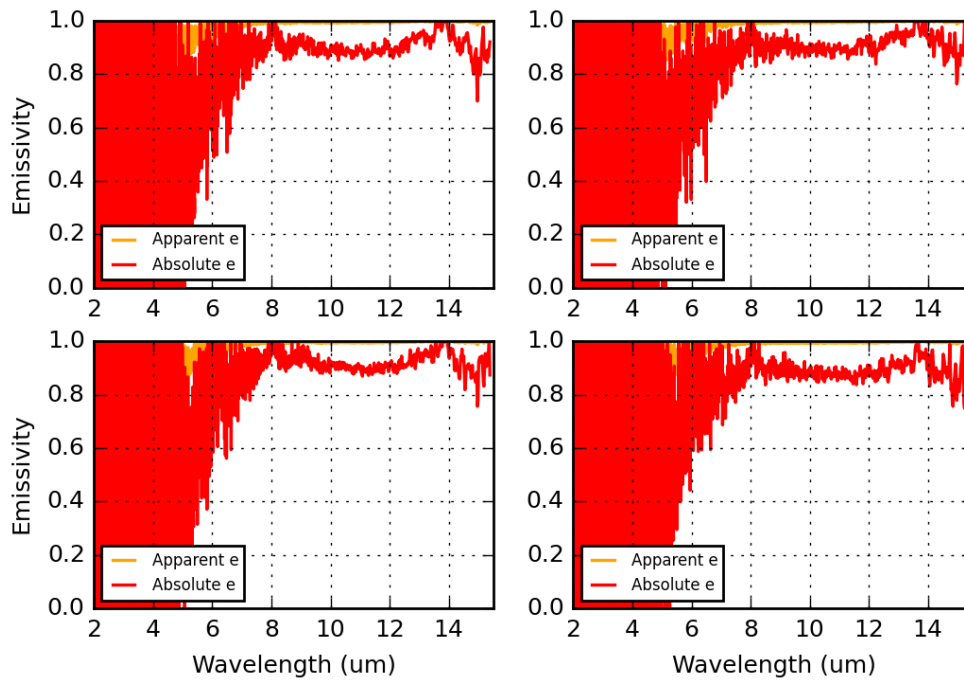

Figure G.4: Comparison of apparent and absolute emissivities retrieved for four samples.

Emissivity_plot_quick.py

"""

Author: Magdalena Smigaj

Institution: School of Civil Engineering and Geosciences, Newcastle University, UK

Contact: m.smigaj@ncl.ac.uk or smigajmagdalena@yahoo.com

Created: Aug 2015

"""

```
#
# READ ME:
#This script plots output files of "Emissivity_calc_script.py"
#Input files are as follows: Raw_input.csv, Intermediate_calc.csv, Emissivities_calc.csv


#############USER INPUT############
#choose emissivity plot mode = 0 (y axis <0,1>), mode = 1 (y axis rescaled if avg em >1
or <0 in 8-14 um)


mode = 1
min_wvl = 2
max_wvl = 15.5
dpi = 200


#specify input files
raw_path = "Raw_input.csv"
cal_path = "Intermediate_calc.csv"
em_path = "Emissivities.csv"


############FUNC TIONS############
import csv, math
import numpy as np
from matplotlib import pyplot as plt
import matplotlib as mpl


mpl.rcParams.update({'font.size':9})
```

```python
def OpenFile(txt):
    if len(txt) == 0:
        res = -99
        return res
    else:
        with open(txt, "rb") as f:
            f.readline()
            reader = csv.reader(f, delimiter = ",")
            arr = np.array(list(reader)).astype("float")
        return arr


def PltLine(arr, xcol, ycol, col, name):
    if np.std(arr[:,ycol]) == 0:
        return
    else:
        plt.plot(arr[:,xcol], arr[:,ycol], col, label = name, linewidth = 1.2)


def PltLine2(arr_x, xcol,arr_y, ycol, col, name):
    if np.std(arr_y[:,ycol]) == 0:
        return
    else:
        plt.plot(arr_x[:,xcol], arr_y[:,ycol], col, label = name, linewidth = 1.2)


def AvEm(arr, ae_col,e_col):
    calc_ae, calc_e = [], []
    for a in range(len(arr)):
        if arr[a,1]>8 and arr[a,1]<14:
            calc_ae.append(arr[a,ae_col])
            calc_e.append(arr[a,e_col])
    ae_avg, e_avg = np.mean(calc_ae), np.mean(calc_e)
    ae_std, e_std = 3*np.std(calc_ae), 3*np.std(calc_e)
    return [ae_avg,e_avg], [ae_std, e_std]
```

```python
def EmPlot(mode, Sname,em,x_col,ae_col,e_col,cal, SPrad_col,Srad_col,DWR_col,
leg_loc,min_wvl,max_wvl):
    plt.subplot(221)
    plt.plot(em[:,x_col], cal[:,SPrad_col], 'k', label='Planck BB ' + Sname, zorder=1,
linewidth=1.2)
    plt.plot(em[:,1], cal[:,Srad_col], 'limegreen', label='Recorded ' + Sname, zorder=1,
linewidth=1)
    StForm(cal,SPrad_col,6,4,min_wvl,max_wvl), plt.ylabel('Radiance
$\mathregular{(W/m^2/sr/um)}$')
    plt.subplot(222)
    plt.plot(em[:,x_col], cal[:,DWR_col], 'dimgray', label='DWR', zorder=1,
linewidth=1.2)
    plt.plot(em[:,x_col], cal[:,Srad_col], 'limegreen', label='Recorded '+Sname, zorder=1,
linewidth=1)
    StForm(cal,SPrad_col,6,4,min_wvl,max_wvl)
    plt.subplot(212)
    plt.plot(em[:,x_col], em[:,ae_col], 'orange', label='Apparent e', zorder=1,
linewidth=1.2)
    plt.plot(em[:,x_col], em[:,e_col], 'red', label='Absolute e', zorder=1, linewidth=1.2)
    StEmForm(em,ae_col,e_col,leg_loc,mode,min_wvl,max_wvl),
plt.ylabel('Emissivity'), plt.xlabel('Wavelength (um)')

def StForm(arr,y_col,leg_s, leg_loc,min_wvl,max_wvl):
    plt.axis([min_wvl,max_wvl, 0, math.ceil(np.max(arr[:,y_col]))+1])
    plt.grid(), plt.legend(prop={'size':leg_s},  loc = leg_loc)
```

```python
def StEmForm(em,ae_col,e_col, leg_loc, mode,min_wvl,max_wvl):
    plt.grid(), plt.legend(prop={'size':6},  loc = leg_loc)
    if mode ==0:
        plt.axis([min_wvl, max_wvl, 0, 1])
    elif mode == 1:
        res, std_res = AvEm(em,ae_col,e_col)
        if min(res) < 0 and max(res)>1:
            plt.axis([min_wvl, max_wvl, round(min(res)-max(std_res)-0.1,1),
round(max(res)+max(std_res)+0.1,1)])
        elif min(res) < 0 and max(res)<1:
            plt.axis([min_wvl, max_wvl, round(min(res)-max(std_res)-0.1,1), 1])
        elif min(res) > 0 and max(res)>1:
            plt.axis([min_wvl, max_wvl, 0, round(max(res)+max(std_res)+0.1,1)])
        else:
            plt.axis([min_wvl, max_wvl, 0, 1])


#############PLOTTING############

raw = OpenFile(raw_path)
cal = OpenFile(cal_path)
em = OpenFile(em_path)

#Raw data plot
plt.figure()
PltLine(raw,1,5,'limegreen','Sample 1'), PltLine(raw,1,6,'limegreen','Sample 2'),
PltLine(raw,1,7,'limegreen','Sample 3'), PltLine(raw,1,8,'limegreen','Sample 4')
PltLine(raw,1,2,'r','BB hot'), PltLine(raw,1,3,'b','BB cold'),
PltLine(raw,1,4,'darkorange','Gold panel')
plt.axis([2, (math.ceil(np.max(raw[:,1]))), (math.floor(np.min(raw[:,2])/100)*100),
(math.ceil(np.max(raw[:,2])/10000)*10000)])
plt.xlabel('Wavelength (um)'), plt.ylabel('Single Beam (DN)'),
plt.legend(prop={'size':8}, frameon=False, loc = 2), plt.tight_layout()
plt.savefig('figure_1.png', dpi = dpi)
```

```
#Planck curves for BBs and gold panel, radiance of gold panel and DWR
plt.figure(2)
plt.subplot(221)
PltLine2(em,1,cal,1,'red','BB hot'), PltLine2(em,1,cal,2,'b','BB cold'),
PltLine2(em,1,cal,5,'orange','Gold panel')
StForm(cal,1,6,4,min_wvl,max_wvl), plt.ylabel('Radiance
$\mathregular{(W/m^2/sr/um)}$')


plt.subplot(222)
PltLine2(em,1,cal,6,'orange','Gold panel'), StForm(cal,1,6,4,min_wvl,max_wvl)


plt.subplot(212)
PltLine2(em,1,cal,7,'dimgray','DWR')
StForm(cal,1,6,4,min_wvl,max_wvl), plt.xlabel('Wavelength (um)'),
plt.ylabel('Radiance $\mathregular{(W/m^2/sr/um)}$')
plt.savefig('figure_2.png', dpi = dpi)


#Samples Emissivities
plt.figure(3)
plt.suptitle('SAMPLE 1')
EmPlot(mode,'S1',em,1,2,3,cal,8,9,7,3,min_wvl,max_wvl)
plt.savefig('sample_1.png', dpi = dpi)


if np.mean(em[:,4]) != 0:
    plt.figure(4)
    plt.suptitle('SAMPLE 2')
    EmPlot(mode,'S2',em,1,4,5,cal,10,11,7,3,min_wvl,max_wvl)
    plt.savefig('sample_2.png', dpi = dpi)


if np.mean(em[:,6]) != 0:
    plt.figure(5)
    plt.suptitle('SAMPLE 3')
    EmPlot(mode,'S3',em,1,6,7,cal,12,13,7,3,min_wvl,max_wvl)
    plt.savefig('sample_3.png', dpi = dpi)
```

```python
if np.mean(em[:,8]) != 0:
    plt.figure(6)
    plt.suptitle('SAMPLE 4')
    EmPlot(mode,'S4',em,1,8,9,cal,14,15,7,3,min_wvl,max_wvl)
    plt.savefig('sample_4.png', dpi = dpi)


#Apparent and absolute emissivities of the 4 samples
plt.figure(7)
plt.subplot(221)
PltLine(em,1,2,'orange','Apparent e'), PltLine(em,1,3,'r','Absolute e')
StEmForm(em,2,3,3,mode,min_wvl,max_wvl), plt.ylabel('Emissivity')


if np.mean(em[:,4]) != 0:
    plt.subplot(222)
    PltLine(em,1,4,'orange','Apparent        e'),        PltLine(em,1,5,'r','Absolute        e'),
StEmForm(em,4,5,3,mode,min_wvl,max_wvl)


if np.mean(em[:,6]) != 0:
    plt.subplot(223)
    PltLine(em,1,6,'orange','Apparent e'), PltLine(em,1,7,'r','Absolute e')
    StEmForm(em,6,7,3,mode,min_wvl,max_wvl),        plt.xlabel('Wavelength        (um)'),
plt.ylabel('Emissivity')


if np.mean(em[:,8]) != 0:
    plt.subplot(224)
    PltLine(em,1,8,'orange','Apparent e'), PltLine(em,1,9,'r','Absolute e')
    StEmForm(em,8,9,3,mode,min_wvl,max_wvl), plt.xlabel('Wavelength (um)')


plt.savefig('figure_3.png', dpi = dpi)


del cal, cal_path, em, em_path, mode, raw, raw_path
```

Appendix H: PLSR models

Table H.1: Variable loadings for all components used in the two investigated partial least squares regressions: PLSR1 and PLSR2. PLSR1 was built on canopy temperature (T_c) and standard deviation of canopy temperature (T_c std). PLSR2 additionally considered LiDAR metrics (kurtosis and height percentiles) obtained from normalised (to 0-1 range) canopy heights.

|	Comp	PLSR1 T_c	PLSR1 T_c std	PLSR2 kur	PLSR2 p5	PLSR2 p75	PLSR2 p95	PLSR2 T_c	PLSR2 T_c std
FLIGHT 2	1	0.779	0.633	0.369	0.172	0.691	-0.178	0.742	0.584
FLIGHT 2	2	X	x	-0.658	-0.794	-0.479	0.733	0.218	0.106
FLIGHT 2	3	X	x	-0.145	x	X	-0.439	x	-0.213
FLIGHT 3	1	0.811	0.607	0.399	-0.306	0.221	0.315	0.757	0.572
FLIGHT 3	2	0.463	-0.886	-0.782	x	x	x	0.353	-0.351
FLIGHT 3	3	X	x	x	x	x	x	x	x
FLIGHT 4	1	0.81	0.6	0.442	0.156	0.567	-0.145	0.75	0.57
FLIGHT 4	2	0.489	-0.872	-0.655	-0.67	-0.544	0.604	0.272	-0.277
FLIGHT 4	3	X	x	-0.228	x	x	-0.513	x	x
FLIGHT 5	1	0.78	0.638	0.414	-0.687	0.594	0.59	0.731	0.6
FLIGHT 5	2	0.533	-0.846	-0.748	x	-0.584	-0.665	0.334	-0.286
FLIGHT 5	3	X	x	-0.114	x	x	x	x	x
FLIGHT 6	1	0.856	0.562	0.407	-0.19	0.29	0.297	0.788	0.54
FLIGHT 6	2	0.355	-0.935	-0.693	x	x	x	0.396	-0.611
FLIGHT 6	3	x	x	x	x	x	x	x	x
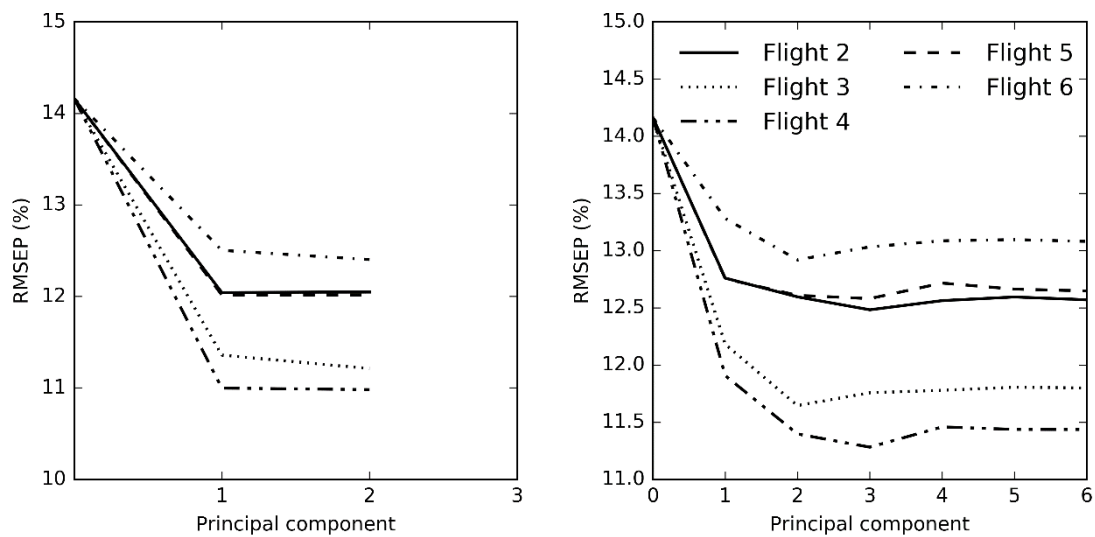
Figure H.1: Cross-validated root mean squared error of prediction curves for each of the flights following 1) a partial least squares regression of canopy temperature and standard deviation of canopy temperature (*left*), and 2) partial least squares regression of canopy temperature, standard deviation of canopy temperature and selected LiDAR metrics - kurtosis, p5, p75 and p95 (*right*).

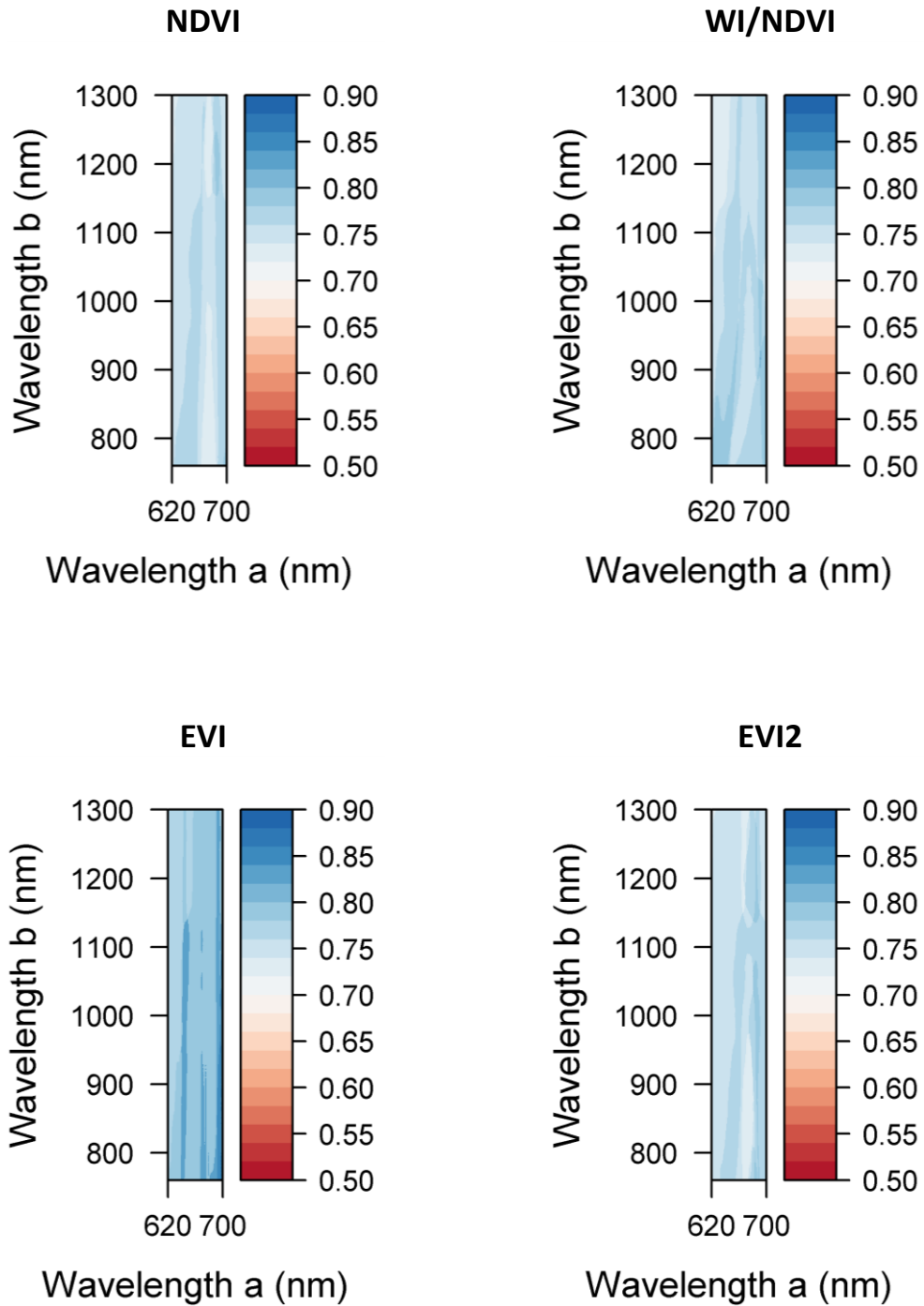# Appendix I: Selected results for leaf hyperspectral analysis

Figure I.1: Accuracy levels achieved by the discriminant function analysis performed on the upper and lower canopy parts for NDVI, EVI, EVI2, WI/NDVI, RDVI and GNDVI. The accuracy levels were retrieved through LOOCV method.
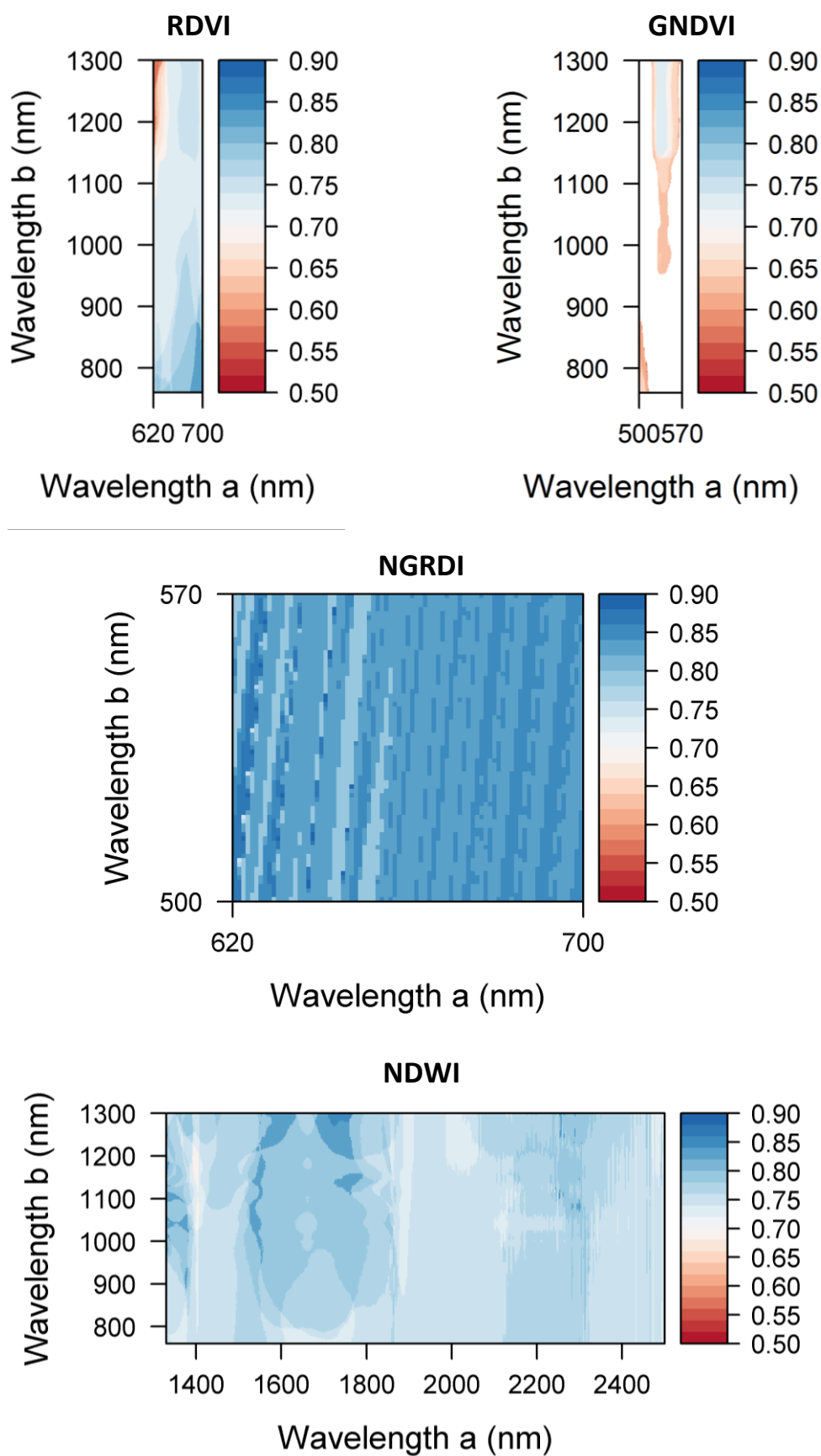
Figure I.2: Accuracy levels achieved by the discriminant function analysis performed on the upper and lower canopy parts for RDVI, GNDVI, NGRDI and NDWI. The accuracy levels were retrieved through LOOCV method.
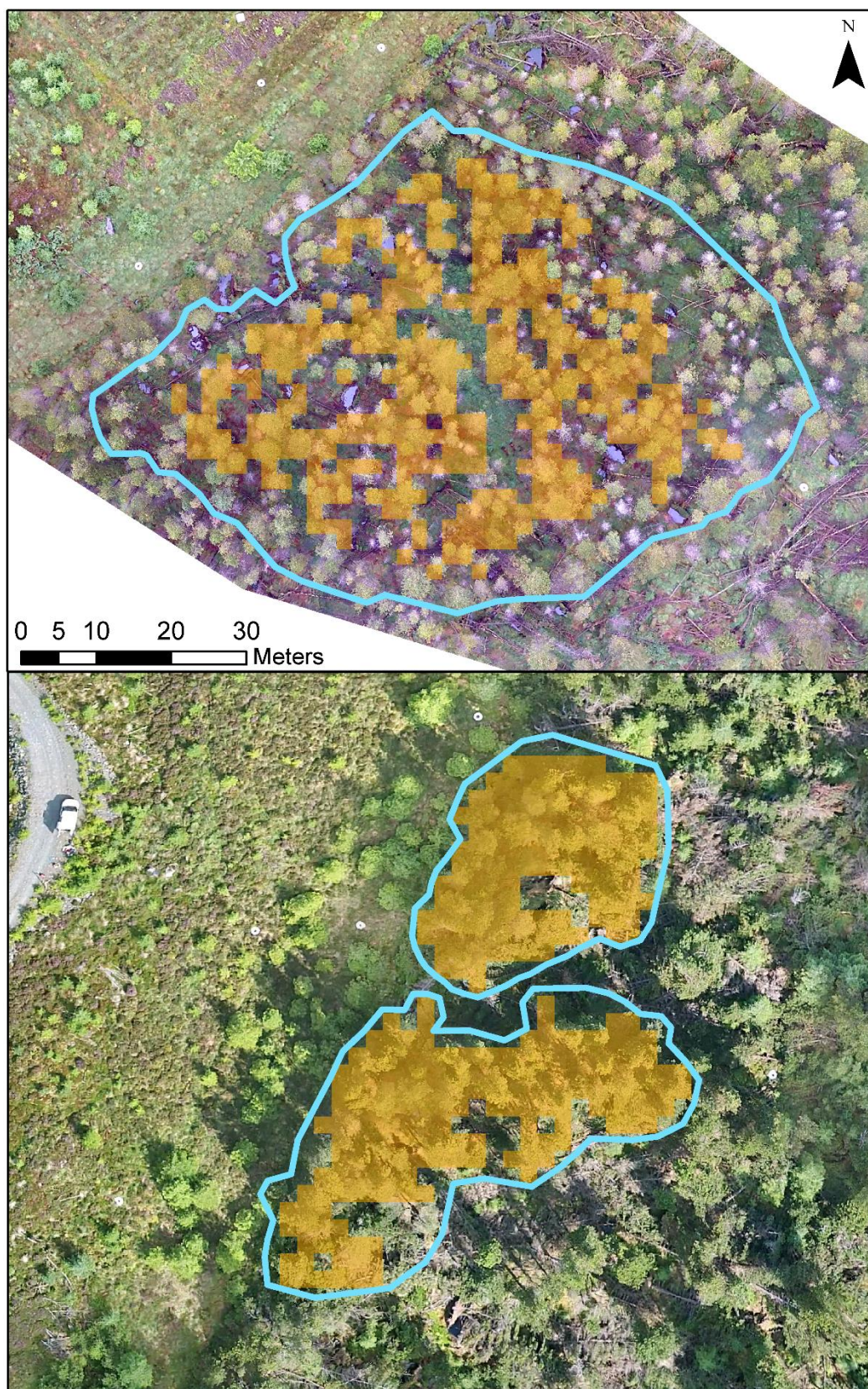
Appendix J: LiDAR-derived processing masks

Figure J.1: Canopy masks derived for plots C (top) and D (bottom), excluding pixels with ≤50% tree cover. Background: UAV orthomosaics.
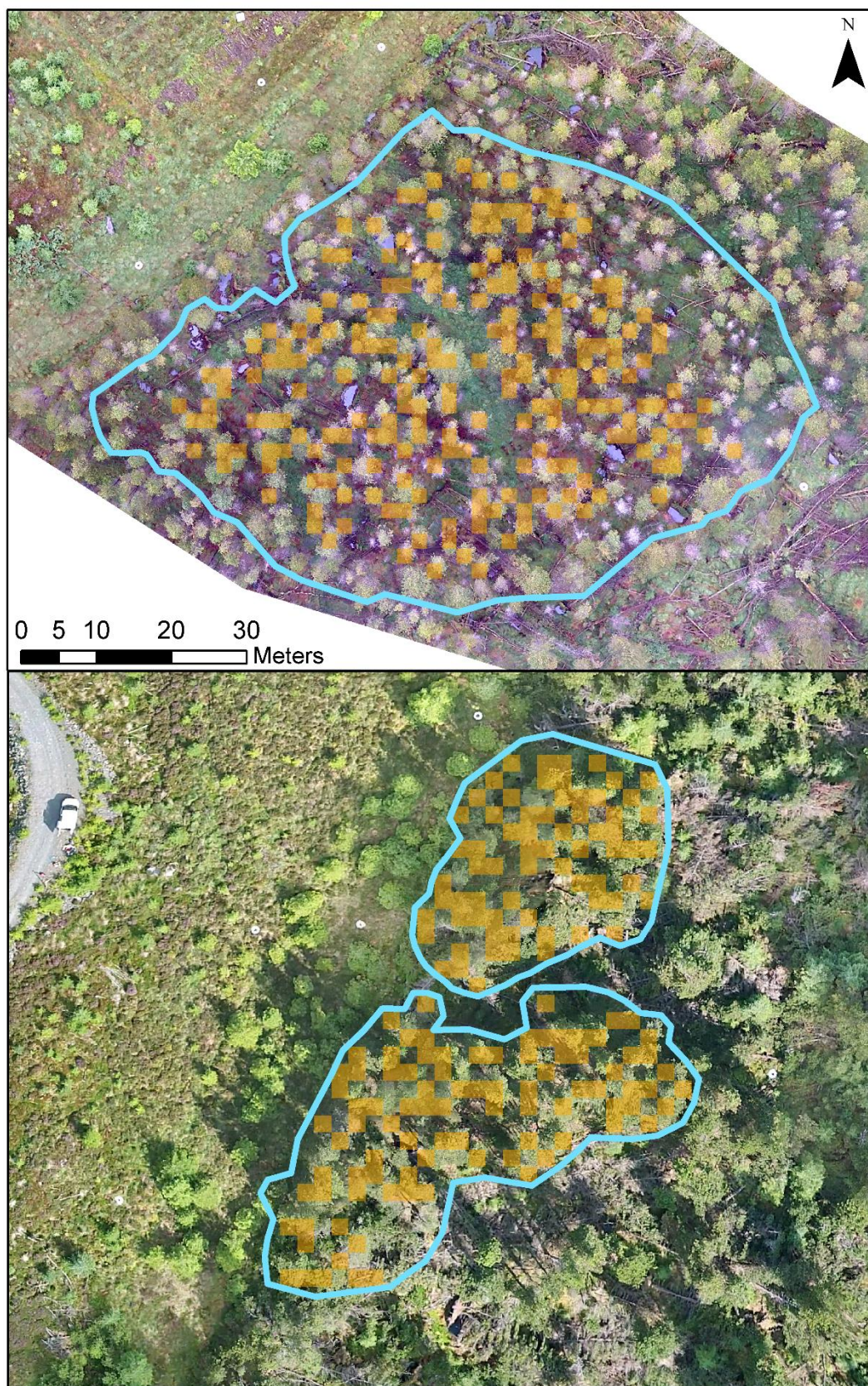
Figure J.2: Canopy masks derived for plots C (top) and D (bottom), retaining pixels which coincided with one of the detected tree tops. Background: UAV orthomosaics.